SCHOLARLY PUBLICATIONS

A CURRENT AWARENESS BULLETIN
OF RESEARCH OUTPUT

@DTU

(71st Edition)

NOVEMBER, 2018

BY: CENTRAL LIBRARY

DELHI TECHNOLOGICAL UNIVERSITY
(FORMERLY *DELHI COLLEGE OF ENGINEERING)*
GOVT. OF N.C.T. OF DELHI
SHAHBAD DAULATPUR, MAIN BAWANA ROAD
DELHI 110042

PREFACE

This is the **Seventy First** Issue of Current Awareness Bulletin started by Delhi Technological University, Central Library. The aim of the bulletin is to compile, preserve and disseminate information published by the faculty, students and alumni for mutual benefits. The bulletin also aims to propagate the intellectual contribution of Delhi Technological University (DTU) as a whole to the academia.

The bulletin contains information resources available in the internet in the form of articles, reports, presentations published in international journals, websites, etc. by the faculty and students of DTU. The publications of faculty and student which are not covered in this bulletin may be because of the reason that the full text either was not accessible or could not be searched by the search engine used by the library for this purpose.

The learned faculty and students are requested to provide their uncovered publications to the library either through email or in CD, etc. to make the bulletin more comprehensive.

This issue contains the information published during **November, 2018**. The arrangement of the contents is alphabetical. The full text of the article which is either subscribed by the university or available in the web is provided in this bulletin.

Central Library

CONTENTS

11. Macro-mechanical Analysis on the Variation of Fibre Orientation in a Composite UAV Landing Gear, ***8.Harsh Raj Chauhan***, ***3.Vikas Rastogi*** and ***3.Atul Kumar Agarwal***, Mechanical, DTU

12. Maximizing Cloud Revenue using Dynamic Pricing of Multiple Class Virtual Machines, Fadi Alzhouri, ***8.1.Anjali Agarwal*** and Yan Liu, ECE, DTU

13. Modelling of structural and material parameters of optical planar waveguide to control birefringence, Yaman Parasher, Akshay Kaushik, ***3.Dr. Gurjit Kaur*** and Prabhjot Singh, Electronics and Communication, DTU

14. Overview of Welding Using Microwave Radiation, ***6.Uma Gautam*** and ***3.Vipin***, Mechanical, DTU

15. Possessions Vehicle Pursuer and Burglary Recognition Scheme by Way of Fervor Fighting Sytem by Means of IOT, ***6.Rani Medhashree***, Manjula B and Devendra Kumar S M, Electronics and Communications, DTU

16. Rheokinetic studies and compressive response of high performance polybenzoxazine syntactic foams, ***6.A. V. Ullas***, ***6.Pratibha Sharma***, ***3.Devendra Kumar*** and Prasun Kumar Roy, Applied Chemistry and Polymer Technology, DTU

17. Thermodynamic analysis of vapour compression refrigeration systems using multiple evaporators at different temperatures with compound compression, individual and compound expansion valves with flash intercoolers, ***3.R.S. Mishra***, Mechanical & Production, DTU

1. *Chancellor*

2. *Pro Vice Chancellor*	***2.1.*** *Ex Pro Vice Chancellor*
3. *Faculty*	***3.1.*** *Ex Faculty*
4. *Teaching-cum-Research Fellow*	***4.1.****Asst. Librarian*

5. *Alumni*

6. *Research Scholar*	***6.1.*** *Ex Research Scholar*
7. *PG Scholar*	***7.1.*** *Ex PG Scholar*
8. *Undergraduate Student*	***8.1.*** *Ex Undergraduate Student*

A parametric study to unravel the alignment mechanism of carbon nanotubes during its plasma-assisted growth

Umang Sharma, and Suresh C. Sharma

Citation: Physics of Plasmas **25**, 103509 (2018); doi: 10.1063/1.5049866
View online: https://doi.org/10.1063/1.5049866
View Table of Contents: http://aip.scitation.org/toc/php/25/10
Published by the American Institute of Physics

PHYSICS OF PLASMAS **25**, 103509 (2018)

A parametric study to unravel the alignment mechanism of carbon nanotubes during its plasma-assisted growth

Umang Sharma and Suresh C. Sharma
Department of Applied Physics, Delhi Technological University (DTU), Shahbad Daulatpur, Bawana Road, Delhi 110042, India

(Received 26 July 2018; accepted 3 October 2018; published online 22 October 2018)

The alignment and catalyst-assisted growth mechanism of carbon nanotubes (CNTs) in a hydrogen-diluted methane plasma are demonstrated in the present work. The consequence of plasma parameters (plasma density and temperature) and bias potential of the substrate on the sheath electric field is examined. The role of the electric field in the plasma sheath to provide the necessary electrostatic force and its repercussion on the carbon nanotubes alignment in the plasma are studied by taking into contemplation the steady state fluid equations, kinetics of the plasma sheath, charged species dynamics (positive ions and electrons) and neutral atoms in a reactive plasma, kinetics of the catalyst particle, and creation of atomic species of carbon and hydrogen over the surface of catalyst nanoparticle and incorporating various processes vital for the growth of carbon nanotube in plasma. Taking into deliberation the initial conditions and the glow discharge parameters determined experimentally for the model, the numerical solutions for the equations are obtained. The outcomes of the studies revealed that the alignment of the nanotube depends on the force exerted at the tip of CNTs, i.e., the catalyst nanoparticle. This force is a consequence of the plasma sheath electric field which is dependent on the plasma parameters and the bias voltage at the substrate. This electrostatic force is also dependent upon the dimensions of the nanotube growing in the plasma environment and modifies itself continuously conferring to the instantaneous nanotube measurement and alignment during the growth. The present study can be apprehended to manufacture carbon nanotubes aligned vertically in plasma for better applications in the areas of field emission devices. The results of the present study have been assessed and compared with the existing experimental observations which accredit the proposed mechanisms. *Published by AIP Publishing*. https://doi.org/10.1063/1.5049866

I. INTRODUCTION

Carbon nanotubes (CNTs) have been deliberated and produced extensively since their discovery in 1991.[1] Carbon nanotubes (CNTs) and carbon nanofibers (CNFs) are considered the major research area owing to their exceptional properties, i.e., high aspect ratio (length to diameter ratio), very high tensile strength, high conductivity, and applications, i.e., in the field of electronics, biological chemistry, mechanics, etc.[2,3] The designing of vertically aligned and elongated graphitic tubules of carbon which have the significant peculiarity of chemical stability, nanoscale tip size, and high aspect ratio helps to manifest it as a strong candidate for field electron emitters.[4–6] CNTs can be produced by many techniques such as thermal chemical vapour deposition (TCVD),[7,8] plasma-enhanced chemical vapour deposition (PECVD),[9–11] laser ablation,[12,13] arc discharge,[14,15] etc. Amongst these procedures, PECVD has been expansively used for producing the vertically aligned CNT (VACNT).[16–18] The forces acting on CNTs due to the plasma sheath electric field during their growth help in their vertical alignment in the plasma. Over the years, several experimental groups worldwide have produced the VACNT using plasma and have derived various observations regarding its vertical orientation.

Bower *et al.*[19] reported that the growth of CNTs is always oriented perpendicular to the substrate irrespective of the inclination or shape of the substrate and the self-bias potential can be considered as the primary reason behind the alignment of CNTs.

Chhowalla *et al.*[10] showed that in the absence of applied bias, randomly oriented or spaghetti-like nanotubes grow whereas on applying bias voltages, the nanotubes begin to align themselves. They also revealed that for small bias voltages, the nanotubes did not align completely with the substrates, in contrast to high bias voltages leading to the higher electric field, CNTs appeared to be perfectly aligned.

Tanemura *et al.*[20] have observed the catalyst material dependence alignment of CNTs, and the positive ions supplied selectively to the tip of nanotube due to biasing at the substrate which controls the morphology could be the possible reason for the alignment of the CNTs.

Merkulov *et al.*[21] anticipated that the non-uniform stresses (tensile, compressive) across the catalyst interface and force acting on the CNTs/CNFs associate a feedback mechanism which initiates the alignment of the nanostructure.

Chen *et al.*[22] proposed that under the effect of electric field, the charged catalyst particle at the tip of nanotube gets pulled in the electric field direction, i.e., normal to the substrate which governs the direction of growth of CNTs and hence their alignment.

Zhang *et al.*[23] demonstrated that the growth of CNTs by CVD is directed by electric field and studied the CNT

alignment with the electric field and gas flow. The nanotubes grown under no electric field exhibited random orientation in contrast to aligned CNTs grown under bias voltages.

Yu *et al.*[24] obtained highly aligned growth of CNTs under applied substrate bias and random growth of CNTs without the bias voltage. Henceforth, it is hypothesized that the chemical bonds formed between the charged species along the direction of the electric field and hence, induce the vertical alignment.

Maiti *et al.*[25,26] deliberated the growth of the CNT in arc discharge and showed that the position of atoms constituting the nanotube tends to straighten the tube under the effect of potential and restrict it from curving and ultimately closing.

Merchan-Merchan *et al.*[27] synthesized a well aligned graphitized concentric graphitic cylinder and suggested that the alignment of the CNT array growing on a substrate is under the effect of a metal catalytic support in the presence of electric field. They proposed that the axial stresses produced by the electric charges on the CNT aid in its growth and the electric field influences the transport of species.

Blazek *et al.*[28] mathematically computed electric field in the plasma sheath, the forces exerted on the catalyst particle, and the resistivity of the substrate.

Bao *et al.*[29] simulated the electric forces on the catalyst tip and nanotube with varying density, length, and diameter of the nanotube which guides the field for probable nanotube alignment and its use in field emitter devices.

Wei *et al.*[30] experimentally verified the change in the electrostatic force acting on a CNF with plasma parameters and inspected the mechanism for possible detachment of the CNF from the substrate.

Bocharov *et al.*[31] computed the effect of the externally applied electric field on the inclination of an initially grown CNT and showed the dependence of bending angle of the CNT on the local value of electric field due to the polarization of charges.

Pal *et al.*[32] stated that the CNT growth gets influenced by the existence of an electric field which applies a ponderomotive force on the nanotube sufficient for its alignment along the field direction.

In the present work, we propose that the vertically aligned CNT growth is owed to the electric field persuaded in plasma sheath and the growth of nanotubes can be guided by varying the operational plasma parameters. The plasma sheath induced electric field produces an electrostatic force on the CNT growing on a substrate immersed in plasma which governs its alignment. The role of the plasma sheath electric field and corresponding electrostatic force in aligning the CNT is explained in Sec. II using the plasma sheath kinetic equations. The time-dependent differential equations describing the growth of the CNT in complex plasma accounting the dynamics of plasma species, dissociation, diffusion, and precipitation of carbon species on the catalyst, the losses prevailing in the plasma chamber and during the growth, and finally the growth equation for the CNT are also considered in this section. The outcomes of the numerical analysis that reveal the alignment and growth phenomena of the CNT under the guidance of plasma electric field are enlightened in Sec. III. Finally, the present study is concluded in Sec. IV.

II. ANALYTICAL MODELING

In the present model, a collisional plasma with finite electron and ion temperature constituted by plasma species (electrons, positively charged ions, and neutral atoms) of methane (CH_4) and hydrogen (H_2), where CH_4 acts as the main hydrocarbon source gas, and H_2 as the etchant gas is considered. The methane and hydrogen species are denoted as types A and B, respectively. Table I details all the ionic and neutral species of methane and hydrogen considered in the present model. Under the influence of plasma, irrespective of the type of plasma source considered [dc, rf, microwave, Inductively Coupled Plasma (ICP), etc.], vertically aligned CNTs are obtained experimentally. The plasma parameters, namely plasma density and electron temperature considered in the present work, are of the rf plasma source range.

The detailed analysis of the growth model of CNT in a plasma is demonstrated subsequently. The elementary course followed in the nucleation and growth of the CNT in specified plasma are:[33–35]

(a) A pre-deposited nickel (Ni) metal catalyst film is disintegrated into many catalyst nanoparticles owing to the bombardment of highly energetic etchant species in the reactive plasma. These catalyst nanoparticles positioned over a negatively biased substrate are the sites for nucleation of CNT growth.
(b) The hydrocarbon species act as the main source for the generation of carbon species for CNT growth. The hydrogen gas present in the plasma aids in the effective shaping of the nanotube.
(c) The CNT growth over the catalyst-substrate surface initiates via carbon species generated on the active surface of the catalyst by different surface processes viz., adsorption and desorption of hydrocarbon and hydrogen species, diffusion of carbon atoms on the surface and bulk of catalyst particle to form a graphitic tubular structure, thermal dehydrogenation of hydrocarbon species, and many others.
(d) Simultaneous vertical alignment of the CNT during the growth process owing to various plasma operating parameters.
(e) The consistent sticking of neutral species on the growing nanotube leads to catalyst poisoning which eventually ceases the growth process.

The schematic representation of the theoretical model of catalyst-assisted growth and alignment mechanisms of CNT growth in a complex plasma considered in the present

TABLE I. Plasma species considered in the present computation.

Type	Neutral species	Positively charged ions
A	CH, CH_2, CH_3, CH_4, C_2H, C_2H_2, C_2H_3, C_2H_4, C_2H_5, C_2H_6, C_3H_8, C_4H_{10}	CH^+, CH_2^+, CH_3^+, CH_4^+, CH_5^+, C_2H^+, $C_2H_2^+$, $C_2H_3^+$, $C_2H_4^+$, $C_2H_5^+$, $C_2H_6^+$
B	H, H_2	H^+, H_2^+, H_3^+

analysis is given in Fig. 1. The growth of the CNT initiates at the surface of the catalyst nanoparticle due to the decomposition process of hydrocarbon species, the diffusion processes of the C-atoms, the precipitation process through the posterior of the catalyst, lifting it off the substrate surface, and formation of graphitic cylindrical layers; hence primarily the CNT grows perpendicular to the planar substrate. After the initialization of growth, the catalyst-nanotube interface experiences tensile-compressive stresses due to inhomogeneous C-precipitation at this interface which deviates the CNT from its initial orientation. As the growth progresses, these stresses tend to balance each other and the electrostatic force then provides the necessary feedback mechanism for CNT alignment. When there is no instability in the C-precipitation at the catalyst-nanoparticle, the CNTs are aligned in the direction of electrostatic force governed by sheath electric field. When the nanotube is aligned, this force holds a minimum value for the structure to be aligned and the growth carries on.

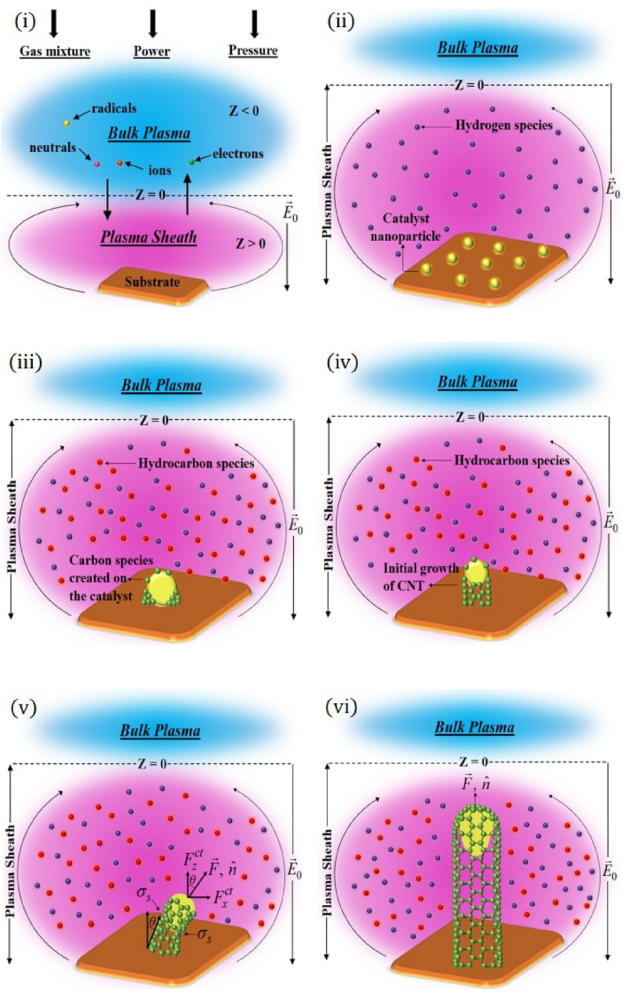

FIG. 1. Schematic representation of the growth and alignment of the CNT in a hydrogen-diluted hydrocarbon plasma. (i) various regions of the plasma model considered, (ii) formation of catalyst nanoparticles in hydrogen plasma, (iii) creation of carbon atoms on the nanoparticle surface, (iv) initialization of growth of the nanotube in the direction of electric field, (v) deviation of CNT alignment due to various components of forces acting on the catalyst surface as well as the catalyst-nanotube interface, and (vi) fully vertically aligned carbon nanotube with the catalyst encapsulated within the carbonaceous layer.

To examine the structure of plasma sheath, energies, and fluxes of the plasma species, a one-dimensional plasma sheath model is considered in the present investigation. Assuming the position of the bulk plasma-sheath interface at $z = 0$, $z < 0$ is the neutral plasma region and $z > 0$ is a non-neutral plasma region [see Fig. 1(i)] governed by the following steady-state fluid equations:[33,36]

$$\vec{\nabla}.(n_{ij}\vec{u_{ij}}) = \nu_{if} n_e\,, \tag{1}$$

$$\vec{\nabla}.(n_e\vec{u_e}) = \sum_{ij} \nu_{if} n_e\,, \tag{2}$$

$$m_{ij} n_{ij} u_{ij} \partial_z(u_{ij}) = e n_{ij} \partial_z(\varphi) - m_{ij} n_{ij} \nu_{cf} u_{ij}, \tag{3}$$

$$0 = e n_e \partial_z(\varphi) - m_e n_e \nu_{cf} u_e, \tag{4}$$

$$\partial_{zz}(\varphi) = 4\pi e\left(n_e - \sum_{ij} \zeta_{ij} n_{ij}\right). \tag{5}$$

Equations (1) and (2) define the ion and electron particle balance equations, respectively. n_{ij}, u_{ij}, and m_{ij} are the number densities, velocities, and masses of the j type ionic species considered in the present model. n_e, u_e, and m_e are the number density, velocity, and mass of the electron. Equations (3) and (4) describe the ion and electron ion-momentum balance equations, respectively. The electrostatic sheath potential is denoted by φ, $\nu_{if}(=\psi_{ij}\zeta_j n_n)$ is the ionization frequency of the neutral atoms due to collision with electrons where ψ_{ij} is the ionization potential of the jth ion, ζ_{ij} is the number density ratio for jth ion to electron, $\sum_{ij}\zeta_{ij} = 0$ and $0 < \zeta_{ij} < 1$, and n_n defines the number density of neutrals. ν_{cf} is the collision frequencies of ions with neutrals. Equation (5) describes the Poisson's equation which determines the electrostatic potential by relating it to the electron and ion number density.

A. Charging of the CNT

Equation (6) represents the time evolution of charge attained by the CNT due to the accretion of positive ions and electrons at the tip and the cylindrical surface of the CNT. Another assumption is made regarding the charge transfer and neutralization of the ionic species incident at the CNT surface

$$\partial_\tau(\mathrm{Z}) = \sum_j \left(\overset{tip}{\underset{ij}{\xi}} + \overset{cyl}{\underset{ij}{\xi}}\right) - \gamma_e\left(\overset{tip}{\underset{e}{\xi}} + \overset{cyl}{\underset{e}{\xi}}\right), \tag{6}$$

where Z is the extent of charge on the CNT surface and γ_e represents the electron sticking coefficient defining the adsorption probability of electrons at the surface

$$\overset{tip}{\underset{ij}{\xi}} = n_{ij}(z)\pi r^2\left(\frac{8k_BT_{ij}}{\pi m_{ij}}\right)^{1/2}[1-\mathrm{Z}\alpha_{ij}]\exp\left[-\frac{E_b}{k_BT_S}\right]\exp\left[-\frac{eU_S}{k_BT_S}\right], \tag{7}$$

$$\overset{cyl}{\underset{ij}{\xi}} = n_{ij}(z) rl\left(\frac{2\pi k_BT_{ij}}{m_{ij}}\right)^{1/2}\left\{\frac{2}{\sqrt{\pi}}\left(\frac{eV_S}{k_BT_{ij}}\right)^{1/2} + \exp\left[\frac{eV_S}{k_BT_{ij}}\right] \times erfc\left[\left(\frac{eV_S}{k_BT_{ij}}\right)^{1/2}\right]\right\} \times \exp\left[-\frac{E_b}{k_BT_S}\right]\exp\left[-\frac{eU_S}{k_BT_S}\right], \tag{8}$$

$$\overset{tip}{\underset{e}{\xi}} = n_e(z)\pi r^2\left(\frac{8k_BT_e}{\pi m_e}\right)^{1/2}\exp\left[Z\alpha_e + \frac{eU_S}{k_BT_S}\right], \quad (9)$$

$$\overset{cyl}{\underset{e}{\xi}} = n_e(z)rl\left(\frac{2\pi k_BT_S}{m_e}\right)^{1/2}\exp\left[\frac{eV_S}{k_BT_e} + \frac{eU_S}{k_BT_S}\right]. \quad (10)$$

Equations (7) and (8) define the collection current of the ionic species at the tip and tubular surface of the CNT, respectively. Equations (9) and (10) define the collection current of electrons at the tip and the tubular surface of the CNT, respectively. The potential at the tubular surface of the CNT is denoted by V_S, the substrate bias is designated by U_S, the temperature of the substrate is defined by T_S, the energy required for the bulk diffusion is symbolized by E_b, r is the radius of the catalyst particle. $\alpha_e\left(=\frac{e^2}{rk_BT_e}\right)$, and α_{ij} $\left(=\frac{e^2}{rk_BT_{ij}}\right)$. The plasma sheath ion and electron density are represented as $n_{ij}(z) = n_{ij0}(1-\frac{2e\varphi(z)}{m_{ij}u_{ij0}^2})^{-1/2}$ and $n_e(z)$ $= n_{e0}\exp(\frac{|e|\varphi(z)}{k_BT_e})$, respectively, where n_{ij0} and n_{e0} are the initial number density for the ionic species and electrons, respectively. u_{ij0} is the initial ion velocity and $\varphi(z) = \varphi_0\exp(-\frac{z}{\lambda_D})$ is the electrostatic potential within the plasma sheath, where $\varphi_0(=U_S)$ is the negative substrate potential and $\lambda_D = \sqrt{\frac{k_BT_e}{n_ee^2}}$ is the Debye length. k_B represents the Boltzmann constant, T_{ij} and T_e symbolise the temperature of the ionic species and electrons, respectively.

B. Dynamics of electron number density

The time evolution of electron density in the bulk plasma is described by the following equation:

$$\partial_\tau(n_e) = \sum_j \beta_j n_j - \sum_j \alpha_j n_e n_{ij} - \gamma_e\frac{n_{CNT}}{\lambda_s}\left(\overset{tip}{\underset{e}{\xi}} + \overset{cyl}{\underset{e}{\xi}}\right) - \mathrm{K}^e_{wall}n_e, \quad (11)$$

where β_j is the j type neutral atom ionization coefficient and $\alpha_j(T_e) = \{\alpha_{j0}(300/T_e)^k\}$ is the recombination coefficient for the ionic species and electrons, where $k = -1.2$ is a constant.[37] n_e, n_j, and n_{ij} represent the electron, neutral, and ion number density, respectively. The CNT number density is represented by n_{CNT}. The last term denotes the electronic species loss rate per unit volume on the discharge wall where $\mathrm{K}^e_{wall} = (\frac{\gamma_e u_e A_{chm}}{4V})$, A_{chm} and V are the surface area and volume of a cylindrical plasma chamber, respectively, having interior diameter of $2R = 32$ cm and length $L = 23$ cm.[38]

In Eq. (11), the first term accounts for the increase in number density of electrons due to dissociative ionization of j type neutral species, the second term accounts for the decrease in the number density of electrons owing to the recombination process between ions and electrons, the third term accounts for the decrease in the number density of electrons due to electron collection at the surface of CNT, and the last term denotes the discharge loss to the wall.

C. Dynamics of positive ion number density

Equations (12) and (13) represent the time evolution of A and B type ion density in the bulk plasma

$$\partial_\tau(n_{iA}) = \beta_A n_A - \alpha_A n_e n_{iA} - \frac{n_{CNT}}{\lambda_s}\left(\overset{tip}{\underset{iA}{\xi}} + \overset{cyl}{\underset{iA}{\xi}}\right) + \sum_{\ell AB} k_\ell n_A n_{iB} - \sum_{qBA} k_q n_B n_{iA} - \mathrm{K}^{iA}_{wall}n_{iA} + \left(\frac{P}{E^{diss}_{CH}V}\right), \quad (12)$$

$$\partial_\tau(n_{iB}) = \beta_B n_B - \alpha_B n_e n_{iB} - \frac{n_{CNT}}{\lambda_s}\left(\overset{tip}{\underset{iB}{\xi}} + \overset{cyl}{\underset{iB}{\xi}}\right) + \sum_{qBA} k_q n_B n_{iA} - \sum_{\ell AB} k_\ell n_A n_{iB} - \mathrm{K}^{iB}_{wall}n_{iB} + \left(\frac{P}{E^{diss}_{H}V}\right), \quad (13)$$

where $\mathrm{K}^{ij}_{wall} = \left(\frac{\gamma_{ij}u_{ij}A_{chm}}{4V}\right)$ represents the discharge loss of j type ions to the wall, γ_{ij} is the sticking coefficient of respective ions,[38] k_q and k_l are the neutral-ion reaction rate coefficients, P is the applied power, and $\delta E^{diss}_{CH}(\approx 2.1\,\mathrm{eV})$ and $\delta E^{diss}_{H}(\approx 2.1\,\mathrm{eV})$ are the hydrocarbon and hydrogen dissociation energies, respectively.[36]

In Eqs. (12) and (13), the first term characterizes the increase in ion number density owing to the j type neutral species dissociative ionization, the second term incorporates the loss in the ion number density due to electron-positive ion recombination process, the third term indicates the loss in the ion number density because of the collection of ions on the CNT surface, the fourth and fifth terms denote the positive ion-neutral reactions in the plasma at different reaction rates, respectively, the sixth term indicates the ion discharge loss to the wall of the chamber, and lastly, the increase in ion number density is due to the dissociation by plasma power.

D. Dynamics of neutral atom number density

The time evolution of A and B type neutral atoms in the bulk plasma is represented as

$$\partial_\tau(n_A) = \alpha_A n_e n_{iA} - \beta_A n_A + \frac{n_{CNT}}{\lambda_s}(1-\gamma_{iA})\left(\overset{tip}{\underset{iA}{\xi}} + \overset{cyl}{\underset{iA}{\xi}}\right) - \frac{n_{CNT}}{\lambda_s}\gamma_A\left(\overset{tip}{\underset{A}{\xi}} + \overset{cyl}{\underset{A}{\xi}}\right) + \mathrm{Q}^{IF}_A - \mathrm{Q}^{OF}_A - \sum_{lBA} k_l n_A n_{iB} + \sum_{qAB} k_q n_B n_{iA} - J^{adsp}_A + J^{desp}_A - \mathrm{K}^A_{wall}n_A, \quad (14)$$

$$\partial_\tau(n_B) = \alpha_B n_e n_{iB} - \beta_B n_B + \frac{n_{CNT}}{\lambda_s}(1-\gamma_{iB})\left(\overset{tip}{\underset{iB}{\xi}} + \overset{cyl}{\underset{iB}{\xi}}\right) - \frac{n_{CNT}}{\lambda_s}\gamma_B\left(\overset{tip}{\underset{B}{\xi}} + \overset{cyl}{\underset{B}{\xi}}\right) + \mathrm{Q}^{IF}_B - \mathrm{Q}^{OF}_B - \sum_{qBA} k_q n_B n_{iA} + \sum_{\ell AB} k_\ell n_A n_{iB} - J^{adsp}_B + J^{desp}_B + J_{thd} - \mathrm{K}^B_{wall}n_B, \quad (15)$$

where $\mathrm{Q}^{IF}_j = \left(\frac{4.4\times10^{17}}{V}J_j\right)$ and $\mathrm{Q}^{OF}_j = \left(\frac{\upsilon_{pump}}{V}n_j\right)$ are the influx and out flux rates of j type species from the chamber,

respectively.[38] γ_j is the neutral atom sticking coefficient, J_j is the inlet flow of the respective gas, and υ_{pump} is the pumping rate. J_j^{adsp} and J_j^{desp} are the fluxes of adsorption and desorption on/from the catalyst-substrate surface, respectively. J_{thd} is the thermal dehydrogenation flux of the hydrogen species, $K_{wall}^{j} = \sigma_j \frac{D_j}{\Lambda^2}$ signifies the discharge loss of j type neutrals, σ_j is the wall reaction coefficient, D_j is the diffusion coefficient which considers the motion of respective species within the plasma constituents which is defined by binary diffusion coefficients $D_{j,j'}$ of j type species on j' through Blanc's law, $\frac{1}{D_j} = \frac{1}{D_{j,CH_4}} + \frac{1}{D_{j,H_2}}$ as the dominant species are CH_4 and H_2, and $\Lambda = \left(\frac{RL}{\left\{(2.405L)^2+(\pi R)^2\right\}^{1/2}}\right)$ is the effective diffusion length of the chamber for a cylindrical setup.[33,39]

In Eqs. (14) and (15), the first term represents the rise in the neutral atom density owing to the electron-positive ion recombination process, the second term represents the loss due to dissociative ionization of j type neutrals, the third term represents the increase in neutral atom density due to neutralization of ionic species after their collection at the CNT surface, and the fourth term represents the loss of neutrals due to collection on the CNT surface. The fifth and sixth terms define the plasma chamber influx and outflux of the j type neutral species, respectively. The seventh and eighth terms define the change in the density of the neutral atoms due to the neutral-positive ion reactions considered in the model (see Table II). The ninth and tenth terms describe the neutral species adsorption and desorption onto/from the surface of the catalyst. The eleventh term of Eq. (15) incorporates the thermal dehydrogenation process corresponding to the rate of increase in hydrogen species density.[40] The last terms of both equations represent the discharge loss of j type neutrals to the cylindrical chamber wall. The wall reaction coefficient σ_j is incorporated to take into account neutral losses to the wall (see Table III). This term represents the rate at which the neutral species are lost to the wall by embedding or recombination. This implies that only fractions of species are lost via diffusion to the walls and the remaining return to the plasma.

TABLE II. Ion-neutral reactions taken into consideration in the CH_4/H_2 plasma model, as well as their reaction rate coefficients (Ref. 46).

Reactions	k (cm^3 s^{-1})
$CH_4^+ + CH_4 \rightarrow CH_5^+ + CH_3$	1.5×10^{-9}
$CH_4^+ + H_2 \rightarrow CH_5^+ + H$	3.3×10^{-11}
$CH_3^+ + CH_4 \rightarrow CH_4^+ + CH_3$	1.36×10^{-10}
$H_2^+ + H_2 \rightarrow H + H_3^+$	2.5×10^{-9}
$CH_3^+ + CH_4 \rightarrow C_2H_5^+ + H_2$	1.2×10^{-9}
$H_3^+ + C_2H_6 \rightarrow C_2H_5^+ + 2H_2$	2.0×10^{-9}
$H_3^+ + CH_4 \rightarrow CH_5^+ + H_2$	1.6×10^{-9}
$H_3^+ + C_2H_4 \rightarrow C_2H_5^+ + H_2$	1.9×10^{-9}
$H_3^+ + C_2H_2 \rightarrow C_2H_3^+ + H_2$	1.94×10^{-9}
$C_2H_2^+ + CH_4 \rightarrow C_2H_3^+ + CH_3$	4.1×10^{-9}
$C_2H_2^+ + CH_4 \rightarrow C_3H_4^+ + H_2$	6.25×10^{-10}
$C_2H_2^+ + CH_4 \rightarrow C_3H_5^+ + H$	1.44×10^{-9}
$C_2H_4^+ + C_2H_4 \rightarrow C_3H_5^+ + CH_3$	3.9×10^{-10}
$C_2H_4^+ + C_2H_4 \rightarrow C_4H_8^+$	4.3×10^{-10}
$CH_5^+ + C_2H_6 \rightarrow C_2H_5^+ + H_2 + CH_4$	5.0×10^{-10}
$C_2H_4^+ + C_2H_6 \rightarrow C_3H_6^+ + CH_4$	2.03×10^{-13}
$C_2H_4^+ + C_2H_6 \rightarrow C_3H_7^+ + CH_3$	1.32×10^{-11}
$C_2H_5^+ + C_2H_2 \rightarrow C_4H_7^+$	6.7×10^{-10}
$C_2H_5^+ + C_2H_4 \rightarrow C_3H_5^+ + CH_4$	3.1×10^{-10}
$C_2H_5^+ + C_2H_4 \rightarrow C_4H_9^+$	3.0×10^{-10}

TABLE III. Neutral-wall reactions for discharge losses considered in the model and their rate coefficients (Ref. 39).

Reactions	Rate coefficient (σ)
$CH_4 \xrightarrow[\sigma]{wall} CH_4$	$\sigma = 0$
$CH_3 \xrightarrow[\sigma]{wall} CH_3$	$\sigma = 0.01$
$CH_2 \xrightarrow[\sigma]{wall} CH_2$	$\sigma = 0.01$
$CH \xrightarrow[\sigma]{wall} CH$	$\sigma = 0.01$
$C_2H_2 \xrightarrow[\sigma]{wall} C_2H_2$	$\sigma = 0.01$
$C_2H_3 \xrightarrow[\sigma]{wall} C_2H_3$	$\sigma = 0.01$
$C_2H_4 \xrightarrow[\sigma]{wall} C_2H_4$	$\sigma = 0.01$
$C_2H_5 \xrightarrow[\sigma]{wall} C_2H_5$	$\sigma = 0.01$
$C_2H_6 \xrightarrow[\sigma]{wall} C_2H_6$	$\sigma = 0.01$
$C_3H_8 \xrightarrow[\sigma]{wall} C_3H_8$	$\sigma = 0.01$
$H_2 \xrightarrow[\sigma]{wall} H_2$	$\sigma = 0.07$
$H \xrightarrow[\sigma]{wall} H$	$\sigma = 1$
$2H \xrightarrow[\sigma]{wall} H_2$	$\sigma = 0.05$

E. Carbon and hydrogen species generated over the catalyst surface

The hydrocarbon and hydrogen precursors decompose over the catalyst surface undergoing numerous surface processes. This decomposition results in the generation of carbon species and hydrogen radicals crucial for the growth of the CNT. The time evolution of the carbon and hydrogen species created per unit area over the surface of the catalyst is given by

$$\begin{aligned}\partial_\tau(n_C) = \Bigg[& \sum_A \left\{ J_A(1-\theta_t) + n_A^{surf}\upsilon \exp\left(-\frac{\delta E_{CH}^{diss}}{k_B T_S}\right) \right. \\ & \left. - n_A \upsilon \exp\left(-\frac{\delta E_{dCH}}{k_B T_S}\right) \right\} + \sum_{iA} \left\{ \left(\sum_A \frac{n_A^{surf} y_d}{\upsilon_0} \right) J_{iA} + J_{iA} \right\} \\ & + J_C + \sum_{iB} \left(\sum_{iA} \frac{J_{iA}\sigma_{ads}}{\upsilon} \right) J_{iB} - \sum_B \left(\sum_A n_A^{surf} \sigma_{ads} \right) J_B \\ & - n_C \upsilon \exp\left(-\frac{\delta E_{ev}}{k_B T_S}\right) - n_C \sigma_{ads} \upsilon n_H \Bigg] \times d_\tau(\Omega_C), \end{aligned} \tag{16}$$

$$\begin{aligned}\partial_\tau(n_H) = & \sum_B \left\{ J_B(1-\theta_t) + n_B^{surf}\upsilon \exp\left(-\frac{\delta E_H^{diss}}{k_B T_S}\right) \right. \\ & \left. - n_B^{surf}\upsilon \exp\left(-\frac{\delta E_{dH}}{k_B T_S}\right) - n_B^{surf}\sigma_{ads} J_B - n_B^{surf}\sigma_{ads} J_{iB} \right\} \\ & + \sum_{iA} \left(\sum_A \frac{n_A^{surf} y_d}{\upsilon_0} \right) J_{iA} + \sum_{iB} J_{iB} - n_H \sigma_{ads} \upsilon n_C, \end{aligned} \tag{17}$$

where n_C and n_H are the number density of carbon and hydrogen species generated per unit area on the catalyst surface, respectively. The functional terms and parameters

TABLE IV. Description of the functions/parameters mentioned in Eqs. (16) and (17).

Functions/parameters	Description
$\upsilon_0 (\approx 10^{15}\,\mathrm{cm}^{-2})$	Adsorption sites per unit area[40]
$\upsilon (\approx 10^{13}\,\mathrm{Hz})$	Thermal vibration frequency[51]
$\sigma_{ads} (= 6.8 \times 10^{-16}\mathrm{cm}^2)$	Cross-section of interaction amongst various species[40]
$n_j^{surf} (= \theta_j \upsilon_0)$	Surface number density of the j type neutral atom[40,52]
θ_j	Surface coverage by the j type neutral species[51]
$\delta E_{ev} (= 1.8\,\mathrm{eV})$	Evaporation energy of the carbon atoms[36]
$\delta E_{dCH} (= 1.8\,\mathrm{eV})$	Desorption energy for hydrocarbon species[36]
$\delta E_{dH} (= 1.8\,\mathrm{eV})$	Desorption energy for hydrogen species[36]
Ω_C	Blocking function for the catalyst particle[41]

mentioned in Eqs. (16) and (17) are described in Table IV. The rate of generation of carbon species over the surface of the catalyst is represented by Eq. (16). The first and second terms designate the increase in carbon number density due to the adsorption of neutral hydrocarbons over the surface of the catalyst and the hydrocarbon thermal dissociation, respectively. The third term denotes decrease in carbon number density owed to the desorption of hydrocarbon species from the surface of the catalyst, and the fourth and fifth terms indicate the increase in carbon density due to the hydrocarbon ion-induced dissociation and positive ion decomposition, respectively. The sixth term represents the carbon influx directly towards the particle surface and the seventh term denotes the increase due to the ion-ion interaction of hydrocarbon and hydrogen ions. The eighth term shows the decrease in carbon species owing to the hydrocarbon neutrals and hydrogen interaction. The ninth and tenth terms incorporate the reduction due to evaporation of carbon species and interaction between the carbon and hydrogen species generated on the catalyst nanoparticle, respectively. The incessant dissociation of hydrocarbon species on the catalyst active regions creates an abundance of carbon species. This leads to the amorphous carbon layer formation, which over time poisons the catalyst and restricts the dissociation of hydrocarbon species any further due to the absence of an active region on the catalyst surface. The term $d_\tau(\Omega_C) = (1 - 4n_C\pi r^2)$ of Eq. (16) indicates the rate of poisoning of the catalyst which depends upon the carbon number density over the catalyst surface generated throughout the growth.[41]

The creation of hydrogen species on the surface of the catalyst is represented by Eq. (17). The first and second terms denote the increase in hydrogen species due to adsorption of hydrogen neutral species on the surface of the catalyst and thermal dissociation of the hydrocarbons, respectively. The third term denotes the loss due to desorption of hydrogen from the surface of the catalyst. The fourth and fifth terms represent the interaction between the hydrogen adsorbed on the surface with the incoming neutrals and ions of hydrogen, respectively. The sixth and seventh terms denote the increase due to the hydrocarbon ion-induced dissociation and hydrogen influx near the particle surface. The last term signifies the loss in hydrogen caused by interaction between the generated hydrogen and carbon species on the nanoparticle.

F. Growth equation and alignment mechanism of the CNT

The growth of the CNT in a reactive plasma is evaluated in Eq. (18), i.e., a volumetric change in the CNT (variation of radius and height) with the number densities of carbon and hydrogen species generated over the surface of the catalyst by considering various growth processes

$$\partial_\tau(\pi r^2 l) = \left[\left\{D_S + D_b + 2\kappa\upsilon r^2\right\} \times \frac{P(8\pi r) n_C}{\upsilon \rho_{CNT} \sum_A \xi_{iA}} + \left\{\frac{D_m}{4\pi r^2} + n_H (4\pi r^2) \sum_B \xi_{iB}\right\}\right] \times \frac{m_{ct}}{\rho_{ct}}. \tag{18}$$

The functional terms and parameters mentioned in Eq. (18) are described in Table V. The first term represents the carbon species diffusion over the surface of the catalyst. The diffusion over the catalyst surface is dominant for the growth of outer shells of the CNT. However, the second term denotes the carbon species bulk diffusion through the catalyst. The third term signifies the incorporation or precipitation of carbon species around the posterior of the catalyst particle and forms an inner cylindrical shell. The dominance of bulk diffusion over the surface diffusion leads to the formation of Multi-walled carbon nanotubes (MWCNTs); otherwise Single-walled carbon nanotubes (SWCNTs) are formed and this generally depends on the substrate temperature and catalyst particle size.[42,43] The formation of graphitic shells develops the stress between the graphene sheet and catalyst rear interface. The fourth term denotes the metal catalyst particle self-diffusion along the growth direction of the CNT. An etching gas, here hydrogen, is added to etch out the terminally stuck carbon atoms and promote the CNT growth along the vertical direction. Thus, the last term represents the hydrogen etching of the growing CNT walls.

For a strongly negative biased substrate, the positively charged ions entering the plasma sheath get accelerated by the plasma potential. The ion flux towards the substrate is defined as ion current density, J_{ij} directed towards the

TABLE V. Description of the functions/parameters mentioned in Eq. (18).

Functions/parameters	Description
$D_S = a_0^2 \upsilon \exp\left(-\frac{E_S}{k_B T_S}\right)$	Surface diffusion coefficient of carbon atoms[40]
$D_b = \frac{\upsilon r}{\pi} \exp\left(-\frac{E_b}{k_B T_S}\right)$	Bulk diffusion coefficient of carbon atoms[40]
$D_m = D_{m0} \exp\left(-\frac{\delta E_{sd}}{k_B T_S}\right)$	Self-diffusion coefficient for metal atoms[40]
$\kappa = a_0 \upsilon \exp\left(-\frac{\delta E_{inc}}{k_B T_S}\right)$	Incorporation rate of carbon atoms into the CNT wall[40,52]
$a_0 (= 0.34\,\mathrm{nm})$	Interatomic distance between carbon atoms
$E_S (= 0.3\,\mathrm{eV})$	Energy barrier for carbon species surface diffusion over catalyst surface[40]
$E_b (= 1.6\,\mathrm{eV})$	Energy barrier for carbon species surface diffusion through the catalyst[40]
$P (\approx 20\,\mathrm{GPa})$	Pressure which the graphitic layers exert on the nanoparticle[53]
$\delta E_{inc} (= \delta E_d = 0.8\,\mathrm{eV})$	Energy barrier for carbon species to diffuse along the nanotube-catalyst boundary[52]

substrate due to negative biasing. The electron current density, J_e, is electron flux directed away from the substrate and antiparallel to J_{ij}. These particle fluxes in the plasma sheath can be represented as $J_{ij} = n_{ij}eu_{ij}$, and $J_e = \left(\frac{-n_e e u_{th}}{4}\right)$, where $u_{ij} = \left(\frac{k_B T_e}{m_{ij}}\right)^{1/2}$ is the Bohm velocity of ions and $u_{th} = \left(\frac{8k_B T_e}{\pi m_e}\right)^{1/2}$ is the thermal velocity of electrons. As there are no electrons present in the high voltage sheath region, Poisson's equation can be solved considering $\varphi(0) = 0$, and $d_z\varphi(0) = 0$, as the boundary conditions, giving

$$-\varphi(z) = \left\{\left(\frac{3}{2}\right)^{4/3}\left(\frac{J_{ij}}{\varepsilon_0}\right)^{2/3}\left(\frac{2e}{m_{ij}}\right)^{-1/3} z^{4/3}\right\}. \tag{19}$$

Taking $\varphi(\lambda_s) = -U_S$ in Eq. (19) and solving gives

$$\lambda_s = \left\{\frac{2}{3}\left(\frac{2e\varepsilon_0^2}{m_{ij}}\right)^{1/4}\frac{U_S^{3/4}}{J_{ij}^{1/2}}\right\}, \tag{20}$$

where U_S is the negative bias on the substrate, λ_s is the plasma sheath width, and ε_0 is the free space permittivity. Equation (20) is notably known as the Child law for space-charge-limited current. The sheath electric field near the substrate (E_0), i.e., where $z = \lambda_s$ can be estimated using the Child law, substitution of Eq. (20) in Eq. (19) and as $E(z) = -d_z(\varphi)$, gives

$$E_0 = \left\{\left(\frac{6m_{ij}}{e\varepsilon_0^2}\right)^{1/3} J_{ij}^{2/3}\lambda_s^{1/3}\right\} = \left\{2\left(\frac{m_{ij}}{2e\varepsilon_0^2}\right)^{1/4} J_{ij}^{1/2}U_S^{1/4}\right\},$$

$$E_0 = \left\{2\left(\frac{m_{ij}}{2e\varepsilon_0^2}\right)^{1/4}(n_{ij}eu_{ij})^{1/2}U_S^{1/4}\right\}$$

$$= \left\{2\left(\frac{k_B e}{2\varepsilon_0^2}\right)^{1/4} n_{ij}^{1/2}T_e^{1/4}U_S^{1/4}\right\}. \tag{21}$$

This electric field varies increasingly with the bias voltage of the substrate as well as the ion current density.

To evaluate the force exerted on a CNT and to study the influence of plasma on the CNT alignment, a simple model is considered where a single CNT with a hemispherical catalyst tip is grown in the presence of a complex plasma. During the growth of the CNT, the generation of carbon species over the catalyst surface forms graphitic layers due to various surface processes and their inhomogeneous C-precipitation leads to the introduction of compressive and tensile stresses between the catalyst-nanotube interfaces leading to the deviation from CNT vertical alignment. These stresses can perhaps aid in the carbon diffusion at the CNT where the carbon concentration is less thereby providing a feedback mechanism.[21] The stress introduced at this interface can be assessed as $\sigma_s = F_n^{ct}/\pi r^2$ where r is the radius of the hemispherical catalyst tip.[27] The electric field (E_0) is present nearby the surface of the substrate in the plasma sheath. Following basic electrostatics, it is known that a conducting surface experiences a downward electrostatic pressure, $p = \left(\frac{1}{2}\varepsilon_0 E^2\right)$ due to the local electric field (E) outward normal to the surface. The pressure acting on the catalyst surface induces a net upward force which causes the vertical alignment. The electric force acting upon the catalyst nanoparticle per unit area is given by $dF_n^{ct} = \frac{1}{2}\varepsilon_0 E^2 dA$, where dA is the unit surface area of the catalyst nanoparticle. The pressure acting on the wall of the cylindrical surface is negligible or due to cylindrical symmetry, it cancels out. The local electric field acting upon this geometry creates a dipole which produces components of a dipolar field. This electric field at the apex of the CNT is estimated using a simple floating sphere model which gives the corresponding field enhancement factor $\beta = \left(\frac{l}{r} + 0.5 + 3\cos\theta\right)$, where r is the radius of the hemispherical catalyst tip, l is the distance of the hemisphere from the substrate surface namely the length of CNT, and θ denotes the angle between the vertical axis and normal to the hemisphere.[44] The total field acting on top of the catalyst particle will be given by $E_{top} = \beta E_0$, where E_0 is the plasma sheath electric field around the substrate vicinity. The electrostatic force acting in the planar direction to the substrate is given as[30]

$$F_x^{ct} = \left\{\frac{1}{2}\varepsilon_0\int (E_{top})^2 dA\hat{r}\,.\,\hat{x}\right\},$$

$$F_x^{ct} = \left\{\frac{1}{2}\varepsilon_0\int (E_0\beta)^2\sin\theta dA\right\},$$

$$F_x^{ct} = \left\{\frac{1}{2}\varepsilon_0\int \left[\frac{l}{r} + 0.5 + 3\cos\theta\right]^2 E_0^2(2\pi r^2\sin\theta)\sin\theta d\theta\right\}. \tag{22}$$

Now, the electrostatic force F_z^{ct} acting in the z direction of a unit area dA on the catalyst particle responsible for vertical alignment is given as

$$F_z^{ct} = \left\{\frac{1}{2}\varepsilon_0\int (E_{top})^2 dA\hat{r}\,.\,\hat{z}\right\},$$

$$F_z^{ct} = \left\{\frac{1}{2}\varepsilon_0\int (E_0\beta)^2\cos\theta dA\right\},$$

$$F_z^{ct} = \left\{\frac{1}{2}\varepsilon_0\int \left[\frac{l}{r} + 0.5 + 3\cos\theta\right]^2 E_0^2(2\pi r^2\sin\theta)\cos\theta d\theta\right\}, \tag{23}$$

$$F_z^{ct} = \left\{\int 4\pi\left(\frac{k_B e}{2}\right)^{1/2}\left(n_{ij}T_e^{1/2}U_S^{1/2}\right) \times [l + (0.5 + 3\cos\theta)r]^2\sin\theta\cos\theta d\theta\right\}. \tag{24}$$

In Eq. (22), the force F_x^{ct} represents the repulsive force acting between the neighbouring CNTs if a CNT array is considered. If an array of nanotubes is considered with s being the inter-CNT separation, the effective electric field at the tip of the catalyst particle will consist of a screening factor defined by $S = 1 - \exp(-1.1586s)$.[30] For simplification

of the model and calculations, only a single carbon nanotube is considered. It may be assumed that the axial stresses and the planar force component together resolve any further fluctuations prevailing in the feedback of carbon precipitation and the force F_z^{ct} represented by Eq. (24) holds the responsibility of aligning the CNT in the direction perpendicular to the substrate.

Some may hypothesize that the alignment of the CNT was due to the selective supply of positive ions at the tip of the CNT under the effect of an applied substrate bias (Ref. 20). This would mean that on undertaking this form of supply under the effect of a small negative bias also, only vertically aligned CNTs and no random CNTs should be observed but experimentally, for a small negative bias, only randomly oriented CNTs were observed. Moreover, this selective supply of positive ions greatly to the tip of the CNT, where the catalyst is present, will lead to a more rapid poisoning of the catalyst due to the increase in generation of carbon atoms on the nanoparticle surface and saturate the growth further. Another hypothesis could be that the electrostatic attraction between neighbouring nanotubes. Bower *et al.*[19] performed an experiment where they grow the CNT by thermal as well as PECVD. During the growth process via PECVD, vertically aligned nanotubes were obtained and on turning off the plasma, i.e., in the thermal environment, nanotubes were observed to be growing in a curly or random way. Similar results demonstrating the electrostatic deflection of nanotube have been obtained by Poncharal *et al.*[45] Thus, if the alignment was a consequence of the Van der Waals forces or the crowding effect amongst the CNTs, the growth would have proceeded to be in an aligned way during thermally assisted growth as was in the case of the plasma-assisted growth.

The growth axis of the CNT coincides with the electrostatic force direction exerted over the catalyst. This force produces an even stress around the CNT-catalyst interface. The carbon species precipitates out of this interface, forming a vertically aligned cylindrical graphitic structure. A compressive stress is produced at the CNT-catalyst interface where a superior growth rate is present and a tensile stress where a lesser growth rate is existent. These contradictory stresses acting on the interface support the carbon incorporation in the region where lesser growth is observed. This effect of stress-induced diffusion equalizes the growth rate around the nanotube-catalyst interface and maintains the vertical alignment of the CNT.

III. NUMERICAL RESULTS AND DISCUSSION

The present work provides an insight on the vertical alignment and growth of the CNT in plasma by developing an analytical model. The carbon and hydrogen species generated over the surface of the catalyst via several inherent surface processes, carbon species diffusing over the surface and bulk of the metal catalyst surface, carbon species precipitating out from the posterior of catalyst, poisoning of the catalyst due to the amorphous carbon layer formation, and nucleation, growth, and alignment of nanotubes have been incorporated in the present work.

The first order simultaneous differential equations described in Sec. II are solved using the initial conditions determined experimentally and plasma glow discharge parameters[9,17,46–48] that are mentioned in Tables VI and VII to study the effect of plasma on the corresponding electrostatic force exerted over the growing CNT structure.

A. Variation of CNT dimensions with growth time

Figures 2(i) and 2(ii) show the temporal behaviour of the CNT radius and length grown in the plasma, respectively, for different number densities of hydrocarbon ions and electron temperature. The result indicates that as the growth time progresses, the CNT radius and length increase and with time attains saturation for a fixed value of number density of hydrocarbon ions and electron temperature. Primarily, the carbon species generated over the surface of the catalyst are deposited and subsequently the amorphous carbon is etched by the hydrogen species which enriches the growth of the CNT. With time, progressive growth of the amorphous carbon layer leads to the catalyst poisoning, and thereby, saturating the CNT growth. For lower hydrocarbon ion density, the ion dissociation and ion-induced dissociation over the catalyst surface decrease and lead to the lower carbon surface concentration as compared to hydrogen radicals [cf. Figs. 3(i) and 3(ii)]. Whereas on increasing the ion number

TABLE VI. Parametric initialization of the number density of various plasma species deliberated in the present computation assumed by the literature of plasma composition of the CH_4/H_2 glow discharge.

Species	Mass (1 amu = 1.66×10^{-27} kg)	Number density (cm^{-3})
E	0.0005486 amu	1.0×10^{10}
CH	13 amu	1.0×10^{10}
CH_2	14 amu	0.2×10^{10}
CH_3	15 amu	0.1×10^{13}
CH_4	16 amu	1.0×10^{14}
C_2H	25 amu	1.0×10^{9}
C_2H_2	26 amu	0.2×10^{14}
C_2H_3	27 amu	0.4×10^{11}
C_2H_4	28 amu	0.4×10^{13}
C_2H_5	29 amu	0.1×10^{11}
C_2H_6	30 amu	0.8×10^{12}
C_3H_8	44 amu	1.0×10^{10}
C_4H_{10}	58 amu	0.1×10^{9}
H	1 amu	0.7×10^{14}
H_2	2 amu	1.0×10^{15}
CH^+	13 amu	0.7×10^{6}
CH_2^+	14 amu	1.0×10^{7}
CH_3^+	15 amu	0.2×10^{9}
CH_4^+	16 amu	0.2×10^{9}
CH_5^+	17 amu	0.5×10^{9}
C_2H^+	25 amu	0.1×10^{7}
$C_2H_2^+$	26 amu	0.2×10^{10}
$C_2H_3^+$	27 amu	0.2×10^{10}
$C_2H_4^+$	28 amu	0.3×10^{9}
$C_2H_5^+$	29 amu	0.1×10^{10}
$C_2H_6^+$	30 amu	0.4×10^{8}
H^+	1 amu	0.4×10^{9}
H_2^+	2 amu	0.6×10^{9}
H_3^+	3 amu	0.1×10^{8}

TABLE VII. Parametric initialization of the various parameters deliberated in the present computation assumed by the experimentally determined conditions.

Parameter	Initial value
rf power	50–200 W
Working pressure	50 mTorr
T_e (electron temperature)	2.5 eV
T_{ij} (ion species temperature)	0.20 eV
T_n (neutral atom temperature)	0.20 eV
$T_s = T_{ct}$ (substrate and catalyst temperature)	300 °C
ρ_{ct} (nickel catalyst density)	8.96 gm/cm^3
γ_e (electron sticking coefficient)	1
γ_{ij} (ions sticking coefficient)	1
γ_j (neutral atoms sticking coefficient)	1
U_S (negative substrate bias voltage)	500 V
θ_t (total surface coverage)	0.01
J_{CH_4} (methane gas flow)	30 sccm
J_{H_2} (hydrogen gas flow rate)	100 sccm
α_{j0} (ion-electron recombination coefficient)	1.12×10^{-7} cm^3/s

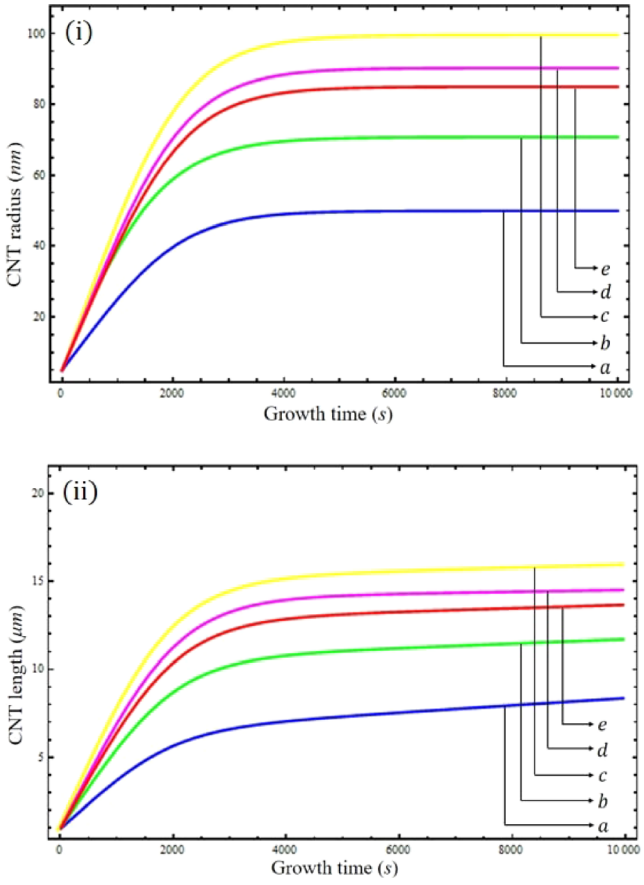

FIG. 2. (i) Time evolution of the CNT radius with changing plasma parameters (where a, b, c, d, and e corresponds to $n_{iA0} = 0.2 \times 10^9$ cm^{-3}, $T_{e0} = 1.5$ eV; $n_{iA0} = 0.4 \times 10^9$ cm^{-3}, $T_{e0} = 1.75$ eV; $n_{iA0} = 0.6 \times 10^9$ cm^{-3}, $T_{e0} = 2.0$ eV; $n_{iA0} = 0.8 \times 10^9$ cm^{-3}, $T_{e0} = 2.25$ eV; and $n_{iA0} = 1.0 \times 10^9$ cm^{-3}, and $T_{e0} = 2.5$ eV, respectively). (ii) Time evolution of the CNT length with changing plasma parameters (where a, b, c, d, and e correspond to $n_{iA0} = 0.2 \times 10^9$ cm^{-3}, $T_{e0} = 1.5$ eV; $n_{iA0} = 0.4 \times 10^9$ cm^{-3}, $T_{e0} = 1.75$ eV; $n_{iA0} = 0.6 \times 10^9$ cm^{-3}, $T_{e0} = 2.0$ eV; $n_{iA0} = 0.8 \times 10^9$ cm^{-3}, $T_{e0} = 2.25$ eV; and $n_{iA0} = 1.0 \times 10^9$ cm^{-3}, and $T_{e0} = 2.5$ eV, respectively).

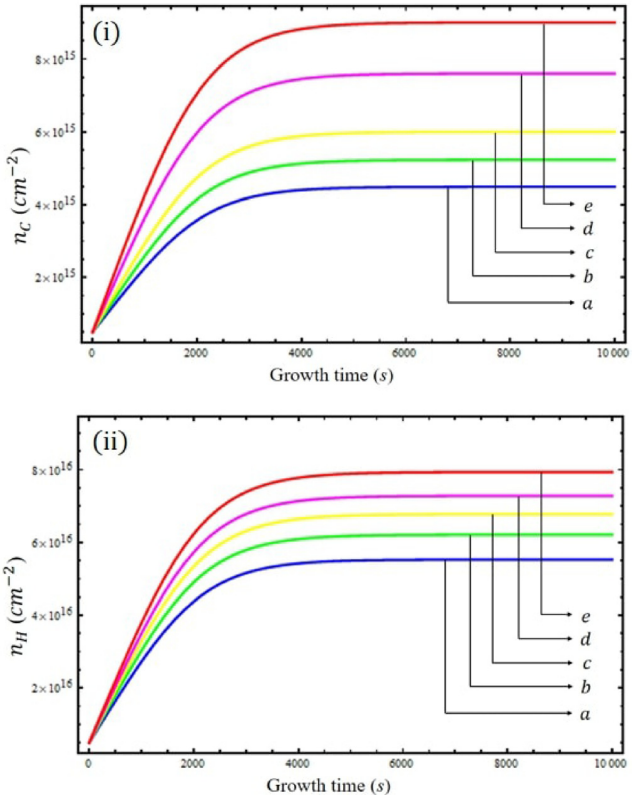

FIG. 3. (i) Temporal behaviour of carbon species number density created on the catalyst surface as a function of different plasma parameters (where a, b, c, d, and e correspond to $n_{iA0} = 0.2 \times 10^9$ cm^{-3}, $T_{e0} = 1.5$ eV; $n_{iA0} = 0.4 \times 10^9$ cm^{-3}, $T_{e0} = 1.75$ eV; $n_{iA0} = 0.6 \times 10^9$ cm^{-3}, $T_{e0} = 2.0$ eV; $n_{iA0} = 0.8 \times 10^9$ cm^{-3}, $T_{e0} = 2.25$ eV; and $n_{iA0} = 1.0 \times 10^9$ cm^{-3}, and $T_{e0} = 2.5$ eV, respectively). (ii) Temporal behaviour of hydrogen species number density created on the catalyst surface as a function of different plasma parameters (where a, b, c, d, and e correspond to $n_{iA0} = 0.2 \times 10^9$ cm^{-3}, $T_{e0} = 1.5$ eV; $n_{iA0} = 0.4 \times 10^9$ cm^{-3}, $T_{e0} = 1.75$ eV; $n_{iA0} = 0.6 \times 10^9$ cm^{-3}, $T_{e0} = 2.0$ eV; $n_{iA0} = 0.8 \times 10^9$ cm^{-3}, $T_{e0} = 2.25$ eV; and $n_{iA0} = 1.0 \times 10^9$ cm^{-3}, $T_{e0} = 2.5$ eV, respectively).

density, carbon species generated over the particle surface increase resulting in enhanced CNT growth. However, it should also be noted that going beyond an optimum value of ion number density, the carbon concentration over the surface of the catalyst increases rapidly which in turn poisons the catalyst quickly. This can be interpreted from the blocking function that for a greater number of carbon species the catalyst particle gets poisoned rapidly.

B. Variation of the electric field with plasma parameters

Figures 4(i) and 4(ii) display the variation of the electric field of the plasma sheath in the substrate vicinity with the electron temperature and negative substrate bias, respectively. The increase in electron temperature decreases the sheath width which leads to an increase in the electron thermal kinetic energy. This leads to the loss of electrons from the plasma bulk to the boundary wall and hence, increases the electric field strength. On increasing the negative bias over the substrate, the plasma potential increases due to a decrease in the sheath width leading to rise in the electric field near the substrate. This high field strength accelerates

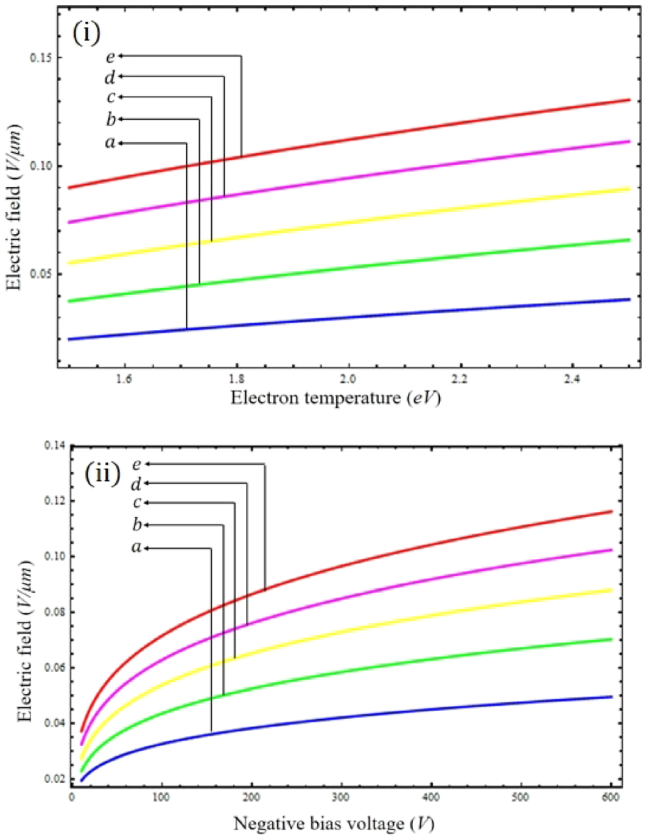

FIG. 4. (i) Effect of electron temperature on the electric field (where a, b, c, d, and e correspond to $n_{iA0} = 0.2 \times 10^9\,\mathrm{cm}^{-3}$, $U_S = 100\,\mathrm{V}$; $n_{iA0} = 0.4 \times 10^9\,\mathrm{cm}^{-3}$, $U_S = 200\,\mathrm{V}$; $n_{iA0} = 0.6 \times 10^9\,\mathrm{cm}^{-3}$, $U_S = 300\,\mathrm{V}$; $n_{iA0} = 0.8 \times 10^9\,\mathrm{cm}^{-3}$, $U_S = 400\,\mathrm{V}$; and $n_{iA0} = 1.0 \times 10^9\,\mathrm{cm}^{-3}$, and $U_S = 500\,\mathrm{V}$). (ii) Effect of bias voltage on the electric field (where a, b, c, d, and e correspond to $n_{iA0} = 0.2 \times 10^9\,\mathrm{cm}^{-3}$, $T_{e0} = 1.5\,\mathrm{eV}$; $n_{iA0} = 0.4 \times 10^9\,\mathrm{cm}^{-3}$, $T_{e0} = 1.75\,\mathrm{eV}$; $n_{iA0} = 0.6 \times 10^9\,\mathrm{cm}^{-3}$, $T_{e0} = 2.0\,\mathrm{eV}$; $n_{iA0} = 0.8 \times 10^9\,\mathrm{cm}^{-3}$, $T_{e0} = 2.25\,\mathrm{eV}$; and $n_{iA0} = 1.0 \times 10^9\,\mathrm{cm}^{-3}$, and $T_{e0} = 2.5\,\mathrm{eV}$, respectively).

the positive ions towards the substrate, i.e., high current density due to high plasma potential, which leads to their abundance in the substrate vicinity.

C. Temporal behaviour of the electric field

Figure 5 (inset) represents the time evolution of the plasma sheath electric field. The electric field nearby the substrate region shows a strong dependency on the electron temperature and negative bias voltage over the substrate as depicted in Fig. 4. The continuous drop in electron temperature over the growth time in the plasma is due to incessant collisions of electrons with gaseous atoms, and the sheath width increases which decreases the ion current density towards the substrate and thereby, decreases the plasma potential. For a given sheath voltage, this leads to a lower sheath electric field strength in the substrate vicinity. Hence, the electric field decreases over the growth period. The result also attributes to the change in the electric field over time on changing the negative substrate bias. When the negative bias over the substrate increases, the plasma sheath electric field increases due to the increase in plasma potential.

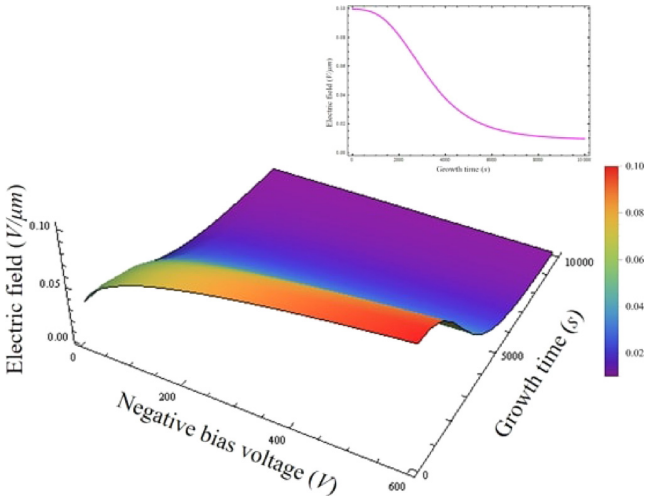

FIG. 5. Variation of the electric field with growth time and negative substrate bias. Inset: Temporal behavior of electric field at $U_S = 500\,\mathrm{V}$.

D. Variation of temporal electrostatic force with temporal plasma parameters and electric field

Figures 6(i)–6(iii) display the relation between the temporal plasma parameters (hydrocarbon ion number density and electron temperature) and plasma electric field with the concurrent force exerted on the CNT tip. The decrease in electric field strength with time as shown in Fig. 5(i) decreases the ion density in the plasma sheath owing to the low plasma potential. The electron temperature in plasma also decreases with growth time due to the loss in electron energy due to continuous collisions in the sheath region. The initial increase in electrostatic force can be comprehended to its dependence on the tip surface area which increases due to the increase in the growth rate and the alignment angle of CNT [cf. Eq. (24)]. This increasing force produces stresses on the catalyst-nanotube interface and deviates the CNT from its vertical growth axis. Once the alignment reaches near about 30°, these stresses start to balance each other and the electrostatic force decreases owing to the decrease in plasma parameters with time which starts to decrease the deviation produced in CNT. The increase in the negative substrate bias leads to the higher plasma potential and the electric field. The family of curves can be elucidated by the increase in electrostatic force exerted on the CNT with the increase in this negative bias over the substrate.

E. Variation of electrostatic force with CNT dimensions

Figures 7(i) and 7(ii) characterize the relation between the CNT radius and length grown in the plasma with the electrostatic force acting on it. For an initial number density of hydrocarbon ions and electron temperature, the variation in the radius and length of the CNT in the plasma is depicted in Fig. 2. The increase in the radius and length of the nanotube increases the ultimate electrostatic force exerted at the tip of CNT in plasma. The increase in the growth of CNT enhances the electric field at the tip of the catalyst which leads to a higher electrostatic force. Hence, for the plasma conditions (denoted by points) leading to a greater CNT

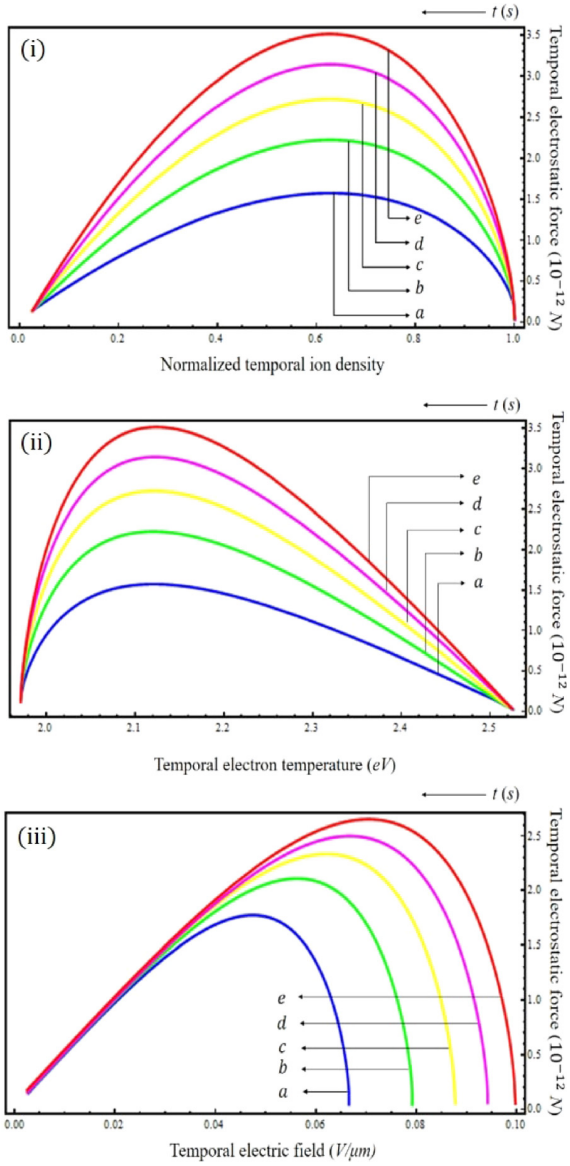

FIG. 6. (i) Variation of temporal electrostatic force with the concurrent ion number density (where a, b, c, d, and e correspond to $U_S = 100\,\text{V}$, 200 V, 300 V, 400 V, and 500 V, respectively). (ii) Variation of temporal electrostatic force with the concurrent electron temperature (where a, b, c, d, and e correspond to $U_S = 100\,\text{V}$, 200 V, 300 V, 400 V, and 500 V, respectively). (iii) Variation of temporal electrostatic force with the concurrent electric field (where a, b, c, d, and e correspond to $U_S = 100\,\text{V}$, 200 V, 300 V, 400 V, and 500 V, respectively).

growth, the electrostatic force becomes stronger. The linear best fit for the points denoting different plasma process conditions shows the linear relation of electrostatic force with the CNT radius and length.

F. Temporal behaviour of the alignment angle

Figure 8 shows the temporal variation of the alignment angle of the CNT. During the nucleation stage, when the growth of the CNT initiates the carbon species starts to precipitate out around the bottom of the catalyst which helps in lifting it up from the substrate forming graphitic layers beneath it. Hence originally, the CNT is growing aligned in the vertical direction. As discussed previously, due to non-

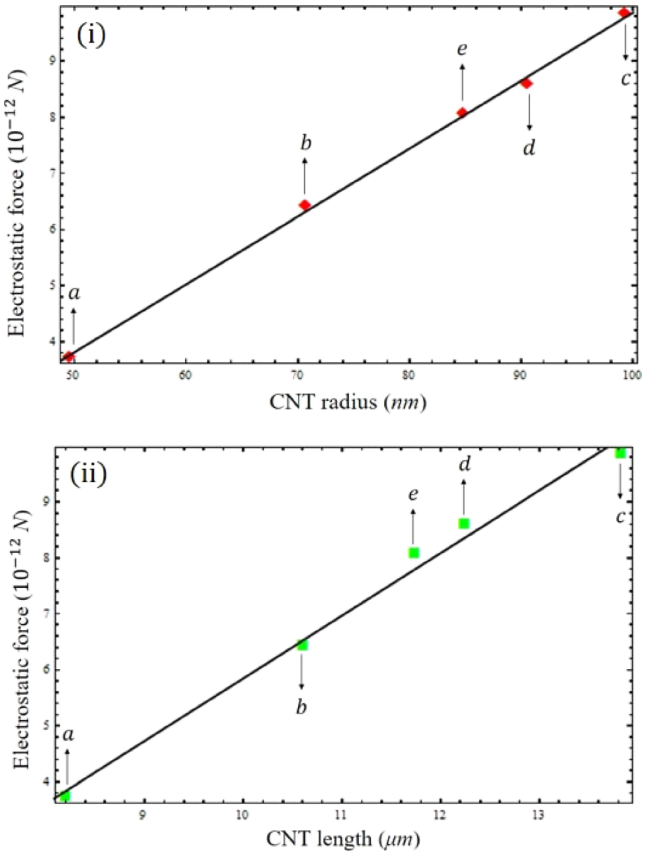

FIG. 7. (i) Effect of the CNT radius on the electrostatic force (where a, b, c, d, and e correspond to $n_{iA0} = 0.2 \times 10^9\,\text{cm}^{-3}$, $T_{e0} = 1.5\,\text{eV}$; $n_{iA0} = 0.4 \times 10^9\,\text{cm}^{-3}$, $T_{e0} = 1.75\,\text{eV}$; $n_{iA0} = 0.6 \times 10^9\,\text{cm}^{-3}$, $T_{e0} = 2.0\,\text{eV}$; $n_{iA0} = 0.8 \times 10^9\,\text{cm}^{-3}$, $T_{e0} = 2.25\,\text{eV}$; and $n_{iA0} = 1.0 \times 10^9\,\text{cm}^{-3}$, and $T_{e0} = 2.5\,\text{eV}$, respectively). (ii) Effect of the CNT length on the electrostatic force (where a, b, c, d, and e correspond to $n_{iA0} = 0.2 \times 10^9\,\text{cm}^{-3}$, $T_{e0} = 1.5\,\text{eV}$; $n_{iA0} = 0.4 \times 10^9\,\text{cm}^{-3}$, $T_{e0} = 1.75\,\text{eV}$; $n_{iA0} = 0.6 \times 10^9\,\text{cm}^{-3}$, $T_{e0} = 2.0\,\text{eV}$; $n_{iA0} = 0.8 \times 10^9\,\text{cm}^{-3}$, $T_{e0} = 2.25\,\text{eV}$; and $n_{iA0} = 1.0 \times 10^9\,\text{cm}^{-3}$, and $T_{e0} = 2.5\,\text{eV}$, respectively).

uniformity in the growth rate of the CNT around catalyst-nanotube interfaces, the axial stresses acting on the nanotube deviate it from its initial vertical alignment and the CNT begins to incline. On reaching an inclination near 30°, the electrostatic force acting on it CNT tip dominates these axial stresses and tend to decrease this inclination angle. As the

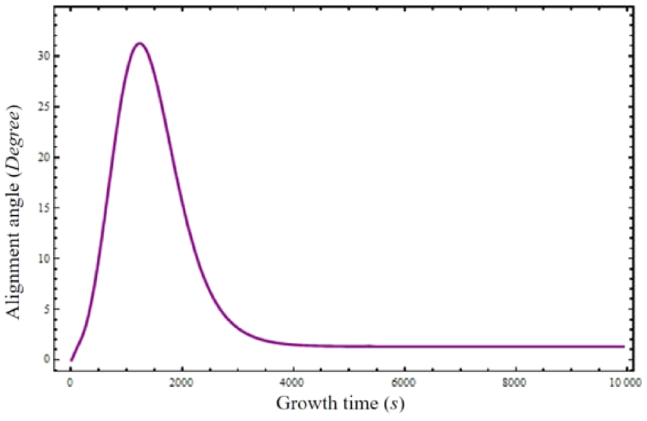

FIG. 8. Temporal variation of the alignment angle of the CNT.

CNT reaches its original vertical configuration, the force acting on its tip also decreases and reaches a saturation to maintain its alignment [cf. Figs. 1(iv)–1(vi)].

G. Temporal behaviour of the force acting on the CNT

Figure 9 (inset) signifies the time variation of the force employed on the carbon nanotube by the plasma. The electrostatic force depends strongly on the inclination angle of the CNT [cf. Eq. (24)]. As the initial alignment of the CNT in its nucleation stage is vertical, the force acting on it holds a small value. As the spatial variation in the C precipitation around the rear of catalyst tends to deviate the nanotube from its initial growth direction during the growth stage, the electrostatic force producing the axial stresses between the catalyst and CNT increases. The compressive and tensile stress act opposing to the higher and lower growth rate, respectively. These conflicting stresses support the C precipitation at the interface undergoing a lower growth rate. This balances the growth rate around the boundary of catalyst and CNT. Hereafter, the CNT tends to align itself again along the field. This electrostatic force decreases and attains a saturation value when the CNT reaches its original alignment. The result also features the change in the electrostatic force with time on changing the negative substrate bias. On increasing the negative bias over the substrate, the electrostatic force on the CNT increases due to the increase in plasma sheath electric field.

H. Variation of force with the alignment angle

Figure 10 shows the influence of an electrostatic force in the alignment of the CNT in the plasma. As discussed before when the growth of the CNT initiates, the CNT grows aligned with the electric field and slowly deviates from its initial axis due to all the axial stresses acting on it due to the electrostatic force. As these opposing stresses (compressive and tensile) start balancing the C precipitation around the catalyst-nanotube interface, this deviation starts to decrease again and align itself along its initial growth axis. Once the nanotube is aligned vertical to the substrate, the force sustains a constant value to retain the alignment and the growth process continues till it reaches a saturation. Figure 10 shows the effect of electrostatic force on aligning back the deviated CNT to its vertical growth axis.

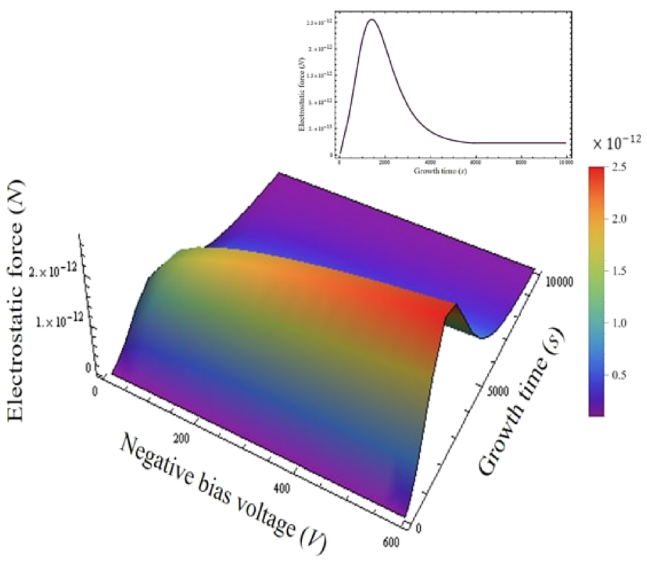

FIG. 9. Variation of the electrostatic force with growth time and negative substrate bias. Inset: Temporal behavior of electrostatic force at $U_S = 500$ V.

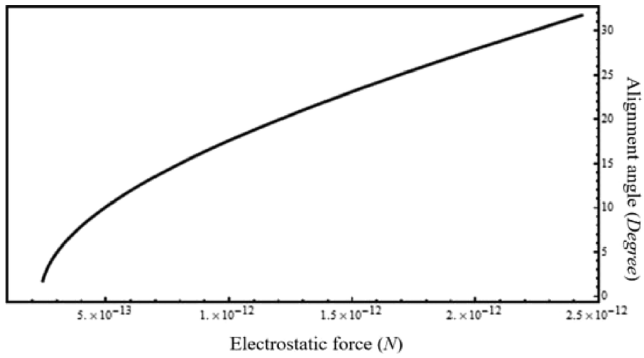

FIG. 10. Variation of the alignment angle of the CNT with the electrostatic force.

I. Comparison with the experimental outcomes

The theoretical outcomes of the analysis are found out to be in agreement with variously available observations as follows. The results from the work of Zhang *et al.*,[23] Merchan-Merchan *et al.*[27] and Pal *et al.*[32] showed the strong effect of electric field in aligning the CNTs along the field direction which are in compliance with our results. The results from Bower *et al.*[19] exhibited the importance of plasma in aligning the CNT perpendicular to the substrate surface, regardless of its orientation or shape. This suggests the importance of plasma parameters in the alignment of CNT as revealed in our study. Roettgen *et al.*[49] studied the time-resolved plasma parameters in pulse discharges and suggested the decrease in plasma density and electron temperatures with time. Hence, this comprehends to the decrease in the plasma sheath electric field and the corresponding electrostatic force as indicated in the present work. Bao *et al.*[29] simulated the electric field influence on the MWCNT and found that the force acting on the nanotubes govern their alignment and their results for the effect of the dimensions of CNT on this force are in direct compliance with the outcomes of the present study. This indicates the faster alignment of CNT with higher electrostatic force due to the high negatively biased substrate. Wang *et al.*[50] studied experimentally the evolution of the CNT growth by PECVD and presented differently aligned nanotubes during the growth time. This justifies the time evolution of the CNT alignment angle during its growth. Tanemura *et al.*[20] suggested the dependence of alignment of the CNT on the negative bias of the substrate which is in accordance with our results. The influence of negative substrate bias on the electrostatic force and the variation of the CNT alignment angle with this force are obtained in the present study.

IV. CONCLUSION

A theoretical analysis has been carried out to focus on the alignment mechanism along with the growth of the carbon nanotube on a catalyst nanoparticle in a complex plasma. The several phenomena involved in the growth of the CNT have been contemplated and the consequence of plasma parameters on the growth as well as the establishment of electrostatic force responsible for the alignment of the CNT has been studied in the present work. The alignment force is comprehended to increase with the growth in the dimensions of the CNT. When the growth starts to decline due to catalyst poisoning, the aligning force acting on the CNT also decays and as the growth saturates, this force holds minimum value to sustain the alignment. The time evolution of the electric field and force in the plasma sheath is also studied. The current study can prove to be beneficial for the production of various 1D nanostructures, namely CNTs/CNFs and their use in various field emission devices due to the great dependency of its properties on the structure, morphology, and alignment of CNTs.

ACKNOWLEDGMENTS

The author (Umang Sharma) is grateful to Mr. Ravi Gupta and Ms. Neha Gupta for their fruitful discussions, kind support, and encouragement. Umang Sharma is also thankful to the Department of Science and Technology (DST), Government of India for providing the necessary financial assistance under INSPIRE Fellowship.

[1]S. Iijima, Nature **354**, 56 (1991).
[2]E. Dervishi, Z. Li, Y. Xu, V. Saini, A. R. Biris, D. Lupu, and A. S. Biris, Part. Sci. Technol. **27**, 107 (2009).
[3]S. B. Sinnott and R. Andrews, Crit. Rev. Solid State Mater. Sci. **26**, 145 (2001).
[4]G. Bocharov and A. Eletskii, Nanomaterials **3**, 393 (2013).
[5]J. M. Bonard, N. Weiss, H. Kind, T. Stöckli, L. Forró, and K. Kern, Adv. Mater. **13**, 184 (2001).
[6]H. Murakami, M. Hirakawa, C. Tanaka, and H. Yamakawa, Appl. Phys. Lett. **76**, 1776 (2000).
[7]R. Andrews, D. Jacques, A. M. Rao, F. Derbyshire, D. Qian, X. Fan, E. C. Dickey, and J. Chen, Chem. Phys. Lett. **303**, 467 (1999).
[8]M. Jung, Diamond Relat. Mater. **10**, 1235 (2001).
[9]C. Bower, O. Zhou, W. Zhu, D. J. Werder, and S. Jin, Appl. Phys. Lett. **77**, 2767 (2000).
[10]M. Chhowalla, K. B. K. Teo, C. Ducati, N. L. Rupesinghe, G. A. J. Amaratunga, A. C. Ferrari, D. Roy, J. Robertson, and W. I. Milne, J. Appl. Phys. **90**, 5308 (2001).
[11]Q. Yang, C. Xiao, W. Chen, A. K. Singh, T. Asai, and A. Hirose, Diamond Relat. Mater. **12**, 1482 (2003).
[12]R. L. Vander Wal, G. M. Berger, and T. M. Ticich, Appl. Phys. A: Mater. Sci. Process. **77**, 885 (2003).
[13]A. A. Puretzky, D. B. Geohegan, H. Schittenhelm, X. Fan, and M. A. Guillorn, Appl. Surf. Sci. **197–198**, 552 (2002).
[14]C. H. Kiang, W. A. Goddard, R. Beyers, J. R. Salem, and D. S. Bethune, J. Phys. Chem. **98**, 6612 (1994).
[15]Z. Shi, Y. Lian, X. Zhou, Z. Gu, Y. Zhang, S. Iijima, L. Zhou, K. T. Yue, and S. Zhang, Carbon N. Y. **37**, 1449 (1999).
[16]M. Meyyappan, L. Delzeit, A. Cassell, and D. Hash, Plasma Sources Sci. Technol. **12**, 205 (2003).
[17]M. S. Bell, K. B. K. Teo, R. G. Lacerda, W. I. Milne, D. B. Hash, and M. Meyyappan, Pure Appl. Chem. **78**, 1117 (2006).
[18]S. Hofmann, C. Ducati, J. Robertson, and B. Kleinsorge, Appl. Phys. Lett. **83**, 135 (2003).
[19]C. Bower, W. Zhu, S. Jin, and O. Zhou, Appl. Phys. Lett. **77**, 830 (2000).
[20]M. Tanemura, K. Iwata, K. Takahashi, Y. Fujimoto, F. Okuyama, H. Sugie, and V. Filip, J. Appl. Phys. **90**, 1529 (2001).
[21]V. I. Merkulov, A. V. Melechko, M. A. Guillorn, D. H. Lowndes, and M. L. Simpson, Appl. Phys. Lett. **79**, 2970 (2001).
[22]Y. Chen, L. Guo, S. Patel, and D. Shaw, J. Mater. Sci. **35**, 5517 (2000).
[23]Y. Zhang, A. Chang, J. Cao, Q. Wang, W. Kim, Y. Li, N. Morris, E. Yenilmez, J. Kong, and H. Dai, Appl. Phys. Lett. **79**, 3155 (2001).
[24]J. Yu, X. D. Bai, J. Ahn, S. F. Yoon, and E. G. Wang, Chem. Phys. Lett. **323**, 529 (2000).
[25]A. Maiti, C. J. Brabec, C. M. Roland, and J. Bernholc, Phys. Rev. B **52**, 14850 (1995).
[26]A. Maiti, C. J. Brabec, C. M. Roland, and J. Bernholc, Phys. Rev. Lett. **73**, 2468 (1994).
[27]W. Merchan-Merchan, A. V. Saveliev, and L. A. Kennedy, Carbon N. Y. **42**, 599 (2004).
[28]J. Blažek, P. Špatenka, F. Pácal, C. Täschner, and A. Leonhardt, Diamond Relat. Mater. **13**, 503 (2004).
[29]Q. Bao, H. Zhang, and C. Pan, Comput. Mater. Sci. **39**, 616 (2007).
[30]H. W. Wei, K. C. Leou, M. T. Wei, Y. Y. Lin, and C. H. Tsai, J. Appl. Phys. **98**, 044313 (2005).
[31]G. S. Bocharov, A. A. Knizhnik, A. V. Eletskii, and T. J. Sommerer, Tech. Phys. **57**, 270 (2012).
[32]A. F. Pal, T. V. Rakhimova, N. V. Suetin, M. A. Timofeev, and A. V. Filippov, Plasma Phys. Rep. **33**, 43 (2007).
[33]M. A. Lieberman and A. J. Lichtenberg, *Principles of Plasma Discharges and Materials Processing*, 2nd ed. (John Wiley & Sons, 2005).
[34]A. Tewari and S. C. Sharma, Phys. Plasmas **21**, 063512 (2014).
[35]R. Gupta, S. C. Sharma, and R. Sharma, Plasma Sources Sci. Technol. **26**, 024006 (2017).
[36]Z. Marvi, S. Xu, G. Foroutan, and K. Ostrikov, Phys. Plasmas **22**, 013504 (2015).
[37]M. S. Sodha, S. Misra, S. K. Mishra, and S. Srivastava, J. Appl. Phys. **107**, 103307 (2010).
[38]I. B. Denysenko, S. Xu, J. D. Long, P. P. Rutkevych, N. A. Azarenkov, and K. Ostrikov, J. Appl. Phys. **95**, 2713 (2004).
[39]A. M. da Cruz Baptista Dias, *Modeling of Low Pressure Plasmas in CH4-H2 Mixtures* (Instituto Superior Técnico, Universidade de Lisboa, 2012).
[40]I. Denysenko and K. Ostrikov, J. Phys. D. Appl. Phys. **42**, 015208 (2009).
[41]R. Gupta and S. C. Sharma, Phys. Plasmas **24**, 073504 (2017).
[42]I. Denysenko and K. Ostrikov, Appl. Phys. Lett. **90**, 251501 (2007).
[43]S. Hofmann, G. Csányi, A. C. Ferrari, M. C. Payne, and J. Robertson, Phys. Rev. Lett. **95**, 036101 (2005).
[44]R. G. Forbes, C. Edgcombe, and U. Valdrè, Ultramicroscopy **95**, 57 (2003).
[45]P. Poncharal, Z. L. Wang, D. Ugarte, and W. A. De Heer, Science **283**, 1513 (1999).
[46]M. Mao and A. Bogaerts, J. Phys. D. Appl. Phys. **43**, 205201 (2010).
[47]D. Herrebout, A. Bogaerts, M. Yan, R. Gijbels, W. Goedheer, and E. Dekempeneer, J. Appl. Phys. **90**, 570 (2001).
[48]W. Wunderlich, Diamond. Relat. Mater. **16**, 369 (2007).
[49]A. Roettgen, I. Shkurenkov, M. Simeni Simeni, V. Petrishchev, I. V. Adamovich, and W. R. Lempert, Plasma Sources Sci. Technol. **25**, 055009 (2016).
[50]H. Wang and Z. F. Ren, Nanotechnology **22**, 405601 (2011).
[51]H. Mehdipour, K. Ostrikov, and A. E. Rider, Nanotechnology **21**, 455605 (2010).
[52]I. Denysenko and N. A. Azarenkov, J. Phys. D. Appl. Phys. **44**, 174031 (2011).
[53]M. Yudasaka, R. Kikuchi, T. Matsui, Y. Ohki, S. Yoshimura, and E. Ota, Appl. Phys. Lett. **67**, 2477 (1995).

Arabian Journal for Science and Engineering
https://doi.org/10.1007/s13369-018-3637-9

RESEARCH ARTICLE - ELECTRICAL ENGINEERING

A Unified AC–MTDC Power-Flow Algorithm with IDCPFC

Shagufta Khan[1] · **Suman Bhowmick**[2] · **Tausif Ahmad**[3]

Received: 27 April 2018 / Accepted: 15 November 2018

Abstract
A unified power-flow algorithm of AC power systems integrated with multi-terminal high-voltage direct current (MTDC) grids incorporating the interline DC power-flow controller (IDCPFC) is presented in this paper. The MTDC grids are based on voltage-sourced converter (VSC) technology. Pulse-width modulation control is employed for the VSCs. As against most of the research works published in this area, in this algorithm, the VSC modulation indices are considered as unknowns. The IDCPFC considered for the power-flow management of the DC grid is a generalized one, with an arbitrary number of DC voltage sources. In the proposed model converter losses are also included. All case studies are carried out in MTDC grids embedded in the IEEE-300 bus test system. For all the case studies, the power-flow algorithms were implemented with MATLAB. In all occurrences, a mismatch error tolerance of 10^{-10} p.u. was selected. Results obtained with case studies on AC–MTDC systems validate the proposed work.

Keywords MTDC · IDCPFC · DC grid · Power-flow algorithm

1 Introduction

In recent years, the demand for electrical energy around the world has increased [1]. Due to this, the renewable energy sources like solar and wind are utilized nearer to the load centers for reducing the peak demand and decreasing the congestion of generation units. Therefore, the power system has been facing technical challenges. To tackle these challenges, a concept of microgrids has proposed which has the capability of bidirectional power flow between generation units and load demands. The intermittent nature of power generation through renewable energy sources participates in creating the technical issues in microgrids. In this respect, the operation of microgrids has optimized in many ways [2–7]. In a similar manner, the capacities of power transmission networks across the globe need to be augmented. VSC-based high-voltage DC (HVDC) links help in promoting this cause. Unlike AC transmission, the length of a HVDC link is unaffected by stability considerations. VSC-based HVDC transmission systems augment system reliability by facilitating interconnection of asynchronous AC grids. They can also be used to improve the network capacity by integrating offshore wind farms with AC grids [8]. Modern VSC-HVDC grids employ IGBTs with pulse-width modulation (PWM) control technique. HVDC links using PWM controlled VSCs have the advantage of rapid and independent controllability of active as well as reactive powers, along with compact and inexpensive AC filters [9–15].

Compared to a HVDC link between two terminals, a MTDC grid is able to exploit the benefits of VSC-HVDC technology in a superior way. Moreover, sources of renewable energy can be easily integrated with a MTDC system, as and when the need arises. A meshed MTDC grid linking offshore wind farms and three asynchronous AC grids of the European Network of Transmission System Operators for Electricity (ENTSO-E) is being envisaged in the North Sea region [16,17].

In a MTDC grid, the VSCs can be connected in a back-to-back (BTB) or a point-to-point (PTP) disposition, depending on whether they are placed nearby or are at distant locations, respectively [18]. The PTP connection is common to most of the MTDC systems in operation, wherein DC links or cables are used to connect the DC terminals.

For proper MTDC operation, DC voltage control is an essential requirement. In this respect, the voltage of one DC terminal is maintained constant. It is known as the DC slack

✉ Shagufta Khan
khan.shagufta7@gmail.com

1 Galgotias University, Greater Noida, UP, India

2 Delhi Technological University, Delhi, India

3 Motihari College of Engineering, Motihari, Bihar, India

Published online: 27 November 2018

bus, and it sustains the power balance of the DC grid. The converter which controls its DC side voltage is known as the master converter. The rest of the converters (also known as slave converters) regulate their power flow [18–22].

Although the converters control the power injections into the DC grid, the power flows within the DC grid depend upon the resistances of the DC lines or cables. Jovcic et al. [23] and Mu et al. [24] present two methods of inserting variable resistance into the transmission line to control DC grid power flow. These methods are advantageous in terms of simpler structure and easier control. However, the losses are more and restricted to single direction. Mainly, two approaches of regulating voltage to control MTDC grid power flow are available. In first approach, DC/DC transformer is used to interconnect DC grids of different voltage levels [25–31]. In this regard, multiple DC/DC transformer topologies have been reported. Jovcic et al. [25–27] have proposed a bidirectional LCL type DC/DC converter which can participate in HV stepping with megawatt level power transfer for future DC transmission networks. Modular multilevel-based DC/DC converters are also useful for HVDC interconnection [28]. The DC/DC transformer approach of power flow control increases the costs and losses. In second approach, an auxiliary variable voltage source is inserted into the transmission line to control power flow [29–32]. Mu et al. [32] propose a two-stage (AC/DC and DC/DC) variable voltage source. Veilleux and Ooi [29] propose a thyristor control variable source to control DC power flow. In comparison with DC/DC transformer, variable voltage source has smaller power rating and can be implemented easily. However, the variable voltage source circuit includes an external AC or DC source to absorb or deliver power and a bulky low-frequency high-voltage insulation isolated transformer which is used to provide galvanic isolation between the AC source and DC grid.

Gyugyi et al. [33] have presented an interline power-flow controller, which is a VSC-based flexible AC transmission systems (FACTS) device to control the power flow of AC grids. The same concept can also be applied in meshed HVDC grids to regulate power flow. The advantages of interline power-flow controller are the elimination of external AC or DC sources, and its voltage rating is lower than grid level DC voltage. In this respect, a current flow controller has proposed in [34] and its control strategies are presented in [35,36]. Chen et al. [37] have proposed an interline DC power-flow controller (IDCPFC) for a three-terminal ring-type HVDC grid.

Now, for planning, operation and control of interconnected AC–MTDC systems incorporating IDCPFC, its power-flow model is required which is not reported in the literature. This paper presents an unified power-flow model of AC–MTDC system incorporating IDCPFC in DC grid. The following shortcomings relative to the power-flow modeling of AC–MTDC system have been addressed in this paper.

(a) A lack of AC–DC power-flow models considering the IDCPFC
(b) A lack of considering the VSC modulation index 'm' as an unknown. For VSC applications, 'm' is a crucial parameter. Typically, $0 < m \leq 1$. Yazdani and Iravani [13] report some of the factors that put a cap on the lower and upper bounds of 'm'.

This paper presents a unified algorithm for the power-flow modeling of AC–MTDC grids incorporating IDCPFC. As against most of the research works published in this area, 'm' is considered as an unknown and can be obtained directly, from the power-flow solution.

The paper is organized as follows: In Sect. 2, the modeling of a hybrid AC–MTDC system with IDCPFC is presented. The power-flow equations of integrated AC–DC system incorporating IDCPFC are presented in Sect. 3. Section 4 details the implementation of Newton Power-flow algorithm. The case studies and results are presented in Sect. 5. The conclusions are presented in Sect. 6.

Throughout this paper, regular and bold quantities are used to represent scalar variables and complex variables as well as matrices, respectively. All the transmission lines are represented by their equivalent-pi models.

2 Modeling of AC–MTDC Systems with IDCPFC

Figure 1 shows an AC power system network comprising 'n' buses, integrated with a MTDC grid. The MTDC grid constitutes 'q' VSCs. The converter transformers are used to interconnect the VSCs with their AC terminal buses. For generalization, it is assumed that the AC buses connected to the 'q' VSCs are numbered as 'i', '$(i+1)$', and so on, up to '$(i+q-1)$'. On their DC sides, the 'q' VSCs follow a PTP connection. Figure 1 also shows an IDCPFC incorporated with the MTDC grid for its power-flow management. The IDCPFC comprises 'z' ($z \leq q-1$) variable DC voltage sources interconnected between DC bus '1' and 'z' other DC buses numbered as '2', '3' and so on, upto '$(z+1)$'. Figure 2 shows the equivalent circuit for the network shown in Fig. 1.

In Fig. 2, 'q' fundamental frequency, positive sequence voltage sources pertaining to the 'q' VSCs are shown. Now, let R_{sha} and X_{sha} be the resistance and the leakage reactance of the ath ($1 \leq a \leq q$) converter transformer, respectively. Also, let $\boldsymbol{y_{sha}} = 1/\boldsymbol{Z_{sha}}$, where $\boldsymbol{Z_{sha}} = R_{\text{sha}} + jX_{\text{sha}}$. Therefore, from Fig. 2, the current in the link (not shown) connecting the ath VSC and its AC terminal bus is

$$\boldsymbol{I_{sha}} = \boldsymbol{y_{sha}}\,(\boldsymbol{V_{sha}} - \boldsymbol{V_i} + \boldsymbol{a} - \boldsymbol{1}) \tag{1}$$

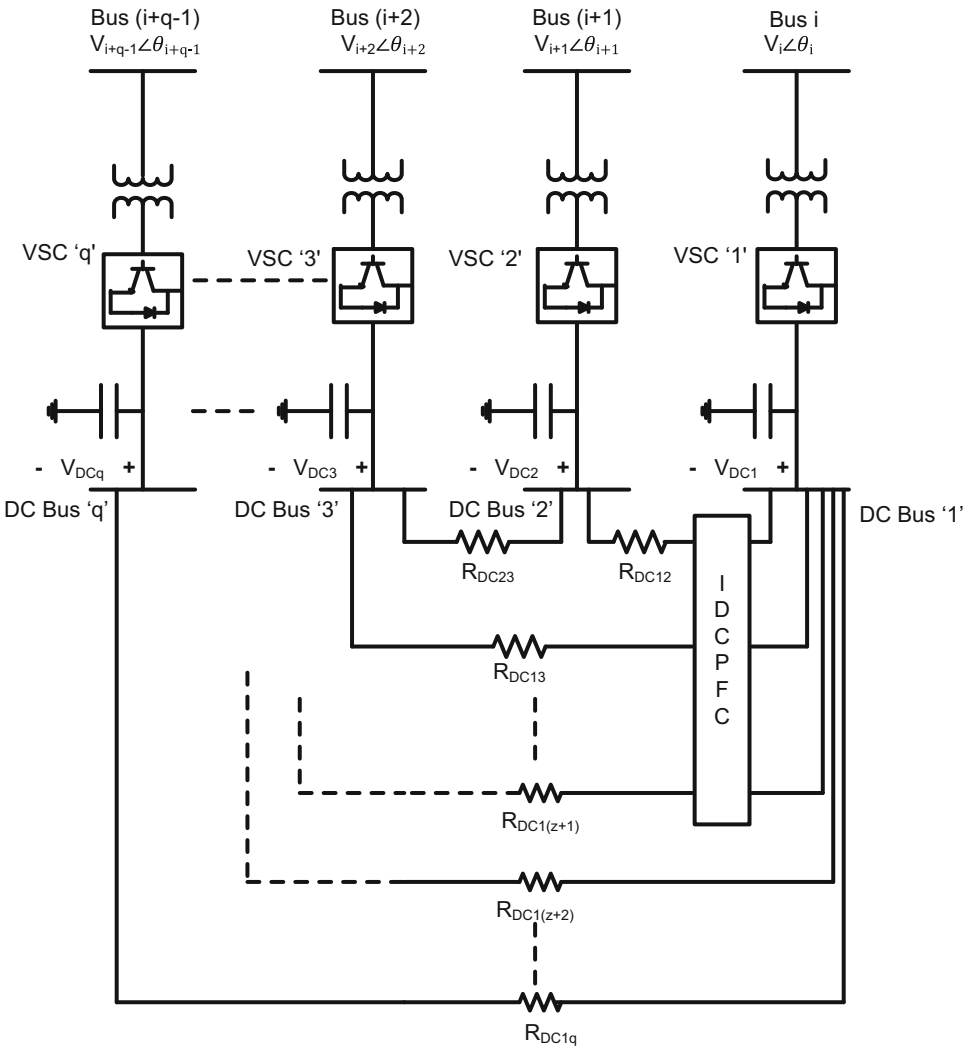

Fig. 1 Schematic diagram of an AC–MTDC system incorporating an IDCPFC

In Eq. (1), $\boldsymbol{V_{sha}}$ is the voltage phasor pertaining to the ath VSC. Also, in Eq. (1), $\boldsymbol{V_{sha}} = V_{\text{sha}}\angle\theta_{\text{sha}} = m_a c V_{\text{DCa}}\angle\theta_{\text{sha}}$ where 'm_a' is the VSC modulation index. The constant 'c' is representative of the VSC architecture [20].

From Figs. 1 and 2, the net current injection at the AC bus '$(i+a-1)$' connected to the ath$(1 \le a \le q)$ converter can be written as

$$\boldsymbol{I_{i+a-1}} = \sum_{k=1}^{n} \boldsymbol{Y_{(i+a-1)k}} \boldsymbol{V_k} - \boldsymbol{y_{sha}} \boldsymbol{V_{sha}} \tag{2}$$

where $\mathbf{Y_{(i+a-1)(i+a-1)}} = \mathbf{Y^{old}_{(i+a-1)(i+a-1)}} + \mathbf{y_{sha}}$ and $\mathbf{Y^{old}_{(i+a-1)(i+a-1)}} = \mathbf{y_{(i+a-1)0}} + \sum_{\mathbf{k=1,k\neq i+a-1}}^{\mathbf{n}} \mathbf{y_{(i+a-1)k}}$ are the values of self admittances of bus '$(i+a-1)$' with the ath VSC connected and the original 'n' bus AC system without any VSC, respectively. Similarly, '$\mathbf{y_{(i+a-1)0}}$' accounts for the shunt capacitances of all the transmission lines connected to bus '$(i+a-1)$'.

Now, in Fig. 2, the IDCPFC comprises 'z' $(z \le q-1)$ variable DC voltage sources and it is assumed, without any loss of generality, that the wth variable DC voltage source 'V_{DCsw}' $(1 \le w \le z)$ is connected in series with the link interconnecting the DC buses '1' and '$(1+w)$' $(1 \le w \le z, \forall z \le q-1)$. Then, from Fig. 2, the current and power in this link (connected between DC buses '1' and '$w+1$') are

$$I_{\text{DC1}(w+1)} = Y_{\text{DC1}(w+1)} \left[V_{\text{DCw+1}} - V_{\text{DC1}} + V_{\text{DCsw}} \right] \tag{3}$$

$$P_{\text{DC1}(w+1)} = V_{\text{DC1}} I_{\text{DC1}(w+1)} \tag{4}$$

Further, with the IDCPFC, the net DC current injection at the 1st DC bus can be written as

$$I_{\text{DC1}} = \sum_{u=1,u\neq 1}^{z+1} I_{\text{DC1}u} + \sum_{u=z+2,u\neq 1}^{q} I_{\text{DC1}u} \tag{5}$$

Writing $I_{\text{DC1}u}$ in the form of Eq. (3) and substituting in Eq. (5), we get

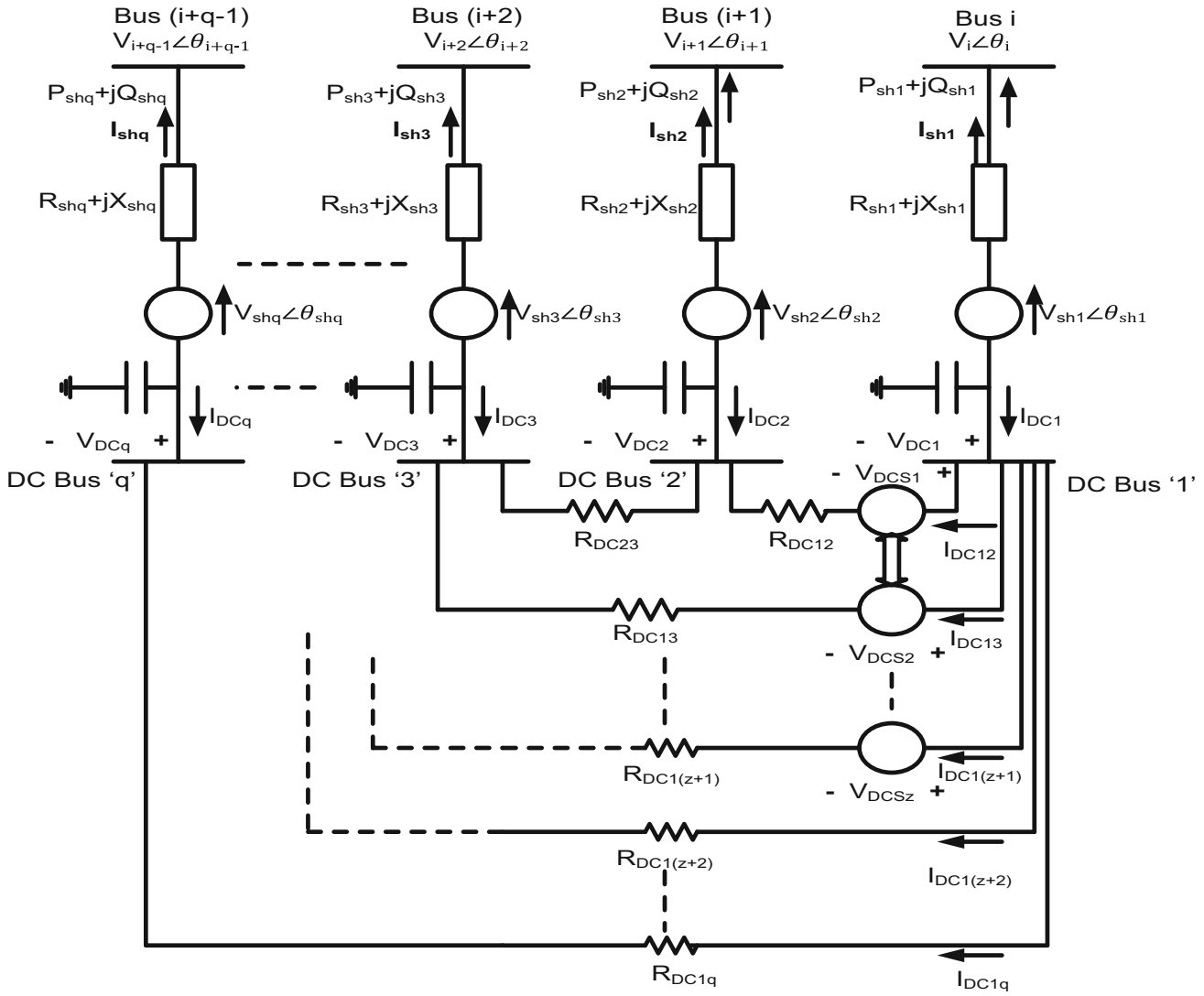

Fig. 2 Equivalent circuit of AC–MTDC system incorporating an IDCPFC

$$I_{\mathrm{DC}} = \sum_{u=1}^{\mathrm{q}} Y_{\mathrm{DC1}u} V_{\mathrm{DCu}} + \sum_{u=1,u\neq 1}^{\mathrm{z+1}} Y_{\mathrm{DC1}u} V_{\mathrm{DCs}(u-1)} \tag{6}$$

In a similar manner, the net DC current injections at the other DC buses can also be written very easily. It can be shown that the net DC current injection at any arbitrary DC node 'u' ($1 \leq u \leq q$) can be generalized as

$$\begin{aligned} I_{\mathrm{DCu}} &= \textstyle\sum_{\mathrm{v}=1}^{\mathrm{q}} Y_{\mathrm{DCuv}} V_{\mathrm{DCv}} + \sum_{\mathrm{v}=1,\mathrm{v}\neq 1}^{\mathrm{z+1}} Y_{\mathrm{DCuv}} V_{\mathrm{DCs}(v-1)} \quad \text{if u} = 1 \\ &= \textstyle\sum_{\mathrm{v}=1}^{\mathrm{q}} Y_{\mathrm{DCuv}} V_{\mathrm{DCv}} - Y_{\mathrm{DCu1}} V_{\mathrm{DCs}(u-1)} \quad \text{if } 2 \leq u \leq z+1 \\ &= \textstyle\sum_{\mathrm{v}=1}^{\mathrm{q}} Y_{\mathrm{DCuv}} V_{\mathrm{DCv}} \quad \text{if } z+2 \leq u \leq q \end{aligned} \tag{7}$$

where $Y_{\mathrm{DCuv}} = -\frac{1}{R_{\mathrm{DCuv}}}$, where '$R_{\mathrm{DCuv}}$' is the resistance of the interconnection between DC buses 'u' and 'v'.

3 Power-flow Equations of AC–MTDC Systems with IDCPFC

Now, from Fig. 2, at the AC bus '$(i + a - 1)$' pertaining to the ath VSC, it can be shown that the net active and reactive power injections are

$$\begin{aligned} P_{i+a-1} = &\sum_{k=1}^{n} V_{i+a-1} V_k Y_{(i+a-1)k} \cos\left[\theta_{i+a-1} - \theta_k - \phi_{(i+a-1)k}\right] \\ &- m_a c V_{\mathrm{DCa}} V_{i+a-1} y_{\mathrm{sha}} \cos(\theta_{i+a-1} - \theta_{\mathrm{sha}} - \phi_{\mathrm{sha}}) \end{aligned} \tag{8}$$

$$\begin{aligned} Q_{i+a-1} = &\sum_{k=1}^{n} V_{i+a-1} V_k Y_{(i+a-1)k} \sin\left[\theta_{i+a-1} - \theta_k - \phi_{(i+a-1)k}\right] \\ &- m_a c V_{\mathrm{DCa}} V_{i+a-1} y_{\mathrm{sha}} \sin(\theta_{i+a-1} - \theta_{\mathrm{sha}} - \phi_{\mathrm{sha}}) \end{aligned} \tag{9}$$

where 'ϕ_{sha}' is the phase angle of $\boldsymbol{y_{sha}}$.

In a similar manner, from Fig. 2, it can be shown that the line active and reactive power flows pertaining to the ath VSC are given as

$$P_{\text{sha}} = Re\left[\boldsymbol{V_{i+a-1}I^{*}_{sha}}\right] = m_a c V_{\text{DCa}} V_{i+a-1} y_{\text{sha}} \cos(\theta_{i+a-1} - \theta_{\text{sha}} - \phi_{\text{sha}}) - V^2_{i+a-1} y_{\text{sha}} \cos\phi_{\text{sha}} \quad (10)$$

$$Q_{\text{sha}} = m_a c V_{\text{DCa}} V_{i+a-1} y_{\text{sha}} \sin(\theta_{i+a-1} - \theta_{\text{sha}} - \phi_{\text{sha}}) + V^2_{i+a-1} y_{\text{sha}} \sin\phi_{\text{sha}} \quad (11)$$

Now, for the ath VSC, the converter losses are [20,38,39]

$$P_{\text{lossa}} = a_1 + b_1 I_{\text{sha}} + c_1 I^2_{\text{sha}} \quad (12)$$

In Eq. (12), the overall converter station losses can be split up into three aggregated loss components. These are written as a function of 'a_1' indicates the VSC losses no load, 'b_1' and 'c_1' are constants representative of the linear and quadratic dependency of the VSC losses on the converter current magnitude (I_{sha}), respectively. The per unit values of coefficients a_1, b_1 and c_1 are given in Result section.

If VSC losses are considered, the AC–DC power balance equations for the ath ($1 \le a \le q$) VSC are,

$$\begin{aligned}
&(\mathrm{m_a c V_{DCa}})^2 \mathrm{y_{sha}} \cos\phi_{\text{sha}} - \mathrm{m_a c V_{DCa}} V_{\mathrm{i}+a-1} \mathrm{y_{sha}} \\
&\quad \cos(\theta_{\text{sha}} - \theta_{\mathrm{i}+a-1} - \phi_{\text{sha}}) \\
&= -\sum_{\mathrm{v}=1}^{\mathrm{q}} V_{\text{DCa}} V_{\text{DCv}} Y_{\text{DCav}} - P_{\text{lossa}} \quad \text{if } (z+2) \le a \le q \\
&= -\sum_{\mathrm{v}=1}^{\mathrm{q}} V_{\text{DCa}} V_{\text{DCv}} Y_{\text{DCav}} + V_{\text{DCa}} V_{\text{DCs}(a-1)} Y_{\text{DCa1}} \\
&\quad - P_{\text{lossa}} \quad \text{if } 2 \le a \le z+1 \\
&= -\sum_{\mathrm{v}=1}^{\mathrm{q}} V_{\text{DCa}} V_{\text{DCv}} Y_{\text{DCav}} \\
&\quad - \sum_{\mathrm{v}=1, v\neq 1}^{\mathrm{z+1}} V_{\text{DCa}} V_{\text{DCs}(v-1)} Y_{\text{DCav}} - P_{\text{lossa}} \quad \text{if a} = 1 \\
&\quad \text{or, } f_{1\mathrm{a}} = 0 \quad \forall\, a, 1 \le a \le q
\end{aligned} \quad (13)$$

Equation (13) represents 'q' independent equations.

Thus, 'q' independent equations are obtained.

Now, in the AC–MTDC system (Fig. 2) with 'q' VSCs, it is important to note that not more than '$(q-1)$' line active and reactive power flows {Eqs. (10) and (11)} can be specified. In addition, if it is assumed that the rth ($1 \le r \le q$) VSC is used for voltage control of its corresponding AC bus, we have

$$V^{\text{sp}}_{i+a-1} - V^{\text{cal}}_{i+a-1} = 0 \quad \forall \quad a, \quad 1 \le a \le q, \quad a = r \quad (14)$$

For the rest of the '$(q-1)$' VSCs controlling the line active and reactive power flows, we get

$$P^{\text{sp}}_{\text{sha}} - P^{\text{cal}}_{\text{sha}} = 0 \quad (15)$$

$$Q^{\text{sp}}_{\text{sha}} - Q^{\text{cal}}_{\text{sha}} = 0 \quad (16)$$

$\forall\, a, 1 \le a \le q, a \ne r$.

Thus, we get '$(2q-2)$' independent equations.

Instead of PQ control mode, if a VSC operates in the PV one, Eq. (16) changes to

$$V^{\text{sp}}_{i+a-1} - V^{\text{cal}}_{i+a-1} = 0 \quad \forall\, a, \quad 1 \le a \le q, \quad a \ne r \quad (17)$$

Further, the net reactive power injection at AC bus '$(i + r - 1)$' can be specified as its voltage is controlled by the rth VSC. Thus, we get

$$Q^{\text{sp}}_{i+a-1} - Q^{\text{sp}}_{i+a-1} = 0 \quad \forall\, a, \quad 1 \le a \le q, \quad a = r \quad (18)$$

In Eqs. (14)–(18), V^{sp}_{i+a-1}, Q^{sp}_{i+a-1}, $P^{\text{sp}}_{\text{sha}}$ and $Q^{\text{sp}}_{\text{sha}}$ are specified values while V^{cal}_{i+a-1}, Q^{cal}_{i+a-1}, $P^{\text{cal}}_{\text{sha}}$ and $Q^{\text{cal}}_{\text{sha}}$ are calculated values {using Eqs. (9)–(11)}.

Now, the IDCPFC is represented by 'z' variable DC voltage sources incorporated in series with 'z' DC links. Hence, the inclusion of the IDCPFC in the hybrid AC–MTDC system introduces 'z' additional unknowns. These call for 'z' specified or known quantities. It is important to note that if the IDCPFC is considered lossless, from Fig. 2, the power delivered by the IDCPFC is

$$P_{\text{IDCPFC}} = [V_{\text{DCs1}}\{-I_{\text{DC12}}\} + V_{\text{DCs2}}\{-I_{\text{DC13}}\} + \ldots V_{\text{DCsz}}\{-I_{\text{DC1}(z+1)}\}] = 0 \quad (19)$$

Equation (19) represents a single, independent equation. Thus, additional '$(z-1)$' equations are required for a complete solution of the IDCPFC variables, which is similar to the degree of freedom of an IPFC [33,37]. These '$(z-1)$' equations are obtained from the control objectives of the IDCPFC. In this work, DC link current control and DC link power control have been considered.

With DC link current control, the line currents in all the 'z' DC links (containing the 'z' variable DC voltage sources of the IDCPFC) except one can be controlled. If it is presumed that the line current in the DC link containing the yth ($1 \le y \le z$) variable DC voltage source 'V_{DCsy}' is not being controlled by the IDCPFC, the control equations for the rest of the '$(z-1)$' DC links are

$$I^{\text{sp}}_{\text{DC1}(w+1)} - I^{\text{cal}}_{\text{DC1}(w+1)} = 0 \quad (20)$$

In a similar manner, the control equations for the power flow in the '$(z-1)$' DC links are

$$P^{\text{sp}}_{\text{DC1}(w+1)} - P^{\text{cal}}_{\text{DC1}(w+1)} = 0 \tag{21}$$

$$\text{Or, } f_{2w} = 0 \quad \forall w, 1 \le w \le z, w \ne y, z \le q-1 \tag{22}$$

In the above equation, $I^{\text{sp}}_{\text{DC1}(w+1)}$ and $P^{\text{sp}}_{\text{DC1}(w+1)}$ is the specified value of the current and the power flow in the DC link between the DC buses 'I' and '$(1+w)$' (and containing the variable DC voltage source 'V_{DCsw}'), while $I^{\text{cal}}_{\text{DC1}(w+1)}$ and $P^{\text{cal}}_{\text{DC1}(w+1)}$ are their calculated value obtained using Eqs. (3) and (4).

4 Implementation in Newton Power-Flow Equations

It is assumed that there are 'p' generators connected at the first 'p' buses of the 'n' bus AC system with bus 1 being the slack bus, then for the AC–MTDC system incorporating an IDCPFC with 'z' variable DC voltage sources and following DC slack bus control, the unified AC–MTDC power-flow problem is of the form

Compute: $\boldsymbol{\theta}, \boldsymbol{V}, \boldsymbol{X}$

Given: $\boldsymbol{P}, \boldsymbol{Q}, \boldsymbol{R}$

With

$$\boldsymbol{\theta} = [\theta_2 \dots \theta_n]^{\text{T}}, \quad \boldsymbol{V} = \left[V_{p+1} \dots V_n\right]^{\text{T}}, \quad \boldsymbol{\theta_{sh}} = \left[\theta_{\text{sh1}} \dots \theta_{\text{shq}}\right]^{\text{T}},$$
$$\boldsymbol{m} = \left[m_1 \dots m_q\right]^{\boldsymbol{T}}, \quad \boldsymbol{V_{DC}} = \left[V_{\text{DC2}} \dots V_{\text{DCq}}\right]^{\boldsymbol{T}}$$
$$\boldsymbol{V_{DCs}} = \left[V_{\text{DCs1}} \dots V_{\text{DCsz}}\right]^{\boldsymbol{T}} \text{ and } \boldsymbol{X} = \left[\boldsymbol{\theta}^{\boldsymbol{T}}_{\boldsymbol{sh}} \ \boldsymbol{m}^{\boldsymbol{T}} \ \boldsymbol{V}^{\boldsymbol{T}}_{\boldsymbol{DC}} \ \boldsymbol{V}^{\boldsymbol{T}}_{\boldsymbol{DCs}}\right]^{\boldsymbol{T}}$$
$$\boldsymbol{P} = [P_2 \dots P_n]^{\text{T}}, \quad \boldsymbol{Q} = \left[Q_{p+1} \dots Q_n\right]^{\text{T}},$$
$$\boldsymbol{P_{sh}} = [P_{\text{sh2}} \dots P_{\text{shq}}], \quad \boldsymbol{Q_{sh}} = \left[Q_{\text{sh2}} \dots Q_{\text{shq}}\right]$$
$$\boldsymbol{f_1} = \left[f_{11} \dots f_{1q}\right], \quad \boldsymbol{f_2} = \left[f_{21} \dots f_{2(z-1)}\right]$$
$$\text{and } \boldsymbol{R} = \left[\boldsymbol{P_{sh}} \ \boldsymbol{Q_{sh}} \ V_{i+r-1} \ P_{\text{IDCPFC}} \boldsymbol{f_1} \boldsymbol{f_2}\right]^{\text{T}}$$

It is presumed that in this model, DC slack bus control is adopted ('V_{DC1}' is specified). Also, VSC 'r' is employed for the voltage control of the AC bus '$(i+r-1)$' unlike the other '$(q-1)$' VSCs, which control the line active as well as reactive power flows.

The Newton power-flow equation is

$$\boldsymbol{J}\left[\Delta\theta^{\boldsymbol{T}} \ \boldsymbol{V}^{\boldsymbol{T}} \ \Delta\theta_{\boldsymbol{sh}}{}^{\boldsymbol{T}} \ \Delta\boldsymbol{m}^{\boldsymbol{T}} \ \boldsymbol{V_{DC}}{}^{\boldsymbol{T}} \Delta\boldsymbol{V_{DCs}}{}^{\boldsymbol{T}}\right]^{\boldsymbol{T}} = \left[\Delta\boldsymbol{P}^{\boldsymbol{T}} \ \Delta\boldsymbol{Q}^{\boldsymbol{T}} \ \Delta\boldsymbol{R}^{\boldsymbol{T}}\right]^{\boldsymbol{T}} \tag{23}$$

where $\mathbf{J}$ is the power-flow Jacobian.

It may be noted that instead of the DC slack bus voltage 'V_{DC1}', if the average voltage of all the DC terminals 'V_{DCav}' is specified, the following modifications are required.

$$\boldsymbol{V_{DC}} = [V_{\text{DC1}} \dots V_{\text{Dcq}}]^{\boldsymbol{T}},$$
$$\boldsymbol{R} = \left[\boldsymbol{P_{sh}} \boldsymbol{Q_{sh}} V_{i+r-1} V_{\text{DCav}} P_{\text{IDCPFC}} \boldsymbol{f_1} \boldsymbol{f_2}\right]^{\text{T}}.$$

Individual elements of $\mathbf{J}$ are appropriately modified.

If 'x' IDCPFCs are present, '$\mathbf{V_{DCs}}$' gets enlarged (with 'xz' elements) and 'P_{IDCPFC}' is replaced by a vector '$\mathbf{P_{IDCPFC}}$' having 'x' elements, each governed by an equation similar to Eq. (19). The individual elements of $\boldsymbol{J}$ are appropriately modified.

Figure 3 depicts the flow chart of the proposed approach with IDCPFC.

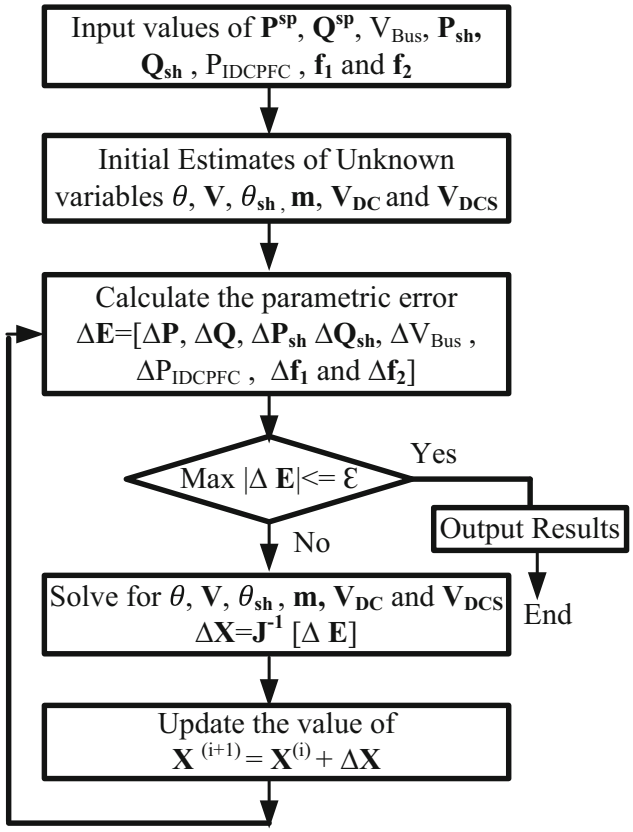

Fig. 3 Flow chart of the proposed approach with IDCPFC

5 Case Studies and Results

For validation of the above model, a large number of studies were executed by employing diverse DC voltage control strategies on MTDC grids embedded within the IEEE 300-bus network [40]. In all the occurrences, the VSC constant was selected as $c = \frac{1}{2\sqrt{2}}$ [12]. Also, for all the VSC coupling transformers, $\text{R}_{\text{sha}} = 0.001$ p.u. and $X_{\text{sha}} = 0.1$ p.u. ($\forall\, a, 1 \le a \le q$). For interconnections between DC termi-

Table 1 Study of IEEE 300 bus system with three-terminal VSC HVDC network incorporating IDCPFC in DC current control mode

The values of bus voltages, powers, currents and droop control gains are denoted in p.u. while phase angles are denoted in degrees			
AC–MTDC power flow without any IDCPFC (VSCs connected to AC buses 268, 272 and 273) $P_{sh2} = 0.35$; $Q_{sh2} = 0.1$; $P_{sh3} = 0.3$; $Q_{sh3} = 0.1$; $V_{DC1} = 3.0$; $V_{DC2} = 2.9988$; $V_{268} = 0.98$; $V_{DC3} = 2.9989$; $I_{DC13} = 0.1098$; NI = 6; CT = 1.45;			
AC–MTDC power flow with IDCPFC			
Given quantities		Solution	
		AC buses	VSCs
V_{268}	0.98	$V_{272} = 1.0086$	$\theta_{sh1} = -43.2336$; $\theta_{sh2} = -29.2839$;
V_{DC1}	3.0	$V_{273} = 1.0366$	$\theta_{sh3} = -5.1793$; $V_{DC2} = 2.9988$;
P_{sh2}	0.35	$\theta_{268} = -39.1739$;	$V_{DC3} = 2.9989$; $m_1 = 0.9418$;
Q_{sh2}	0.1	$\theta_{272} = -31.2289$	$m_2 = 0.9615$; $m_3 = 0.9874$;
P_{sh3}	0.3	$\theta_{273} = -6.7581$	IDCPFC
Q_{sh3}	0.1		$V_{DCs1} = 0.00016$; $V_{DCs2} = -0.00014$;
			$I_{DC12} = 0.0815$; $I_{DC13} = 0.0933$; $P_{DC12} = 0.2444$;
IDCPFC			DC power Converter loss (%)
I_{DC13}	0.12		$P_{DC1} = 0.6754$; $P_{loss1} = 1.54$;
			$P_{DC2} = -0.3628$; $P_{loss2} = 1.26$;
			$P_{DC3} = -0.3124$; $P_{loss3} = 1.23$;
		NI = 6; CT = 1.51;	

nals $R_{DCuv} = 0.01$, p.u. ($\forall\, u, v, 1 \le u \le q, 1 \le v \le q, u \ne v$), throughout the paper [38]. The converter loss constants 'a_1', 'b_1' and 'c_1' are chosen as 0.011, 0.003 and 0.0043, respectively [38]. All the case studies were implemented in MATLAB software. In all occurrences, a termination error tolerance of 10^{-10} p.u. was selected.

Study 1: MTDC grid inclusive of IDCPFC in DC current control mode

A study is conducted on the AC–MTDC network with the VSCs connected to AC buses 268, 272 and 273. The AC–MTDC power-flow solution without any IDCPFC is shown in the first row of Table 1, with the current in the DC link between the DC buses 1 and 3 computed to be 0.1098 p.u. Subsequently, a IDCPFC (having two variable DC voltage sources) is again incorporated in the three-terminal VSC-MTDC grid integrated with the IEEE 300-bus test network and the AC–MTDC power flow is again carried out. The IDCPFC maintains the DC current between DC buses 1 and 3 to a value of 0.12 p.u (the DC link current without any IDCPFC is 0.1098 p.u.). The specified quantities for this study are shown in the rows 3–11 and columns 1–2 of Table 1. The AC–MTDC power-flow solution with the IDCPFC is shown in the rows 3–11 and columns 3–4 of Table 1. NI is same in both the cases without IDCPFC and with IDCPFC. It is observed from Table 1 a computational time of the algorithm incorporating IDCPFC increased to a value of 1.51 s than the algorithm without IDCPFC (1.45 s). The value of computational time increased due to the increase in number of variables.

Study 2: MTDC grid inclusive of IDCPFC in DC power control mode

Subsequently, a study is executed on the same three-terminal AC–MTDC network but with the three VSCs connected to AC buses 268, 272 and 273. The AC–MTDC power-flow solution without any IDCPFC is shown in the first row of Table 2, with the sending end power flow in the DC link between the DC buses 1 and 2 computed to be 0.3461 p.u. Subsequently, a IDCPFC (having two variable DC voltage sources) is incorporated in the three-terminal VSC-MTDC grid integrated with the IEEE 300-bus test network and the AC–MTDC power flow is again carried out. The IDCPFC is used to control the sending end power in the DC link between DC buses 1 and 2 to a specified value of 0.36 p.u. (the sending end DC link power without any IDCPFC is 0.3461 p.u.). The specified quantities are shown in the rows 3–11 and columns 1–2 of Table 2. The AC–MTDC power-flow solution with the IDCPFC is shown in the rows 3–11 and columns 3–4 of Table 2.

From Tables 1 and 2, it is noticed that in all the studies (base case, IDCPFC in DC current control mode and the IDCPFC in DC power control mode), '*IN*' remains same. Thus, '*IN*' is independent of the MTDC grid control technique. This shows that the proposed approach is robust.

The convergence features of base case (without IDCPFC), rows 3–11 of Table 1 and rows 3–11 of Table 2 are presented in Figs. 4, 5 and 6, respectively. From Figs. 4, 5 and 6, it is noticed that the AC–MTDC model considered displays

Table 2 Study of IEEE 300 bus system with three-terminal VSC HVDC network incorporating IDCPFC in DC power control mode

The values of bus voltages, powers, currents and droop control gains are denoted in p.u. while phase angles are denoted in degrees			
AC–MTDC power flow without any IDCPFC (VSCs connected to AC buses 268, 272 and 273) $P_{sh2} = 0.35$; $Q_{sh2} = 0.1$; $P_{sh3} = 0.3$; $Q_{sh3} = 0.1$; $V_{DC1} = 3.0$; $V_{DC2} = 2.9988$; $V_{268} = 0.98$; $V_{DC3} = 2.9989$; $P_{DC12} = 0.3461$; NI = 6; CT = 1.45;			
AC–MTDC power flow with IDCPFC			
Given quantities		Solution	
		AC buses	VSCs
V_{268}	0.98	$V_{272} = 1.0086$;	$\theta_{sh1} = -43.2335$; $\theta_{sh2} = -29.2837$;
V_{DC1}	3.0	$V_{273} = 1.0366$;	$\theta_{sh3} = -5.1792$; $V_{DC2} = 2.9989$;
P_{sh2}	0.35	$\theta_{268} = -39.1738$;	$V_{DC3} = 2.9989$; $m_1 = 0.9418$;
Q_{sh2}	0.1	$\theta_{272} = -31.2288$;	$m_2 = 0.9615$; $m_3 = 0.9874$;
P_{sh3}	0.3	$\theta_{273} = -6.7581$;	IDCPFC
Q_{sh3}	0.1		$V_{DCs1} = -0.000064$; $V_{DCs2} = 0.000074$;
			$I_{DC12} = 0.12$; $P_{DC13} = 0.3571$; $I_{DC13} = 0.119$;
IDCPFC			DC power Converter loss (%)
P_{DC12}	0.36		$P_{DC1} = 0.6754$; $P_{loss1} = 1.54$;
			$P_{DC2} = -0.3628$; $P_{loss2} = 1.26$;
			$P_{DC3} = -0.3124$; $P_{loss3} = 1.23$;
		NI = 6; CT = 1.52;	

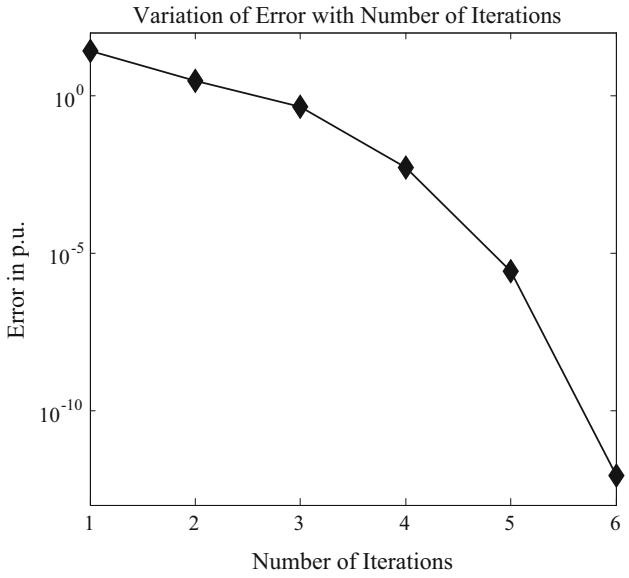

Fig. 4 Convergence characteristic for the case study of row 1 in Table 1

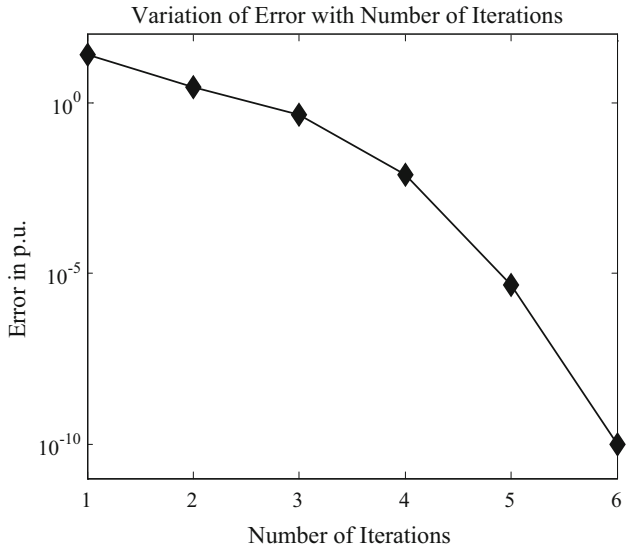

Fig. 5 Convergence characteristic for the case study of rows 3–11 in Table 1

superior convergence (quadratic convergence). This validates the model.

6 Conclusions

In this paper, a unified algorithm for the development of power-flow models of integrated AC–MTDC systems incorporating IDCPFC in DC grid is proposed. In this work, the modulation indices of the VSCs are obtained directly from the power-flow solution. The IDCPFC is operated in both the DC current control and DC power-flow control mode. In addition, converter losses are included in the proposed works. The algorithm displays superior convergence features, independent of the MTDC grid control technique employed. This validates the proposed model.

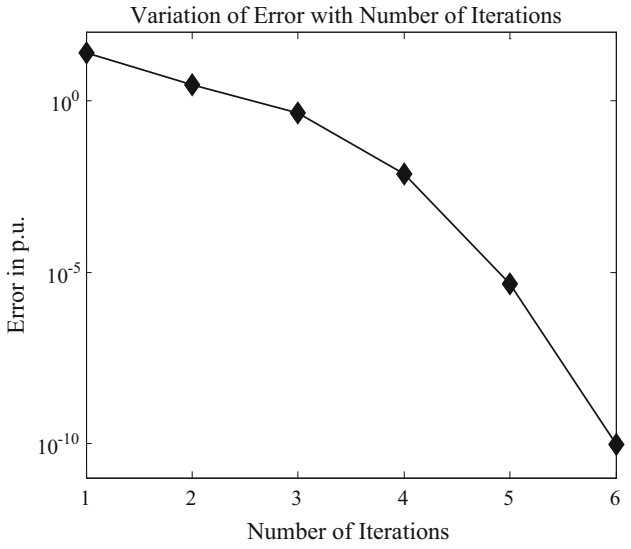

Fig. 6 Convergence characteristic for the case study of rows 3–11 in Table 2

Newton power-flow model of hybrid AC–MTDC system incorporating IDCPFC is useful for power system planning and operation control of large scale power systems. The multiline control capability of the IDCPFC plays an important role in solving many problems such as DC transmission network congestion management and integration of renewable energy sources into the DC grid.

References

1. https://www.bp.com/content/dam/bp/en/corporate/pdf/energy-economics/statistical-review/bp-stats-review-2018-full-report.pdf
2. Valinejad, J.; Marzband, M.; Akorede, M.F.; Barforoshi, T.: Generation expansion planning in electricity market considering uncertainty in load demand and presence of strategic GENCOs. Electr. Power Syst. Res. **152**, 92–104 (2017)
3. Marzband, M.; Azarinejadian, F.; Savaghebi, M.; Pouresmaeil, E.; Guerredo, J.M.; Lightbody, G.: Smart transactive energy framework in grid connected multiple home microgrids under independent and coalition operations. Renew. Energy **126**, 95–106 (2018)
4. Marzband, M.; Fouladfar, M.H.; Akorede, M.F.; Lightbody, G.; Pouresmaeil, E.: Framework for smart transactive energy in home microgrids considering coalition formation and demand side management. Sustain. Cities Soc. **40**, 1 (2018)
5. Tavakoli, M.; Shokridehaki, F.; Akorede, M.F.; Marzband, M.; Vechiu, I.; Pouresmaeil, E.: CVaR based energy management scheme for optimal resilience and operational cost in commercial building microgrids. Electr. Power Energy Syst. **100**, 1–9 (2018)
6. Marzband, M.; Javadi, M.; Pourmousavi, S.A.; Lightbody, G.: An advanced retail electricity market for active distribution systems and home microgrid interoperability based on game theory. Electr. Power Syst. Res. **157**, 187–199 (2018)
7. Tavakoli, M.; Shokridekhari, E.; Marzband, M.; Godina, R.; Pouresmaeil, E.: A two stage hierarchical control approach for the optimal energy management in commercial building microgrids based on local wind power and PEVs. Sustain. Cities Soc. **41**, 332–340 (2018)
8. Khan, S.; Bhowmick, S.: A generalized power flow model of VSC based Hybrid AC–DC systems integrated with offshore wind farms. IEEE Trans. Sustain. Energy **2018**, 1 (2018)
9. Arrillaga, J.; Liu, Y.H.; Watson, N.R.: Flexible Power Transmission: The HVDC Options. Wiley, London (2007)
10. Sood, V.K.: DVDC and FACTS Controllers—Applications of Static Converters in Power Systems. Kluwer, Dordrecht (2004)
11. Acha, E.; Agelidis, V.G.; Lara, O.Anaya; Miller, T.J.E.: Power Electronic Control in Electrical Systems. Newnes, Butterworth (2002)
12. Padiyar, K.R.: HVDC Power Transmission Systems, 2nd edn. New Age International Publishers, London (2012)
13. Yazdani, A.; Iravani, R.: Voltage-Sourced Converters in Power Systems: Modeling, Control and Applications, p. 171. Wiley, London (2010)
14. Flourentzou, N.; Agelidis, V.G.; Demetriades, G.D.: VSC-based HVDC power transmission systems: an overview. IEEE Trans. Power Electron. **24**(3), 592–602 (2009)
15. Asplund, G.: Application of HVDC light to power system enhancement. In: Proceeding of IEEE PES Winter Meeting (January 2000)
16. Blau, J.: Europe plans a north sea grid. IEEE Spect. **1**, 12–13 (2010)
17. Haileselassie, T.M.; Uhlen, K.: Power system security in a meshed north sea HVDC grid. IEEE Proc. Invited Pap. **101**(4), 978–990 (2013)
18. Zhang, X.P.: Multiterminal voltage-sourced converter-based HVDC models for power flow analysis. IEEE Trans. Power Syst. **19**(4), 1877–1884 (2004)
19. Angeles-Camacho, C.; Tortelli, O.L.; Acha, E.; Fuerte-Esquivel, C.R.: Inclusion of a high voltage DC voltage source converter model in a Newton raphson power flow algorithm. Proc. Inst. Elect. Eng. Gen., Transm. Distrib. **150**(6), 691–696 (2003)
20. Baradar, M.; Ghandhari, M.: A multi-option unified power flow approach for hybrid AC/DC grids incorporating multi-terminal VSC-HVDC. IEEE Trans. Power Syst. **28**(3), 2376–2383 (2013)
21. Gengyin, L.; Ming, Z.; Jie, H.; Guangkai, L.; Haifeng, L.: Power flow calculation of power systems incorporating VSC-HVDC. In: Proceeding of International Conference Power System Technology (PowerCon), vol. 2, pp. 1562–1566 (2004)
22. Khan, S.; Bhowmick, S.: A novel power flow model of multiterminal VSC HVDC systems. Electr. Power Syst. Res. **133**, 219–227 (2016)
23. Jovcic, D.; Hajian, M.; Zhang, H.; Asplund, G.: Power flow control in dc transmission grids using mechanical and semiconductor based DC/DC devices. In: Proceeding of IET International Conference AC DC Power Transmission, pp. 1–6 (2012)
24. Mu, Q.; Liang, J.; Li, Y.; Zhou, X.: Power flow control devices in DC grids. In: Proceeding of IEEE Power Energy Society General Meeting, pp. 1–7 (2012)
25. Jovcic, D.; Ooi, B.: Developing DC transmission networks using DC transformers. IEEE Trans. Power Del. **25**(4), 2535–2543 (2010)
26. Jovcic, D.; Zhang, L.: LCL DC/DC converter for DC grids. IEEE Trans. Power Del. **28**(4), 2071–2079 (2013)
27. Jovcic, D.; Lin, W.: Multiport high power LCL DC hub for use in DC transmission grids. IEEE Trans. Power Del. **29**(2), 760–768 (2014)
28. Kish, G.; Ranjram, M.; Lehn, P.: A modular multilevel DC/DC converter with fault blocking capability for HVDC interconnects. IEEE Trans. Power Electron. **30**(1), 148–162 (2015)
29. Veilleux, E.; Ooi, B.: Multiterminal HVDC with thyristor power flow controller. IEEE Trans. Power Del. **27**(3), 1205–1212 (2012)
30. Series Connected DC/DC Converter for Controlling the Power Flow in a HVDC Power Transmission System, PCT WO 2012/037964A1 (2012)

31. An Arrangement for Controlling the Electrical Power Transmission in a HVDC Power Transmission Systems, PCT WO 2013/091700A1 (2013)
32. Mu, Q.; Liang, J.; Li, Y.; Zhou, X.: Power flow control devices in DC grids. In: IEEE Power and Energy Society General Meeting, pp. 1–7 (2012)
33. Gyugyi, L.; Sen, K.K.; Schauder, C.D.: The interline power flow controller concept: a new approach to power flow management in transmission systems. IEEE Trans. Power Del. **14**(3), 1115–1123 (1999)
34. Barker, C.; Whitehouse, R.: A current flow controller for use in HVDC grids. In: IET International Conference on AC and DC Power Transmission (ACDC), pp. 1–5 (2012)
35. Whitehouse, R.; Barker, C.: Current flow controller. US Patent Application, 2015/0180231 A1 (2015)
36. Deng, N.; Wang, P.; Zhang, X.; Tang, G.; Cao, J.: A DC current flow controller for meshed modular multilevel converter multiterminal HVDC grids. CSEE J. Power Energy Syst. **1**(1), 43–51 (2015)
37. Chen, W.; Zhu, X.; Yao, L.Y.; Ruan, X.; Wang, Z.; Cao, Y.: An interline DC power flow controller (IDCPFC) for multi-terminal HVDC system. IEEE Trans. Power Del. **30**(4), 2027–2036 (2015)
38. Cao, J.; Du, W.; Wang, H.F.: Minimization of transmission loss in meshed AC/DC grids with VSC-MTDC networks. IEEE Trans. Power Syst. **28**(3), 3047–3055 (2013)
39. Daelemans, G.: VSC-HVDC in meshed networks. M.Eng. Thesis, Katholieke Universiteit Leuven, Leuven (2008)
40. http://www.ee.washington.edu/research/pstca

Bulletin of Engineering Geology and the Environment
https://doi.org/10.1007/s10064-018-1415-2

CASE HISTORY

Automatic calculation of rainfall thresholds for landslide occurrence in Chukha Dzongkhag, Bhutan

Stefano Luigi Gariano[1] · Raju Sarkar[2,3] · Abhirup Dikshit[2] · Kelzang Dorji[2] · Maria Teresa Brunetti[1] · Silvia Peruccacci[1] · Massimo Melillo[1]

Received: 17 July 2018 / Accepted: 20 October 2018

Abstract

Bhutan is highly prone to landslides, particularly during the monsoon season. Several landslides often occur along the Phuentsholing–Thimphu highway, a very important infrastructure for the country. Worldwide, empirical rainfall thresholds represent a widely used tool to predict the occurrence of rainfall-induced landslides. Nevertheless, no thresholds are currently designed and proposed for any region in Bhutan. In this work, we define empirical cumulated event rainfall–rainfall duration thresholds for the possible initiation of landslides using information on 269 landslides that occurred between 1998 and 2015 along the 90-km highway stretch between the towns of Phuentsholing and Chukha, in southwestern Bhutan, and daily rainfall measurements obtained from three rain gauges. For this purpose, we apply a consolidated frequentist method and use an automatic tool that identifies the rainfall conditions responsible for the failures and calculates thresholds at different exceedance probabilities and the uncertainties associated with them. Analyzing rainfall and landslide data, we exclude from the analysis all the landslides for which the rainfall trigger is not certain, so we reduce the number of landslides from 269 to 43. The calculated thresholds are useful to identify the triggering conditions of rainfall-induced landslides and to predict the occurrence of the failures in the study area, which is, to date, poorly studied. These rainfall thresholds might be implemented in an early warning system, in order to reduce the risk posed by these phenomena to the population living and traveling along the investigated road stretch.

Keywords Landslide prediction · Rainfall events · Road · Triggering rainfall · Himalaya

Introduction

Worldwide, landslides are widespread and hazardous phenomena, threatening population, infrastructures, and properties (Petley 2012; Haque et al. 2016; Froude and Petley 2018). Rainfall is the main trigger of landslides; therefore, defining the rainfall conditions responsible for landslide occurrence in a given area is an important scientific and social issue. Rainfall thresholds are the most commonly adopted tools to define quantitatively the rainfall conditions that, when reached or exceeded, are likely to trigger landslides. There is a huge amount of literature on the statistical analysis of the rainfall conditions that have triggered landslides and on the methods used to calculate rainfall thresholds all over the world (e.g., Brunetti et al. 2010; Cepeda et al. 2010; Tiranti and Rabuffetti 2010; Saito et al. 2010; Peruccacci et al. 2012; Staley et al. 2013; Chen and Wang 2014; Zêzere et al. 2015; Rosi et al. 2016; Lainas et al. 2016; Li et al. 2017; Soto et al. 2017; Marjanović et al. 2018; Martinović et al. 2018; Valenzuela et al. 2018). Diverse procedures and methods were presented to select rainfall parameters, to collect landslide data, and to define, calibrate, and validate rainfall thresholds. Overall, the widely used empirical rainfall thresholds are relationships linking rainfall conditions or variables to landslide occurrences. Most of the thresholds present in the scientific literature link the duration of the rainfall (D, usually expressed in h) to the cumulated event rainfall (E, in mm) or to the mean rainfall intensity (I, in mm·h^{-1}) of known rainfall events that have triggered landslides (Guzzetti

✉ Stefano Luigi Gariano
stefano.gariano@irpi.cnr.it

[1] Research Institute for Geo-Hydrological Protection, Italian National Research Council (CNR-IRPI), Perugia, Italy

[2] Center for Disaster Risk Reduction and Community Development Studies, Royal University of Bhutan, Rinchending, Bhutan

[3] Delhi Technological University, Shahbad Daulatpur, Delhi, India

Published online: 01 November 2018

et al. 2008; Peruccacci et al. 2017; Segoni et al. 2018). Recently, several attempts were made to develop standardized and automatized procedures for the definition of the thresholds, aiming at reducing uncertainties and enhancing the threshold objectivity, reproducibility, and robustness (e.g., Vessia et al. 2016; Melillo et al. 2015, 2016, 2018).

The study area of this work is located in Bhutan, a country that is highly prone to landslides, mostly triggered by monsoons (Norbu et al. 2003; Kuenza et al. 2010; Petley 2012). Recently, an increasing landslide trend has been observed in the region, also linked to modifications in the rainfall patterns, likely due to climate changes (Meenawat and Sovacool 2011; Gyeltshen and Norbu 2013; Gariano and Guzzetti 2016). Areas most prone to rainfall-induced failures, such as the southern part of Bhutan, are characterized by heavily fractured and weathered rocks of phyllites, slates, and schists that contain high amounts of clay minerals. The risk posed by such slope failures is considerably high given the numerous road cuttings (Kuenza et al. 2010).

In the last ten years, rainfall thresholds were defined in several areas of the world, particularly in Eastern Asia. However, contrarily to the neighboring countries such as China, Nepal, and India [e.g., thresholds for the North Sikkim and Kalimpong districts, proposed by Sengupta et al. (2010) and Dikshit and Satyam (2018), respectively], rainfall thresholds for specific areas in Bhutan are not yet present in the scientific literature (Segoni et al. 2018). Moreover, a research conducted on the Scopus database using the keywords "landslide*" and "Bhutan" resulted in only 28 records, indicating that the area is, to date, poorly studied. No early warning systems for rainfall-induced landslides are currently operating or designed in Bhutan (Piciullo et al. 2018).

In this work, we propose empirical rainfall thresholds for landslide occurrence in Chukha Dzongkhag, southwestern Bhutan, which is an area that is highly prone to rainfall-induced landslides. Figure 1 shows examples of recent failures along the Phuentsholing–Thimphu highway in the region, after the 2016 monsoon (Dawson et al. 2018). We use information on the spatial and temporal location of 269 landslides that occurred between 1998 and 2015 in the area and daily rainfall measurements obtained from three rain gauges. We calculate the thresholds adopting an automatic tool recently proposed by Melillo et al. (2018), which reconstructs the rainfall conditions responsible for past failures and calculates rainfall thresholds at different exceedance probabilities and related uncertainties.

Fig. 1 Panoramic (**a**) and close view (**b**) of landslides that occurred on the Phuentsholing–Thimphu highway in Chukha Dzongkhag after the 2016 monsoon

Study area

The study area (covering 0.25 km^2) is located in the Chukha Dzongkhag, southwestern Bhutan (Fig. 2a). The Kingdom of Bhutan extends for an area of 46,500 km^2 in the Eastern Himalaya, between the Tibetan plateau (China) to the north and India to the south, with elevations ranging between 200 and 7500 m a.s.l. The study area is selected due to the importance of the Phuentsholing–Thimphu highway, which represents the main trade link of Bhutan connecting the capital Thimphu with India. Several landslides often block the highway, causing serious economic damage (Kuenza et al. 2010).

Chukha Dzongkhag is located in the western part of Bhutan Himalaya, in the subtropical and temperate climatic zone, where one of the highest annual rainfall (4000–6000 mm) and the most frequent heavy rains (up to 800 mm·day^{-1}) along the whole of the Himalayan front are recorded (Prokop and Walanus 2017). According to the Köppen classification, the climate is subtropical monsoonal with at least ten times as much rain in the wettest month of summer as in the driest month of winter. About 80% of the annual rainfall occurs during the southwestern monsoon between June and September. The contribution of pre-monsoon (March to May) and post-monsoon (October to December) rainfall to the annual rainfall is about 15 and 5%, respectively. However, during both seasons, rainstorms may occur and are associated with local convection and tropical cyclone activity over the Bay of Bengal (Prokop and Walanus 2017). Relatively drier conditions prevail in January and February (Dunning et al. 2009). Steep slope terrains also increase the landslide susceptibility, often causing blockage of the highway.

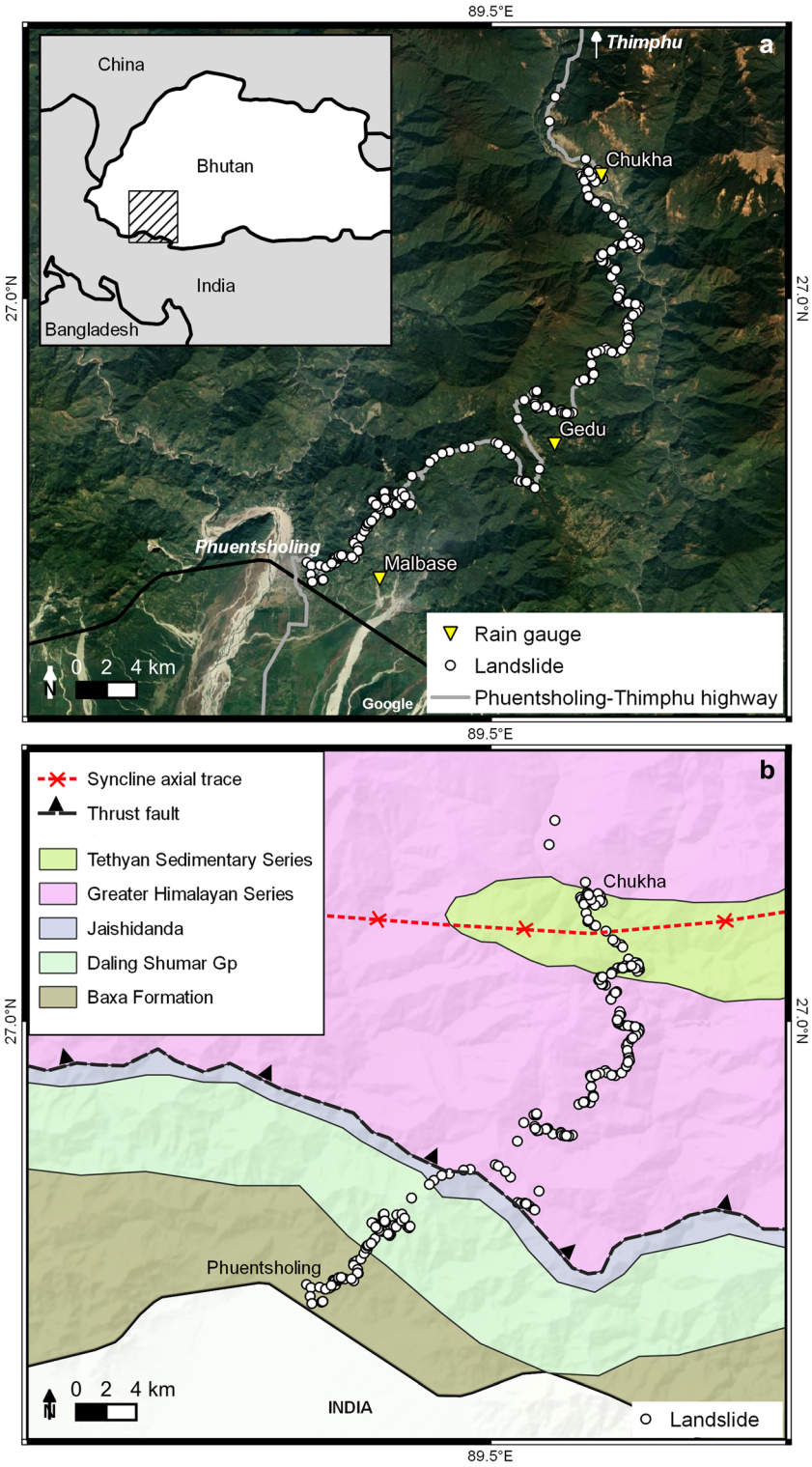

Fig. 2 (**a**) Map showing the study area and location of landslides (*white dots*) and rain gauges (*yellow triangles*). Background image from Google®. (**b**) Geological map of the study area, based on the geological map of Bhutan, with structures and semi-continuous geological units, modified after Greenwood et al. (2016)

The regional geological setting of the Bhutan Himalaya is described by Gansser (1983). Most of Bhutan is dominated by the Higher Himalayan Crystalline Complex, which outcrops over a north–south width of about 60–100 km between the South Tibetan Detachment along the northern border of Bhutan and the Main Central Thrust. The tectonic setting of Bhutan Himalaya shares similarities with Himalayas of Nepal and India. The geologic fragility of the Himalayan area is highlighted in the literature (Kuenza et al. 2010). In more detail, the study area is located in correspondence of the Tethyan Sedimentary Series–Greater Himalayan Series (TSS–GHS) contact, recently investigated by Greenwood

et al. (2016). The area is characterized by low-grade quartzite with ~ 2-cm pelitic layers, limestone, and calc-schist. TSS pelites contain garnet, muscovite, and much less biotite than in the underlying GHS paragneiss; they also lack any evidence of partial melting or high grade of metamorphism. The northern contact of the TSS near Chukha separates cliffs of TSS phyllite and quartzite from structurally lower, high-strain GHS kyanite garnet biotite paragneiss. Figure 2b shows the geological map of the study area, based on the geological map of Bhutan made by Greenwood et al. (2016).

Data

We use spatial and temporal information on 269 landslides that occurred along the Phuentsholing–Thimphu highway from July 1998 to July 2015 (Fig. 2), provided by the Border Roads Organisation of the Government of India (http://www.bro.gov.in) in the framework of the DANTAK project. The majority of the failures are localized along a 90-km stretch of the highway, between the towns of Chukha and Phuentsholing. For each landslide in the catalog, the occurrence day and geographic coordinates (latitude and longitude, EPSG: 4326) are known. Based on the classification system of Cruden and Varnes (1996), the types of movement identified by the Indian Border Roads Organisation in the study area are: rock fall, rock slide, debris flow, debris slide, and earth slide. The involved materials are: quartzite, phyllite, dolomite, and gneiss in a slaty matrix, silt, sand gravel, and boulders—non-plastic, granular and sorted, debris—saturated and partially saturated (since failures mostly occurred during or after the monsoon). Based on visual and onsite depth measurements, the depths of the landslides range from a few decimeters to some meters. The landslides are mapped as single points.

Figure 3 shows the landslide annual and monthly distribution. Almost 70% of the failures occurred between 2007 and 2011 (181 out of 269), while 77% (208) of the total landslides were recorded in the monsoon season of June–September. The month (year) with the highest number of documented landslides is July (2008) with 74 (54) records. The figure also shows (in red) the distribution of the 115 "single triggered landslides"; i.e., if more landslides are reported in the same day and in the same area as being associated to the same triggering rainfall condition, they are counted only once.

Regarding rainfall data, we use daily measurements from three rain gauges located at Chukha, Gedu, and Malbase (Fig. 2a), managed by the National Center for Hydrology and Meteorology of the Royal Government of Bhutan (http://www.hydromet.gov.bt). Rainfall data cover the period from 1 January 1990 to 31 December 2015. Figure 4a shows the annual variation in monthly rainfall calculated considering the three rainfall series. The typical monsoon regime is clearly visible, with most of the annual rainfall occurring between

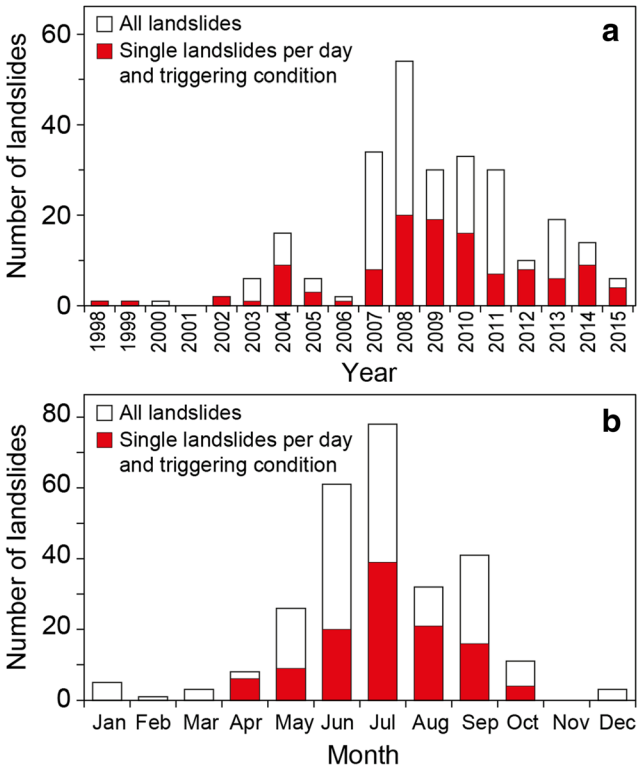

Fig. 3 Number of landslides in Chukha Dzongkhag per year (**a**) and per month (**b**). The bars represent all the landslides in the catalog; in *red* are highlighted the "single triggered landslides" (e.g., one reported landslide per each day and per associated triggering rainfall condition; see text for a thorough explanation)

June and August, with a very high rainfall variability, as highlighted in the box and whisker plot (Fig. 4a).

Method

We use the comprehensive tool CTRL-T (Calculation of Thresholds for Rainfall-Induced Landslides-Tool) recently proposed by Melillo et al. (2018). This tool automatically extracts rainfall events from continuous rainfall series, reconstructs triggering rainfall conditions responsible for landslide occurrences, and calculates rainfall thresholds at various exceedance probabilities. CTRL-T needs the following as input: spatial (geographic coordinates) and temporal (day and time) information on landslide occurrences, continuous hourly rainfall series from localized rain gauges (the station coordinates are also needed), and a few setting parameters. CTRL-T is structured in three blocks, accomplishing different and related tasks. The first one receives as input continuous rainfall series and reconstructs distinct rainfall events, calculating their duration (D, in h) and cumulated event rainfall (E, in mm), by using rainfall series and a few parameters to account for different seasonal and climatic settings. Starting from the reconstructed rainfall events and using spatial and temporal

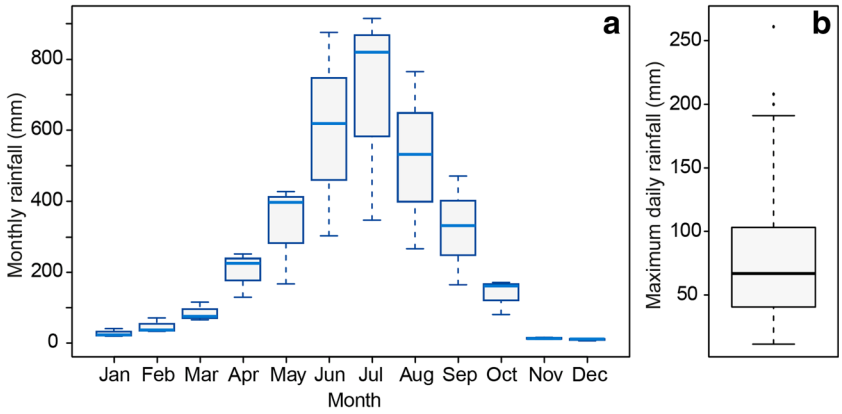

Fig. 4 Box and whisker plots showing: (**a**) annual variation of monthly rainfall measures in the study area for the 26-year period 1990–2015 and (**b**) variation of maximum daily rainfall in the three years preceding the landslides. Legend: the bottom and top of the rectangular boxes are 25th and 75th percentiles, respectively; the horizontal thick lines inside boxes are 50th percentiles (median values); the whiskers show 1.5 times the interquartile range; the points represent outliers

information on landslides, the second block performs the selection of the rain gauges representative for each landslide and the reconstruction of single or multiple rainfall conditions (MRC) likely responsible for the failures, also attributing a weight to each of them. In more detail, CTRL-T selects all rain gauges located within a circular area of a pre-fixed radius (15 km in this work), centered on each landslide. The radius depends on the morphological settings of the study area and is generally smaller in mountainous regions. For each rain gauge in the area, CTRL-T selects the rainfall event associated with the landslide by comparing the start and end dates of the rainfall event and the date of occurrence of the landslide. Next, the tool reconstructs the MRC within the selected rainfall event and assigns to each of them a weight, *w*, proportional to the cumulated rainfall and the mean intensity of the MRC and to the inverse square distance between the rain gauge and the landslide. For each landslide, the highest *w* is used to identify the representative rain gauge and to determine the maximum probability rainfall conditions (MPRC). Finally, using only the MRC with the maximum weight (MPRC) for each failure, the third block calculates objective rainfall thresholds at several exceedance probabilities and the uncertainties associated with them. More details on CTRL-T can be found in Melillo et al. (2015, 2016, 2018).

To calculate the thresholds, CTRL-T employs the frequentist method proposed by Brunetti et al. (2010). The threshold equation is a power law linking the cumulated event rainfall E (in mm) to the rainfall duration D (in h):

$$E = (\alpha \pm \Delta\alpha) \cdot D^{(\gamma \pm \Delta\gamma)} \quad (1)$$

where α is a scaling parameter and γ is the shape parameter, defining the intercept and slope of the power law curve, respectively. Moreover, $\Delta\alpha$ and $\Delta\gamma$ represent the uncertainties associated with the two parameters, calculated using a bootstrap nonparametric statistical technique (Peruccacci et al. 2012). Calculating 5000 synthetic series of rainfall conditions, the bootstrap technique allows defining the mean values of α and γ and their associated uncertainties $\Delta\alpha$ and $\Delta\gamma$.

Results and discussion

Using CTRL-T, we reconstruct 2517 rainfall events in the 16-year period 1990–2015. Two consecutive rainfall events are separated by considering a period of at least one day without rainfall between them. Afterwards, starting from the 269 occurrences of landslides in the period 1998–2015, we then reconstruct 43 rainfall conditions (MPRC) responsible for the failures. Diverse reasons do not allow associating a rainfall condition responsible for the failure to a large number of landslide records.

For a large number of landslides, it is not possible to associate a rainfall condition responsible for the failure. This is due to several reasons: no rainfall measured by close rain gauges; distance between rain gauges and landslides greater than 15 km (radius of the buffer into which we search for rain gauges representative for the failures); multiple landslides occurred simultaneously, or almost so, and in the same or in very close areas. Generally, severe rainfall events can trigger multiple landslides. To define minimum rainfall thresholds, we use only the rainfall conditions responsible for the first failure. Successive failures, occurring later during the same rainfall event, are not used for the definition of the threshold. Considering these three criteria, we select 115 "first triggered landslides" associated to unique rainfall conditions (red bars in Fig. 3). Then, we further analyze these conditions. In particular, we investigate the distribution of the maximum daily rainfall in the three days preceding the landslides (including the day on which the landslides occurred). The distribution, shown in Fig. 4b, is very wide, with a median value equal to 67 mm. The values range between 12 and 261 mm, with

an average value of 78.4 mm. This analysis is useful to identify the triggering rainfall event and to discard landslides not clearly and/or solely related to rainfall, particularly those failures associated with a daily rainfall lower than the 25th percentile (i.e., 41 mm). Occasionally, rainfall events that triggered landslides are partially or even not detected by the rain gauges, likely due to a lack of measurement stations in the neighborhood of the failure or to station malfunctioning. Therefore, in these cases, we exclude other landslides, since we are not able to reconstruct the rainfall responsible for the failure. More generally, when the measured rainfall is not reasonable (i.e., it is unlikely the landslide-triggering rainfall), it is not used to calculate the thresholds. Finally, in order to consider only rainfall-triggered landslides, we consult the United States Geological Survey earthquake repository (https://earthquake.usgs.gov/earthquakes/map) and we exclude landslides that occurred on days in which an earthquake with a local magnitude > 4.5 was recorded in the area. As an example, four landslides occurred on 18 and 19 September 2011 are discarded due to a 4.5 magnitude earthquake striking the region. For all the above-mentioned reasons, the number of rainfall-induced landslides used to define the thresholds is drastically reduced, from 269 to 43. This is necessary for having in the dataset only homogeneous phenomena and only landslides for which the rainfall trigger is certain, in order to obtain reliable empirical thresholds. Finally, we reconstruct only 43 reliable rainfall conditions responsible for landslide occurrences. Almost half of the MPRC (20 out of 43, 46.5%) are reconstructed using the rain gauge located in Gedu. The remaining conditions are calculated analyzing data from the Malbase (15) and Chukha (8) stations.

Figure 5 shows, in log–log coordinates, the 43 rainfall conditions (red points) that resulted in landslides, the *ED* rainfall threshold at a 5% ($T_{5,B}$) exceedance probability level (red line),

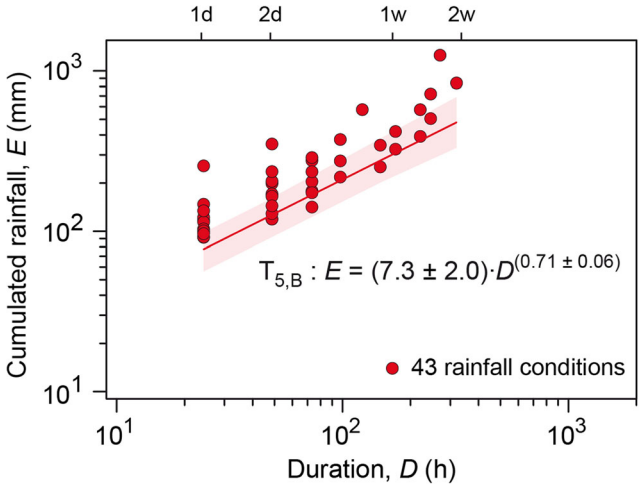

Fig. 5 Rainfall conditions (*red points*) responsible for the 43 landslides in Chukha Dzongkhag, Bhutan, and related rainfall threshold at a 5% exceedance probability level ($T_{5,B}$). The *shaded area* shows the uncertainty associated with the threshold. The data are in log–log coordinates

Table 1 Number of maximum probability rainfall conditions (MPRC) and minimum, mean, and maximum values of cumulated event rainfall (E) for classes of duration (D)

D (h)	No. of MPRC	E (mm)		
		Min	Mean	Max
24	12	93.0	124.9	261.0
48	10	121.0	187.2	358.0
72–96	10	144.0	241.2	382.0
120–312	11	257.0	580.9	1329.4

and the uncertainty region associated with it (shaded area). Rainfall conditions associated with the landslides cover the range of duration $24 \le D \le 312$ h (i.e., $1 \le D \le 13$ days), which is the range of validity for the thresholds, and the range of cumulated rainfall $93.0 \le E \le 1329.4$ mm. Half of the 43 rainfall conditions (22) have duration ≤ 48 h. The minimum, mean, and maximum values of E increase as the values of D increase (Table 1).

Threshold parameters α, γ, $\Delta\alpha$, and $\Delta\gamma$ for different exceedance probabilities are reported in Table 2. The relative uncertainty in the γ parameter, $\Delta\gamma/\gamma$, is 8.5%, which is lower than the 10% "acceptable value" proposed by Peruccacci et al. (2012) for reliable thresholds. On the other hand, the relative uncertainty in α varies according to the exceedance probability but it is always lower than 30%. Here, the high uncertainty is attributable to the relatively limited number of empirical data used to calculate the thresholds and to the clustering of the (D, E) data points in the logarithmic plane, linked to the daily temporal resolution of the rainfall data. The uncertainty can be reduced by increasing the number of landslide records and by using a higher temporal resolution for rainfall data (e.g., hourly records).

Considering the $T_{5,B}$ threshold, the results depict that a rainfall event lasting 24 (48) h with a cumulated rainfall of 69.7 (114.0) mm can cause landslides in the investigated area. The thresholds calculated here are steeper than that defined for the Kalimpong area, India (about 100 km west of Chukha Dzongkhag, at the same latitude) by Dikshit and Satyam (2018), who used daily rainfall data and information on 61 landslides in the period 2010–2016, obtaining $E = 3.52 \cdot D^{0.41}$.

Table 2 Parameters α and γ, and related uncertainties $\Delta\alpha$ and $\Delta\gamma$, of *ED* thresholds at different exceedance probabilities

Exceedance probability (%)	α	$\Delta\alpha$	γ	$\Delta\gamma$
50	11.9	3.3	0.71	0.06
35	10.6	2.9	0.71	0.06
20	9.3	2.5	0.71	0.06
10	8.1	2.2	0.71	0.06
5	7.3	2.0	0.71	0.06
1	6.2	1.7	0.71	0.06

Conclusions

Using information on the occurrence of 269 landslides in the period 1992–2015 and applying an automatic tool, we reconstruct 43 rainfall conditions responsible for failures in Chukha Dzongkhag (Bhutan) and determine regional cumulated event rainfall–rainfall duration (*ED*) thresholds at different exceedance probabilities for the possible initiation of landslides. In order to obtain a reliable dataset of rainfall-induced landslides, we discard many landslide records for which the rainfall was not available or reliable.

The proposed thresholds are the first calculated and published for a specific area in Bhutan. They are useful to identify the triggering conditions of rainfall-induced landslides and to predict their occurrences in the analyzed road stretch. Thresholds can be used only in their range of validity (1–13 days); thus, they cannot be adopted for sub-daily landslide predictions. Given the relatively low number of triggering rainfall conditions used to define the thresholds, an increase in the landslide number would be necessary to reduce the uncertainties and obtain more reliable predictions. In addition, more data will allow performing an independent validation, necessary for evaluating the prediction performance of the thresholds and for including them in a landslide early warning system (e.g., Piciullo et al. 2017). Moreover, in order to solve the issues related to the coarse distribution of the empirical data points in the *DE* plane, it would be necessary to adopt rainfall data with a higher temporal resolution (e.g., hourly data). This might also result in a better fit of the threshold model to the rainfall conditions.

Finally, this work should be considered as a preliminary attempt to define rainfall thresholds in an area totally devoid of models and instruments for the prediction of rainfall-induced landslides, aiming at mitigating the landslide risk for the population living and traveling along the Phuentsholing–Thimphu highway.

Acknowledgements The authors thank the various agencies of the Royal Government of Bhutan for providing rainfall data and the Border Roads Organisation, Government of India (DANTAK project) for providing landslide data. The authors also thank the staff and students of the College of Science and Technology, Royal University of Bhutan, Rinchending. Stefano Luigi Gariano was supported by a grant from NERC in the framework of the LANDSLIP project (grant number NERC/DFID NE/P000681/1). Raju Sarkar was supported by a grant from the BRACE project (grant number NERC/GCRF NE/P016219/1). The authors acknowledge the two anonymous reviewers for their useful comments and suggestions.

References

Brunetti MT, Peruccacci S, Rossi M, Luciani S, Valigi D, Guzzetti F (2010) Rainfall thresholds for the possible occurrence of landslides in Italy. Nat Hazards Earth Syst Sci 10:447–458. https://doi.org/10.5194/nhess-10-447-2010

Cepeda J, Höeg K, Nadim F (2010) Landslide-triggering rainfall thresholds: a conceptual framework. Q J Eng Geol Hydrogeol 43:69–84. https://doi.org/10.1144/1470-9236/08-066

Chen HX, Wang JD (2014) Regression analyses for the minimum intensity-duration conditions of continuous rainfall for mudflows triggering in Yan'an, northern Shaanxi (China). Bull Eng Geol Environ 73:917–928. https://doi.org/10.1007/s10064-013-0567-3

Cruden DM, Varnes DJ (1996) Landslide types and processes. In: Turner AK, Schuster RL (eds) Landslides: investigation and mitigation. Transportation Research Board special report 247. National Academy Press, Washington DC, pp 36–75

Dawson AR, Neves LAC, Sarkar R, Dijkstra T (2018) Bhutanese road and bridge resilience to floods and landslides—first suggestions for assessment and response. Proc. of 37th Annual Southern African Transport Conference, 9-12 July 2018, Pretoria, South Africa, pp 48–57

Dikshit A, Satyam DN (2018) Estimation of rainfall thresholds for landslide occurrences in Kalimpong, India. Innov Infrastruct Solut 3:24. https://doi.org/10.1007/s41062-018-0132-9

Dunning SA, Massey CI, Rosser NJ (2009) Structural and geomorphological features of landslides in the Bhutan Himalaya derived from terrestrial laser scanning. Geomorphol 103:17–29. https://doi.org/10.1016/j.geomorph.2008.04.013

Froude MJ, Petley DN (2018) Global fatal landslide occurrence from 2004 to 2016. Nat Hazards Earth Syst Sci 18:2161–2181. https://doi.org/10.5194/nhess-18-2161-2018

Gansser A (1983) Geology of the Bhutan Himalaya. Birkhaüser Verlag, Basel, Switzerland, 181 pp

Gariano SL, Guzzetti F (2016) Landslides in a changing climate. Earth Sci Rev 162:227–252. https://doi.org/10.1016/j.earscirev.2016.08.011

Greenwood LV, Argles TW, Parrish RR, Harris NBW, Warren C (2016) The geology and tectonics of central Bhutan. J Geol Soc 173(2):352–369. https://doi.org/10.1144/jgs2015-031

Guzzetti F, Peruccacci S, Rossi M, Stark CP (2008) The rainfall intensity–duration control of shallow landslides and debris flows: an update. Landslides 5(1):3–17. https://doi.org/10.1007/s10346-007-0112-1

Gyeltshen P, Norbu C (2013) Strategies and options to address land degradation due to landslides: Bhutanese scenarios. In: Margottini P, Canuti P, Sassa K (eds) Landslide science and practice. Volume 4: global environmental change. Springer-Verlag, Berlin Heidelberg, pp 177–182. https://doi.org/10.1007/978-3-642-31337-0_23

Haque U, Blum P, da Silva PF, Andersen P, Pilz J, Chalov SR, Malet J-P, Jemec Auflič M, Andres N, Poyiadji E, Lamas PC, Zhang W, Peshevski I, Pétursson HG, Kurt T, Dobrev N, García-Davalillo JC, Halkia M, Ferri S, Gaprindashvili G, Engström J, Keelling D (2016) Fatal landslides in Europe. Landslides 13(6):1545–1554. https://doi.org/10.1007/s10346-016-0689-3

Kuenza K, Dorji Y, Wangda D (2010) Landslides in Bhutan. In: Proceedings of the SAARC Workshop on Landslide Risk Management in South Asia, Thimphu, Bhutan, 11–12 May 2010, pp 73–80

Lainas S, Sabatakakis N, Koukis G (2016) Rainfall thresholds for possible landslide initiation in wildfire-affected areas of western Greece. Bull Eng Geol Environ 75(3):883–896. https://doi.org/10.1007/s10064-015-0762-5

Li Y, Ma C, Wang Y (2017) Landslides and debris flows caused by an extreme rainstorm on 21 July 2012 in mountains near Beijing, China. Bull Eng Geol Environ 1–16. https://doi.org/10.1007/s10064-017-1187-0

Marjanović M, Krautblatter M, Abolmasov B, Đurić U, Sandić C, Nikolić V (2018) The rainfall-induced landsliding in Western Serbia: a temporal prediction approach using decision tree technique. Eng Geol 232:147–159. https://doi.org/10.1016/j.enggeo.2017.11.021

Martinović K, Gavin K, Reale C, Mangan C (2018) Rainfall thresholds as a landslide indicator for engineered slopes on the Irish Rail network. Geomorphol 306:40–50. https://doi.org/10.1016/j.geomorph.2018.01.006

Meenawat H, Sovacool BK (2011) Improving adaptive capacity and resilience in Bhutan. Mitig Adapt Strat Glob Change 16(5):515–533. https://doi.org/10.1007/s11027-010-9277-3

Melillo M, Brunetti MT, Peruccacci S, Gariano SL, Guzzetti F (2015) An algorithm for the objective reconstruction of rainfall events responsible for landslides. Landslides 12(2):311–320. https://doi.org/10.1007/s10346-014-0471-3

Melillo M, Brunetti MT, Peruccacci S, Gariano SL, Guzzetti F (2016) Rainfall thresholds for the possible landslide occurrence in Sicily (southern Italy) based on the automatic reconstruction of rainfall events. Landslides 13(1):165–172. https://doi.org/10.1007/s10346-015-0630-1

Melillo M, Brunetti MT, Peruccacci S, Gariano SL, Roccati A, Guzzetti F (2018) A tool for the automatic calculation of rainfall thresholds for landslide occurrence. Environ Model Softw 105:230–243. https://doi.org/10.1016/j.envsoft.2018.03.024

Norbu C, Baillie I, Dema K, Tamang HB, Turkelboom F (2003) Types of land degradation in Bhutan. J Bhutan Stud 8:88–114

Peruccacci S, Brunetti MT, Luciani S, Vennari C, Guzzetti F (2012) Lithological and seasonal control on rainfall thresholds for the possible initiation of landslides in central Italy. Geomorphol 139–140:79–90. https://doi.org/10.1016/j.geomorph.2011.10.005

Peruccacci S, Brunetti MT, Gariano SL, Melillo M, Rossi M, Guzzetti F (2017) Rainfall thresholds for possible landslide occurrence in Italy. Geomorphol 290:39–57. https://doi.org/10.1016/j.geomorph.2017.03.031

Petley D (2012) Global patterns of loss of life from landslides. Geology 40(10):927–930. https://doi.org/10.1130/G33217.1

Piciullo L, Gariano SL, Melillo M, Brunetti MT, Peruccacci S, Guzzetti F, Calvello M (2017) Definition and performance of a threshold-based regional early warning model for rainfall-induced landslides. Landslides 14:995–1008. https://doi.org/10.1007/s10346-016-0750-2

Piciullo L, Calvello M, Cepeda JM (2018) Territorial early warning systems for rainfall-induced landslides. Earth Sci Rev 179:228–247. https://doi.org/10.1016/j.earscirev.2018.02.013

Prokop P, Walanus A (2017) Impact of the Darjeeling–Bhutan Himalayan front on rainfall hazard pattern. Nat Hazards 89:387–404. https://doi.org/10.1007/s11069-017-2970-8

Rosi A, Peternel T, Jemec-Auflič M, Komac M, Segoni S, Casagli N (2016) Rainfall thresholds for rainfall-induced landslides in Slovenia. Landslides 13:1571–1577. https://doi.org/10.1007/s10346-016-0733-3

Saito H, Nakayama D, Matsuyama H (2010) Relationship between the initiation of a shallow landslide and rainfall intensity–duration thresholds in Japan. Geomorphol 118:167–175. https://doi.org/10.1016/j.geomorph.2009.12.016

Segoni S, Piciullo L, Gariano SL (2018) A review of the recent literature on rainfall thresholds for landslide occurrence. Landslides 15(8):1483–1501. https://doi.org/10.1007/s10346-018-0966-4

Sengupta A, Gupta S, Anbarasu K (2010) Rainfall thresholds for the initiation of landslide at Lanta Khola in North Sikkim, India. Nat Hazards 52:31–42. https://doi.org/10.1007/s11069-009-9352-9

Soto J, Palenzuela JA, Galve JP, Luque JA, Azañón JM, Tamay J, Irigaray C (2017) Estimation of empirical rainfall thresholds for landslide triggering using partial duration series and their relation with climatic cycles. An application in southern Ecuador. Bull Eng Geol Environ 1–17. https://doi.org/10.1007/s10064-017-1216-z

Staley DM, Kean JW, Cannon SH, Schmidt KM, Laber JL (2013) Objective definition of rainfall intensity–duration thresholds for the initiation of post-fire debris flows in southern California. Landslides 10:547–562. https://doi.org/10.1007/s10346-012-0341-9

Tiranti D, Rabuffetti D (2010) Estimation of rainfall thresholds triggering shallow landslides for an operational warning system implementation. Landslides 7:471–481. https://doi.org/10.1007/s10346-010-0198-8

Valenzuela P, Domínguez-Cuesta MJ, Mora García MA, Jiménez-Sánchez M (2018) Rainfall thresholds for the triggering of landslides considering previous soil moisture conditions (Asturias, NW Spain). Landslides 15(2):273–282. https://doi.org/10.1007/s10346-017-0878-8

Vessia G, Pisano L, Vennari C, Rossi M, Parise M (2016) Mimic expert judgement through automated procedure for selecting rainfall events responsible for shallow landslide: a statistical approach to validation. Comput Geosci 86:146–153. https://doi.org/10.1016/j.cageo.2015.10.015

Zêzere JL, Vaz T, Pereira S, Oliveira SC, Marques R, Garcia RAC (2015) Rainfall thresholds for landslide activity in Portugal: a state of the art. Environ Earth Sci 73(6):2917–2936. https://doi.org/10.1007/s12665-014-3672-0

American Journal of Electrical and Electronic Engineering, 2018, Vol. 6, No. 3, 85-89
Available online at http://pubs.sciepub.com/ajeee/6/3/2

DOI:10.12691/ajeee-6-3-2

Current-mode Quadrature Oscillator Using CFCC

Alok Kumar Singh[1], Pragati Kumar[2], Raj Senani[3,*]

[1]Department of Electronics and Communication Engineering, Delhi Technological University, New Delhi, India
[2]Department of Electrical Engineering, Delhi Technological University, New Delhi, India
[3]Division of Electronics and Communication Engineering, Netaji Subhas Institute of Technology, New Delhi, India
*Corresponding author: senani@ieee.org

Receive September 02, 2018; Revised October 16, 2018; Accepted November 02, 2018

Abstract In this communication, a Current Follower Current Conveyor (CFCC)-based quadrature oscillator circuit has been proposed which employs a resonator-negative resistor configuration and provides oscillations in quadrature from two high impedance current output terminals of the CFCCs. The workability of the quadrature oscillator has been verified using PSPICE simulations using a CMOS CFCC implementable in 0.18 micron TSMC technology.

Keywords: *current follower, current conveyor, current-follower-current-conveyor, quadrature oscillator, current-mode oscillator, current- mode circuits*

Cite This Article: Alok Kumar Singh, Pragati Kumar, and Raj Senani, "Current-mode Quadrature Oscillator Using CFCC." *American Journal of Electrical and Electronic Engineering*, vol. 6, no. 3 (2018): 85-89. doi: 10.12691/ajeee-6-3-2.

1. Introduction

A quadrature sinusoidal oscillator (QSO) circuit provides two sinusoids with 90^0 phase difference and finds several applications in communication and measurement systems. In communication systems they are used in quadrature mixers, single-sideband generators and direct-conversion receivers while in measurement systems such oscillators are used in vector generators or selective voltmeters (see [1] and references cited therein).

During the last two decades, many new active building blocks have been proposed in the domain of analog signal processing, a comprehensive review of which was presented in [2], wherein several new active building blocks (ABB) were also proposed. Many of the new ABBs proposed in [2] have been employed in the past to realize QSOs and other signal processing applications, which include Current Differencing Buffered Amplifier (CDBA) [3,4], Voltage Differencing Buffered Amplifier (VDBA) [5], Voltage Differencing Transconductance Amplifier (VDTA) [6], Voltage Differencing current conveyor (VDCC) [7], Current Differencing Transconductance Amplifier (CDTA) [8-12], Multiple-Output Current Controlled Current Differencing Transconductance Amplifier (MO-CCCDTA) [13], Modified Current Differencing Transconductance Amplifier (MCDTA) [14], Current Follower Transconductance Amplifier (CFTA) [15], Z-copy Current Follower Transconductance Amplifier (ZC-CFTA) [16], Second-Generation Current Conveyor Transconductance Amplifier (CCII-TA) [17], Differential-Input Buffered and Transconductance Amplifier (DBTA) [18], Current-Feedback Operational Amplifier (CFOA) [19], Differential Voltage Current Conveyor (DVCC) [20], Differential Voltage Current-Controlled Conveyor Transconductance Amplifier (DVCCCTA) [21], Voltage Differencing Inverting Voltage Buffered Amplifier (VDIBA) [22], Voltage Differencing-Differential Input Buffered Amplifiers (VD-DIBA) [23,24] and Programmable Current Amplifier [25].

It may be mentioned that while the QSOs presented in [3,4,5,7,16-24] operate in voltage mode (VM), those presented in [6,8-17,21,25] operate in current mode (CM). Also, of the various QSO circuits quoted above, only the circuits presented in [3,4] and [12] offer fully-decoupled condition of oscillation and frequency of oscillation. Furthermore, out of [3,4] and [12], the QSOs described in [3,4] are VM oscillators while the QSO described in [12] is a CM oscillator.

It has been observed from the literature survey that a new building block named Multi-output Current Follower Current Conveyor (MO-CFCC) which was also proposed in [2] has not been utilized for the realization of QSOs so far while recently its applications in the realization of simulated impedances have been reported in [26,27]. In this letter, we propose a QSO realized with CFCC to fill this void. The workability of the proposed oscillator has been verified using PSPICE simulations in 0.18 micron TSMC technology.

2. CFCC-based Realization of the Current-mode Quadrature Oscillator

CFCC [2] is a five-terminal ABB with the following functionalities: the current at the z terminal is an inverted copy of the input current at 'p' terminal; the terminal 'i' tracks the potential at the terminal z and two complementary currents at the output terminals are available which are copies of the current at the 'i' terminal. To provide

additional functionality to the CFCC, a copy of the current at the 'z' terminal may also be provided resulting in the Z-copy CFCC (ZC-CFCC). The symbolic representation and relations between the various port variables for this ABB are shown in Figure 1, and equation (1) respectively.

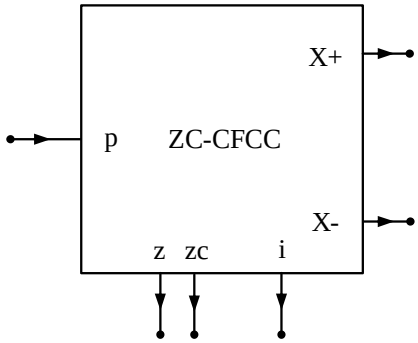

Figure 1. Symbolic notation of the ZC-CFCC

$$\begin{bmatrix} V_p \\ I_z \\ V_i \\ I_{x+} \\ I_{x-} \\ I_{zc} \end{bmatrix} = \begin{bmatrix} 0 & 0 & 0 & 0 & 0 & 0 \\ 1 & 0 & 0 & 0 & 0 & 0 \\ 0 & 1 & 0 & 0 & 0 & 0 \\ 0 & 0 & 1 & 0 & 0 & 0 \\ 0 & 0 & -1 & 0 & 0 & 0 \\ 1 & 0 & 0 & 0 & 0 & 0 \end{bmatrix} \begin{bmatrix} I_p \\ V_z \\ I_i \\ V_{x+} \\ V_{x-} \\ V_{zc} \end{bmatrix}. \quad (1)$$

The proposed current-mode quadrature oscillator circuit using CFCCs is shown in Figure 2 which consists of a parallel RLC resonator made from the CFCC along with R_4, R_5, C_1 and C_2 and a NIC-simulated negative resistor realized by the ZC-CFCC along with the resistors R_1, R_2 and R_3.

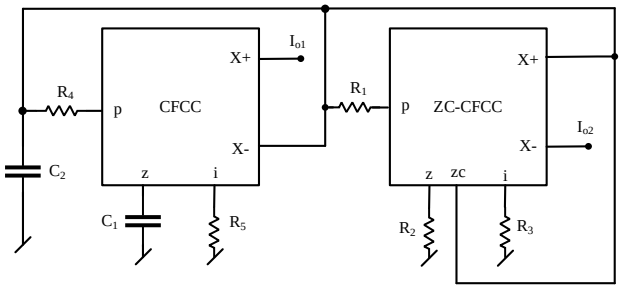

Figure 2. The proposed CFCC-based current mode quadrature oscillator

A straight forward routine analysis of the circuit given in Figure 2 yields the following characteristic equation (CE):

$$s^2 R_1 R_3 R_4 R_5 C_1 C_2 + s R_5 C_1 \left(R_1 R_3 - R_2 R_4 \right) + R_1 R_3 = 0. \quad (2)$$

From equation (2), the condition of oscillation (CO) and frequency of oscillation (FO) are found to be:

CO:

$$R_1 R_3 = R_2 R_4. \quad (3)$$

FO:

$$\omega_{osc} = \frac{1}{\sqrt{R_4 R_5 C_1 C_2}} \quad (4)$$

However, for quadrature oscillator design, we must look into the interrelationship between I_{01} and I_{02} which is found to be

$$\frac{I_{01}}{I_{02}} = -\frac{R_1 R_3}{s R_2 R_4 R_5 C_1}. \quad (5)$$

Under sinusoidal steady state, equation (5) reduces to

$$\frac{I_{01}}{I_{02}} = \frac{j}{\omega_0 R_5 C_1}. \quad (6)$$

The phase difference φ is, thus, equal to 90^o.

3. Non-ideal Considerations

For a non-ideal analysis of the proposed oscillator, we have considered the various parasitic resistances and capacitances associated with the different terminals of the CFCC as follows: R_p represents the parasitic input resistance of the **p** port whereas R_z, C_z represent the resistance and capacitance at the z-terminal of the CFCC; similarly, R_{zc} and C_{zc} represent resistance and capacitance at the **zc** terminal while R_i represents the output resistance of the voltage buffer of the MO-CCII (resistance looking into the i terminal); on the other hand, R_{x+} and C_{x+} represent output resistance and output capacitance at the x+ terminals of the CFCC and finally, R_{x-} and C_{x-} represent the output resistance and the output capacitance at the x-terminals of the CFCC. A straight forward analysis of the proposed oscillator, incorporating all the parasitic immittances described above, gives the following third order characteristic equation:

$$\begin{aligned} & s^3 R_a R_b R_c R_d R_e R_f R_z C_a C_b C_z \\ & + s^2 (R_a R_c R_d R_e R_f R_z C_a C_b + \\ & R_a R_b R_c R_e R_f R_z C_a C_z + R_a R_b R_c R_d R_e R_z C_a C_z \\ & + R_a R_b R_c R_d R_e R_f C_b C_z) \\ & + s(R_a R_c R_e R_f R_z C_a + R_a R_c R_d R_e R_z C_a \\ & + R_a R_c R_d R_e R_f C_b + R_a R_b R_c R_f R_z C_z \\ & + R_a R_b R_c R_e R_f C_z + R_a R_b R_c R_d R_e C_z \\ & - R_b R_d R_e R_f R_z C_a) + R_a R_c R_f R_z \\ & + R_a R_c R_e R_f + R_a R_c R_d R_e - R_b R_d R_e R_f = 0 \end{aligned} \quad (7)$$

where

$$\begin{aligned} & R_a = R_1 + R_p, \; R_b = R_2 \| R_z, \\ & R_c = R_3 + R_i, \; R_d = R_4 + R_p, \\ & R_e = R_5 + R_i, \; R_f = R_{x+} \| R_{x-} \| R_{zc}, \\ & C_a = C_1 + C_z \; and \; C_b = C_2 + C_{zc} + C_{x+} + C_{x-}. \end{aligned}$$

We have measured the values of the various parasitic resistances and capacitances of the CFCC employed in the present work (see Figure 3) by carrying out detailed PSPICE simulations. The measured values of these non ideal parameters are found to be as summarized in Table 1.

Table 1. The SPICE-measured values of the various parasitics of the CMOS ZC-CFCC

S.No.	Parameter	Value
1	**R_p**	**591Ω**
2	**R_i**	**591Ω**
3	**R_z**	**4.9178 M Ω**
4	**C_z**	**6.2988×10^{-14}F**
5	**R_{zc}**	**4.9178 M Ω**
6	**C_{zc}**	**7.3938×10^{-15}F**
7	**R_{x+}**	**4.9862 MΩ**
8	**C_{x+}**	**7.3954×10^{-15}F**
9	**R_{x-}**	**4.7752 MΩ**
10	**C_{x-}**	**7.4062×10^{-15}F**

The following approximations (ensured by selecting appropriate values of the terminating resistances and capacitances) R_1 , R_2, R_3 ,R_4 ,R_5, << R_f and C_1, C_2>>C_{x+}, C_{x-}, C_z and C_{zc} lead to a second order approximation of the CE from which the non-ideal CO and FO are now given by

CO:

$$(R_1+R_p)(R_3+R_i)=(R_2\parallel R_z)(R_4+R_p) \tag{8}$$

FO:

$$\omega_{osc}^{'}=\omega_{osc}\frac{1}{\sqrt{\left[\left(1+\frac{R_p}{R_4}\right)\left(1+\frac{R_i}{R_5}\right)\left(1+\frac{C_z}{C_1}\right)\times\left(1+\frac{(C_{zc}+C_{x+}+C_{x-})}{C_2}\right)\right]}}. \tag{9}$$

The interrelationship between I_{01} and I_{02} is found to be

$$\frac{I_{01}}{I_{02}}=-\frac{R_z(1+sR_bC_z)}{R_e(1+sR_zC_a)}=-\frac{R_z[1+s(R_2\parallel R_z)C_z]}{(R_5+R_i)[1+sR_z(C_1+C_z)]}. \tag{10}$$

The non-ideal expression of the phase difference φ is given by

$$\varphi=\tan^{-1}\omega_{osc}^{'}R_zC_a-\tan^{-1}\omega_{osc}^{'}R_bC_z=\tan^{-1}R_z\sqrt{\frac{(C_1+C_z)}{\left[\begin{matrix}(C_2+C_{zc}+C_{x+}+C_{x-})\\\times(R_1+R_p)(R_5+R_i)\end{matrix}\right]}}-\tan^{-1}\frac{(R_2\parallel R_z)C_z}{\sqrt{\left[\begin{matrix}(R_1+R_p)(R_5+R_i)(C_1+C_z)\\\times(C_2+C_{zc}+C_{x+}+C_{x-})\end{matrix}\right]}}. \tag{11}$$

Subject to the approximations used in the non-ideal analysis, it may be observed that the phase difference between the two output currents would be very close to 90° (as the angle corresponding to the argument of the first arctangent term will be close to ninety degree because of the very large value of R_z while the angle corresponding to the argument of the second arctangent term will be very small because of the very small value of C_z). We have calculated the phase difference using the values of different parasitic resistances and capacitances given in Table 1 as per equation (11) and found it to be equal to 89.52° for a design frequency of 1.59 MHz.

4. PSPICE Simulation Results

We now present some SPICE simulation results to demonstrate the workability of the proposed structure. The CMOS implementation of the CFCC [27] shown in Fig. 3 using 0.18 micron TSMC process technology has been used to verify the workability of the circuit presented in this paper. The values of the DC bias currents and voltages were taken as 40 µA and ± 2.5V respectively. The oscillator was designed for a frequency of 1.59 MHz by appropriately selecting the passive components as follows: C_1= C_2=10 pF, R_1=10 kΩ, R_2=10700 Ω, R_3=10 kΩ, R_4=10 kΩ, R_5=10 kΩ. From SPICE simulations the oscillation frequency was found to be 1.50 MHz. The output waveforms are shown in Figure 4(a). The quadrature relationship of the generated waveform is indicated by the Lissajous pattern shown in Figure 4(b). The measured phase difference was found to be 90.91°. Figure 5 shows the FFT of the generated waveforms. Total harmonic distortion (THD) for current output I_{01} was found to be 3.2 % and for the current output I_{02} as 5.3 %. These simulation results thus, prove the workability of the proposed circuit.

5. Concluding Remarks

In this letter, a recently proposed active building block, namely, the CFCC has been used to devise a current-mode QSO. The workability of the circuit has been substantiated by SPICE simulations based on a CMOS CFCC implementable in 0.18 µm CMOS technology. The letter has, thus, added a new application of the CFCC in the area of quadrature oscillator realization, whose applications explored and known so far were only in the realization of the simulated impedances of various kinds [26,27].

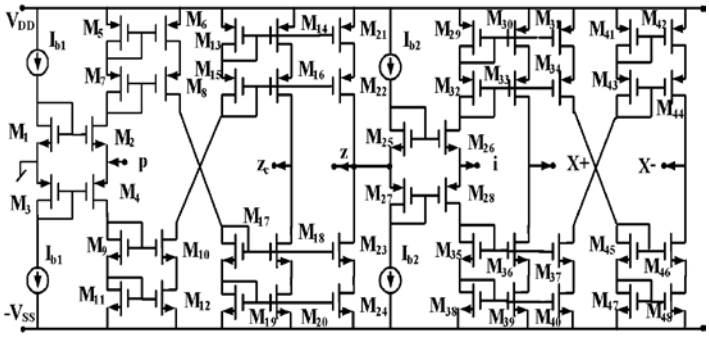

Figure 3. An exemplary CMOS implementation of the ZC-CFCC [26]

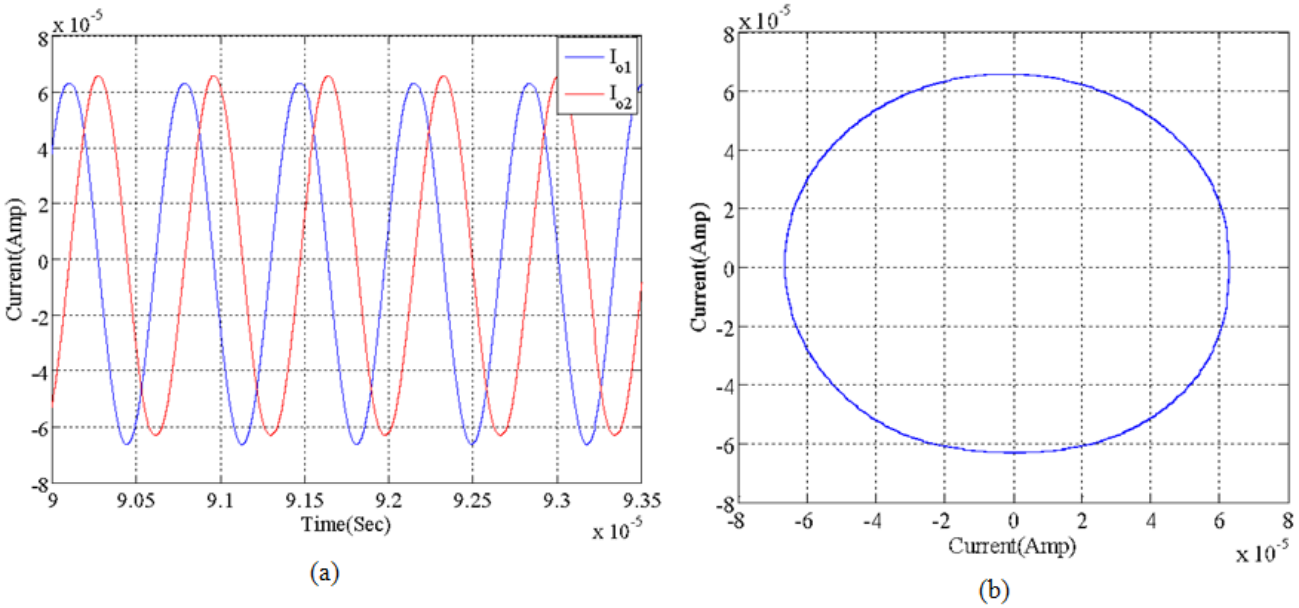

Figure 4. PSPICE Simulation Results (a) Quadrature oscillator waveforms (b) Lissajous pattern

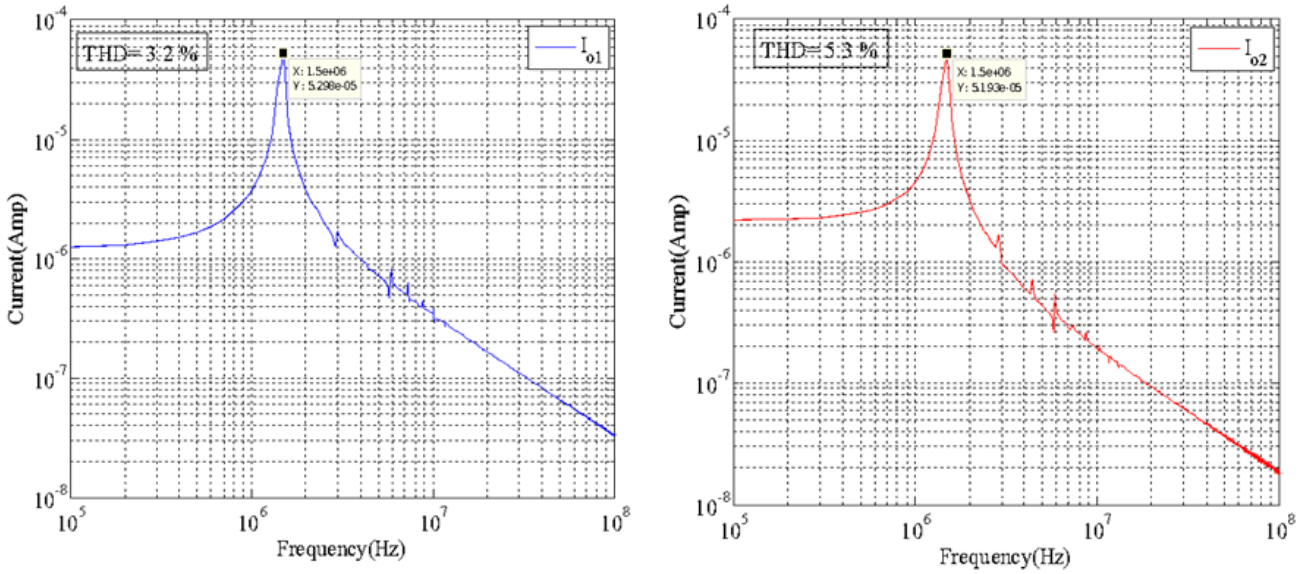

Figure 5. FFT of the waveforms of $I_{o1}$and I_{o2} at 1.50 MHz

References

[1] Senani, R., Bhaskar, D. R., Singh, V. K., and Sharma, R. K., Sinusoidal oscillators and waveform generators using modern electronic circuit building blocks, Springer International Publishing, Switzerland, 2016.

[2] Biolek, D., Senani, R., Biolkova, V., and Kolka, Z., "Active elements for analog signal processing: Classification, review, and new proposals", *Radioengineering*, 17(4), 15-32. Dec.2008.

[3] Pathak, J. K., Singh, A. K., and Senani, R., "Systematic realisation of quadrature oscillators using current differencing buffered amplifiers", *IET Circuits, Devices and Systems*, 5(3), 203-211, Mar.2011.

[4] Lahiri, A., "New Realizations of Voltage-Mode quadrature oscillators using current differencing buffered amplifiers", *Journal of Circuits, Systems and Computers*, *19*(05), 1069-1076, May 2010.

[5] Malhotra, C., Ahalawat, V., Kumar, V. V., Pandey, R., and Pandey, N., "Voltage differencing buffered amplifier based quadrature oscillator", in *2016 IEEE 1st International conference on power electronics, intelligent control and energy systems (ICPEICES)*, 1-4.

[6] Prasad, D., Srivastava, M., and Bhaskar, D. R., "Electronically controllable fully-uncoupled explicit current-mode quadrature oscillator using VDTAs and grounded capacitors", *Circuits and Systems*, 4(2), 169-172, 2013.

[7] Sotner, R., Kledrowetz, V., Jerabek, J., and Prokop, R., "Simple CMOS voltage differencing current conveyor-based electronically tunable quadrature oscillator", *Electronics Letters*, 52(12), 1016-1018, 2016.

[8] Jin, J., and Wang, C., "Current-mode universal filter and quadrature oscillator using CDTAs", *Turkish Journal of Electrical Engineering and Computer Sciences*, 22(2), 276-286, 2014.

[9] Summart, S., Thongsopa, C., and Jaikla, W., "New current-controlled current-mode sinusoidal quadrature oscillators using CDTAs", *AEU - International journal of electronics and communications*, 69(1), 62-68, 2015.

[10] Lahiri, A., "New current-mode quadrature oscillators using CDTA. *IEICE Electronics Express*, 6(3), 135–140, 2009.

[11] Jaikla, W., Siripruchyanun, M., Bajer, J., and Biolek, D. (2008). A simple current-mode quadrature oscillator using single CDTA", *Radioengineering*, 17(4), 33-40.

[12] Keskin, A. U., and Biolek, D., "Current mode quadrature oscillator using current differencing transconductance amplifiers (CDTA)", *IEE Proceedings- Circuits, Devices and Systems*, 153(3), 214-218, 2006.

[13] Prasad, D., Bhaskar, D. R., and Singh, A. K., "Electronically controllable grounded capacitor current-mode quadrature oscillator using single MO-CCCDTA", *Radioengineering"*, 20(1), 354-359, 2011.

[14] Li, Y., "Electronically tunable current-mode quadrature oscillator using single MCDTA", *Radioengineering"*, 19(4), 667-671, 2010.

[15] Kumari, S., and Gupta, M., "Design and analysis of high Transconductance Current Follower Transconductance Amplifier (CFTA) and its applications", *Analog Integrated Circuits and Signal Processing"*, 93(3), 489-506, 2017.

[16] Tangsrirat, W., Mongkolwai, P., and Pukkalanun, T., "Current-mode high-Q bandpass filter and mixed-mode quadrature oscillator using ZC-CFTAs and grounded capacitors", *Indian Journal of Pure and Applied Physics*, 50(8), 600-607, 2012.

[17] Lahiri, A., "Explicit-current-output quadrature oscillator using second-generation current conveyor transconductance amplifier", *Radioengineering*, 18(4), 522-526, 2009.

[18] Herencsar, N., Koton, J., Vrba, K., and Lahiri, A., "New voltage-mode quadrature oscillator employing single DBTA and only grounded passive elements", *IEICE Electronics Express*, 6(24), 1708-1714, 2009.

[19] Tangsrirat, W., and Surakampontorn, W., "Single-resistance-controlled quadrature oscillator and universal biquad filter using CFOAs", *AEU-International Journal of Electronics and Communications*, 63(12), 1080-1086, 2009.

[20] Maheshwari, S., Mohan, J., and Chauhan, D. S., "High input impedance voltage-mode universal filter and quadrature oscillator", *Journal of Circuits, Systems and Computers*, 19(7), 1597-1607, 2010.

[21] Jaikla, W., Siripruchyanun, M., and Lahiri, A., "Resistorless dual-mode quadrature sinusoidal oscillator using a single active building block", *Microelectronics Journal*, 42(1), 135-140, 2011.

[22] Channumsin, O., and Tangsrirat, W., "VDIBA-based sinusoidal quadrature oscillator", *Przeglad Electrotechniczny*, 93(3), 248-25, 2017.

[23] Pushkar, K. L., "Electronically controllable quadrature sinusoidal oscillator using VD-DIBAs", *Circuits and Systems*, 9(3), 41-48, 2018.

[24] Bajer, J., Vavra, J., and Biolek, D., "Voltage-mode quadrature oscillator using VD-DIBA active elements", in 2014 *IEEE Asia Pacific Conference on Circuits and Systems* (Ishigaki), 197-200.

[25] Herencsar, N., Lahiri, A., Vrba, K., and Koton, J.,"An electronically tunable current-mode quadrature oscillator using PCAs", *International Journal of Electronics*, 99(5), 609-62, 2012.

[26] Singh, A. K., Kumar, P., and Senani, R.,"New grounded immittance simulators employing a single CFCC, *The Journal of Engineering*, 17(8), 435-447, 2017.

[27] Singh, A. K., Kumar, P., and Senani, R., "Electronically tunable grounded/floating inductance simulators using Z-copy CFCCC. *Turkish Journal of Electrical Engineering and Computer Sciences*, 26(2), 1041-1055, (2018).

DYNAMIC STUDY OF STEP BACK AND SET BACK BUILDING

Research · May 2018

DOI: 10.1016/j.egypro.2017.03.005.

4 authors, including:

Sristi Gupta
Lovely Professional University
2 PUBLICATIONS **0** CITATIONS

SEE PROFILE

International Journal of Civil Engineering and Technology (IJCIET)
Volume 9, Issue 5, May 2018, pp. 185–190, Article ID: IJCIET_09_05_021
Available online at http://www.iaeme.com/ijciet/issues.asp?JType=IJCIET&VType=9&IType=5
ISSN Print: 0976-6308 and ISSN Online: 0976-6316

DYNAMIC STUDY OF STEP BACK AND SET BACK BUILDING

Krishna Kumar
Lovely Professional university, Phagwara, (Punjab), India

Sristi Gupta
Department of Civil Engineering, Lovely Professional University, Phagwara, Punjab, India

Shivam Kumari
Delhi Technological University (Formerly Delhi College of engineering), New Delhi, India

Ravi Kumar
Lovely Professional university, Phagwara, (Punjab), India

ABSTRACT

In this study, behavior of step back building will be analyzed. Position of shear walls and infill walls will varies in a building. These structural models will be analyzed for dynamic analysis on flat ground. Different parameters like lateral displacement, story drift, base shear, time period, bending moment, shear force will be analyzed and compared using ETABS software. Reference of IS 456 and IS 1893: 2002 will be considered. Etabs helps in 3D structural analysis and designing steel as well as concrete structures. It can increase work productivity, reduces the project cost and save time and helps in designing and analyzing with a greater accuracy.

Keywords: E-Tabs, Step Back Building, Set Back Building IS 1893:2002, Story Drift, Base Shear, India

Cite this Article: Krishna Kumar, Sristi Gupta, Shivam Kumari and Ravi Kumar, Dynamic Study of Step Back and Set Back Building, International Journal of Civil Engineering and Technology, 9(5), 2018, pp. 185–190.
http://www.iaeme.com/IJCIET/issues.asp?JType=IJCIET&VType=9&IType=5

1. INTRODUCTION

Now a days it can be seen the tremendous increase in the construction of the high rise buildings due to the construction of higher buildings the streets are being dense and it stops the sun light. The roads on that particular area are always in the dark even in the day time which leads to use the electricity to lighten the roads in that area. Now this study shows that

by constructing the STEP BACK buildings in that particular area is useful. By this study we will fully analyze the behavior of building due to dynamic loading like Response Spectrum method to make the building safe n long lasting.

Step Back building

It is used in high rise buildings, the step back is done in buildings to allow the sunlight to reach the lower floor, and a setback is used because the buildings should take another step back from the street from every specified added height interval. Without the set back and step back buildings the street of any commercial market would be in always shadow.

2. LITERATURE REVIEW

Kumar. M. V et al[6] (2016), "Influence of shear walls and coupling beam dimensions on seismic behavior". In this study, four multistory buildings are analyzed by using Etab software and deflection and stress concentration are calculated. Mainly by shear wall length to beam depth ratio and shear wall length to beam length ratio are calculated.

It is observed from the study that stress decreases from top floor to first floor and stress at the fourth floor is less as compared to other floors. It is concluded that the deflection is least when shear wall length to beam depth ratio is 3 and stress is maximum when this ratio is 5. It is also concluded that deflection is minimum when shear wall length to beam length ratio is 2.2 and stress is maximum when this ratio is 2.

Arjun. S et al[7] (2016), "A study on dynamic characteristics of RC building on hill slopes". In this study, G+3 building with 3 bays in longitudinal as well as transverse direction is analyzed in zone III. The model is of step back setback configuration as shown in figure 2.2 Analysis is done with the help of Staad.Pro software. Slopes used for building are 16.7°, 21.8°, 26.57° and 30.96°. For the analysis, base shear and displacement are computed and compared. It is concluded from the results that 16.7° slope has maximum storey displacement due to low stiffness in columns. With the increase in slope angle of the building, top story displacement decreases. It is also observed that with the increase in slope, base shear increases.

Jitendra Babu et al[4] (2012) He has done pushover analysis for different symmetric and asymmetric structure which is on plane and sloping ground and the structure is under different loads. The structure is of different bay and size in mutual direction. The model was of 4 storey building in which one storey was above ground level at slope of 30* with horizontal he observed that short column is in the severity level beyond collapse prevention. By pushover analysis the displacement and base share was obtained to be 106*10^-3M and 2.17*10^3 KN. He noticed that base share resist more displacement until failure limit by symmetric structure by 70% through asymmetric building slope is 24% greater than base share resist through asymmetric building on plane ground. He concluded that structure which is vertical irregularity the chances of critical is higher than structure which has plain irregularity.

3. PROPERTIES AND MATERIAL PROPERTIES AS FOLLOWINGS

S.N.	Properties	Values
1	Height of Floor (m)	5
2	X Direction Spacing (m)	5
3	Y Direction Spacing (m)	5
4	Poisson's Ratio	.2
5	Size of beam (mm)	500*450
6	Size of column (mm)	550*500

7	Live Load	.375t\m^2
8	Dead Load on roof	.2t\m^2
9	Dead Load on floor	.48 t\m^2
10	Modulus of elasticity	235600000KN\m^2
11	Steel bar	HYSD415
12	Steel bars for stirrups	HYSD500

4. MODEL

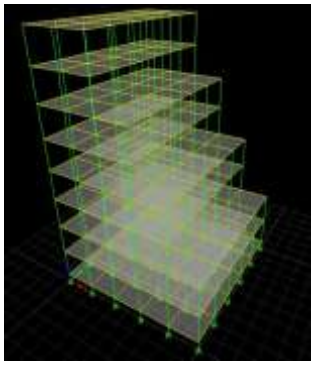

3-D Structure

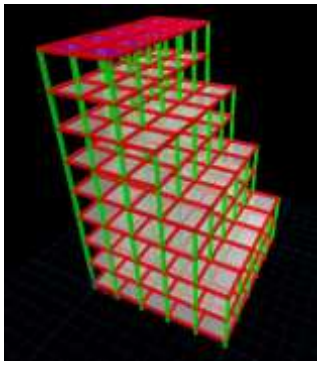

3-D with properties

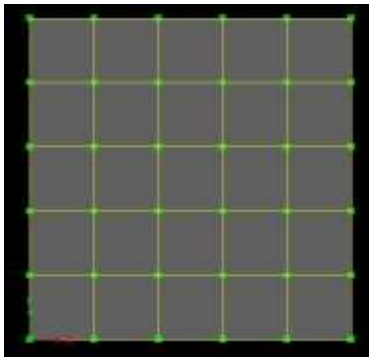

Top View

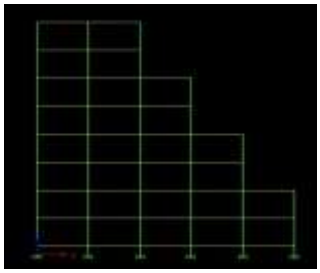

Side View

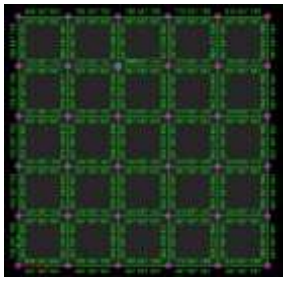

With Steel Bar detailing

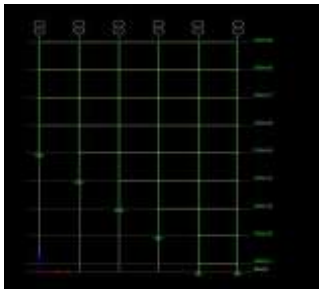

Side View of step Back building

5. RESULT ANALYSIS

Response Spectrum Method

Story	Shear(tonf)		Drift(mm)		Stiffness(tonf/mm)	
	In x	In y	In X	In y	In X	In Y
9	.0081	.007	.00222	.0017	3.645	4.099
8	.0147	.0131	.00312	.0026	4.714	4.867
7	.0199	.0175	.00343	.0030	5.802	5.696
6	.024	.0207	.00376	.0035	6.362	5.904
5	.0281	.0236	.00376	.0035	7.462	6.686
4	.032	.0266	.00395	.0038	8.095	6.941
3	.0369	.0306	.00382	.0037	9.640	8.049
2	.0414	.0349	.00317	.0032	13.038	10.712
1	.0417	.0353	0	0	171.72	142.19

Result obtained for share, drift, stiffness by the Response Spectrum in X direction

Story	Shear(tonf)		Drift(mm)		Stiffness(tonf/mm)	
	In x	In y	In X	In y	In X	In Y
9	.027	.024	.008615	.006726	3.137	3.5741
8	.0586	.053	.01357	.01197	4.319	4.425
7	.0952	.085	.01728	.0154	5.507	5.517
6	.127	.1131	.02069	.01951	6.135	5.795
5	.1595	.1404	.02193	.02066	7.273	6.796
4	.1856	.1627	.02336	.02297	7.945	7.0827
3	.2071	.1806	.02195	.02175	9.437	8.304
2	.2187	.1907	.01744	.01778	12.5395	10.726
1	.2195	.1914	.001316	.001331	166.78	143.72

Result obtained for share, drift, stiffness by the Response Spectrum in Y direction

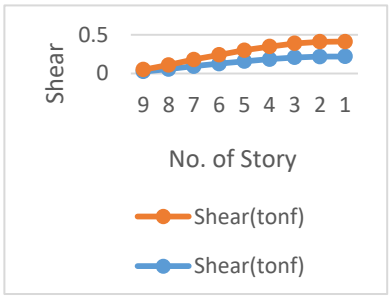

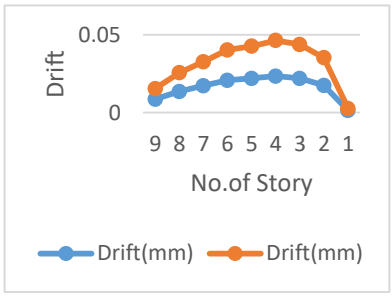

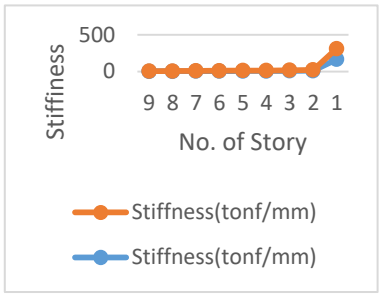

Shear Due to RS in Y Direction Drift Due to RS in Y Direction Stiffness Due to RS in Y Direction

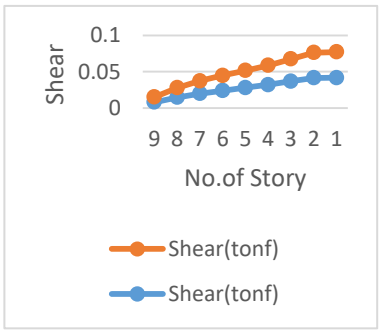

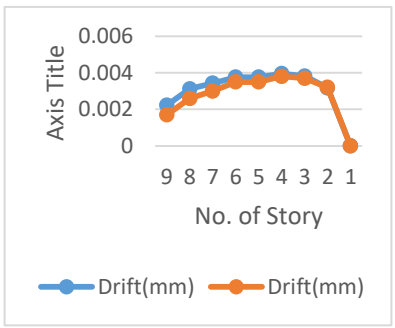

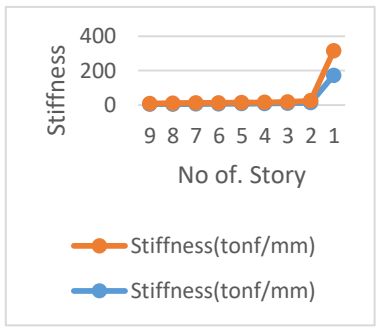

Shear Due to RS in X Direction Drift Due to RS in X Direction Stiffness Due to RS in X Direction

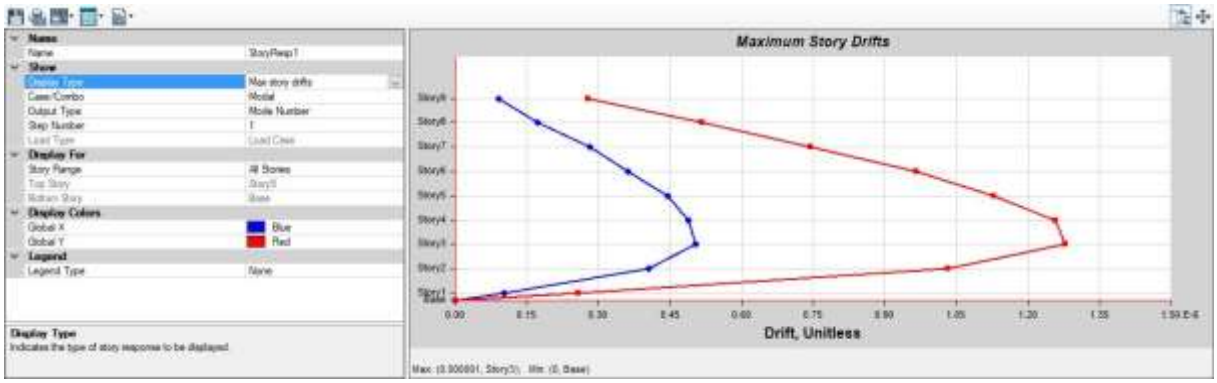

Graph for the maximum Story Drift of the Building.

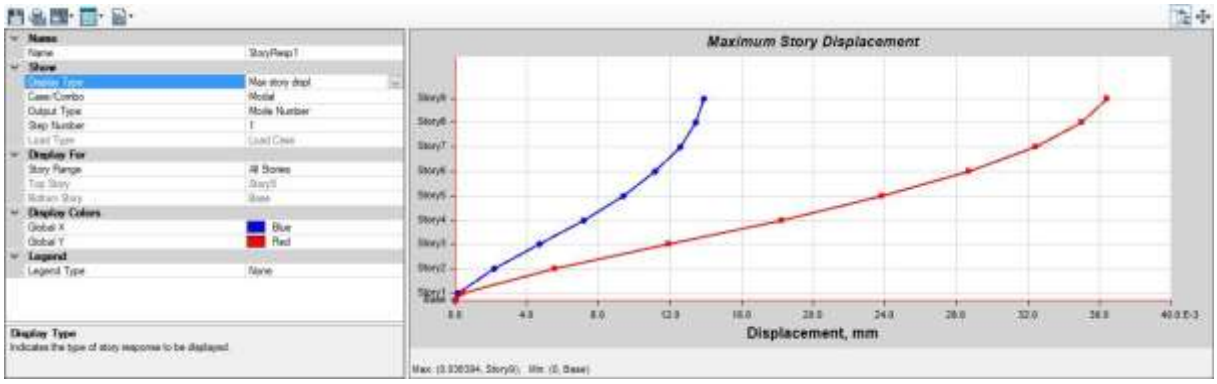

Graph for the maximum Story Displacement of the Building.

The story displacement of step back building in x-direction is maximum at story9 i.e .01864mm which is at the elevation of 41.5 m and the displacement in the y-direction is maximum at the story9 i.e .04518mm which is much greater than the displacement in the x-direction. According to the is code 1893: 2002 the displacement is under permissible value.

6. CONCLUSION

The building Share due to the response spectrum method in y direction is much more than in the x direction and the drift in the y direction is higher than the x direction but the stiffness in both are almost same. If you see the graph for the maximum Story Drift it keep on increasing till the story 3 which has maximum story drift and then it reduces to zero on the base but the difference between the Response Spectrum in X direction n y direction much high the drift due RS in Y is much higher than RS in X.

REFERENCES

[1] Dr. S. A. Halkude et al Seismic Analysis of Buildings Resting on Sloping Ground With Varying Number of Bays and Hill Slopes International Journal of Engineering Research and Technology ISSN:2278-0181,Vol.2 Issue 12, December-2013

[2] Hemal J shah, Dr.S and S.S Gandhy (2014) Seismic Time History Analysis Of Building On Sloping Ground Considering Near/Far field Earthquake (2014)

[3] Pandey A.D, Prabhat Kumar, Sharad Sharma Seismic soil structure interaction of buildings on hill slopes Volume 2, No 2, 2011

[4] K.S.L Nikhila, Dr. B Pandunangrao Static Linear and Nonlinear analysis of R.C Building on Sloping Ground with Varying Hill Slope American Journal of Engineering Research (AJER) e-ISSN:2320-0847 p-ISSN :2320-0936 Volume-03. Issue-11 (2014).

[5] N. Jitendra Babu, K.Y.G.D Balaji Pushover analysis of unsymmetrical framed structures on sloping ground" International Journal of Civil, Structural, Environmental and Infrastructure Engineering Research and Development (IJCSEIERD) ISSN 2249-6866 Vol. 2 Issue 4 Dec- 2012 45-54.

[6] Patel, Mohammed Umar Farooque, A. V. Kulkarni, and Nayeemulla Inamdar. A Performance study and seismic evaluation of RC frame buildings on sloping ground. IOSR Journal of Mechanical and Civil Engineering (IOSR-JMCE) e-ISSN: 2278-1684.

[7] S.M.Nagargoje and K.S.Sable, Seismic performance of multi-storeyed building on sloping ground, Elixir International Journal, 53 (2012) 11980-11982, 7 December 2012.

[8] Ravikumar C M, Babu Narayan K S Effect of Irregular Configurations on Seismic Vulnerability of RC Buildings Architecture Research 2012,2(3):20-26DOI: 10.5923/j.arch.20120203.01.

[9] IS: 1893 (I)-2002. Criteria for Earthquake Resistant Design of Structures BIS, New Delhi.

[10] Structural Analysis program ETABS V 9.7.4, User's manual, computers and structures, Inc.

[11] S .K.Duggal Earthquake resistant design of structures Oxford university press 2007, ISBN-13:978-0-19-568817-7.

[12] Humar, J.L. and Wright, E.W. (1977). Earthquake Response of Steel-Framed Multistory Buildings with Set-Backs, Earthquake Engineering & Structural Dynamics, Vol. 5, No. 1, pp. 15-39.

[13] Moehle, J.P. and Alarcon, L.F. (1986). "Seismic Analysis Methods for Irregular Buildings", Journal of Structural Engineering, ASCE, Vol. 112, No. 1, pp. 35-52.

[14] Wong, C.M. and Tso, W.K. (1994). Seismic Loading for Buildings with Setbacks, Canadian Journal of Civil Engineering, Vol. 21, No. 5, pp. 863-87.

[15] Wood, S.L. (1992). Seismic Response of R/C Frames with Irregular Profiles, Journal of Structural Engineering, ASCE, Vol. 118, No. 2, pp. pp. 545-566.

[16] Hema Venkata Sekhar and T. Venkata Das, Analysing The Seismic Behaviour of Set Back Building by Using E-Tabs. International Journal of Civil Engineering and Technology, 8(1), 2017, pp. 444–451.

[17] K. Naga Sai Gopal and N. Lingeshwaran Analysis and Design of G+5 Residential Building by Using E- Tabs, International Journal of Civil Engineering and Technology, 8(4), 2017, pp. 2098-2103.

BIOGRAPHY:

Corresponding Author- Krishna Kumar, M.Tech in Structure, Lovely Professional University, Phagwara Punjab (India).

Co-Author- Sirsti Gupta, Assistant Professor in Department of Civil Engineering, Lovely Professional University, Phagwara, (Punjab), India

Co-Author- Shivam Kumari, Perusing B.Tech in Civil Engineering, Delhi Technological University (Formerly Delhi Collage of Engineering), New Delhi, India

Co-Author- Ravi Kumar, B,tech in Civil Engineering, Lovely Professional University, Phagwara Punjab (India).

Ecofriendly Techniques for Treatment of Crude oil: A Review

Conference Paper · August 2018

CITATIONS
0

READS
5

3 authors, including:

Sumit Dagar
Delhi Technological University
1 PUBLICATION **0** CITATIONS

SEE PROFILE

Ecofriendly Techniques for Treatment of Crude oil: A Review

Sumit Dagar[1], Vandana Shan[1], S.K.Singh[1]

Delhi Technological University, Bawana Road, Delhi-110042

Abstract

A number of cyclic, polycyclic hydrocarbons derived from crude oil are present in varying concentration in different environmental sections. The harmful residues can bio-accumulate in food-chains and interrupt various physiological or biochemical activities of various human beings and other organisms.Long term exposure to these hazardous compounds will cause carcinogenesis of some organs, mutation in the genetic material, infertility or causing hemorrhage in population. Biomarkers, the biological end point factors are basically used for quantify the effect of oil pollutant. Oil spills is the most limiting factor of soil contamination which affects the soil fertility and hence affect the crop productivity. So it is necessary to measure the various deleterious effects of petroleum hydrocarbon contaminants in environment. Bioremediation is the most effective application of Environmental Biotechnology for treatment of sites contaminated with petroleum hydrocarbons. Bioremediation consists of the primary mechanism for the degradation of hydrocarbons from polluted sites by populations of natural existing microorganisms. In this process microorganisms are used to ameliorate the harmful components of petroleum hydrocarbons in a cost effective and environmental friendly manner under some specified conditions of temperature and nutrients. Most of bioremediation techniques are used to clear the sites contaminated with hydrocarbons but still some of the bioremediation processes are inefficient and ineffective in treatment of these hydrocarbons waste due to their complex structure and insolubility in water. A number of eco-friendly techniques are being discovered in future for treatment of contaminated sites with harmful petrochemicals and hydrocarbons.

Key words: Environmental biotechnology, Petroleum hydrocarbons, Bioremediation

1. Introduction

Petroleum industry produces a large amount of oil sludge or residues during crude oil exploration, production, transportation, storage, and refining processes (Wang et. al 2009). In recent years, the considerable amount of sludge generated during the petroleum refining process has received increased attention all over the world. Crude oil contains a large concentration of petroleum hydrocarbons (PHCs) and other hazardous components. In many countries oil sludge is considered as hazardous waste which causes harmful effects on the environment as well as on human health (Hu et. al. 2013). Improper disposal and insufficient treatment of this hydrocarbon waste is creating nuisance in surface water and ground water resources. After the 2nd World War, the economic base vary from coal energy to crude oil energy, petroleum and its products which increased the value and importance of this merchandise and transported overseas. Underground storage of crude oil and its products are responsible for higher environmental risks. Currently contamination of ground water by crude oil is of major concern all major cities in world. After 1970s and till date many advance techniques have been recorded for treatment of sites contaminated oil spills in the field of Environmental Biotechnology with respect to crude oil pollution control and clean up operations. Onwards 1970s and till now many advance techniques have been recorded for treatment of sites contaminated with oil spills in field of Environmental Biotechnology with respect to crude oil pollution control and clean up operations. Due to various harmful effects, oil pollution became great concern to the world. Safe disposal of crude oil residue from refineries and petrochemical industries is one of the main issues which can produce severe impacts on various environment components and potential risk to human health (Cerqueiraet et al. 2013) .Due to the broad distribution, complex composition, inhabited time and toxicity, petroleum hydrocarbons are the highly dangerous organic pollutants on earth surface.

These compounds have tendency to bio-accumulate in food chains of higher trophic levels where they disturb the normal functioning like biochemical or physiological processes in various organisms, which cause carcinogenesis in a variety of organs, mutagenesis in the genetic matter and mutilation in reproductive ability (Onwurah et al. 2007). Aliphatic, branched and cyclo-aliphatic alkanes, monocyclic and polycyclic aromatic hydrocarbons (PAHs) are most common petroleum hydrocarbons. Naphthalene, phenanthrene, fluorene, fluoranthene, anthracene, pyrene, benzoanthracene, benzopyrene are also well known compounds related to PAHs category. Hundreds or varying number of hydrocarbon molecules constitute a single petroleum fraction.

Petrochemical Hydrocarbons and its fractions are differ in terms of bioavailability, degradability, volatility, toxicity and diligence. Complex chemical composition of hydrocarbon compounds introspects the great challenge for designing efficient bioremediation techniques [Atlas & Hazen, 2011 and Fuentes et al.2014]. A huge number of physicochemical ways are used for the treatment of residues generated from petrochemical industries, crude oil processings. But many of suggested processes are expensive, unproductive, energy exhaustive and non-eco-friendly.

Bio-remediation technology is a sustainable, economic, environment friendly and an alternative clean up technology of degradation of waste at polluted sites by natural microbial population (Das & Kazi ,2014).Bioremediation techniques are successfully adapted to treat hydrocarbon polluted sites based on the biodegrading tendencies of native microorganisms (Ramirez et al.2014).

The real issues related to fast degradation of petroleum sludge and its waste byproducts in biodegradation phenomenon are the low accessibility of hydrocarbons to the microbial population and their dissolvability in water and nature of complex blend of many hydrocarbons , intermediated and added structures. It is important to alleviate the unfavorable impacts of oil contamination from the earth. For this, multidisciplinary approach will be required in various fields of Biology, Chemistry, Engineering, Education and Economics. This audit paper incorporates the destructive effects of raw petroleum on condition and imaginative and eco-accommodating methods in Environmental Biotechnology.

2. Characteristics & Sources of Crude Oil

Raw petroleum and oil are composite mix of various polycyclic aromatic compounds and hydrocarbons (Domask, 1984). The fuel(Diesel)contains usually alkanes that are quickly degraded whereas alkanes and cycloalkanes are difficult to degrade due to their complexand different structures eg. isoprenoids, aromatics and polar mixes of sulfur, element and element (Mackay et al., 1985). Typical composition of petroleum based on distillation properties and water solubility of hydrocarbon compounds are generally analyzed in petroleum are tabulated in Table 1 & 2 respectively (Adams and Jackson, 1996).

Table 1. Distillation Components of Nigerian Brass Crude Oil

Distillation Residues or Distillation Fraction	Composition (%)	Chain length of Hydrocarbon
Gasoline	11.6	C_4 -C_{10}
Kerosene	16.4	C_{10} – C_{20}
Gas oil	15.3	C_{15}-C_{40}
Naphtha	18.7	C_4-C_{10}
Heavy gas	25.2	C_{40} and above

Table 2. Solubility of Components Easily Analysed in Crude Oil:

Components	**Examples**	**Solubility(mg/L) APPROX** **28 ± 3 °C**
Alkanes	butane	102.00
	decane	0.07
Olefins	1-pentene	149
Branched alkanes	2-methyl-pentane	79
Cycloalkanes	Cyclo-hexane	57
Monoaromatics	Benzene	1762
	Toluene	472
	Ethyl-Benzene	142

Polyaromatics	Naphthalene	31
Phenols	Phenol	84000
	2,6. dimethyl phenol	4700
	2,4,6- trimethyl phenol	13000

Non hydrocarbon compounds might likewise found in unrefined petroleum that largely incorporates porphyrins and their subordinates (Callot and Ocampo, 2000). Metals that would be found in crude oil for the foremost part incorporate nickel, vanadium, iron, zinc, cobalt, Ti and copper (Chicarelli, et al., 1990).

Assorted segments of fossil fuel and crude oil for the foremost part polycyclic perfumed hydrocarbons (PAHs) are found in kind of water contamination due to release of unprocessed effluents and petrochemical items (Beckles, et al., 1998). Major problems related to petroleum hydrocarbon contamination emerged from oil well drilling activities, transportation and capability within the upstream business whereas processing, transportation, and showcasing within the downstream business (Oberdorster and Cheek, 2000). Amid the procedure of gas flaring some non-combusted hydrocarbons escape into the world as saw in nigeria. Wellsprings of petroleum and its items on nature additionally incorporate incidental spills and from break oil pipelines (Beller, et al., 1996). Spilled petroleum hydrocarbons on the world are usually attracted due to gravity into the dirt till the purpose that associate impenetrable compass is met like bedrock, watertight mud or associate geological formation. the collection of free oil on the surface of groundwater due to poor miscibility of raw petroleum is one of the sources which can move on the side over a large separation to contaminate totally different zones organized exceptionally far from the purpose wellspring of contamination. Industrial and metropolitan releases alongside urban run-offs, atmospherical affidavit and regular leaks to boot contribute for oil hydrocarbon contamination on the world. an outline of a few sources and assessed quantity of unrefined fossil fuel discharged into some biological system is appeared in Table 3(Baker, 1983). it's discovered that groundwater goes regarding as commonplace media by that people; greenery and fauna inherit contact with oil hydrocarbon contamination for the foremost part contributed by unrefined petroleum.

Table 3. Sources and estimates of crude oil or its products released into the marine environment (Baker, 1983)

Sources	Quantities (K. tones) appx.
Transportation accident	395
Atmospheric/fuel combustion	350
Tanker operations (washings)	715
Natural seeps / erosion	350
Municipal, industrial and surface run-offs	1420

3. Harmful impacts of Petroleum hydrocarbon(Crude oil) contamination on Environment

Crude oil, is formed from various kinds of hydrocarbon which can be from many sources. Effects of crude oil vary from one source to another Details of potential biological damage depend on ecosystem where spill occurred.

Aquatic ecosystem, specially marines are highly vulnerable (Cairns et al., 1984). Crude oil sources in few marine ecosystem are listed in Table 2. Oil spills affect marine environment organisms by direct poisoning or by physical suffogaion (Perry, 1980).

Generally, oil spills cause many damages to wetland vegetations. It reduces stem length, growth, photosynthesis rate, density, and may cause their death (Krebs et al., 1981). Crude oil spill at sea creates oily surface with byproduct that follow into many drive. Some enter into mass of seawater. Reportedly they exist for long before mortification by microorganisms in sea. Slick usually becomes more adhesive. Oil in water results reduction of dissolved oxygen. It is because of conversion of organic component in inorganic compounds, loss of biodiversity by decrease in amphipod population which is crucial in food chain, and eutrophication. (Onwurah, 2002a).

Spilled oil in sea resulted in killing of thousands of sea birds (Dunnet, 1982). In fishes includes 'lymphocytosis', 'epidermal hyperplasia' and 'hemorrhagic septicemia' (Beeby, 1993). Extinct 'mangrove trees', 'assail beaches' and reducing 'fish catches' are real threats to viability of some ecosystem; for example 'Niger Delta' areas of 'Nigeria'. Ultra violet (U.V) radiation enhances effect. This is called 'photo enhanced toxicity' (Barron, *et al*., 2003). Pelletier, *et al*. (1997) reported 'Prudhoe Bay' crude oil was one hundred times higher toxic to shrimps and bivalve embryos after contact with U.V light. Photo enhanced toxicity in fish and aquatic invertebrates becomes on activation of chemical residues which bioaccumulate in such organisms (Calfee, *et al.*, 1999). Toxicity of crude oil is because of presence of PAH (Heintz *et al*., 1999). PAH exposed to UV radiation produces CO_2. on photosynthesis (Babu, *et al*., 2002). This results disorder in 'development', 'immunity', 'reproduction', 'growth' and 'survival' of aquatic organisms (Brown, *et al*., 1996). Oil spill in environment increases harmful effect of PAHs to human as well other living organisms. This increase infectious disease risk (Hall, *et al.*, 2006) and reproductive capacity (Tiido, *et al.*, 2006). However, carcinogenic pathway of crude mixture of PAHs is less than sum total of anticipated carcinogenicity when potency of known PAHs (carcinogen) in crude mixture is considered (Falk, *et al*., 1964).

Oil slicks, happened on the dry land in Nigeria during 1978 and 1979, affected fields of rice, maize, yams, cassava (Onyefulu et al., 1979). Unrefined petroleum affects production and growth of a few plants (Onwurah 1999a). Soil ripeness is likewise affected by this with scale depending level and sort of oil. Substantial raw petroleum spill in 'Cross-River state', Nigeria forced agriculturists to drive out. This is because of oil hydrocarbons sterlised soil and reduced productivity for long time. Hydrocarbons have influenced yield of steroidal sapogening from tuber tissues of Dioscuri deltoidea (Hardman et al., 1977). 'Niger Delta' of 'Nigeria' vegetative cover and mangrove are destroyed by oil slicks (Odu, 1987). Oil spill contamination of soil affect the nutrient concentration,total organic carbon ,cations exchange capacity of soil.Ph and aerobic oxidation in soil is also affected due to oil contamination. Unrefined petroleum makes nonaerobic condition in soil with water logging and acidic metabolites. High amount of of aluminium and manganese particles, which are harmful to plant development are also identified during soil polluted with crude oil .

It is justified that there is a connection between ecological wellbeing and human wellbeing. While human wellbeing is a profound field of science from hundreds of years , the idea of 'natural wellbeing 'can be seen as an advanced science, which is estimated as the suitability of tenants of a given biological system as influenced by encompassing ecological components (Shields, 1990). For all intents and purposes, ecological wellbeing includes the judgment of the soundness of the individual life forms and connect watched changes in wellbeing with changes in natural conditions. A few illnesses have been broke down to be the end product of unrefined petroleum contamination. The significant reason of wellbeing problems because of oil slicks affected nourishment and/or water, discharge and vapours. Poisonous portion in oil may influence human through protein union inhabitation, nerve neural connection capacity, and harm of in film transport framework and harm to plasma layer (Prescott, et al., 1996). Unrefined petroleum hydrocarbons influence hereditary immaculateness of numerous life forms. It result in carcinogenesis, mutagenesis and hindrance of regenerative limit (Short et al., 1997). Danger of drinking water debased by unrefined petroleum can be conjecture from its impact on rats which created haemorrhagic inclination on presentation to water solvent segments of raw petroleum (Onwurah, 2002). Raw petroleum unstable part after a spill have been embroiled in 'asthma', 'bronchitis' and 'quickening maturing' of 'lungs' (Kaladumo, 1996). Other conceivable wellbeing impacts of oil slick are extrapolated from rate presented to tainted destinations and his incorporate expanded liver, kidney and spleen weights and in addition lipid per-oxidation and protein oxidation (Anozie and Onwurah, 2001).

4. Eco-friendly Techniques for Degradation of Crude Oil contaminated Sites

4.1. Bioremediation

An innovation that adventures the capacities of microorganisms & other common habitants of the biosphere to enhance natural quality for all species is called bioremediation. Bioremediation process includes examination of contaminated sites according to governing regulations and various action plan.Most challenging and difficult task of bioremediation is characterization of contaminated sites. Also cation exchange capacity and nutrient availability of soil,aeration, oxygen content, acidity and various hydraulic property are primary parameter required for the assistanance of subject expertise.Bioremediation of a polluted sites majorly depend on the physiology ; biology of the regular bacterial populaces found in sullied locales (Olson and Tsai, 1992; Bouwer, 1992) engaged in biodegradation (Olson and Tsai, 1992; Bouwer, 1992).

Not all the contaminants are biodegraded but a huge numbers of petroleum hydrocarbons mixtures are generally changed to metabolites of obscure diligence and poisonous quality. Subsequently some essential

procedure that might be huge for an effective bioremediation undertaking will incorporate consistence investigation, site portrayal, technique determination achievability thinks about, remediation legitimate and end for venture examination (Bonaventura, et al., 1995). Consistence investigation incorporates examination of the polluted site in consistence with representing control and the activity design.

The last phase of any bioremediation undertaking ought to incorporate bioassay trial of the treated site which affirms finish or almost entire expulsion of the PHC contaminant from the sullied destinations. As per Lovely (2003), joining models including scientific models that can estimate the movement of microorganisms include in bioremediation with existing geochemical and hydrological models ought to change bioremediation innovation. Ecosystems polluted with crude oil require full-scale bioremediation technologies which also incorporate many limiting factors including the presence of other toxic compounds other than crude oil pollutant, the level of available oxygen, nutrients, temperature, pH, moisture content, biodiversity of species like hydrocarbonoclastic & co-metabolising bacteria at the polluted sites, adsorptive capacity of the hydrocarbons to the soil & sediment, rate of mixing and mass transfer (Atlas, 1991; Prince, 1992).

Spilled oil adsorbs to the soil particles in terrestrial ecosystem, forming a toxic mixture which is harmful to the indigenous microorganisms. Sufficient amount of oxygen supply as electron acceptor is required for effective metabolism of crude oil . In the mangrove ecosystem due to low availability of .oxygen , the use of biologically active absorbent to fix the oil and effective medium for biodegradation is desirable (Gregorio, 1996).

4.2. Land Farming

In situ land treatment is the simplest method of bioremediation of soil contaminated with crude oil which includes standard farming procedures like plugging the oil-polluted soil with a tractor, periodical irrigation and aeration. Aerobic microorganisms are used to degrade the PHC and other derivatives to carbon dioxide & water, or other less harmful toxic forms. As per specialists when land-farming technology when properly performed the non-volatile components of petroleum & other related products are fastly immobilized from contaminated sites which may not be flitered out into groundwater. It also involves nutrient enrichment in the form of fertilizer application to the site conditions such as inoculations with selected or adopted microbial population, mixing and aeration of the soil surface, pH adjustment and irrigation. It also enhance the decontamination of 50 cm topsoil of an area previously polluted with crude oil was attained (Compeau, *et al*., 1991).

4.3. Composting

The prime technology in the treatment of oil polluted coastal area is composting which involves the mechanized mixing of contaminated soil or sediment with compost-containing hydrocarbonoclastic bacteria, under aerobic and warm conditions. Addition of corn slice comes results into microbial nitrogen fixation has been co-upgraded with oil hydrocarbon degradation (Paerl, et al., 1996).

4.4. Phytoremediation

Phytoremediation is the greener technology in which plants are used to clean up of contaminated sites . It is an spring up technology that promises effective, inexpensive, and less intrusive clean up and reclamation of oil-contaminated environments (Stomp, *et al.*, 1993; Schnoor, *et al.*, 1995). A green plant is a sunlight based driven, pumping, and viable separating framework furnished with quantifiable stacking degradative and fouling limits (Salt, et al., 1995). Salt swamp plants devours hydrocarbons from oil-polluted dregs and increment the hydrocarbon or aggregate lipid division of the aerial parts of plants (Lytle and Lytle, 1987).

There are three set up instruments by which plants degrade oil contaminated sites and these are immediate take-up of oil hydrocarbons into their tissues; release of enzymes and exudates that fortify the action of hydrocarbonoclastic organisms and direct biochemical change (compounds) of oil hydrocarbons; incresed in the degradation of the contaminants in the rhizospheredue to mycorrhizal growths and the action of soil microbial consortia (Schnoor et al., 1995). Plants that are impervious to unrefined petroleum harmfulness, for example, dark poplar and willows, and additionally miscanthus grass (elephant grass) have been observed to be compelling in the decrease of oil dirtied soil (Shank and McEwan, 1998). One noteworthy set back in phytoremediation is that the plants have a tendency to be challenge with the hydrocarbonoclastic microbial populace for accessible settled nitrogen and phosphorus. However, phytoremediation can increase speed for the reduction of oil concentration in both surface and deep soil, and thus reconstruct crop sustaining potential and reducing marsh erosion after a spill.

5. Discussion:

Cleaning up of petroleum hydrocarbons in the subsurface environment is a real world problem. The maximum utilization of crude oil as a major source of energy has increased the increased risk of accidental spills and environmental pollution. Currently, there is need to decrease the harmful impacts of PHC pollution due to crude oil spills is attracting many researchers to generate various innovative techniques in various aspects of environmental biotechnology that will help in sustainable development and sustainable environment. The integration of several eco- friendly techniques advances for ameliorating the negative impacts of oil spills in the environment will be most expedient. This review aimed at highlighting various harmful impacts of crude oil pollution in environment and advancement of various eco-friendly techniques to treat polluted sites with hydrocarbons and its product. A proper knowledge of the various biotechnological advance processes so far made in clean-up of petroleum hydrocarbon compounds contaminated ecosystems will further equip bioremediation engineers in designing programs for a more effective and comprehensive clean-up operations.

Biodegradation of hydrocarbon contaminated ecosystem should be approached in a cost effective and environmentally friendly manner. Bioremediation is still the most acceptable and efficient technology that can meets the all conditions and regulations that govern clean up of oil-polluted sites. However, all aspects of bioremediation should be integrated with respect to the site in question for rapid and effective remediation efforts, and monitoring should be an integral aspect of any bioremediation program.

References

- Cerqueira VS, Maria do Carmo RP, Camargo FA, Bento FM (2014) "Comparison of bioremediation strategies for soil impacted with petrochemical oily sludge". International Biodeterioration and Biodegradation 95: 338-345.
- Xu N, Wang W, Han P, Lu X (2009) "Effects of ultrasound on oily sludge deoiling". Journal of hazardous materials 171: 914-917
- Hu G, Li J, Zeng G (2013) "Recent development in the treatment of oily sludge from petroleum industry: A review". Journal of hazardous materials 261: 470- 490
- Fuentes S, Méndez V, Aguila P, Seeger M (2014) "Bioremediation of petroleum hydrocarbons: catabolic genes, microbial communities, and applications". Applied microbiology and biotechnology 98: 4781-4794.
- Onwurah INE, Ogugua VN, Onyike NB, Ochonogor AE, Otitoju OF (2007) "Crude oil spills in the environment, Effects and Some Innovative Clean-up Biotechnologies". International Journal of Environmental Research 1: 307-320
- Atlas RM, Hazen TC (2011) "Oil Biodegradation and Bioremediation: A Tale of the Two Worst Spills in U.S. History". Environmental science and technology 45: 6709-6715.
- Adams, P. J., (1996). "Bioremediation of oil spills: Theory and Practice". Proceedings of the 8th. Biennial International NNPC Seminar. In: The Petroleum Industry and the Nigeria Environment, Port Harcourt, Nigeria, 183-203.
- Das R, Kazy SK (2014) "Microbial diversity, community composition and metabolic potential in hydrocarbon contaminated oily sludge: prospects for in situ bioremediation". Environmental Science and Pollution Research 21: 7369- 7389
- Diaz-Ramirez IJ, Escalante-Espinosa E, Favela-Torres E, Gutiérrez-Rojas M, Ramírez-Saad H (2008) "Design of bacterial defined mixed cultures for biodegradation of specific crude oil fractions, using population dynamics analysis by DGGE". International Biodeterioration & Biodegradation 62: 21-30.
- Anozie, O., Onwurah, I. N. E., (2001). "Toxic effects of Bonny light crude oil in rats after ingestion of contaminated diet". Nigerian J. Biochemistry and Molecular Biology (Proceedings Supplement). 16 (3), 1035-1085.
- Alexander, S. K. and Webb, J. W., (1987). "Relationship of Spartina alterniflora growth to sediment oil content following on oil spill. Proceeding of the 1987-Oil Spill Conference", American Petroleum Institute, Washington, DC, 445-449.
- Anual. Report on National Biotechnology Policy. White House Councilon competitivenessWashington DC,1991.
- Atlas, R. M., (1991). "Microbial hydrocarbon degradation: bioremediation of oil spills". J. Chem. Technol. Biotechnol., 52, 149-156.

- Babu, T. S., Huang, X. D., Greenberg, B. M., (2002). “Reactive oxygen species mediated toxicity of environmental contaminants In: Learned Discourses”: TimelyScientific Opinions SETACGlobe, **3**(3), 26-28.
- Atlas, R. M., (1988). “Biodegradation of hydrocarbons in the environment”, In: Environmental Biotechnology Omenn, GS EdPlenum Press, NewYork.
- Baker, J. M., (1983). Impact of Oil Pollution on Living Resources: Commission on Ecology Papers No 4 International Union for Conservation of Nature and Natural Resources , Gland, Switzerland.
- Barron, M. G., Carls, M. G., Short, J. W. and Rice, S. D., (2003). Photoenhanced toxicity of aqueous phase and chemically dispersed weathered Alaska North Slope Crude oil to pacific herring eggs and lavae. Environ. Toxicol. Chem., 22 (3). 650-660.
- Banerjee, D. K., Fedora, P. M., Hashimoto, A., Masliyah, J. H., Pickard, M.A. andGray, M. R., (1995). Monitoring the biological treatment of anthracite-contaminated soil in a rotating –drum bioreactor. Appl. Microbial. Biotechnol., 43, 521-528.
- Barbee, G. C., Brown, K. W., Thomas, J. C., Donelley, K. C., Murray, H. E., (1996). Mutagenic activity (Ames test) of wood-preserving waste sludge applied to soil Bull. Environ Contam Toxicol., 57, 54-62.
- Bonaventura, C., Boneventura, J., Bodishbaugh, D. F., (1995). Environmental Bioremediation:Approaches and processes. In: Eco toxicity and Human Health (Eds) de serres, F.J and Bloom, AD CRS Lewis Publ. Boca Raton, New York. 199-200
- Beckles, M. D., Ward, C. H., Hughes, J. E., (1998). Effect of mixtures of polycyclic aromatic hydrocarbons and sediments of fluoromethane biodegradation pattern Environ. Toxicol. Chem., **17**, 1246-1257.
- Beeby, A., (1993). Measuring the effect of pollution. In: Applying Ecology. Chapman and Hall, London, New York.
- Brown, E. D., Norcross, B. L. and Short, J. W., (1996). An introduction to studies on the effects of Exxen valdez oil spill in early life history stages of Pacific herring, clupae pallasi, in Prince.Williian Sound, Alaska. Can J Fish Aquat, Sci., 53, 2337-2342
- Beller, M., Schoenmaker, H., Huuskonen, E., (1996). Pipeline inspection environmental protection through on-line inspection, Proceeding of the NNPC Seminar In: Oil industry and the Nigerian Environment, Port Harcourt, Nigeria. 233-241
- Bouwer, E. J., (1992). Bioremediation of organic contaminants in the subsurface. Environmental Microbiology. ed Ralph Mitchell. John Wiley and Sons Pub. NewYork. 287-318.

Effects of Glass Fiber on the Mechanical Properties of Hybrid Bocomposite: A Review

Article · October 2017

DOI: 10.22214/ijraset.2017.10134

1 author:

Mohit Mittal
Delhi Technological University
10 PUBLICATIONS **1** CITATION

SEE PROFILE

International Journal for Research in Applied Science & Engineering Technology (IJRASET)
ISSN: 2321-9653; IC Value: 45.98; SJ Impact Factor:6.887
Volume 5 Issue X, October 2017- Available at www.ijraset.com

Effects of Glass Fiber on the Mechanical Properties of Hybrid Bocomposite: A Review

Mohit Mittal[1], Rajiv Chaudhary[2]
[1,2]*Department of Mechanical Engineering, Delhi Technological University, Delhi*

Abstract: Application of biocomposites is rapidly increasing in various sectors caused by technical, environmental, and economic advantages. Hybridization with synthetic fibers makes them suitable for structural applications such as automobile, aerospace, and constructional work etc. This article focussed on the effects of glass fiber on mechanical properties of PALF, sisal, OPEFB, hemp, and kenaffibers.Outcomes show that addition of glass fiber in biocomposite material lead to increases the tensile, flexural, and impact properties of NFC's.
Keywords: Biocomposite; Glass fiber; Mechanical properties

I. INTRODUCTION

Environmental issues related to the use of petro based polymer composites have actuated the development of agro based materials. Moreover, government regulations are forcing the manufacturers to reduce the impact on environment by shifting from petroleum based sources to renewable sources [1,2]. Natural fiber reinforced composite (NFRC) have provide opportunities to manufacturers for recyclable, bio-degradable material having low cost, lessenergy requirement for processing, low tool wear, as well as good acoustic & thermal insulation properties [3,4]. Inspite of their wide variety of advantageous properties, NFRC have many shortcomings such as low strength, low stiffness, low processing temperature, and poor moisture resistance which resultsits applications restricted to upholstery purpose rather than structural work. In order to overcome these shortcomings and to enhance the mechanical properties of NFRC, an optimum solution is to hybridize the natural fiber with glass fiberin polymeric resindue to its high strength & stiffness, dimensional stability, and resistance to corrosion. Hybrid composite provide an opportunity to engineers for achieving a balanced combination of mechanical properties i.e. strength, stiffness, and ductility[6]. The performance of hybrid composite is function of various factors such as nature of fiber, nature of matrix, relative composition of reinforcement, fiber-matrix interface, and arrangement of both the fibers& extent to intermingling. Hybrid laminate of E-glass/Flax was more impact resisted than neat flax composite. It was due to the better stress transfer from matrix to fiber. The hybridization of low strain to failure fiber with high strain to failure results in an increase energy absorption and improved impact resistance [7,8]. Hybridization of oil-palm fiber with glass fiber results an increase thermal stability of oil palm/PF composite [5]. This work gives a review on the effects of glass fiber addition on the mechanical properties of natural fiber reinforced composites.

II. EFFECT OF GLASS FIBER ON TENSILE PROPERTIES OF NFRC

A. Tensile Properties

Important tensile properties of PALF, hemp, sisal, OPEFB, kenaf, epoxy, polyester and glass are shown in Table 1. It is cleared from table 1 that glass fiber have higher tensile properties compared to natural fibers. Addition of glass fiber in natural fiber composites results the increment in mechanical properties.

Properties	PALF	Hemp	Sisal	OPEFB	Kenaf	Glass	Epoxy	Polyester
Tensile Strength (MPa)	413-1627	46.4	468-640	248	284-800	2000-3500	35-100	8-19
Young's Modulus (GPa)	34.5-82.51	7.2	9.4-22.0	3.2	21-60	70	3-6	0.58
Elongation at Break (%)	1.6	1.6	3-7	25	1.6	2.5	1-6	1.6

Table 1. Mechanical properties of natural fibers and glass fiber

B. Tensile properties of EFB/glass fiber hybrid polyester composite

Abdul Khalil et al. [9] studied the effect of glass fiber on the tensile properties of EFB fiber polyester composite. Figures 1 and 2 shows the variation of tensile properties of EFB/glass hybrid polyester composites.It was observed that tensile properties of hybrid composite was increased with increasing the total fiber content and glass fiber content in the composite. Among all the hybrid composites, a maximum tensile property was observed at 45 wt% glass fiber content. It may be due to effective stress transfer from matrix to fiber and uniform dispersion of fiber takes place in polyester resin. Beyond 45 wt% of glass fiber, fiber-fiber interaction increases which results poor dispersion.

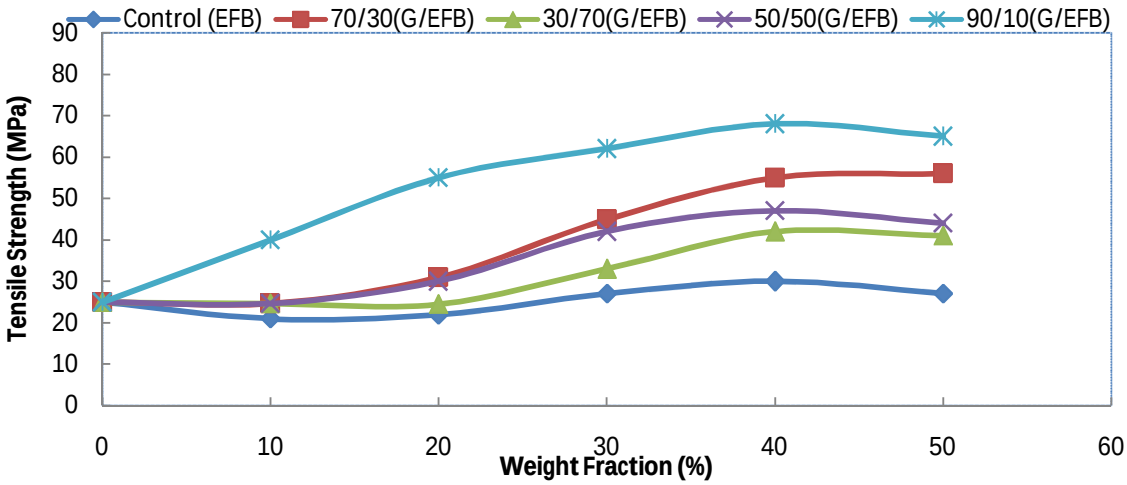

Figure 1.Tensile strength of EFB/glass hybrid composites and EFB polyester composites at different fiber loading.

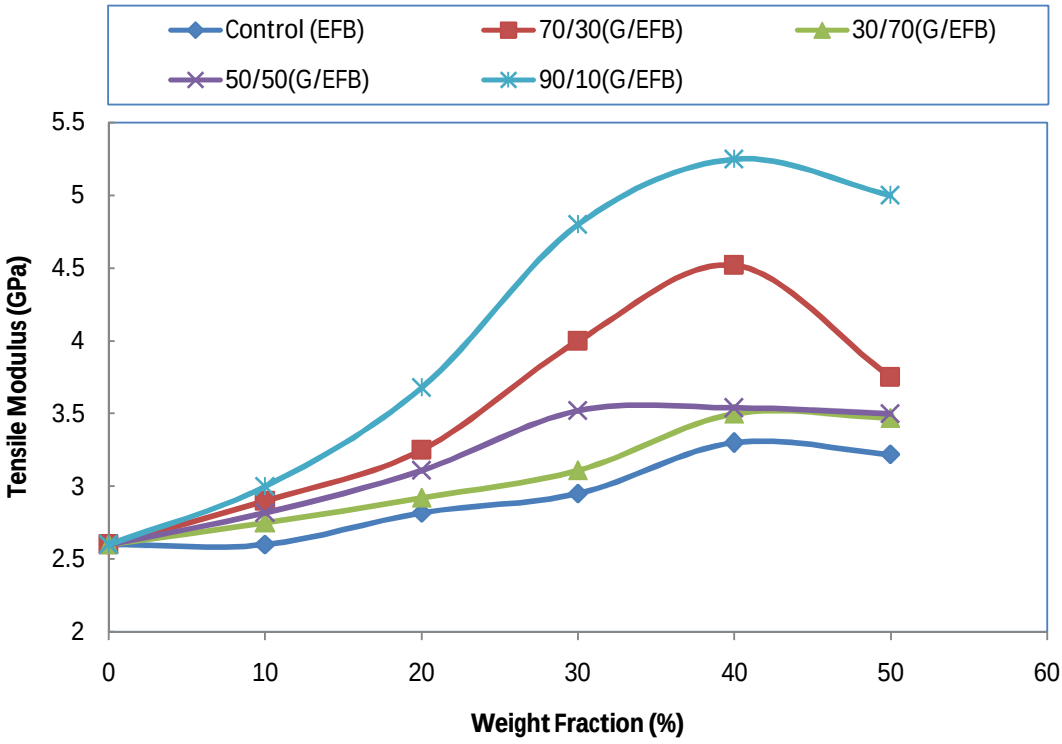

Figure 2.Tensile modulus of EFB/glass hybrid composites and EFB polyester composites at different fiber loading.

C. Tensile properties of hemp/glass fiber hybrid composite

SuharaPanthpulakkal et al. [10] studied the effect of glass fiber content on the tensile properties of hemp/glass fiber hybrid PP composite. Figures 3 and 4 clearly show that as the glass fiber content increased, tensile strength and modulus of hybrid hemp/glassfiber PP composite increases. This is due to the high strength and stiffness of glass fiber compared to hemp fiber. Tensile strength increased by 13% and modulus by 17% with incorporation of 15 wt% glass fiber in hemp/glass hybrid composite.

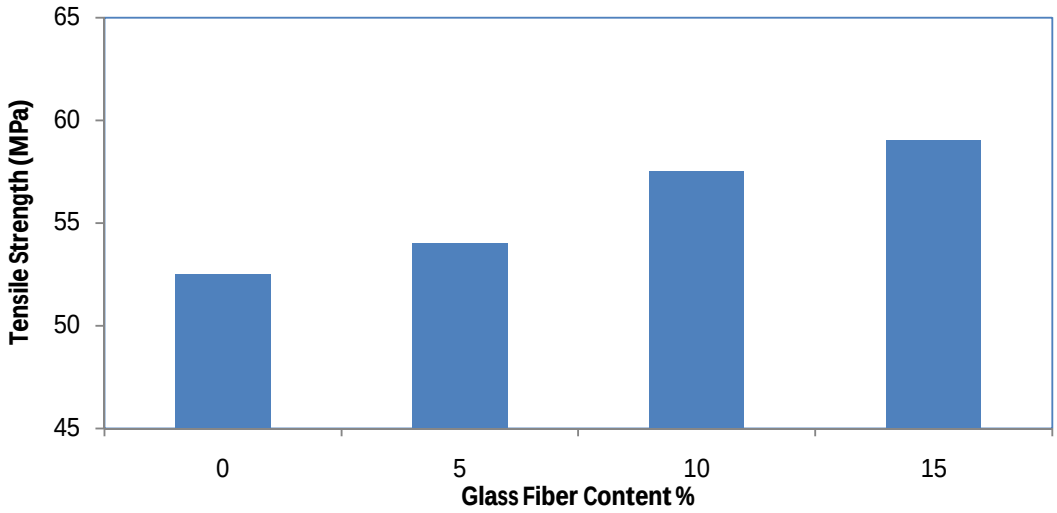

Figure 3.Effect of glass fiber content on the tensile strength of hemp/glass fiber hybrid polypropylene composites.

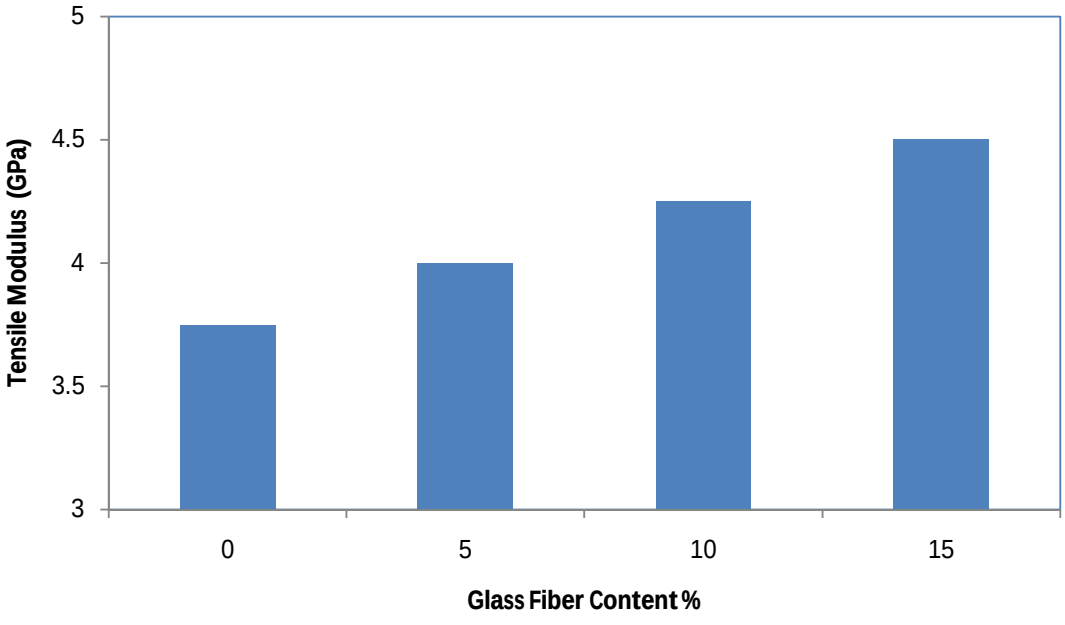

Figure 4.Effect of glass fiber content on the tensile modulus of hemp/glass fiber hybrid polypropylene composites.

D. Tensile strength of PALF/glass hybrid polyester composite

S. Mishra et al. [6] investigate the effect of glass fiber loading on the tensile strength of PALF/glass hybrid polyester composite. Figure 5 shows the variation of tensile strength with glass fiber in PALF/glass hybrid composite. The figure clearly indicates that addition of 8.6 wt% of glass fiberleads to increases the ultimate tensile strength of hybrid composite by about 66% but beyond addition up to 12.9% decreases the tensile strength by 10%.

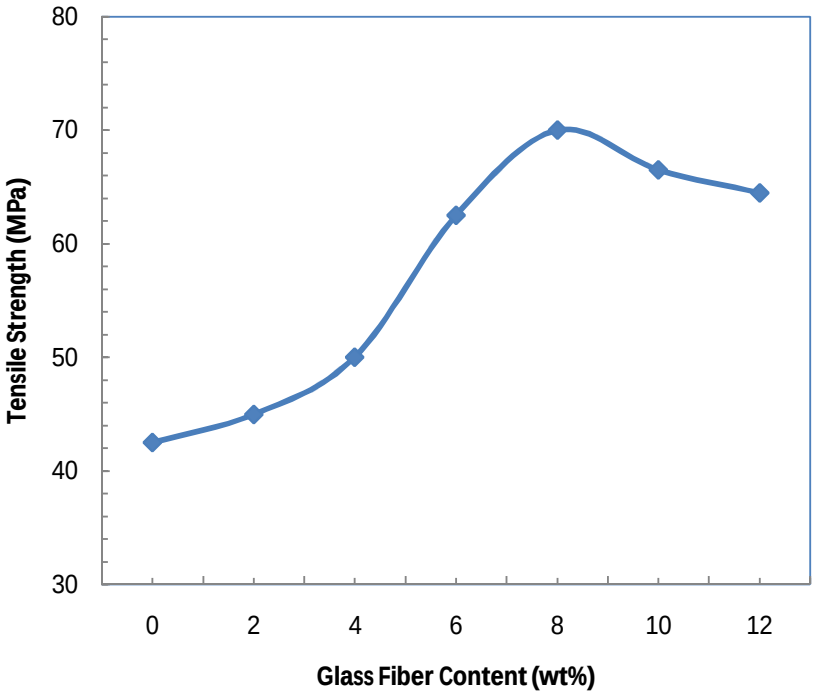

Figure 5. Effect of glass fiber loading on the tensile strength of PALF/glass hybrid polyester composite (total fiber content=25 wt %).

F. Tensile strength of Sisal/glass hybrid polyester composite

S. Mishra et al. [6] studied the effect of glass fiber loading on the tensile strength of sisal/glass hybrid polyester composite having 30 wt% of fiber content. Figure 6 shows that tensile strength of hybrid composite increases with glass fiber loading and reached to saturation stage at 5.7 wt% of glass fiber content in sisal/glass hybrid composite. This behaviour is due to the effective stress transfer from high modulus glass fiber to sisal fiber.

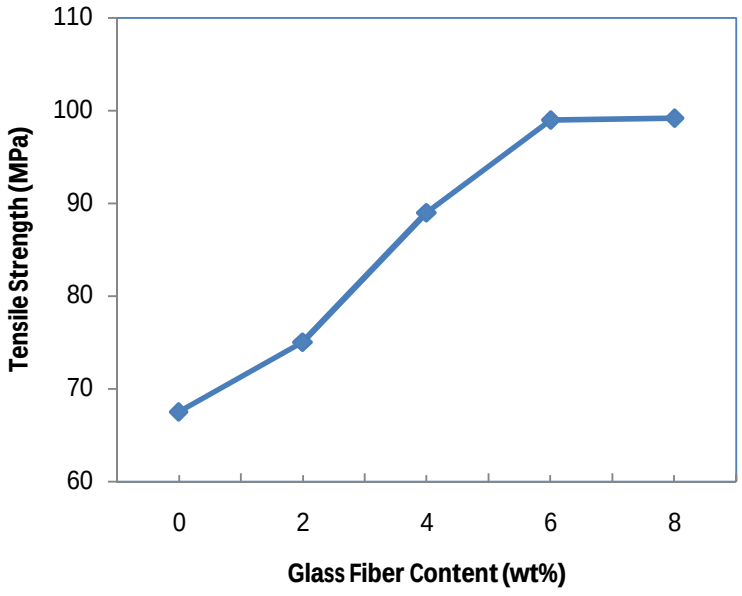

Figure 6. Effect of glass fiber loading on the tensile strength of sisal/glass hybrid polyester composite (total fiber content=30wt %).

G. Tensile properties of hemp/glass hybrid unsaturated polyester composite

AsimShahzad et al. [11] investigate the effect of glass fiber on the mechanical performance of hemp/glass hybrid polyester composite. He found that hybridization of hemp fiber with glass fiber in polyester composite results increment in tensile properties of hemp fiber composite. Table 2 shows the tensile properties of hemp-CSM glass hybrid composite compared to hemp composite. For hemp-skin glass core composite, the tensile strength and modulus is increased by 50% and 15% respectively. While glass skin-hemp core composite, the tensile strength is increased by 75% and tensile modulus is increased by 7%.

Fiber Configuration	Tensile Strength (MPa)	Tensile Modulus (GPa)	Strain to failure (%)
Hemp Only	46.4	7.2	1.03
Hybrid: Hemp skin, glass core	70.1	8.3	1.31
Hybrid: Glass skin, hemp core	81.6	7.7	1.73

Table 2.Comparison of tensile properties of hemp and hemp-CSM glass fiber hybrid composites.

III. EFFECT OF GLASS FIBER ON FLEXURAL PROPERTIES OF NFRC

A. Flexural Properties

In flexural loading, the composites are subjected to tension, compression, and shear stresses. These stresses are mainly carried by glass fiber in hybrid composite which result flexural strength of hybrid composite increases with increasing the glass fiber content. In a three-point flexure test, failure occurs due to bending and shearing.

B. Flexural properties of EFB/glass hybrid polyester composite

Abdul Khalil et al. [9] investigate the effect of glass fiber on flexural properties of EFB/glass hybrid composite. Figure 7 and 8 shows the variation of flexural strength and modulus of EFB/glass hybrid composite according to wt% of total fiber content and glass fiber content. It was observed that the flexural properties increase as the glass fiber loading increases up to 35 wt%. At higher loading (>35 wt %) flexural properties decreases due to poor dispersion of fiber in polyester resin and fiber-fiber interaction increases.

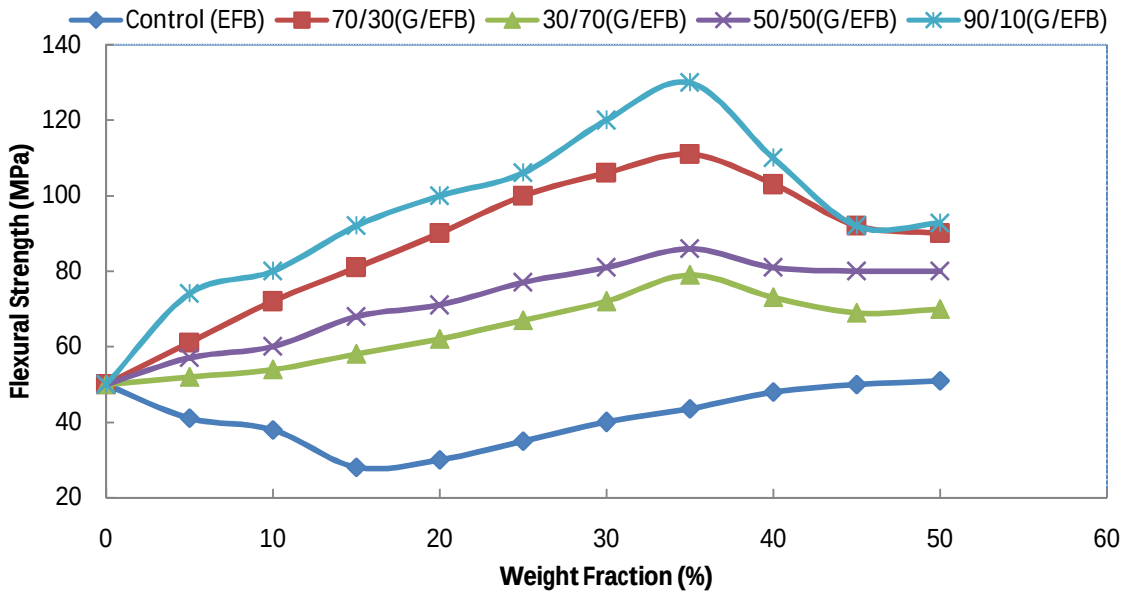

Figure 7.Flexural strength of EFB/glass hybrid composites and EFB polyester composites at different fibers loading.

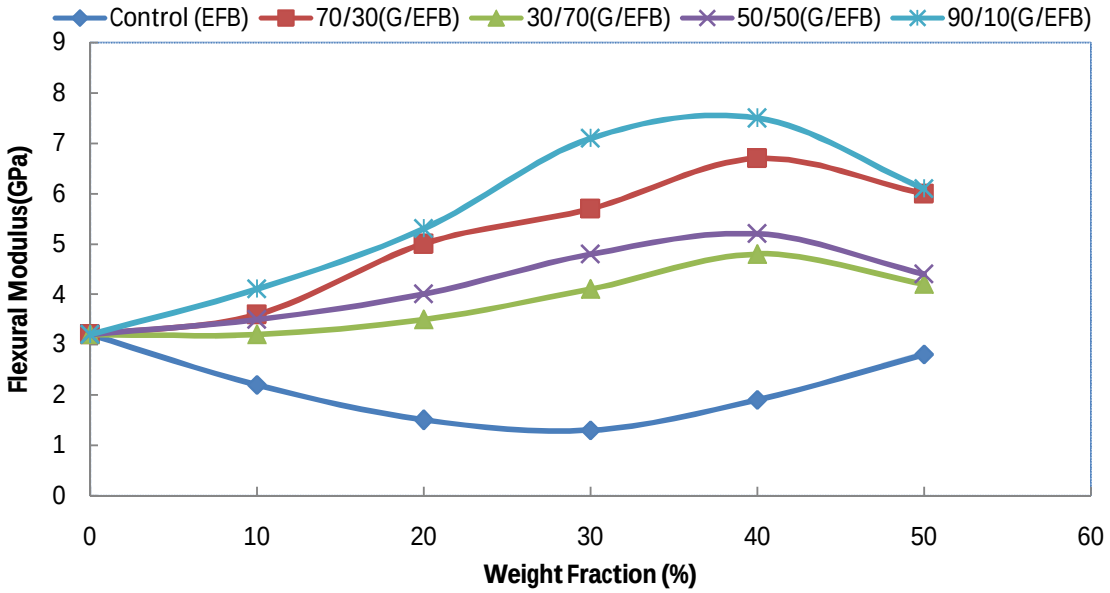

Figure 7.Flexural modulus of EFB/glass hybrid composites and EFB polyester composites at different fibers loading.

C. Flexural properties of hemp/glass fiber hybrid composite

SuharaPanthpulakkal et al. [10] studied the effect of glass fiber on the flexural strength and modulus of hemp/glass hybrid composite is shown in figures 8 and 9. He was observed that increasing the glass fiber content from 0 to 15 wt%, increased the flexural strength from 97.5 to 101 MPa, and modulus from 4.5 to 5.4 GPa.

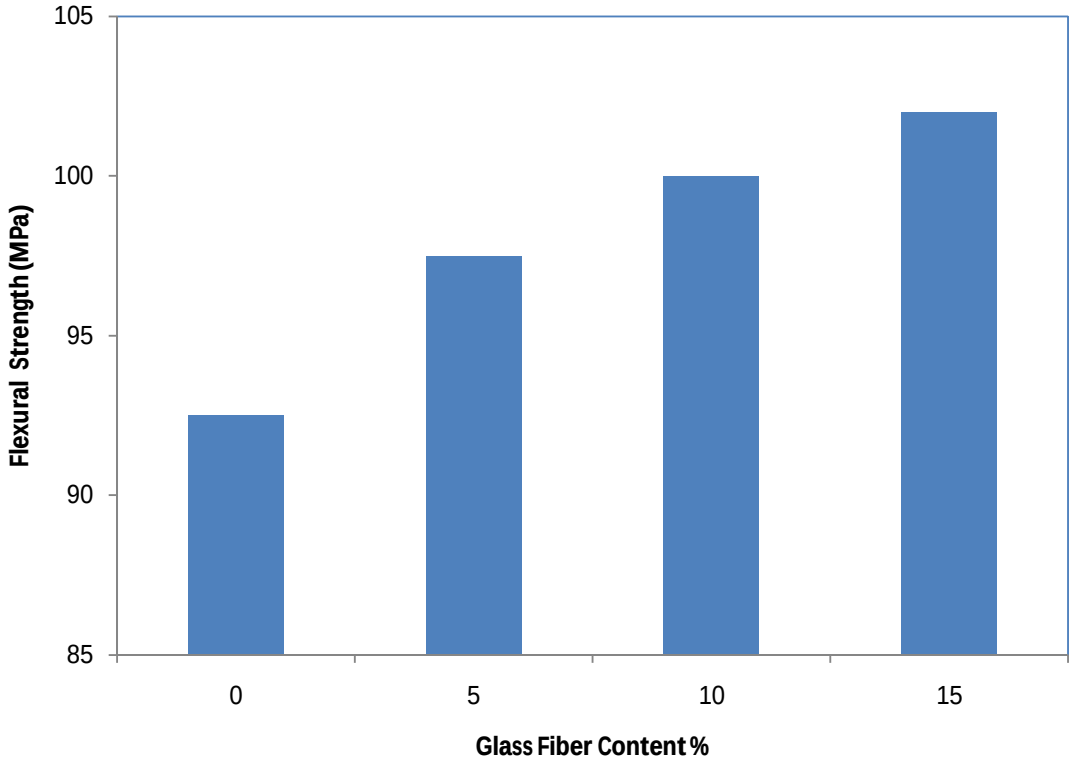

Figure 8.Effect of glass fiber content on the flexural strength of hemp/glass hybrid polypropylene composites.

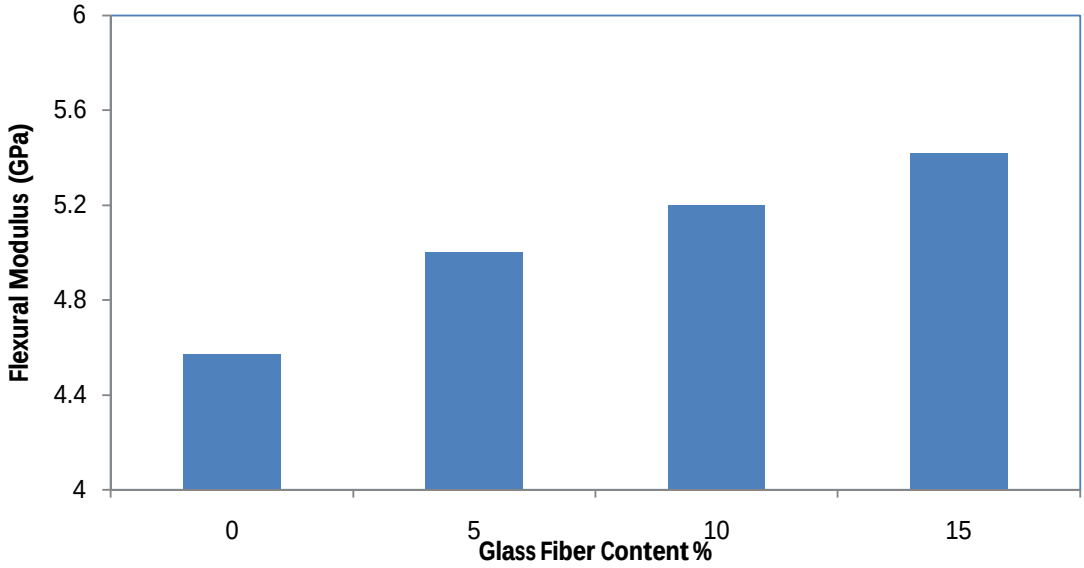

Figure 9.Effect of glass fiber content on the flexural modulus of hemp/glass hybrid polypropylene composites.

D. Flexural strength of PALF/glass hybrid polyester composite

S. Mishra et al. [6] investigate the effect of glass fiber loading on the flexural strength of PALF/glass hybrid composite is shown in figure 10. It was observed that addition of 12.9wt% of glass fiber, the flexural strength of hybrid composite increases from 68.29 to 101.25 MPa.

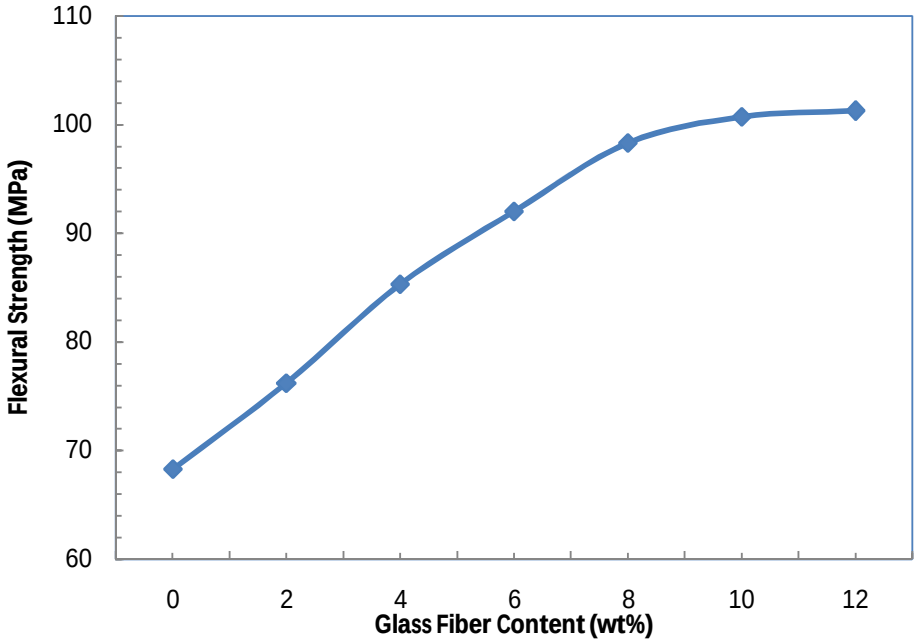

Figure 10. Effect of glass fiber loading on the flexural strength of PALF/glass hybrid polyester composite (total fiber content=25 wt %).

E. Flexural strength of Sisal/glass hybrid polyester composite

S. Mishra et al. [6] studied the effect of glass fiber loading on the flexural strength of sisal/glass hybrid composite is shown in figure 11. The flexural strength of sisal/glass hybrid composite was increased with the small wt% of glass fiber (2.8 wt%) by about 25 %.

Further addition of glass fiber increases the flexural strength as compared to sisal-polyester composite which saturate at 5.7 wt% of GF content.

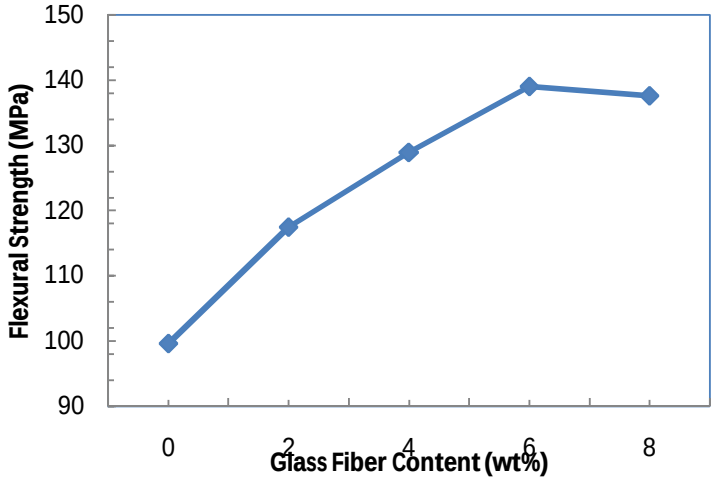

Figure 11. Effect of glass fiber loading on the flexural strength of sisal/glass hybrid polyester composite (total fiber content=30 wt %).

IV. EFFECT OF GLASS FIBER ON IMPACT STRENGTH OF NFRC

A. Impact Strength

Impact strength of a material is related to toughness of material and it is the ability of material to resist fracture failure under stress applied at high speed. Work of fracture of composite is greatly influenced by interlaminar and interfacial strength. The impact energy is dissipated by fiber and/or matrix fracture, fiberdebonding and pulls out. Ifthe applied load on a composite exceeds the interfacial bond strength, fiber-matrix debondingresults which lead to ultimate failure of composite [12-14].

B. Impact strength of EFB/glass hybrid polyester composite

Abdul Khalil et al. [9] studied the effect of glass fiber content on the impact strength of hybrid EFB composite is shown in figure 12. It was observed that fracture resistance of composite under impact load was increased with an increase in the fiber content of composite up to 35 wt%. At higher loading (>35 wt%), inter fiber interaction increases which result decrease the effective stress transfer from matrix to fiber. It was found from the figure 12 that incorporation of glass fiber in EFB/polyester composite results to increment in impact strength. Maximum impact strength was achieved at (90:10, glass:EFB) high loading of glass fiber.

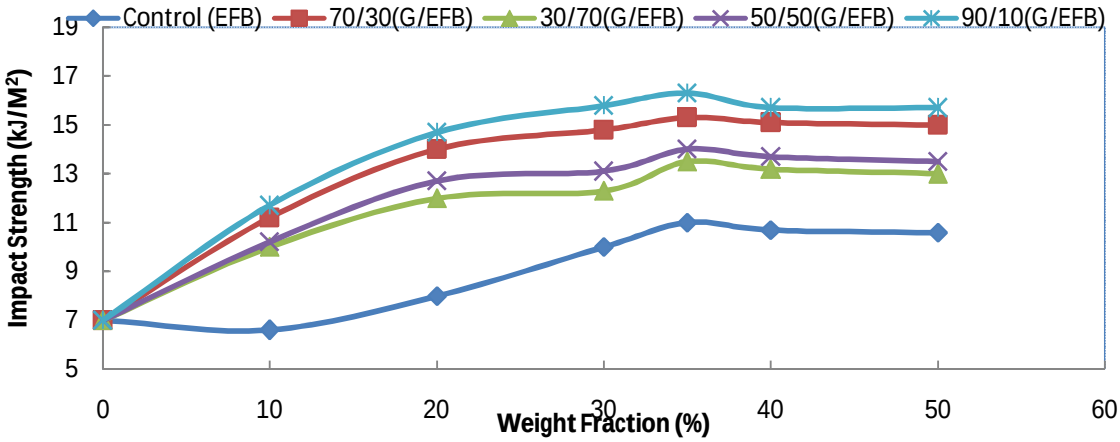

Figure 12.Impact strength of EFB/glass hybrid composites and EFB polyester composites at different fibers loading.

C. Impact strength of hemp/glass fiber hybrid composite

SuharaPanthpulakkal et al. [10] studied the effect of glass fiber addition on the impact strength of hemp/glass hybridcomposite is shown in figure 13. Impact strength of hybrid composite was increased by 35% with the addition of glass fiber (15 wt %) and this may be attributed to high fracture resistance offered by glass fiber in hemp/polypropylene composite.

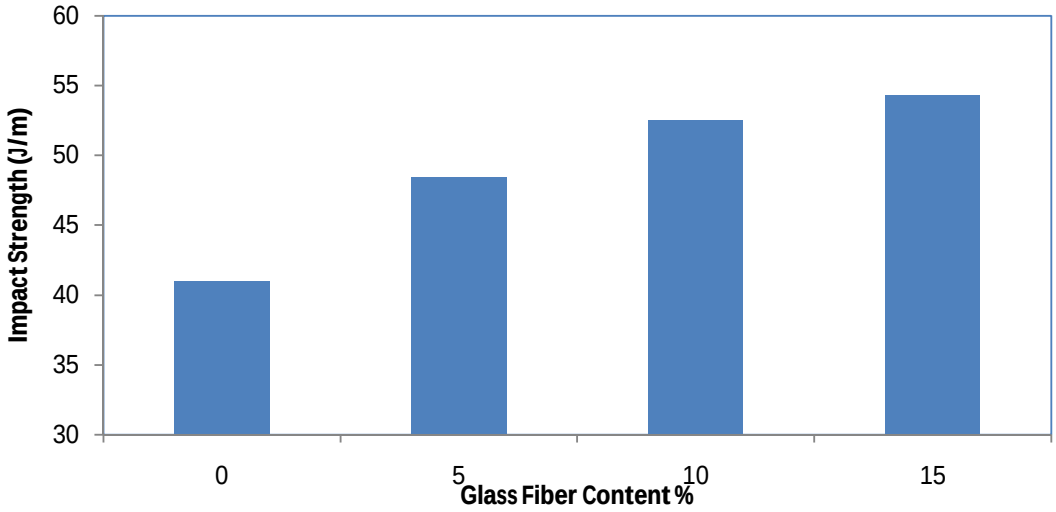

Figure 13.Effect of glass fiber content on the impact strength of hemp/glass hybrid polypropylene composites.

D. Impact strength of PALF/glass hybrid polyester composite

S. Mishra et al. [6] investigate the effect of glass fiber loading on the impact strength of PALF/glass hybrid composite is shown in figure 14. Work of fracture increase with the glass fiber loading and increases by 87% with the 8.6 wt% glass fiber content in hybrid composite. With further glass fiber loading, there is no significant increase in impact strength.

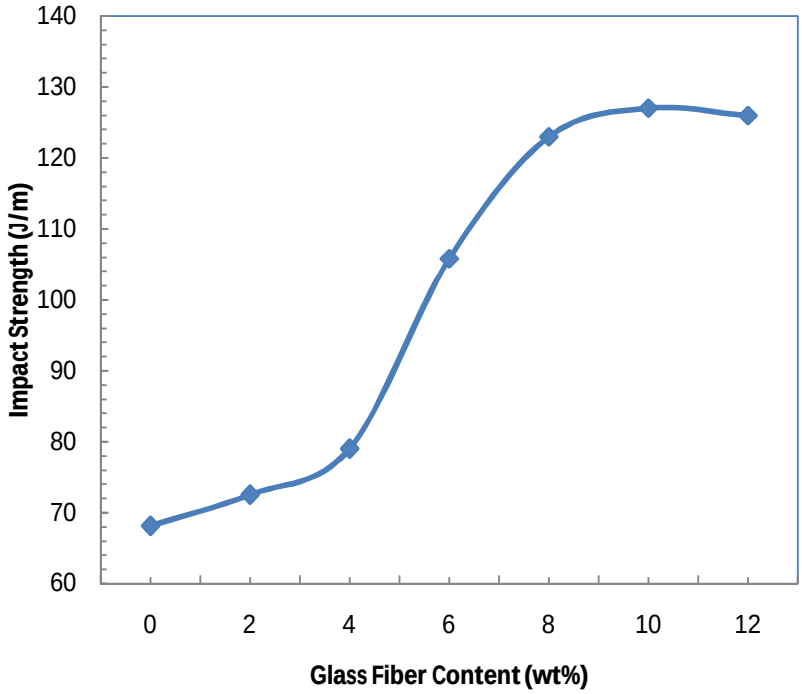

Figure 14. Effect of glass fiber loading on the impact strength of PALF/glass hybrid polyester composite (total fiber content=25 wt %).

F. Impact strength of Sisal/glass hybrid polyester composite

S. Mishra et al. [6] investigates the effect of glass fiber loading on the impact strength of sisal/glass hybrid composite is shown in figure 15. Impact strength of sisal/glass hybrid composite was increased by 34% with the loading of glass fiber from 0 to 8.5 wt%.

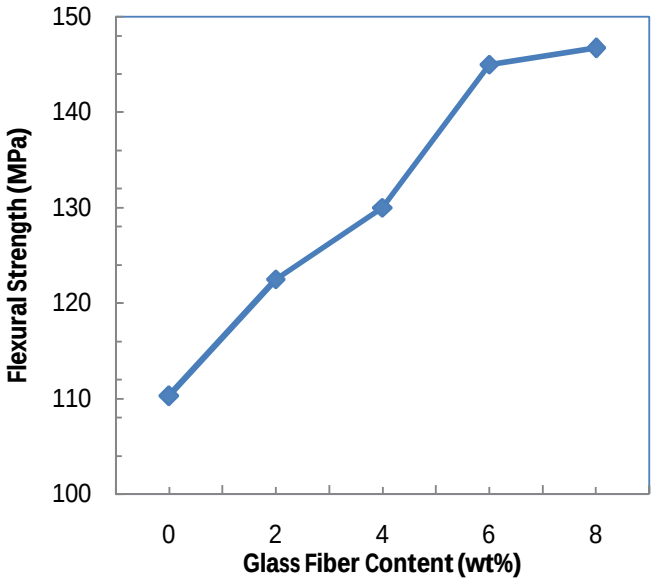

Figure 15. Effect of glass fiber loading on the impact strength of sisal/glass hybrid polyester composite (total fiber content=30 wt %).

V. CONCLUSIONS

This paper presents the effects of glass fiber content on the mechanical properties of hybrid biocomposites. The conclusions from this study are summarized as follows:

Hybridization of EFB fiber with glass fiber in polyester matrix has resulted in the improvement of tensile, flexural, and impact strength of the composites. Composites showed the highest impact and flexural properties at 35 wt% of glass fiber loading but tensile strength was increased up to 45 wt% of glass fiber content. Mechanical properties of composite were increased with addition of EFB and glass fiber.This is due to the effective stress transfer from matrix to fiber and better dispersion of fiber.Incorporation of glass fiber in hemp-polypropylene composite leads to enhance the mechanical properties of composite. Tensile strength and modulus increased by 13 and 17% respectively with the addition of 15 wt% glass fiber. Work of fracture and flexural strength of biocomposite is alsoincreased with the optimum loading (15 wt%) of glass fiber. This is due to the high fracture and shearing .Mechanical properties of PALF/glass and sisal/glass hybrid polyester composites showing positive hybrid effect with small amount of glass fiber loading. Optimum glass fiber content in PALF/glass hybrid polyester and sisal/glass polyester composites are 8.6 and 5.7 wt% respectively under which significant improvement in mechanical properties takes place.

REFERENCES

[1] Rasshofer W, Weigand E, Frisch KC. Advances in plastics: automotive polyurethane, vol. II. Lancaster: Technomic Publishing Company Inc.; 2001.
[2] Davoodi MM, Sapuan SM, Ahmad D, Aidy A, Khalina A. A review on natural fiber composites in automotive industry. In: Sapuan SM, editor. Research in natural fiber reinforced polymer composite. Selangor: UPM Press; 2008. p. 247-62.
[3] Mohanty AK, Misra M, Drzal LT. Natural fibers, biopolymers, and biocomposites. Boca Raton: CRC Press; 2005.
[4] Faruk O. Cars from jute and other biofibers; 2006.
[5] Miwa M, Horiba N. J Mater Sci 2000; 29:973.
[6] Mishra S, Mohanty AK, Drzal LT, Misra M, Parija S, Nayak SK, et al. Studies on mechanical performance of biofiber/glass reinforced polyester hybrid composite. Compos SciTechnol 2003, 63:1377-85.
[7] Chamis CC, Hanson MP and Serafini TT. Impact resistance of unidirectional fiber composites. Compos Mater: Test Design 1972; ASTM STP 497: 324-349.
[8] Beaumont PWR, Riewald PG and Zweben C. Methods for improving the impact resistance of composite materials. Foreign Object Damage Compos 1974; ASTM STP 568: 134-158.

[9] H.P.S. Abdul Khalil, S. Hanida, et al. Agro-hybrid composite: The effects on mechanical and physical properties of oil palm fiber (EFB)/ glass hybrid reinforced polyester composite. Journal of reinforced plastics and composites 2007, 26:203.
[10] SuharaPanthapulakkal, Mohinisain. Injection-molded short hemp fiber/glass fiber-reinforced polypropylene hybrid composites-mechanical, water absorption and thermal properties.Wiley Interscience Publishing, pp. 2432-2441 (2006).
[11]AsimShahzad. Impact and fatigue properties of hemp-glass fiber hybrid biocomposites. Journal of reinforced plastics & composites 2011; 30(16): 1389-1398.
[12] Jang J, Moon S-I. Sung-In Moon Polym Comp 1995; 16:325.
[13] Reed PE, Bevan L. Polym Comp 1993; 14:286
[14] Sela N, Ishai O. Composites 1989; 20:423.

International Journal of Research in Engineering and Innovation (IJREI)
journal home page: http://www.ijrei.com
ISSN (Online): 2456-6934

Energy and exergy analysis of multiple evaporators and compressors with individual or multiple expansion valves vapour compression refrigeration system using ecofriendly refrigerants

R.S. Mishra

Department of Mechanical & Production Engineering, Delhi Technological University Delhi, India

Abstract

Lots of literature was available on the thermal performances of vapour compression refrigeration systems and based on the literature it was observed that researchers have gone through detailed first law and second law analysis in terms of coefficient of performance and second law analysis in term of exergetic efficiency of simple vapour compression refrigeration system with single evaporator. Researchers did not go through for finding the irreversibility of system and exergy losses /destruction using entropy generation of simple (double stage and triple stage)VCR and stages in compression and Multiple evaporators systems with multi-stage expansion and compound compression in vapour compression refrigeration systems. In this paper, comparative thermodynamic analysis of system-1 (multiple evaporators and compressors with individual expansion valves) and system-2 (multiple evaporators and compressors with multiple expansion valves) has been presented which is based on energy and exergy principles. The comparison of systems-1 and -2 using eco-friendly R410A, R290, R1234YF, R502, R404A, R152A and R134A refrigerants was done in terms of first law efficiency (COP) known as energetic efficiency, exergetic efficiency and rational efficiency and exergy destruction ratio based on exergy of fuel and total irreversibility occurred in the system (%) Exergy losses in the various components known as system defect. Numerical model has been developed for systems-1 and -2 for finding out irreversibility and it was observed that system-1 is better system in comparison with system-2 for selected refrigerants. It was also found that R123 shows better performances than other considered refrigerants for both systems. The comparison was also done using eighteen eco-friendly refrigerants with R12 and it was found that R600, R600a, R290 and R152A show better performances than other refrigerants for both systems but due to flammable property of R600, R600a and R290 and R152a, HFO refrigerant R1234yf and R1234ze are preferred for both systems.

Keywords: Thermodynamic Analysis, Energy-Exergy Analysis, Entropy Generation principle, Irreversibility Analysis

1. Introduction

Nowadays most of the energy utilize in cooling and air conditioning in industrial as well as for domestic applications. In addition with energy consumption, using of refrigerants in cooling and air conditioning having high GWP and ODP are responsible for global warming and ozone depletion. The primary requirements of ideal refrigerants is having good physical and chemical properties, due to good physical and chemical properties such as non-corrosiveness, non-toxicity, non- flammability, low boiling point, Chlorofluorocarbons (CFCs) have been used over the last many decades. But hydro chlorofluorocarbons (HCFCs) and Chlorofluorocarbons (CFCs) having large amount of chlorine content as well as high GWP and ODP, so after 90s refrigerants under these categories are almost prohibited [1].

Most of the study has been carried out for the performance evaluation of vapour compression refrigeration system using energetic analysis. But with the help of first law analysis irreversibility destruction or losses in components of system unable to determined , so that exergetic or second law analysis is the advanced approach for thermodynamic analysis which give a additional practical view of the processes [2]. In addition to this second law analysis also provides new thought for

Corresponding author: R. S. Mishra
Email Address: hod.mechanical.rsm@dtu.ac.in

development in the existing refrigeration and air conditioning systems [3]

1.1 Energy Exergy Analysis of Vapour Compression Refrigeration Systems

The most commonly-used method for analysis of an energy-conversion process is the first law of thermodynamics. But in the recent decades, the exergetic performance based on the second law of thermodynamics has found as useful method in the design, evaluation, optimization and improvement of vapour compression refrigeration systems.

The exergetic performance analysis can not only determine magnitudes, location and causes of irreversibilities in the vapour compression refrigeration systems, but also provides more meaningful assessment of power plant individual components efficiency. A conventional exergetic analysis reveals irreversibilities within each component of a vapour compression refrigeration systems. Exergetic analysis provides the tool for a clear distinction between energy losses to the environment and internal irreversibilities in the process because exergy analysis is a methodology for the evaluation of the performance of devices and processes, and examining the exergy at different points in a series of energy-conversion steps. With this information, efficiencies can be evaluated, and the process steps having the largest losses (i.e., the greatest margin for improvement) can be identified. For these reasons, the modern approach uses the exergy analysis in the vapour compression refrigeration systems, which provides a more realistic view of the process and a useful tool for engineering evaluation.

The second law analysis (i.e. exergy Computation) is widely accepted as a useful tool for obtaining overall performances of any system for finding various exergy losses occurred in its components Exergy analysis also helps in taking account the important engineering decisions regarding design parameters of a system by finding maximum exergy destruction using entropy generation principle.

Many researchers have carried out exergy studies of different thermal energy conversion systems describing various approach for exergy analysis and its usefulness for improving existing designs by reducing exergy destruction in a more simple and effective manner [2-3]. Cabello et al. [4] studied the effect of condensing pressure, evaporating pressure and degree of superheating was experimentally investigated on single stage vapour compression refrigeration system using R22, R134a and R407C.It was observed that mass flow rate is greatly affected by change in suction conditions of compressor in results on refrigeration capacity because refrigeration capacity depended on mass flow rate through evaporator. It was also found that for higher compression ratio R22 gives lower COP than R407C.Padilla et al. [5] carried out exergy analysis of domestic vapour compression refrigeration system with R12 and R413A was done. They concluded that performance in terms of power consumption, irreversibility and exergy efficiency of R413A is better than R12, so R12 can be replaced with R413A in domestic vapour compression refrigeration system. Kumar et al.[6] did energy and exergy analysis of vapour compression refrigeration system by the use of exergy-enthalpy diagram. They did first law analysis or energy analysis for calculating the coefficient of performance and exergy analysis for evaluation of various losses occurred in different components of vapour compression cycle using R11 and R12 as refrigerants. In this paper great emphasis put on saving of energy and using of ecofriendly refrigerants due to increase of energy crises, global warming and depletion of ozone layer. In this investigation the work input required running the vapour compression refrigeration system reduced by using compound compression and work input.

2. Thermodynamic Analysis

2.1 Models description of multiple evaporators and compressors with individual expansion valves (system-1) and multiple evaporators and compressors with multiple expansion valves (system-2) vapour compression refrigeration systems.

The multiple evaporators and compressors with individual expansion valves vapour compression refrigeration system (system-1) consists of compressors (C_1, C_2,C_3) throttle valves (TV_1, TV_2,TV_3), condenser and evaporators(EP_1, EP_2,EP_3)as shown in Fig.1(a).The pressure versus enthalpy chart for this system is shown in Fig.1(b). In this system all refrigerant coming out at point '77' from sub-cooler distributed by mass $\dot{m}_1$,$\dot{m}_2$, $\dot{m}_3$ to expansion valves TV_1, TV_2, and TV3 respectively. Both liquid and vapour formed by TV_1 ,TV_2 ,TV_3 represented by point '10', '9' and '8' take care the load of EP_1 ,EP_2 and EP_3 respectively. The low pressure vapours formed by EP_1 ,EP_2 and EP_3 supplied to the compressor C_1 ,C_2 and C_3 represented by point '1', '3' and '5' respectively. The high pressure vapours formed by compressor C_1 ,C_2 and C_3 respectively represented by points '2', '4' and '6' .then high pressure vapours coming out from compressor C_1 , C_1 ,C_1 collectively enter through condenser by point '7'.The main components of multiple evaporators and compressors with individual expansion valves vapour compression refrigeration system (system-2) are compressors (C_1, C_2,C_3) throttle valves (TV_1, TV_2,TV_3), condenser and evaporators(EP_1, EP_2,EP_3)as shown in Fig. 2(a).The corresponding pressure versus enthalpy chart for this system is shown in Fig. 2(b).In this system all the refrigerant from condenser at point 'g' followed by sub-cooler exit at point 'gg' flows through the throttle valve TV3 where its pressure is reduced from condenser pressure of the third evaporator. All the vapours formed after leaving the expansion valve TV3 at point 'h' plus enough liquid to take care of the load of evaporator EP3.The remaining refrigerant then enter at point 'i' through the expansion valve TV2 where its pressure is reduced from pressure of the third evaporator to pressure of the second evaporator. Again all the vapour formed after leaving the expansion valve TV_2 at point 'j' plus enough liquid to take care of the load of evaporator EP_2 passes through this

evaporator .The remaining liquid now enter at point 'k' through the expansion valve TV_1 and exit at point 'l' which supplied it to the first evaporator EP_1.The vapours formed by EP_1, EP_2 , EP_3 supplied to compressors C_1, C_2 and C_3 shown by point 'a','c' and 'e' respectively. High pressure vapours formed by compressors C_1, $C_2$and C_3 as shown by points 'b','d' and 'f' respectively supplied to the condenser.

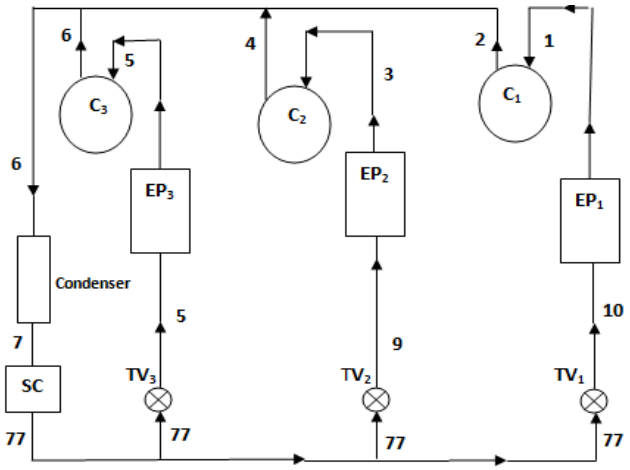

Figure 1 (a) Schematic diagram of multiple evaporators at different temperatures with individual compressors and individual expansion valves

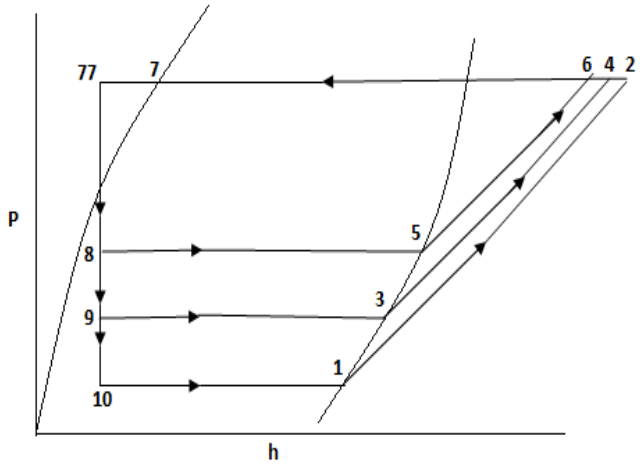

Figure 1 (b): Pressure enthalpy diagram of multiple evaporators at different temperatures with individual compressors and individual expansion valves.

2.2 First law analysis (COP & work input analysis) of multiple evaporators and compressors with individual or multiple expansion valves vapour compression refrigeration systems

The multiple evaporators and compressors with individual or multiple expansion valves vapour compression refrigeration system as shown in Fig.1 and Fig.2 respectively. From the energy analysis point of view first law of thermodynamics, evaluate the performance of the vapour compression systems as given below:

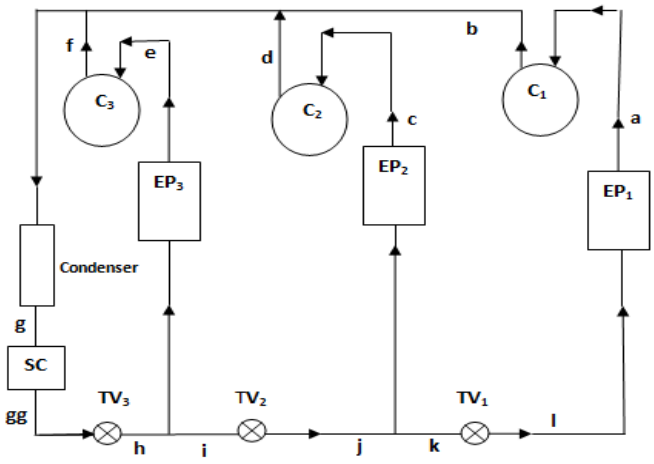

Fig.2 (a) Schematic diagram of multiple evaporators at different temperatures with individual compressors and multiple expansion valves

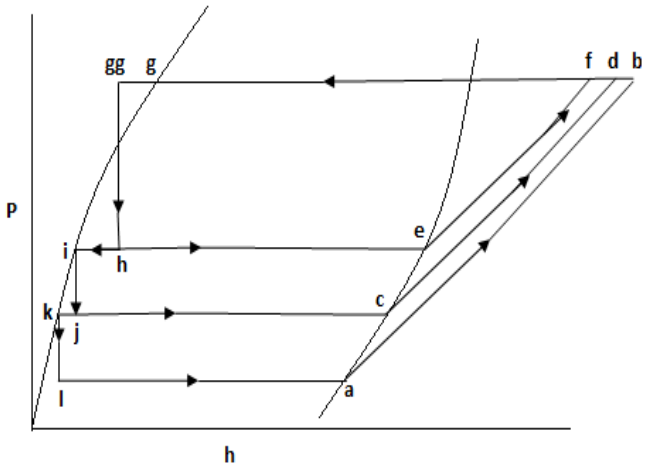

Fig.2 (b) Pressure enthalpy diagram of multiple evaporators at different temperatures with individual compressors and multiple expansion valves

System-1

$$\dot{m}_{e1} = \dot{m}_{c1} \quad (1)$$
$$\dot{m}_{e2} = \dot{m}_{c2} \quad (2)$$
$$\dot{m}_{e3} = \dot{m}_{c3} \quad (3)$$
$$\dot{Q}_{e\_1} = \dot{Q}_{e1} + \dot{Q}_{e2} + \dot{Q}_{e3} \quad (4)$$
$$\dot{W}_{comp1} = \dot{m}_{c1}(\psi_2 - \psi_1) \quad (5)$$
$$\dot{W}_{comp2} = \dot{m}_{c2}(\psi_4 - \psi_3) \quad (6)$$
$$\dot{W}_{comp3} = \dot{m}_{c3}(\psi_6 - \psi_5) \quad (7)$$
$$\dot{W}_{comp\_1} = \dot{W}_{comp1} + \dot{W}_{comp2} + \dot{W}_{comp3} \quad (8)$$
$$COP\_1 = \frac{\dot{Q}_{e\_1}}{\dot{W}_{comp\_1}} \quad (9)$$

System-2

$$\dot{m}_{c1} = \dot{m}_{e1} \quad (10)$$

$$\dot{m}_{c2} = \dot{m}_{e2} = \dot{m}_2 + \dot{m}_{e1}\left(\frac{\varphi_j}{1-\varphi_j}\right) \quad (11)$$

$$\dot{m}_2 = \left(\frac{\dot{Q}_{e2}}{\psi_c - \psi_j}\right) \quad (12)$$

$$\dot{m}_{c3} = \dot{m}_{e3} = \dot{m}_3 + (\dot{m}_{e1} + \dot{m}_{e2})\left(\frac{\varphi_h}{1-\varphi_h}\right) \quad (13)$$

$$\dot{m}_3 = \left(\frac{\dot{Q}_{e3}}{\psi_e - \psi_h}\right) \quad (14)$$

$$\dot{Q}_{e\_2} = \dot{Q}_{e1} + \dot{Q}_{e2} + \dot{Q}_{e3} \quad (15)$$

$$\dot{W}_{comp1} = \dot{m}_{c1}(\psi_b - \psi_a) \quad (16)$$

$$\dot{W}_{comp2} = \dot{m}_{c2}(\psi_d - \psi_c) \quad (17)$$

$$\dot{W}_{comp3} = \dot{m}_{c3}(\psi_f - \psi_e) \quad (18)$$

$$\dot{W}_{comp\_2} = \dot{W}_{comp1} + \dot{W}_{comp2} + \dot{W}_{comp3} \quad (19)$$

$$COP\_2 = \frac{\dot{Q}_{e\_2}}{\dot{W}_{comp\_2}} \quad (20)$$

3. *Second law analysis of multiple evaporators and compressors with individual or multiple expansion valves vapour compression refrigeration system*

The concept of exergy was given by Second law of thermodynamics. Exergy is the measure of usefulness, quality or potential of a stream to cause change and an effective measure of the potential of a substance to impact the environment.

3.1 Exergy destruction (ED)

Exergy destruction in each component of the multiple evaporators and compressors with individual expansion valves vapour compression refrigeration system (System-1) is evaluated as per Eqs. (21)– (32) given below:

Evaporators

(EP$_1$) System-1

$$\dot{E}D_{e1} = \dot{E}_{x10} + \dot{Q}_{e1}\left(1 - \frac{T_0}{T_{r1}}\right) - \dot{E}_{x1} = \dot{m}_{e1}(\psi_{10} - T_0 s_{10}) + \dot{Q}_{e1}\left(1 - \frac{T_0}{T_{r1}}\right) - \dot{m}_{e1}(\psi_1 - T_0 s_1) \quad (21)$$

(EP$_2$) System-1

$$\dot{E}D_{e2} = \dot{E}_{x9} + \dot{Q}_{e2}\left(1 - \frac{T_0}{T_{r2}}\right) - \dot{E}_{x3} = \dot{m}_{e2}(\psi_9 - T_0 s_9) + \dot{Q}_{e2}\left(1 - \frac{T_0}{T_{r2}}\right) - \dot{m}_{e2}(\psi_3 - T_0 s_3) \quad (22)$$

(EP$_3$) System-1

$$\dot{E}D_{e3} = \dot{E}_{x8} + \dot{Q}_{e3}\left(1 - \frac{T_0}{T_{r3}}\right) - \dot{E}_{x5} = \dot{m}_{e3}(\psi_8 - T_0 s_8) + \dot{Q}_{e3}\left(1 - \frac{T_0}{T_{r3}}\right) - \dot{m}_{e3}(\psi_5 - T_0 s_5) \quad (23)$$

Compressors

(C$_1$) System-1

$$\dot{E}D_{comp1} = \dot{E}_{x1} + \dot{W}_{comp1} - \dot{E}_{x2} = \dot{m}_{c1}(T_0(s_2 - s_1)) \quad (24)$$

(C$_2$) System-1

$$\dot{E}D_{comp2} = \dot{E}_{x3} + \dot{W}_{comp2} - \dot{E}_{x4} = \dot{m}_{c2}(T_0(s_4 - s_3)) \quad (25)$$

(C$_3$) System-1

$$\dot{E}D_{comp3} = \dot{E}_{x5} + \dot{W}_{comp3} - \dot{E}_{x6} = \dot{m}_{c3}\big(T_0(s_6 - s_5)\big) \quad (26)$$

Condenser

(Condenser) System-1

$$\dot{E}D_c = (\dot{E}_{x2} - \dot{E}_{x7}) + (\dot{E}_{x4} - \dot{E}_{x7}) + (\dot{E}_{x6} - \dot{E}_{x7}) = \dot{m}_{c1}\big((\psi_2 - T_0 s_2) - (\psi_7 - T_0 s_7)\big) + \dot{m}_{c2}\big((\psi_4 - T_0 s_4) - (\psi_7 - T_0 s_7)\big) + \dot{m}_{c3}\big((\psi_6 - T_0 s_6) - (\psi_7 - T_0 s_7)\big) \quad (27)$$

Sub cooler

(SC) System-1

$$\dot{E}D_{sc} = \dot{E}_{x7} - \dot{E}_{x77} = (\dot{m}_{c1} + \dot{m}_{c2} + \dot{m}_{c3})((\psi_7 - T_0 s_7) - (\psi_{77} - T_0 s_{77})) \quad (28)$$

Throttle valves

TV$_1$) System-1

$$\dot{E}D_{TV_1} = \dot{E}_{x77} - \dot{E}_{x10} = \dot{m}_{c1}(T_0(s_{10} - s_{77})) \quad (29)$$

(TV-2) System-1

$$\dot{E}D_{TV_2} = \dot{E}_{x77} - \dot{E}_{x9} = \dot{m}_{c2}(T_0(s_9 - s_{77})) \quad (30)$$

(TV-3)System-1

$$\dot{E}D_{TV_3} = \dot{E}_{x77} - \dot{E}_{x8} = \dot{m}_{c3}(T_0(s_8 - s_{77})) \quad (31)$$

The total irreversibility (%) in terms of system exergy losses in the system-1 is the sum of irreversibility in each components of the system and is given by

$$\sum \dot{E}D_k = \dot{E}D_{e1} + \dot{E}D_{e2} + \dot{E}D_{e3} + \dot{E}D_{comp1} + \dot{E}D_{comp2} + \dot{E}D_{comp3} + \dot{E}D_c + \dot{E}D_{sc} + \dot{E}D_{TV_1} + \dot{E}D_{TV_2} + \dot{E}D_{TV_3} \quad (32)$$

Similarly exergy destruction in each component of the multiple evaporators and compressors with multiple expansion valves vapour compression refrigeration system (System-2) is evaluated as per Eqs. (33)– (44) given below:

Evaporators

(EP1)System-2

$$\dot{E}D_{e1} = \dot{E}_{xl} + \dot{Q}_{e1}\left(1 - \frac{T_0}{T_{r1}}\right) - \dot{E}_{xa} = \dot{m}_{e1}(\psi_l - T_0 s_l) +$$

$$\dot{Q}_{e1}\left(1-\frac{T_0}{T_{r1}}\right)-\dot{m}_{e1}(\psi_a-T_0 s_a) \quad (33)$$

(EP2)System-2

$$\dot{E}D_{e2}=\dot{E}_{xj}+\dot{Q}_{e2}\left(\frac{1-}{\frac{T_0}{T_{r2}}}\right)-\dot{E}_{xc}=\dot{m}_{e2}(\psi_j-T_0 s_j)+\dot{Q}_{e2}\left(1-\frac{T_0}{T_{r2}}\right)-\dot{m}_{e2}(\psi_c-T_0 s_c) \quad (34)$$

(EP3)System-2

$$\dot{E}D_{e3}=\dot{E}_{xh}+\dot{Q}_{e3}\left(1-\frac{T_0}{T_{r3}}\right)-\dot{E}_{xe}=\dot{m}_{e3}(\psi_h-T_0 s_h)+\dot{Q}_{e3}\left(1-\frac{T_0}{T_{r3}}\right)-\dot{m}_{e3}(\psi_e-T_0 s_e) \quad (35)$$

Compressors

(C-1)System-2

$$\dot{E}D_{comp1}=\dot{E}_{xa}+\dot{W}_{comp1}-\dot{E}_{xb}=\dot{m}_{c1}(T_0(s_b-s_a)) \quad (36)$$

(C-2)System-2

$$\dot{E}D_{comp2}=\dot{E}_{xc}+\dot{W}_{comp2}-\dot{E}_{xd}=\dot{m}_{c2}(T_0(s_d-s_c)) \quad (37)$$

(C-3)System-2

$$\dot{E}D_{comp3}=\dot{E}_{xe}+\dot{W}_{comp3}-\dot{E}_{xf}=\dot{m}_{c3}(T_0(s_f-s_e)) \quad (38)$$

(Condenser)System-2

$$\dot{E}D_{cond}=(\dot{E}_{xb}-\dot{E}_{xg})+(\dot{E}_{xd}-\dot{E}_{xg})+(\dot{E}_{xf}-\dot{E}_{xg})=\dot{m}_{c1}\left((\psi_b-T_0 s_b)-(\psi_g-T_0 s_g)\right)+\dot{m}_{c2}\left((\psi_d-T_0 s_d)-(\psi_g-T_0 s_g)\right)+\dot{m}_{c3}\left((\psi_f-T_0 s_f)-(\psi_g-T_0 s_g)\right) \quad (39)$$

(SC)System-2

$$\dot{E}D_{sc}=\dot{E}_{xg}-\dot{E}_{xgg}=(\dot{m}_{c1}+\dot{m}_{c2}+\dot{m}_{c3})\left((\psi_g-T_0 s_g)-(\psi_{gg}-T_0 s_{gg})\right) \quad (40)$$

Throttle valves: (TV-1) System-2

$$\dot{E}D_{TV_1}=\dot{E}_{xk}-\dot{E}_{xl}=\dot{m}_{c1}(T_0(s_l-s_k)) \quad (41)$$

(TV-2)System-2

$$\dot{E}D_{TV_2}=\dot{E}_{xi}-\dot{E}_{xj}=(\dot{m}_{c1}+\dot{m}_{c2})(T_0(s_j-s_i)) \quad (42)$$

(TV-3)System-2

$$\dot{E}D_{TV_3}=\dot{E}_{xgg}-\dot{E}_{xh}=(\dot{m}_{c1}+\dot{m}_{c2}+\dot{m}_{c3})(T_0(s_h-s_{gg})) \quad (43)$$

The total irreversibility in the system-2 is the sum of irreversibility in each components of the system and is given by

$$\sum \dot{E}D_k=\dot{E}D_{e1}+\dot{E}D_{e2}+\dot{E}D_{e3}+\dot{E}D_{comp1}+\dot{E}D_{comp2}+\dot{E}D_{comp3}+\dot{E}D_c+\dot{E}D_{sc}+\dot{E}D_{TV_1}+\dot{E}D_{TV_2}+\dot{E}D_{TV_3} \quad (44)$$

Exergetic efficiency $\eta_{ex}=\frac{\text{Exergy in product}}{\text{Exergy of fuel}}=\frac{\dot{E}P}{\dot{E}F}$ (45)

For the multi evaporators vapour compression refrigeration system, product is the exergy of the heat abstracted in to the evaporators' i.e.Q_e =Q_{e1} +Q_{e2}+Q_{e3} from the space to be cooled at temperature T_r, and exergy of fuel is actual compressor work input. Hence, exergetic efficiency is given by

$$\dot{E}P=\dot{Q}_{e1}+\dot{Q}_{e2}\left|\left(1-\frac{T_0}{T_{r2}}\right)\right|+\dot{Q}_{e3}\left|\left(1-\frac{T_0}{T_{r3}}\right)\right| \quad (46)$$

$$\eta_{ex}=\frac{\dot{Q}_{e1}\left|\left(1-\frac{T_0}{T_{r1}}\right)\right|+\dot{Q}_{e2}\left|\left(1-\frac{T_0}{T_{r2}}\right)\right|+\dot{Q}_{e3}\left|\left(1-\frac{T_0}{T_{r3}}\right)\right|}{(W_{comp1}+W_{comp2}+W_{comp3})} \quad (47)$$

3.2 Exergy destruction ratio (EDR)

EDR is the ratio of total exergy destruction in the system to exergy in the product [9] and it is given by Eq. (48). EDR is related to the exergetic efficiency by Eq. (49)

$$EDR=\frac{\dot{E}D_{total}}{\dot{E}P}=\frac{1}{\eta_{ex}}-1 \quad (48)$$

$$\eta_{ex}=\frac{1}{1+EDR} \quad (49)$$

4. Result and Discussion

The method for improving thermal performance of vapour compression refrigeration system using multiple evaporators and compressors with individual or multiple expansion valves have been considered by using first law and second law analysis. Numerical computation was carried out for finding thermal performances vapour compressor refrigeration system with Multiple evaporators at same temperature with single compressor, individual expansion valves of developed models , the following input parameters were considered [9] to verified proposed thermal model.

Table 1(a): System-1: validation of results from developed model Vapour compressor refrigeration system with multiple evaporators at same temperature with single compressor, individual expansion under actual conditions (for compressors efficiency=100%)

Parameters	Model	Ref [9]
First Law Efficiency (COP)	6.196	5.96
Exergy of Fuel (kW)	33.92	35.20

The following data have been taken for numerical computation for table-1(b)

We considered vapour compressor refrigeration system with multiple evaporators at different temperatures with compound compression, individual expansion valves with sub coolers (System-1) for energy-exergy- analysis. To validate computational results from developed thermal model of system-1, the following input values have been taken. The computed results of system-1 for 100% compressors efficiency were compared and shown in Table-3(a) respectively. For

finding thermal performances in terms of first law efficiency (COP), EDR (Exergy Destruction Ratio based on exergy of input) exergetic efficiency using energy-exergy analysis. For finding various exergetic losses (Exergy defects)in terms of irreversibility of system occurred in the components and total exergy destruction in system along with rational efficiency and second law efficiency of the Vapour compressor refrigeration system with Multiple evaporators at different temperatures with compound compression, individual expansion valves are shown in Table-2(a) to Table-2 (c) respectively. It was found that refrigerant R123 gives highest COP and R-245fa give slightly less performances and results are shown in Tables-1(a) to (1(b) for system-2 and Table-1(c) for system-2 .respectively. vapour compressor refrigeration system with Multiple evaporators at different temperatures with multiple compressors, individual expansion valves . We considered vapour compressor refrigeration system with multiple evaporators at different temperatures with compound compression, individual expansion valves with sub coolers (System-2) for energy-exergy-analysis table-1(c). To validate computational results from developed thermal model of system-6, the following input values have been taken. The computed results of system-2 for 100% compressors efficiency were compared and shown in Table-1(a) respectively. For finding thermal performances in terms of first law efficiency (COP), EDR (Exergy Destruction Ratio based on exergy of input) exergetic efficiency using energy-exergy analysis. For finding various exergetic losses (Exergy defects) in terms of irreversibility of system occurred in the components and total exergy destruction in system along with rational efficiency and second law efficiency of the vapour compressor refrigeration system with Multiple evaporators at different temperatures with compound compression, individual expansion valves are shown in Table-2(a) to Table-2 (c) respectively. It was found that refrigerant R123 gives highest COP and R-245fa give slightly less performances

Compressor efficiency_1= Compressor efficiency_2= Compressor efficiency_3=80%) T_{EVA}_1=263"K", T_{EVA}_2=278"K", T_{EVA}_3=283"K", T_R_1=268"K", T_R_2=283"K", T_R_3=288"K", Q_{EVA_1}=70 "kW", Q_{EVA_2}=105"kW",Q_{EVA_3}=35"kW',T_subcooled=303"K"under actual conditions for compressors efficiency=0.80)

Table-1.(b)Thermal Performances (First law efficiency and Second law efficiency, etc.) of vapour compression refrigeration system (System-1) using alternative refrigerants

Refrigerants	First Law Efficiency (COP)	Exergy Destruction Ratio (EDR_{System})	Exergetic Efficiency	Exergy_of Fuel (KW)	Exergy of Product (KW)	Second Law Efficiency
R12	4.953	1.844	0.3447	42.4	14.62	0.6591
R134a	4.905	1.867	0.3414	42.81	14.62	0.6528
R1234yf	4.804	1.915	0.3344	43.71	14.62	0.6393
R1234ze	4.919	1.858	0.3424	44.69	14.62	0.6546
R227ea	4.69	1.98	0.3265	44.77	14.62	0.6242
R236fa	4.822	1.878	0.3405	42.93	14.62	0.6510
R245fa	5.07	1.791	0.3529	41.42	14.62	0.6747
R5.07a	4.586	2.024	0.3192	45.79	14.62	0.6103
R407c	4.036	2.501	0.2809	52.03	14.62	0.5372
R404a	4.498	2.087	0.3131	46.68	14.62	0.5986
R125	4.426	2.114	0.3080	47.45	14.62	0.5889
R123	5.116	1.769	0.3561	41.05	14.62	0.6809
R410a	4.67	1.987	0.3250	44.97	14.62	0.6214
R152a	5.003	1.824	0.3482	41.97	14.62	0.6658
R143a	4.613	2.012	0.3211	45.53	14.62	0.6139
R32	4.689	1.996	0.3263	44.79	14.62	0.624
R290	4.829	1.99	0.3361	43.49	14.62	0.6426
R600	5.037	1.807	0.3506	41.69	14.62	0.6704
R600a	4.941	1.853	0.3439	42.51	14.62	0.6575
R717	4.902	1.902	0.3412	42.51	14.62	0.6524

Table-1(c) Thermal Performances (First law efficiency and Second law efficiency, etc.) of vapour compression refrigeration system (System-2)using alternative refrigerants.

Refrigerants	First law Efficiency (System COP)	EDR	% Exergetic Efficiency	Exergy_Fuel (KW)	Exergy_Product (KW)	Secnd Law Efficiency
R12	4.697	2.195	30.58	36.86	11.27	0.7569
R134a	4.654	2.213	30.35	37.14	11.27	0.7524
R1234yf	4.560	2.253	29.85	37.77	11.27	0.740
R1234ze	4.624	2.199	30.49	36.97	11.27	0.7559
R-32	4.445	2.320	29.23	38.56	11.27	0.7247
R227ea	4.461	2.309	29.32	38.45	11.27	0.7268
R236fa	4.664	2.213	30.45	37.08	11.27	0.7538
R245fa	4.832	2.136	31.34	35.97	11.27	0.7769
R123	4.877	2.118	31.55	35.73	11.27	0.7821

Table-2.(a) Exergy Destruction of various components based on exergy of fuel of vapour compression refrigeration system using alternative refrigerants .

Refrigerants	% loss Eva	% loss valve	% loss Condenser	% loss comp	% Total Losses	Rational Efficiency
R12	9.685	8.071	27.33	18.48	63.67	36.43
R134a	9.559	8.881	26.73	18.57	63.74	36.26
R1234yf	7.834	9.914	27.31	18.97	64.02	35.98
R1234ze	9.186	9.330	26.10	18.99	63.61	36.39
R227ea	8.897	11.99	24.74	19.02	64.64	35.36
R236fa	9.566	9.573	25.75	19.04	63.93	36.07
R245fa	9.889	7.34	27.02	18.96	63.21	36.79
R5.07a	8.968	12.6	24.35	18.68	64.6	35.40
R407c	23.18	4.575	24.76	17.76	70.27	29.73
R404a	10.57	12.04	24.13	18.60	65.34	34.66
R125	8.631	14.79	22.92	18.78	65.12	34.88
R123	9.811	6.553	27.93	18.72	63.01	36.99
R410a	9.499	9.563	27.64	17.89	64.59	35.41
R152a	9.775	7.065	28.57	18.10	63.51	36.49
R143a	9.009	12.04	25.04	18.51	64.61	35.39
R32	9.169	7.854	31.05	17.05	65.13	34.87
R290	9.45	9.611	26.28	18.59	63.93	36.07
R600	9.927	7.349	27.11	18.98	63.37	36.63
R600a	9.662	7.754	26.29	19.01	63.72	36.28
R717	9.571	4.122	35.44	15.78	64.91	35.09

Table-2.(b)Exergy Destruction of various components based on exergy of fuel of vapour compression refrigeration system (System-1)using alternative refrigerants

Refrigerants	% loss Eva	% loss valve	% loss Condenser	% loss comp	Total % Losses	Rational Efficiency
R12	10.86	6.944	30.67	18.56	67.03	0.3297
R134a	10.74	7.614	30.07	18.63	67.06	0.3294
R1234yf	8.731	8.397	31.0	18.97	67.1	0.3290
R1234ze	10.40	7.931	29.56	19.01	66.9	0.3310
R-32	10.29	6.992	33.73	17.29	68.30	0.3120
R227ea	10.07	10.15	28.22	19.02	67.46	0.3254
R236fa	11.87	8.047	29.25	19.04	67.14	0.3286
R245fa	11.14	6.137	30.53	18.99	66.79	0.3321
R123	11.01	5.501	31.43	18.77	66.72	0.3328

Table-2.(c) Exergy Destruction of various components based on Total exergy destruction of vapour compression refrigeration system (System-2)using alternative refrigerants

Refrigerants	% loss Eva	% loss valve	% loss Condenser	% loss comp	%Irreversibility	II Law effectiveness
R12	16.20	10.36	45.75	27.68	67.03	0.3297
R134a	16.02	11.35	44.84	27.78	67.06	0.3294
R1234yf	13.01	12.51	46.2	28.27	67.1	0.3290
R1234ze	15.54	11.86	44.19	28.41	66.9	0.3310
R-32	15.06	10.24	49.39	25.31	68.30	0.3120
R227ea	14.93	15.04	41.83	28.2	67.46	0.3254
R236fa	16.09	11.99	43.57	28.36	67.14	0.3286
R245fa	16.68	9.188	45.71	28.42	66.79	0.3321
R123	16.5	8.245	47.11	28.14	66.72	0.3328

4. Conclusion

Numerical models have been developed for parallel and series expansion valves in the VCR. The comparison of above systems have been done in terms of first law efficiency, second law efficiency and exergy destruction ratio by using R410a, R290, R600, R600a, R1234yf, R502, R404a, R1234ze, R134a and R152a.it was observed that for same degree of sub-cooling, fixed evaporators and condenser temperatures multiple evaporators and compressors with multiple expansion valves system is the best system with comparisons of system with individual expansion valves. The following conclusions were drawn:

(i) Use of HFO refrigerants for Replacing HFC -134a is more significant due to low GWP as compared to R134a of 1430.
(ii) Thermal performances using HFO refrigerants is slightly less than by using R134a although R123 refrigerant gives higher first law efficiency (COP).
(iii) Performances of R600, R152a and R717 better with comparison of other selected refrigerants for system-1 and system-2. But hydrocarbons R290, R600a &R600)are highly flammable and R717 is toxic and R152a is limited to industrial application, so R1234yf and R1234ze are recommended for both systems.
(iv) By altering evaporator load effects thermal performances considerably.
(v) The maximum exergy destruction in the system components it is found maximum (i.e. higher) in the condenser and low in the throttle valves.
(vi) The percentage exergy destruction in the evaporator varies with the type of refrigerants. It becomes high when R236fa is used and lower when R32 is used.
(vii) Energetic and exergetic performance of system-1 is higher than system-2 for selected temperature range of condenser and evaporators for chosen ecofriendly refrigerants.
(viii) System defect in sytem-1 is less as compare with system-2, so system-1 is better system than system-2 for selected refrigerants.
(ix) R407C shows minimum performance in terms of first law efficiency, second law efficiency and system defect in terms of exergy losses for both systems

References

[1] Johnson. E. Global warming from HFC. Environ. Impact Asses.1998; 18:485-492.
[2] R. S. Mishra, Appropriate Vapour CompressionRefrigeration Technologies for Sustainable Development International Journal of Advance Research & Innovations, 2014, 551-556.
[3] K. Chopra, V. Sahni, R. S. Mishra, Methods for improving first and second law efficiencies of vapour compression refrigeration systems using flash intercooler with ecofriendly refrigerants, 1, 2014, 50- 64.
[4] R.Cabello a, E.Torrella b, J.Navarro-Esbr. Experimental evaluation of a vapour compression plant performance using R134a, R407C and R22 as working fluids. Int J Applied Thermal Engineering.2004; 24:1905-1917.
[5] M. Padilla, R. Revellin, J. Bonjour. Exergy analysis of R413A as replacement of R12 in a domestic refrigeration system. Int J Energy Conversion and Management.2010; 51:2195-2201.
[6] S.Kumar, M.Prevost, R.Bugarel- Exergy analysis of a vapour compression refrigeration system. Heat Recovery Systems & CHP.1989;9:151-157.
[7] K. Chopra, V. Sahni, R. S. Mishra, Thermodynamic Analysis of Multiple evaporators vapour compression Refrigeration Systems with R-410a, R290, R1234yf, R502, R404a, R152a and R134a, International Journal of Air conditioning and Refrigeration, 22(1), 2014, 14.
[8] R. S. Mishra, Irriversibility Analysis of MultiEvaporators Vapour Compression Refrigeration Systems Using New and Refrigerants: R134a, R290, R600, R600a, R1234yf,R502, R404a and R152a and R12, R502" International Journal Advance Research & Innovations International Journal of Advance Research & Innovations, 1, 2013, 180-193.
[9] Arora & Domkundwar (2009), Refrigeration and air conditioning, Dhanpat Rai & Sons, New Delhi.

Nomenclature

COP	coefficient of performance (non-dimensional)
VCR	vapour compression refrigeration
CFC	chlorofluorocarbon
HCFC	hydrochlorofluorocarbon
HFC	hydrofluorocarbon
$\dot{Q}$	rate of heat transfer (kW)
$\dot{W}$	work rate (kW)
T	temperature (K)
ΔT_{sc}	degree of subcooling
$\dot{EP}$	exergy rate of product (kW)
TV	throttle valve

φ	dryness fraction(non-dimensional)
EP	evaporator
Ψ	specific enthalpy (kJ/kg)
$\dot{E}D$	rate of exergy destruction (kW)
E_x	exergy rate of fluid (kW)
$\dot{m}$	mass flow rate (kg/s)
s	specific entropy (kJ/kgK)
$\dot{E}F$	exergy rate of fuel (kW)
η	efficiency (non-dimensional)
c	compressor
sc	sub-cooler
ODP	ozone depletion potential
GWP	global warming potential

Subscript

e	evaporator
comp	compressor
o	dead state
II	second law efficiency
r	refrigerant, space to be cooled
TV	throttle valve
sc	sub-cooler
k	kth component
cond	condenser
ev	expansion valve
ex	exergetic

Cite this article as: R.S. Mishra, Energy and exergy analysis of multiple evaporators and compressors with individual or multiple expansion valves vapour compression refrigeration system using ecofriendly refrigerants, *International journal of research in engineering and innovation (IJREI)*, vol 2, issue 6 (2018), 572-580.

Journal of Materiomics xxx (xxxx) xxx

Contents lists available at ScienceDirect

Journal of Materiomics

journal homepage: www.journals.elsevier.com/journal-of-materiomics/

Enhanced thermoelectric performance in p-type ZrCoSb based half-Heusler alloys employing nanostructuring and compositional modulation

Nagendra S. Chauhan [a, b], Sivaiah Bathula [a, b, *], Avinash Vishwakarma [a, b], Ruchi Bhardwaj [a, b], Kishor Kumar Johari [a, b], Bhasker Gahtori [a, b], Ajay Dhar [a, b, **]

[a] Academy of Scientific & Innovative Research (AcSIR), CSIR-National Physical Laboratory, New Delhi 110012, India
[b] Division of Advanced Materials and Devices Metrology, CSIR-National Physical Laboratory, Dr. K. S. Krishnan Marg, New Delhi 110012, India

ARTICLE INFO

Article history:
Received 30 July 2018
Received in revised form
31 October 2018
Accepted 1 November 2018
Available online xxx

Keywords:
Half Heuslers
Iso-electronic
Waste heat recovery
Mid-temperature
Efficiency
Compositional modulation

ABSTRACT

ZrCoSb based half-Heusler (HH) alloys have been widely studied as a p-type thermoelectric (TE) material for power generation applications in the mid-temperature regime. However, their intrinsically high thermal conductivity has been found to be detrimental for the improvement in their thermoelectric figure-of-merit (ZT), which presently is far below unity. In the current work, a state-of-the-art *ZT* ~1.1 at 873 K was realized in an optimized composition of nanostructured $Zr_{1-x}Hf_xCoSb_{0.9}Sn_{0.1}$ HH alloys by employing compositional modulation i.e. grain-by-grain compositional variations, which leads to a substantial increase in its power factor coupled with a concurrent decrease in its thermal conductivity. Significant reduction in the phonon mean-free-path is observed on Hf substitution, which is comparable to the average crystallite size (~25 nm), thus leading to a very low thermal conductivity of ~2.2 $W m^{-1}K^{-1}$ at 873 K, which is amongst the lowest reported in HH alloys. The TE device characteristics, estimated using cumulative temperature dependence model for quantitative evaluation of TE performance, yielded an output power density of ~10 Wcm^{-2} with a leg efficiency of ~10% in the optimized composition of nanostructured $Zr_{1-x}Hf_xCoSb_{0.9}Sn_{0.1}$ HH alloys, which is comparable to the reported efficiencies of other state-of-the-art TE materials.

1. Introduction

In energy production worldwide, approximately two-third of the energy remains unutilized and discharged in the form of waste heat [1]. Waste heat recovery using a thermoelectric (TE) materials is a promising avenue which provides a convenient means for reliable, sustainable and scalable power generation by harnessing the waste heat [2,3]. As energy materials, TE materials have been developed by various schemes which mutually aims to improve TE energy conversion efficiency by maximizing the Seebeck coefficient, (α), and balancing the competing requirements of high electrical conductivity, (σ) and low thermal conductivity, (κ) at the absolute temperature (T). The thermoelectric figure-of-merit (ZT), represents a useful metric which characterizes the energy conversion of a thermoelectric material and is given as [4,5] $ZT = \left(\frac{\alpha^2\sigma}{\kappa}\right)T$. The ZT of a material provides a qualitative measure of its TE performance, as the direct evaluation of efficiency and output power generation is rather tedious and time-consuming. However, numerical and analytical methods presents a possibility to theoretically estimate intrinsic efficiency and output power. In this context, the Cumulative Temperature Dependence (CTD) model, based on overall temperature dependence of materials properties at given temperature boundary conditions provide a reliable approximation of thermoelectric materials and devices performance [6,7]. Such an estimate provides valuable insights of material's TE conversion potential and various factors contributing towards inefficiencies in a TE device.

The half-Heusler (HH) class of thermoelectric materials with

* Corresponding author. Academy of Scientific & Innovative Research (AcSIR), CSIR-National Physical Laboratory, New Delhi-110012, India.
** Corresponding author. Corresponding author. Academy of Scientific & Innovative Research (AcSIR), CSIR-National Physical Laboratory, New Delhi-110012, India.
E-mail addresses: sivaiahb@nplindia.org (S. Bathula), adhar@nplindia.org (A. Dhar).

Peer review under responsibility of The Chinese Ceramic Society.

https://doi.org/10.1016/j.jmat.2018.11.003

high mechanical strength, non-toxicity and high thermal stability have been widely explored as potential candidates for TE power generation in the mid-temperature regime [8–10]. There exist numerous possible combination by which HH [11,12] alloys can be formed, among which ZrNiSn [13–17] (n-type), TiNiSn [18,19] (n-type), ZrCoSb [20–22] (p-type), TiCoSb [23] (p-type) and NbFeSb [24] (p-type) have been widely studied. Although ZT > 1 has already been realized in n-type HHs, the p-type HH alloys are still being explored for replicating the superior performance of their electron-doped n-type counterparts. In this context, ZrCoSb based alloys have been widely studied by over-compensating hole-doping (via. proper substitution and doping at Zr, Co and/or Sb sites) [20,25,26] and have displayed compatibility with the n-type HH on secondary metrics such as thermal expansion coefficient and long-term thermal and mechanical stability. However, their high thermal conductivity (κ) has remained a major limitation, reduction of which has long remained the main focus for enhancing TE performance of HH alloys.

The enhancement of ZT in HH alloys employing elemental substitution of Ti, and/or Hf on Zr site [27–29], Co by Fe [30], Ir [28], or Rh [29], and Sb by Sn [25,27–29,31] has been previously reported. Despite employing several alloying strategies in HH alloys the highest ZT ≤ 0.8 has been achieved thus far in p-type ZrCoSb HH alloys [20,32,33]. It suggested that finer grain samples with average grain size less than 100 nm is desirable for further strengthening of the phonon scattering to achieve maximal reduction in thermal conductivity [33], while 10% Sn substitution at Sb site is optimal for attaining higher power factor [25]. In general, advanced material strategies include simultaneous integration of effective schemes together in a material [34]. While traditional approach of uniform doping or alloying have been widely studied for tuning the Fermi level and carrier concentration optimization, it was found to be detrimental to carrier mobility. Recently prospects of compositional modulation doping scheme was demonstrated as an advanced scheme for ZT enhancement by carrier mobility promotion [35,36]. Thus, subsuming nanostructuring paradigm in the compositionally modulated p-type ZrCoSb HH is a worthy prospect for realization of enhancing its TE performance.

In the current study, we report a state-of-the-art ZT ~1.1 at 873 K in an optimized composition of $Zr_{1-x}Hf_xCoSb_{0.9}Sn_{0.1}$ based p-type HH alloys synthesized employing high energy ball milling of pulverized arc-melted ingots followed by spark plasma sintering. This enhancement in ZT is due to the synergistic integration of nanostructuring and iso-electronic alloying for attaining compositional modulation i.e. grain-by-grain compositional variations, which leads to an enhanced scattering of heat-carrying phonons and the favourable tuning of electrical transport properties. In addition, the TE conversion characteristics of synthesized thermoelectric unicouple material was quantitatively estimated using the CTD model. The as-sintered samples were structurally characterised employing XRD, HR-TEM and FE-SEM, based on which the enhancement in their TE performance has been discussed.

2. Experimental details

High purity elemental Zr (foil, 99.97%), Hf (powder, 99.99%), Co (powder, 99.97%), Sb (shots, 99.999%) and Sn (shots, 99.999%) were weighed in stoichiometric amount according to their nominal compositions $Zr_{1-x}Hf_xCoSb_{0.9}Sn_{0.1}$ (where x = 0–0.5), and arc melted in argon atmosphere. The arc melted ingots (~5 g) were flipped and re-melted multiple times to ensure homogeneity. The ingots were then subsequently broken into small pieces and grounded to a fine powder using mortar and pestle and milled to finer grain size using high energy mechanical ball milling (HEBM, Fritsch, Pulverisette-4) at 300 rpm for 12 h with ball-to-powder weight ratio of 20:1. The grinding jars (250 ml) and balls (diameter: 5 mm) used in which are made of hardened stainless steel. The resulting nano-powders were loaded into the graphite die with an inner diameter of 12.7 mm and compacted by spark plasma sintering at 1473 K under 50 MPa in a vacuum to obtained bulk dense pellets. The density of the as-sintered samples measured using Archimedes method was found to be ~98.4% of the theoretical density.

The Seebeck coefficient (α) and electrical resistivity (σ) were measured simultaneously employing commercial equipment (ULVAC, ZEM3) over the temperature range of 323 K–873 K on samples of polished bars of about $3 \times 2 \times 10\ mm^3$. Thermal diffusivity (D) was measured in the range 323–873 K using a laser flash technique (Lineseis, LFA 1000) on disk-shaped specimens of diameter 12.7 mm and thickness of 2.0 mm sprayed with a layer of graphite in order to minimize errors due to emissivity. Specific heat (Cp) was measured using a differential scanning calorimetry (DSC) instrument. The accuracies in transport measurement are: ± 6% for thermal diffusivity, ± 7% for electrical conductivity, ± 7% for Seebeck coefficient, ± 10% for specific heat and ± 0.5% for density. The carrier concentration and mobility were determined using Hall Effect Measurement System (HEMS, Nano-magnetics), under a magnetic field of 0.5T. The constituent phases were determined by X-Ray Diffractometer (XRD; Rigaku Mini Flex II) using Cu Kα radiation (λ = 1.5406 Å). The morphology and elemental ratios of the samples are characterised by a field-emission scanning electron microscope (FE-SEM, Zeiss; Model: Supra 40VP), while microstructural analysis was carried out using High resolution transmission electron microscopy (HRTEM model: Tecnai G2F30 STWIN operated at the electron accelerating voltage of 300 kV).

3. Results and discussion

3.1. Phase composition and microstructure

Fig. 1(a) represents the crystal structure of the synthesized $Zr_{1-x}Hf_xCoSb_{0.9}Sn_{0.1}$ HH alloy, which consists of four inter-penetrating face centered cubic (FCC) sub-lattices where the Zr, Co and Sn/Sb atoms occupy the Wyckoff positions (0, 0, 0), (¼, ¼, ¼) and (½, ½, ½), while the fourth sub-lattice located at (¾, ¾, ¾) remains vacant and the Sb atom is partially replaced by Sn [25]. XRD pattern of the synthesized $Zr_{1-x}Hf_xCoSb_{0.9}Sn_{0.1}$ HH alloy for different compositions are shown in Fig. 1(b). The diffraction peaks of all compositions are well-indexed to the cubic half-Heusler $ZrCoSb_{0.9}Sn_{0.1}$ (PDF4+: 04-015-2508) with the space group $F\bar{4}3m$ [25] with no noticeable impurity phases. The estimated lattice parameters of all samples with different Hf/Zr ratios were plotted with respect to the Hf concentration in the $Zr_{1-x}Hf_xCoSb_{0.9}Sn_{0.1}$ HH alloy and are shown in Fig. 1(c). The lattice parameter was found to linearly decrease with increasing Hf content, following the Vegard's law suggesting complete incorporation of Hf in the HH matrix. The average crystallite size, as determined using Williamson Hall method [37] by employing the XRD data (Fig. 1(b)), was found to be around ~20 nm (Table 1) for all the synthesized HH alloys.

The FE-SEM images of a typical synthesized $Zr_{0.8}Hf_{0.2}CoSb_{0.9}Sn_{0.1}$ HH alloy is shown in Fig. 2(a–c), which reveals a densely packed microstructure, as an outcome of rapid heating rates attained by spark plasma sintering, which prevents grain growth and result in high densification. The equiaxed microstructure at low (Fig. 2(b) and higher (Fig. 2(c)) magnification exhibits nano-grained microstructure with the fine crystallites ~ 10–30 nm, which are in close agreement to that estimated using the XRD data (Fig. 1(b)). Additionally, an equiaxed microstructure at low and higher magnification of another synthesized

Please cite this article as: Chauhan NS et al., Enhanced thermoelectric performance in p-type ZrCoSb based half-Heusler alloys employing nanostructuring and compositional modulation, Journal of Materiomics, https://doi.org/10.1016/j.jmat.2018.11.003

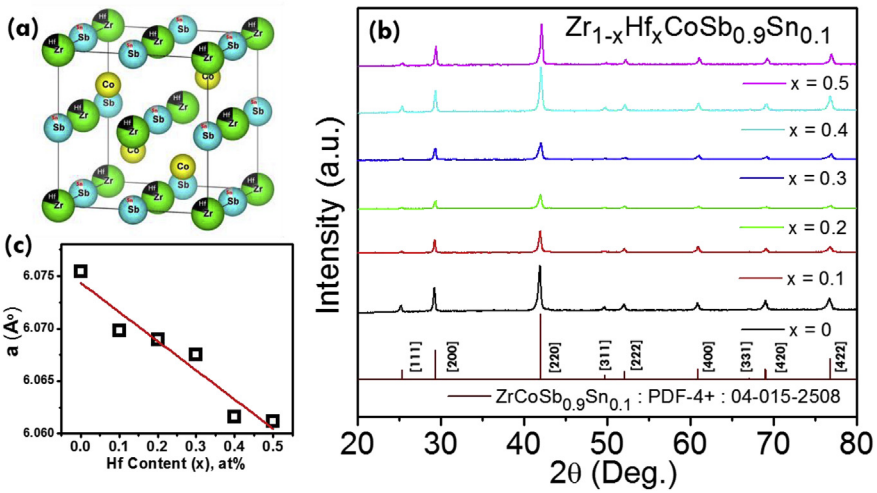

Fig. 1. Structural parameters of the synthesized $Zr_{1-x}Hf_xCoSb_{0.9}Sn_{0.1}$ (x = 0–0.5) half-Heusler alloys (a) Atomic Structure, (b) XRD patterns for different compositions, and (c) Lattice constant variation with composition.

Table 1
Room temperature physical parameters of half-Heusler $Zr_{1-x}Hf_xCoSb_{0.9}Sn_{0.1}$ (x = 0–0.5).

Parameters		x = 0	x = 0.1	x = 0.2	x = 0.3	x = 0.4	x = 0.5
Hall Coefficient R_H ($m^3\ C^{-1}$)		1.6×10^{-8}	8.3×10^{-8}	9.4×10^{-8}	1.1×10^{-8}	9.7×10^{-8}	8.6×10^{-8}
Carrier Concentration n (cm^{-3})		3.9×10^{20}	7.5×10^{19}	6.6×10^{19}	5.4×10^{19}	6.4×10^{19}	7.3×10^{19}
Hall Mobility μ ($cm^2\ V^{-1}\ s^{-1}$)		15	73	94	125	115	112
Effective Mass		$3.68m_e$	$1.33m_e$	$1.23m_e$	$1.08m_e$	$1.14m_e$	$1.17m_e$
Average Carrier MFP (Å)		26.6	15.8	19.4	24.0	23.4	23.7
Average Phonon MFP (nm)	323K	27.3	15.5	11.3	9.5	8.2	7.6
	873K	14.0	9.3	6.7	5.3	5.4	6.2
Average Crystallite Size (nm)		22	20	22	21	22	23
E_F (meV)		52.9	48.9	48.5	47.9	51.3	54.2

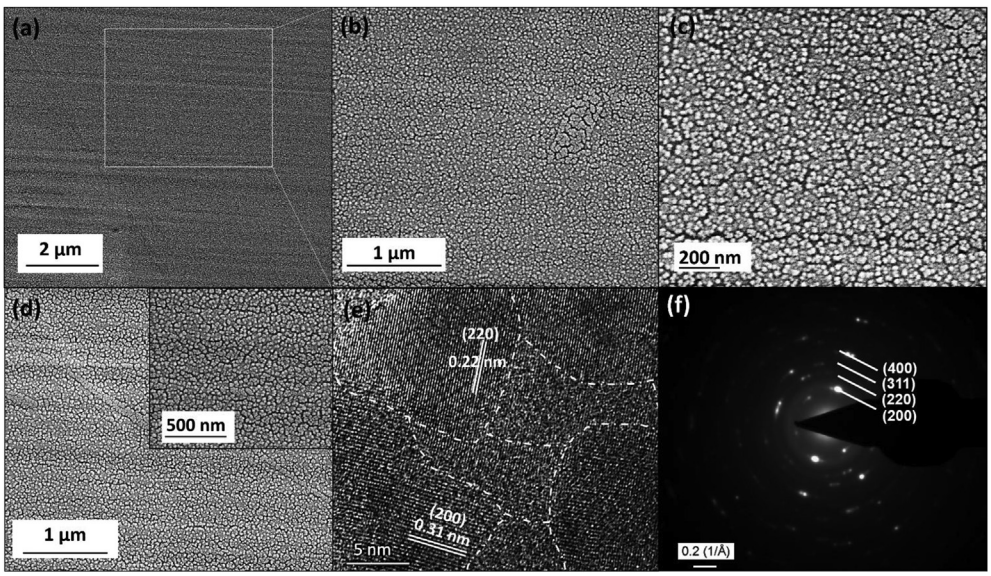

Fig. 2. FE-SEM image of typical $Zr_{0.8}Hf_{0.2}CoSb_{0.9}Sn_{0.1}$ half-Heusler alloy at (a) Low-magnification showing dense microstructure and at (b–c) high magnification indicating nanostructured morphology; (d) FE-SEM image of $Zr_{0.7}Hf_{0.3}CoSb_{0.9}Sn_{0.1}$ half-Heusler alloy at low and high magnification. HR-TEM micrographs showing (e) lattice scale image of nanostructured $Zr_{0.8}Hf_{0.2}CoSb_{0.9}Sn_{0.1}$, exhibiting the presence of different orientations of the crystallographic planes and their interface boundaries image, and its corresponding (f) Selected area electron diffraction pattern (SAED) confirming polycrystalline half-Heusler phase.

Please cite this article as: Chauhan NS et al., Enhanced thermoelectric performance in p-type ZrCoSb based half-Heusler alloys employing nanostructuring and compositional modulation, Journal of Materiomics, https://doi.org/10.1016/j.jmat.2018.11.003

HH alloys ($Zr_{0.7}Hf_{0.3}CoSb_{0.9}Sn_{0.1}$) is shown in Fig. 2(d), which also confirms the presence of nanosized grains.

To further investigate the microscopic features in the representative $Zr_{0.8}Hf_{0.2}CoSb_{0.9}Sn_{0.1}$ HH alloy, HR-TEM analysis was performed in real and reciprocal space. Fig. 2(e), presents the obtained lattice scale image of nanostructured $Zr_{0.8}Hf_{0.2}CoSb_{0.9}Sn_{0.1}$ for a single particle. The image indicates the presence highly crystalline nanograins having different orientations of the crystallographic planes and their interface boundaries, which reveals the polycrystalline nature of individual particles. It can be seen that particles consist of grains up to 20 nm in size, similar to the size of the obtained nanostructured powder after ball milling, indicating insignificant grain growth during spark plasma sintering. This also agrees fairly well with the size calculated from the XRD spectra (Fig. 1(b)). A corresponding selected area electron diffraction pattern (SAED) recorded for Fig. 2(e), is shown in Fig. 2(f), which also reveals the presence of atomic planes of HH (hkl: 200, 220, 311 and 400) in the reciprocal space.

Overall, the low magnification FESEM micrographs (Fig. 2(a) – (d)) suggests that the synthesized HH samples are quite dense without any evidence of porosity or cracks, which is also supported by the high magnification HR-TEM lattice image (Fig. 2(e)) and the measured density of the synthesized HH sample (~98.4% of the theoretical density). This is primarily due to the sintering employing SPS, which is known not only to result in dense samples but also maintain the nanoscale features post-sintering.

Furthermore, the microstructure at higher magnification of the representative HH alloy ($Zr_{0.8}Hf_{0.2}CoSb_{0.9}Sn_{0.1}$) alongwith its elemental mapping is shown in Fig. 3 (a). The microstructure exhibited nanostructured morphology whose elemental mapping, clearly indicates the signatures of the constituent elements with Hf-rich and Hf-deficient regions heterogeneously distributed within the HH matrix (marked as region 1 & 2 in the figure). The variation in the stoichiometry in these two region was examined using energy-dispersive x-ray spectroscopy (EDX) and the resulting spectrum is shown in Fig. 3 (b), and quantitatively tabulated in Fig. 3(c). These observations quantitatively confirm the grain-by-grain compositional variations and presence of Hf-rich and Hf-deficient regions, heterogeneously distributed throughout the sample. Such compositionally modulated samples, although single-phase, behave similar to phase-separated composite material that exhibit grain-by-grain compositional variations, thus leading to an enhancement in the electrical transport properties, which is discussed in the forthcoming section.

3.2. Thermoelectric transport properties

The temperature dependence of TE transport properties of the synthesized $Zr_{1-x}Hf_xCoSb_{0.9}Sn_{0.1}$ HH alloys for different compositions are depicted in Fig. 4. All the samples exhibit a p-type degenerate semiconducting behaviour indicated by the positive values of α and decreasing σ with increasing temperature shown in Fig. 4(a, b). Furthermore, the σ increases with increasing content of Hf, while α initially increases up to a composition $x = 0.3$ in $Zr_{1-x}Hf_xCoSb_{0.9}Sn_{0.1}$ exhibiting a maximum value of ~255 μV/K at 873 K and decreases thereafter. The effect of Hf substitution on the electrical transport can be understood in terms of the Hall data, as shown in Table 1. The measured hall coefficient for the base composition $ZrCoSb_{0.9}Sn_{0.1}$ was found to be in similar order with high carrier concentrations (~10^{20}/cm^3) as reported previously for similar Sn content [31]. It is well known that any substitution, at such high levels of carrier concentration, tends to cause strong ionized impurity scattering of charge carriers, which severely limits the carrier mobility and electronic conductivity. However, it was previously reported [38,39] that very high carrier mobility can be attained via. modulating doping by minimizing the ionized impurity scattering. A typical modulation doped material contains heavily doped regions and undoped regions within the material,

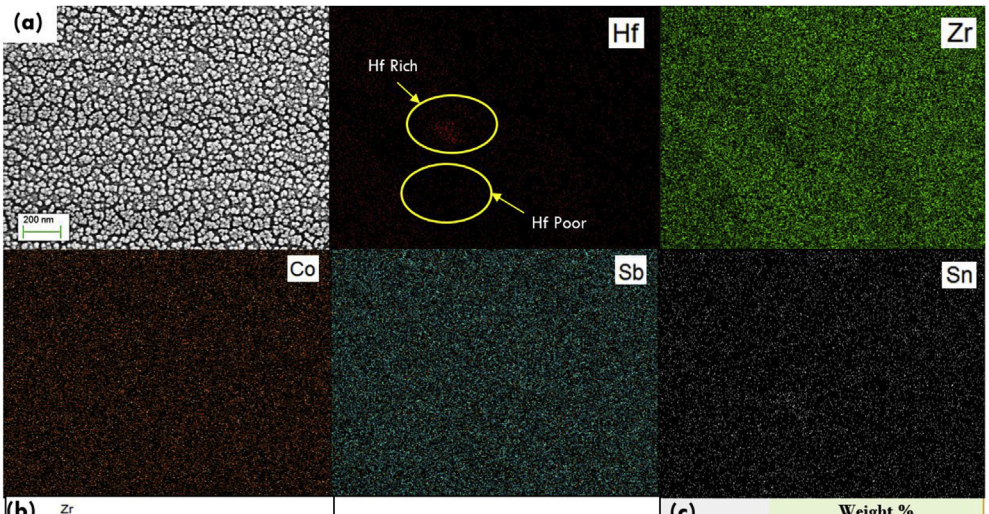

(c)

Element	Weight % Region 1	Region 2
Zr	24.63	20.63
Hf	11.65	16.04
Co	27.04	26.63
Sb	35.29	35.20
Sn	1.39	1.50

Fig. 3. (a) FE-SEM image exhibiting the nano-sized grains alongwith elemental distribution of constituent elements and (b, c) EDS analysis; of the synthesized $Zr_{0.8}Hf_{0.2}CoSb_{0.9}Sn_{0.1}$ half-Heusler alloys.

Please cite this article as: Chauhan NS et al., Enhanced thermoelectric performance in p-type ZrCoSb based half-Heusler alloys employing nanostructuring and compositional modulation, Journal of Materiomics, https://doi.org/10.1016/j.jmat.2018.11.003

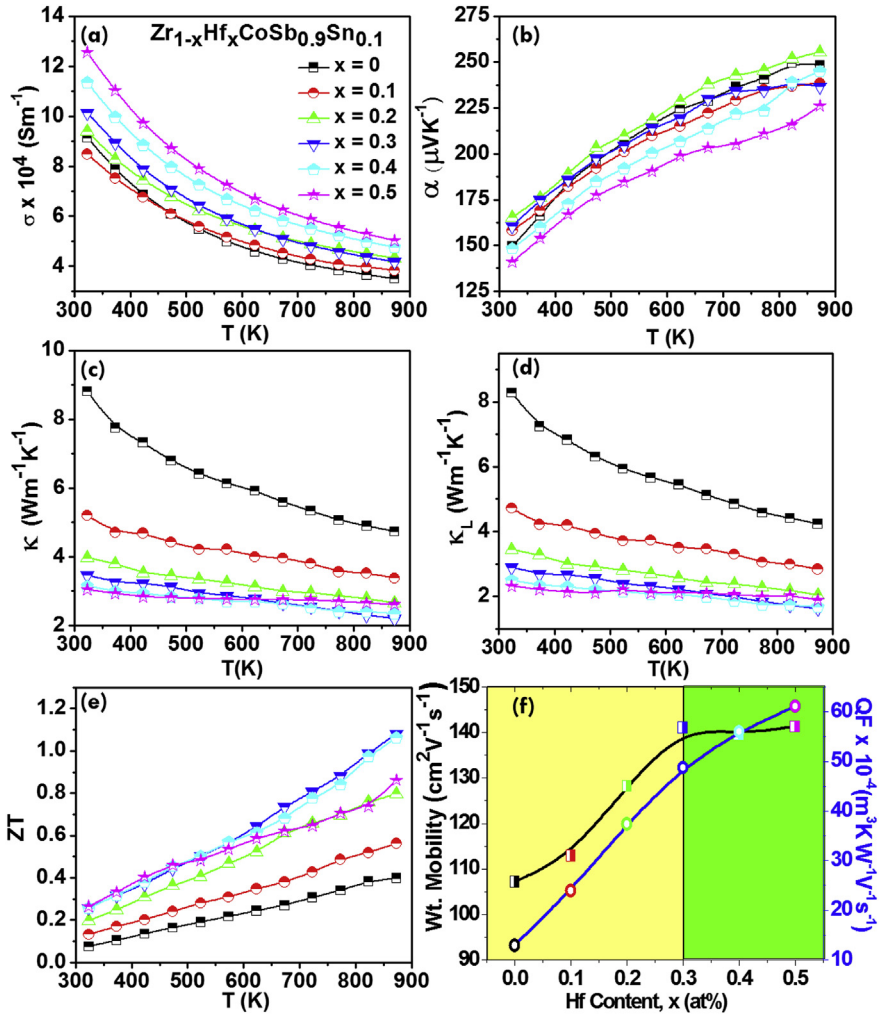

Fig. 4. Temperature dependence of thermoelectric transport properties of $Zr_{1-x}Hf_xCoSb_{0.9}Sn_{0.1}$ (x = 0–0.5) half-Heusler alloys (a) Electrical Conductivity; (b) Seebeck coefficient; (c) Total thermal conductivity; (d) Lattice thermal conductivity; (e) Thermoelectric figure of merit (ZT) and (f) Weighted mobility and Quality factor as a function of Hf concentration.

and remote doping is provided by heavily doped regions to the active undoped region. In our synthesized HH samples, it was observed (Fig. 3) that non-uniform distributions of Hf (dopant) atoms results in heavily doped Hf-rich regions and undoped Hf-deficient regions, heterogeneously distributed within the HH matrix.

It is apparent from Table 1 that with increasing Hf substitution the carrier concentration decreases drastically due to carrier scattering up to x = 0.3, and increases thereafter. While in contrast, the carrier mobility exhibits an increasing trend. The Hall data thus suggests the occurrence of a carrier filtering mechanism, which may be due to the grain-by-grain compositional variation in the synthesized HH alloys owing to the presence of Hf-rich and Hf-deficient regions within the HH matrix. As a result of this, a significant increase in the carrier mobility at lower Hf composition (x < 0.3) was observed, wherein the Hf-rich regions provide the high mobility carriers to the active undoped regions, resulting in an improved carrier mobility (Table 1). The compositional modulation approach thus mitigates the detrimental effects of Hf substitution on the carrier mobility, especially at high carrier concentrations.

As shown in Fig. 4(a), the σ of the all Hf substituted samples are higher than that of the pristine counterpart ($ZrCoSb_{0.9}Sn_{0.1}$), which suggest that despite a decrease in carrier concentration at lower concentration of Hf substitution, the increase in the carrier mobility results in an overall improvement of σ. However, the decrease in the carrier mobility at higher Hf content was subjugated by an increase in the carrier concentration. To further elucidate the electrical transport features of synthesized HH alloys, the carrier dependency of Fermi energy ($E_F = \frac{\pi^2 k_B^2 T}{3e\alpha}$), effective mass $\left(m^* = \frac{3eh^2\alpha}{8\pi^2 k_B^2 T}\left(\frac{3p}{\pi}\right)^{3/2}\right)$ and average carrier mean free path ($MFP = \sqrt{2E_F m^*}\frac{\mu}{e}$) were estimated using the experimental Seebeck coefficient data [40]. Table 1 show the calculated values of E_F, m^* and carrier MFP, whose variation trends are consistent with corresponding changes in α and σ observed in this study (Fig. 4(a and b)).

The temperature dependence of the total thermal conductivity (κ) and the lattice thermal conductivity ($κ_l$) of the synthesized HH samples is presented in Fig. 4(c & d), respectively. The $κ_l$ was obtained using $κ_l = κ - κ_e$, where the electronic thermal conductivity ($κ_e$) is calculated using the Wiedemann–Franz Law as $κ_e = L\sigma T$ (where L is the Lorenz number, estimated using the temperature dependent Seebeck coefficient data [41]. A value of κ ~2.2 W $m^{-1}K^{-1}$ at 873 K was observed in the optimized HH compositions $Zr_{1-x}Hf_xCoSb_{0.9}Sn_{0.1}$ (x = 0.3–0.4), which is amongst the lowest reported in p-type HH alloys thus far [21,32,33]. On comparing Fig. 4(c and d) it can be inferred that the major contribution comes to the κ originates from $κ_l$. The FE-SEM image

Please cite this article as: Chauhan NS et al., Enhanced thermoelectric performance in p-type ZrCoSb based half-Heusler alloys employing nanostructuring and compositional modulation, Journal of Materiomics, https://doi.org/10.1016/j.jmat.2018.11.003

(Fig. 4(a)) indicates that the synthesized HH alloys comprise of nanoscale crystallites (~10–30 nm) with a high density of nanocrystallite boundaries, which scatter heat-carrying phonons thereby leading to a substantial reduction in κ_l, which majorly contributes to the reduction in κ of the HH alloys. The nanostructuring contributes effectively in reducing the κ_l of pristine as well as the Hf-substituted HH samples, although this contribution is much higher at lower temperatures. Further, mass fluctuations owing to a large atomic mass difference between Zr and Hf also contribute towards lowering of the κ.

To further understand the phonon dynamics, the average phonon mean free path (MFP) was estimated using $l = 3\kappa_l/C_v u$ [42,43] where C_v , u and l represents the specific heat at constant volume, average phonon velocity and mean free path, respectively. The estimated average phonon MFP (shown in Table 1) which is substantially lowered than those reported earlier for similar HH compositions [44–47]. Table 1 also indicates that the phonon MFP decreases substantially with increasing Hf substitution although the crystallite size varies marginally. This suggest that Hf-substitution additionally contributes towards reduction in the phonon MFP, by creating defect scattering for phonons due to mass fluctuation and strain field fluctuation. Additionally, has also been reported earlier that in HH alloys most of the heat is transported by phonons with MFP in the range ~0.6–30 nm [48] and the calculated phonon MFP of our synthesized HH samples (Table 1) lie in this phonon-scattering favourable range, which also explains the significantly low κ in our HH samples. Thus, the compositional modulation in the synthesized $Zr_{1-x}Hf_xCoSn_{0.9}Sn_{0.1}$ HH alloys demonstrates the effectiveness of Hf substitution and nanostructuring in suppressing the κ_l.

3.3. Thermoelectric performance and compatibility factor

As shown in Fig. 4(e), a maximum ZT of ~1.1 was achieved at 873 K in the optimized p-type HH composition of $Zr_{1-x}Hf_xCoSn_{0.9}Sn_{0.1}$ (at $x = 0.3$, 0.4), which is the state-of-the-art value for p-type HH alloys, higher than those previously reported for ZrCoSb [20,25,27,29,31–33,49] and comparable to TiCoSb [21,23,49] and FeNbSb [50–52] based HH alloys. Such enhancement corresponds to ~170% increase in ZT compared to base composition $ZrCoSb_{0.9}Sn_{0.1}$ and is also comparable to the other actively explored p-type TE materials [53–56]. This enhancement in ZT is due to the synergistic contribution of nanostructuring as well as substitutional alloying, however it is rather tedious to separate their individual contribution. Additionally, the weighted mobility, $\mu_w = \mu\,(m^*/m_e)^{3/2}$ and TE quality factor $QF = \mu(m^*/m_e)^{3/2}\kappa_l^{-1}$, which primarily determines the optimal electrical performance, was also estimated and is shown in Fig. 4(f). This figure indicates that both the weighted mobility and TE quality factor increase with increasing Hf content and suggests $Zr_{0.7}Hf_{0.3}CoSn_{0.9}Sn_{0.1}$ as the optimized HH composition at which ZT exhibits a maxima.

The relationship between ZT and energy conversion efficiency (η_{max}) based on cumulative temperature dependence (CTD) of the thermoelectric transport properties formulated by Kim et al. [6,7] was used for reliable prediction of the TE performance of the synthesized HH alloys. The engineering figure-of-merit $(ZT)_{eng}$, as direct indicators, which exhibit linear correlations to efficiency is shown in Fig. 5(a). In all the Hf-substituted samples, an improvement in $(ZT)_{eng}$ was observed when compared with pristine $ZrCoSb_{0.9}Sn_{0.1}$ sample. The output power density (P_d) at the maximum efficiency estimated using the CTD model is expressed as [57] $P_d = \frac{(PF)_{eng}\,(T_H - T_C)^2}{4L}$. Where, L is the length of the TE material, T_h is the temperature at the hot junction and T_c the temperature at the cold junction. Considering, $T_H = 323$ K and leg length = 2 mm, a cubic-shaped TE leg is assumed for comparison with the output power prediction reported previously [6,7] for state-of-the-art p-type TE material (including SnSe, $MnSi_{1.78}$, $Pb_{0.98}Te_{0.75}Se_{0.25}K_{0.02}$). The calculated P_d as shown in Fig. 5(b), indicates enhancement in P_d of all the Hf-substituted samples, reaching a maximum of 10 Wcm^{-2}. The output power density is dependent on the TE leg's dimensions as well as the material properties whereas the efficiency is determined only by the material's characteristics.

Conventionally, the maximum efficiency of a TE device is

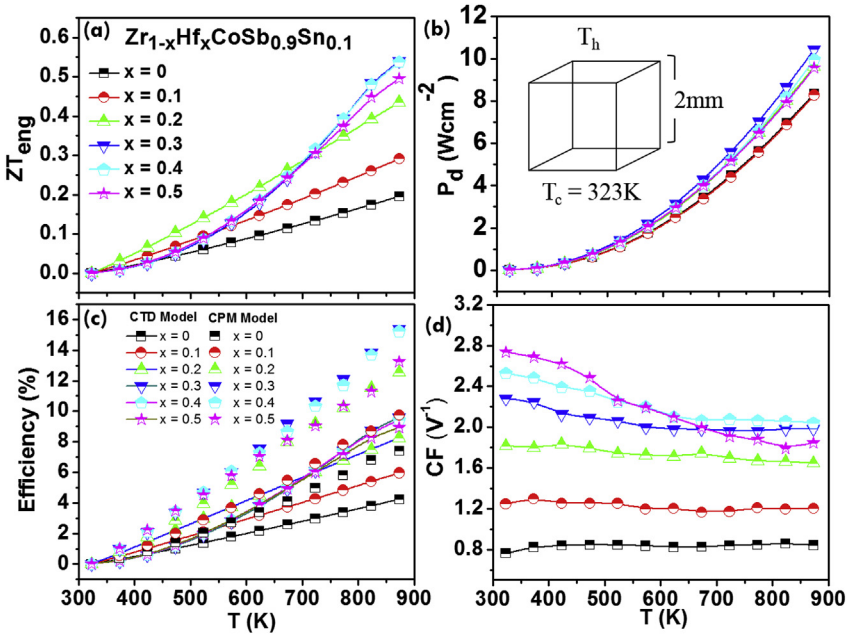

Fig. 5. Theoretically estimated TE device parameters of $Zr_{1-x}Hf_xCoSb_{0.9}Sn_{0.1}$ ($x = 0$–0.5) half-Heusler alloys (a) Engineering Thermoelectric figure of Merit; (b) Output Power Density; (c) Thermoelectric efficiency and (d) Compatibility factor.

Please cite this article as: Chauhan NS et al., Enhanced thermoelectric performance in p-type ZrCoSb based half-Heusler alloys employing nanostructuring and compositional modulation, Journal of Materiomics, https://doi.org/10.1016/j.jmat.2018.11.003

generally derived based on a constant property model (CPM) [6]. Fig. 5 (c) shows the efficiency prediction using CPM and CTD model with the temperature boundary condition that T_h increases while T_c is kept constant at 323 K [6]. It is reported that the calculation by CPM model overestimates the efficiency which is found to be almost twice of the efficiency calculated using the CTD model [6]. As shown in Fig. 5(c), maximum efficiency of ~10% for p-type was obtained using CTD model which represents significant TE conversion which is comparable to those reported earlier [6,7] for state-of-the-art p-type TE material (including SnSe, $MnSi_{1.78}$, $Pb_{0.98}Te_{0.75}Se_{0.25}K_{0.02}$) by the CTD model. As explicit indicators of TE performance, the output power density and efficiency provide a viewpoint for the applicability of the synthesized materials in TE devices, however, due to the device related issues such as, contact resistance and heat losses, the actual TE performance, is expected to be lower than the theoretical estimates.

The efficacy of segmentation, proposed for increasing the TE efficiency, is estimated using TE compatibility factor (CF) given as [58], $CF = \frac{\sqrt{1+ZT}-1}{\alpha T}$. From the applicability viewpoint, difference in compatibility factors for the two TE materials should be less than a factor of 2. Fig. 5(d) shows the calculated CF of synthesized TE materials, which increases with increasing temperature and is significantly enhanced compared to the pristine $ZrCoSb_{0.9}Sn_{0.1}$, while being comparable to the other state-of-the-art p-type TE materials such as TAGS, PbTe, $CeFe_4Sb_{12}$, SnTe etc. [59]. Thus, the synthesized p-type HH alloys could be a suitable TE material for segmentation with various TE materials for achieving highly efficient TE based power generation in the mid-temperature regime.

4. Conclusion

A state-of-the-art ZT ~1.1 at 873 K was achieved by integrating alloying and nanostructuring to attain compositional modulation i.e. grain-by-grain compositional variations in p-type ZrCoSb-based HH alloys. The HH alloys were synthesized using high-energy ball-milling of the arc-melted ingots, followed by the spark plasma sintering of the resulting HH alloy nano-powders. The efficacy of Hf-substitution and nanostructuring has been experimentally realized to attain a very low thermal conductivity, which enhances the ZT in ZrCoSb-based Half-Heusler TE alloys, making them promising candidates for mid-temperature power generation applications. The fundamental understanding of cumulative temperature dependence on thermoelectric characteristics of the materials is also presented using CTD model to enable better understanding of rational materials selection and device engineering to achieve higher thermoelectric conversion efficiency.

Conflicts of interest

Authors declare that there are no conflicts of interest.

Acknowledgements

The authors acknowledge the Board of Research in Nuclear Sciences, India for the financial support under the Scheme: 37(3)/14/22/2016-BRNS with BSC. Nagendra S. Chauhan acknowledges CSIR- Senior Research Fellowship. (Grant No : 31/001(0430)/2014-EMR-1)The technical support rendered by Dr. Vidya Nand Singh, Mr. Radhey Shyam, and Mr. Naval Kishor Upadhyay is also gratefully acknowledged.

Appendix A. Supplementary data

Supplementary data to this article can be found online at https://doi.org/10.1016/j.jmat.2018.11.003.

References

[1] Gingerich DB, Mauter MS. Quantity, quality, and availability of waste heat from United States thermal power generation. Environ Sci Technol 2015;49:8297–306.
[2] Bell LE. Cooling, heating, generating power, and recovering waste heat with thermoelectric systems. Science 2008;321:1457–61.
[3] LeBlanc S. Thermoelectric generators: linking material properties and systems engineering for waste heat recovery applications. Sustainable Materials and Technologies 2014;1:26–35.
[4] Snyder GJ, Toberer ES. Complex thermoelectric materials. Nat Mater 2008;7:105–14.
[5] Zebarjadi M, Esfarjani K, Dresselhaus M, Ren Z, Chen G. Perspectives on thermoelectrics: from fundamentals to device applications. Energy Environ Sci 2012;5:5147–62.
[6] Kim HS, Liu W, Chen G, Chu C-W, Ren Z. Relationship between thermoelectric figure of merit and energy conversion efficiency. Proc Natl Acad Sci Unit States Am 2015;112:8205–10.
[7] Kim HS, Liu W, Ren Z. The bridge between the materials and devices of thermoelectric power generators. Energy Environ Sci 2017;10:69–85.
[8] Zhu T, Fu C, Xie H, Liu Y, Zhao X. High efficiency half-heusler thermoelectric materials for energy harvesting. Advanced Energy Materials 2015;5.
[9] Chen S, Ren Z. Recent progress of half-Heusler for moderate temperature thermoelectric applications. Mater Today 2013;16:387–95.
[10] Poon SJ, Wu D, Zhu S, Xie W, Tritt TM, Thomas P, Venkatasubramanian R. Half-Heusler phases and nanocomposites as emerging high-ZT thermoelectric materials. J Mater Res 2011;26:2795–802.
[11] Graf T, Felser C, Parkin SS. Simple rules for the understanding of Heusler compounds. Prog Solid State Chem 2011;39:1–50.
[12] Bos J-WG, Downie RA. Half-Heusler thermoelectrics: a complex class of materials. J Phys Condens Matter 2014;26:433201.
[13] Chauhan NS, Bathula S, Vishwakarma A, Bhardwaj R, Gahtori B, Kumar A, Dhar A. Vanadium doping induced resonant energy levels for the enhancement of thermoelectric performance in Hf-free ZrNiSn half-heusler alloys. ACS Appl Energy Mater 2018;1(2):757–64.
[14] Chen S, Lukas KC, Liu W, Opeil CP, Chen G, Ren Z. Effect of Hf concentration on thermoelectric properties of nanostructured N-type half-heusler materials HfxZr1−xNiSn0. 99Sb0. 01. Advanced Energy Materials 2013;3:1210–4.
[15] Bhardwaj A, Chauhan N, Sancheti B, Pandey G, Senguttuvan T, Misra D. Panoscopically optimized thermoelectric performance of a half-Heusler/full-Heusler based in situ bulk composite Zr 0.7 Hf 0.3 Ni 1+ x Sn: an energy and time efficient way. Phys Chem Chem Phys 2015;17:30090–101.
[16] Chauhan NS, Bathula S, Vishwakarma A, Bhardwaj R, Gahtori B, Srivastava AK, Saravanan M, Dhar A. A nanocomposite approach for enhancement of thermoelectric performance in Hafnium-free Half-Heuslers. Materialia 2018;1:168–74.
[17] Chauhan NS, Bathula S, Vishwakarma A, Bhardwaj R, Johari KK, Gahtori B, Saravanan M, Dhar A. Compositional tuning of ZrNiSn half-Heusler alloys: thermoelectric characteristics and performance analysis. J Phys Chem Solid 2018;123:105–12.
[18] Bhattacharya S, Pope A, Littleton IV R, Tritt TM, Ponnambalam V, Xia Y, Poon S. Effect of Sb doping on the thermoelectric properties of Ti-based half-Heusler compounds, TiNiSn 1− x Sb x. Appl Phys Lett 2000;77:2476–8.
[19] Misra D, Rajput A, Bhardwaj A, Chauhan N, Singh S. Enhanced power factor and reduced thermal conductivity of a half-Heusler derivative Ti9Ni7Sn8: a bulk nanocomposite thermoelectric material. Appl Phys Lett 2015;106:103901.
[20] Chauhan NS, Bhardwaj A, Senguttuvan T, Pant R, Mallik R, Misra D. A synergistic combination of atomic scale structural engineering and panoscopic approach in p-type ZrCoSb-based half-Heusler thermoelectric materials for achieving high ZT. J Mater Chem C 2016;4:5766–78.
[21] Yan X, Liu W, Chen S, Wang H, Zhang Q, Chen G, Ren Z. Thermoelectric property study of nanostructured p-type half-heuslers (Hf, Zr, Ti) CoSb0. 8Sn0. 2. Advanced Energy Materials 2013;3:1195–200.
[22] Chauhan NS, Bathula S, Vishwakarma A, Bhardwaj R, Johari KK, Gahtori B, Dhar A. Facile fabrication of p-and n-type half-Heusler alloys with enhanced thermoelectric performance and low specific contact resistance employing spark plasma sintering. Mater Lett 2018;228:250–3.
[23] Yan X, Liu W, Wang H, Chen S, Shiomi J, Esfarjani K, Wang H, Wang D, Chen G, Ren Z. Stronger phonon scattering by larger differences in atomic mass and size in p-type half-Heuslers Hf 1− x Ti x CoSb 0.8 Sn 0.2. Energy Environ Sci 2012;5:7543–8.
[24] Joshi G, He R, Engber M, Samsonidze G, Pantha T, Dahal E, Dahal K, Yang J, Lan Y, Kozinsky B. NbFeSb-based p-type half-Heuslers for power generation applications. Energy Environ Sci 2014;7:4070–6.
[25] Sekimoto T, Kurosaki K, Muta H, Yamanaka S. High-thermoelectric figure of merit realized in p-type half-Heusler compounds: ZrCoSnxSb1-x. Jpn J Appl Phys 2007;46:L673.
[26] Rausch E, Balke B, Ouardi S, Felser C. Enhanced thermoelectric performance in the p-type half-Heusler (Ti/Zr/Hf) CoSb 0.8 Sn 0.2 system via phase separation. Phys Chem Chem Phys 2014;16:25258–62.
[27] Culp SR, Simonson J, Poon SJ, Ponnambalam V, Edwards J, Tritt TM. (Zr, Hf) Co

(Sb, Sn) half-Heusler phases as high-temperature (> 700° C) p-type thermoelectric materials. Appl Phys Lett 2008;93, 022105.
[28] Takas NJ, Shabetai MR, Poudeu PF. Effect of Sn doping on the thermoelectric performance of the complex p-type Zr0. 5Hf0. 5Co0. 3Ir0. 7Sb1−ySn y half-heusler system. Sci Adv Mater 2011;3:571−6.
[29] Maji P, Takas NJ, Misra DK, Gabrisch H, Stokes K, Poudeu PF. Effects of Rh on the thermoelectric performance of the p-type Zr 0.5 Hf 0.5 Co 1− xRhxSb 0.99 Sn 0.01 half-Heusler alloys. J Solid State Chem 2010;183:1120−6.
[30] Hsu C-C, Ma H-K. Microstructure and thermoelectric properties in Fe-doped ZrCoSb half-Heusler compounds. Mater Sci Eng, B 2015;198:80−5.
[31] Yuan B, Wang B, Huang L, Lei X, Zhao L, Wang C, Zhang Q. Effects of Sb substitution by Sn on the thermoelectric properties of ZrCoSb. J Electron Mater 2017;46:3076−82.
[32] He R, Kim HS, Lan Y, Wang D, Chen S, Ren Z. Investigating the thermoelectric properties of p-type half-Heusler Hf x (ZrTi) 1− x CoSb 0.8 Sn 0.2 by reducing Hf concentration for power generation. RSC Adv 2014;4:64711−6.
[33] Yan X, Joshi G, Liu W, Lan Y, Wang H, Lee S, Simonson J, Poon S, Tritt T, Chen G. Enhanced thermoelectric figure of merit of p-type half-Heuslers. Nano Lett 2010;11:556−60.
[34] Zhou X, Yan Y, Lu X, Zhu H, Han X, Chen G, Ren Z. Routes for high-performance thermoelectric materials, Materials Today 2018.
[35] Berry T, Fu C, Auffermann G, Fecher GH, Schnelle W, Serrano-Sanchez F, Yue Y, Liang H, Felser C. Enhancing thermoelectric performance of TiNiSn half-heusler compounds via modulation doping. Chem Mater 2017;29:7042−8.
[36] Wang J, Zhang B-Y, Kang H-J, Li Y, Yaer X, Li J-F, Tan Q, Zhang S, Fan G-H, Liu C-Y. Record high thermoelectric performance in bulk SrTiO3 via nano-scale modulation doping. Nanomater Energy 2017;35:387−95.
[37] Williamson G, Hall W. X-ray line broadening from filed aluminium and wolfram. Acta Metall 1953;1:22−31.
[38] Yu B, Zebarjadi M, Wang H, Lukas K, Wang H, Wang D, Opeil C, Dresselhaus M, Chen G, Ren Z. Enhancement of thermoelectric properties by modulation-doping in silicon germanium alloy nanocomposites. Nano Lett 2012;12:2077−82.
[39] Pei Y-L, Wu H, Wu D, Zheng F, He J. High thermoelectric performance realized in a BiCuSeO system by improving Carrier mobility through 3D modulation doping. J Am Chem Soc 2014;136:13902−8.
[40] Zhu T, Gao H, Chen Y, Zhao X. Ioffe−Regel limit and lattice thermal conductivity reduction of high performance (AgSbTe 2) 15 (GeTe) 85 thermoelectric materials. J Mater Chem 2014;2:3251−6.
[41] Kim H-S, Gibbs ZM, Tang Y, Wang H, Snyder GJ. Characterization of Lorenz number with Seebeck coefficient measurement. Apl Mater 2015;3, 041506.
[42] Cahill DG, Braun PV, Chen G, Clarke DR, Fan S, Goodson KE, Keblinski P, King WP, Mahan GD, Majumdar A. Nanoscale thermal transport. II. 2003−2012. Appl Phys Rev 2014;1, 011305.
[43] Kittel C. Interpretation of the thermal conductivity of glasses. Phys Rev 1949;75:972.
[44] Zhu T, Fu C, Xie H, Liu Y, Feng B, Xie J, Zhao X. Lattice thermal conductivity and spectral phonon scattering in FeVSb-based half-Heusler compounds. EPL (Europhysics Letters) 2013;104:46003.
[45] Hermet P, Jund P. Lattice thermal conductivity of NiTiSn half-Heusler thermoelectric materials from first-principles calculations. J Alloy Comp 2016;688:248−52.
[46] Sharp J, Poon S, Goldsmid H. Boundary scattering and the thermoelectric figure of merit. Phys Status Solidi 2001;187:507−16.
[47] Bhattacharya S, Skove M, Russell M, Tritt T, Xia Y, Ponnambalam V, Poon S, Thadhani N. Effect of boundary scattering on the thermal conductivity of TiNiSn-based half-Heusler alloys. Phys Rev B 2008;77:184203.
[48] Fu C, Liu Y, Xie H, Liu X, Zhao X, Jeffrey Snyder G, Xie J, Zhu T. Electron and phonon transport in Co-doped FeV0. 6Nb0. 4Sb half-Heusler thermoelectric materials. J Appl Phys 2013;114:134905.
[49] Rausch E, Balke B, Stahlhofen JM, Ouardi S, Burkhardt U, Felser C. Fine tuning of thermoelectric performance in phase-separated half-Heusler compounds. J Mater Chem C 2015;3:10409−14.
[50] Fu C, Zhu T, Liu Y, Xie H, Zhao X. Band engineering of high performance p-type FeNbSb based half-Heusler thermoelectric materials for figure of merit zT> 1. Energy Environ Sci 2015;8:216−20.
[51] Fu C, Zhu T, Pei Y, Xie H, Wang H, Snyder GJ, Liu Y, Liu Y, Zhao X. High band degeneracy contributes to high thermoelectric performance in p-type half-heusler compounds. Advanced Energy Materials 2014;4.
[52] Yu J, Fu C, Liu Y, Xia K, Aydemir U, Chasapis TC, Snyder GJ, Zhao X, Zhu T. Unique role of refractory Ta alloying in enhancing the figure of merit of NbFeSb thermoelectric materials. Advanced Energy Materials 2018;8:1701313.
[53] Bathula S, Jayasimhadri M, Gahtori B, Singh NK, Tyagi K, Srivastava A, Dhar A. The role of nanoscale defect features in enhancing the thermoelectric performance of p-type nanostructured SiGe alloys. Nanoscale 2015;7:12474−83.
[54] Prasad KS, Rao A, Tyagi K, Chauhan NS, Gahtori B, Bathula S, Dhar A. Enhanced thermoelectric performance of Pb doped Cu2SnSe3 synthesized employing spark plasma sintering. Phys B Condens Matter 2017;512:39−44.
[55] Prasad KS, Rao A, Chauhan NS, Bhardwaj R, Vishwakarma A, Tyagi K. Thermoelectric properties of p-type sb-doped Cu2SnSe3 near room and mid temperature applications. Appl Phys A 2018;124:98.
[56] Upadhyay NK, Kumaraswamidhas L, Gahtori B, Bathula S, Muthiah S, Shyam R, Chauhan NS, Bhardwaj R, Dhar A. Enhancement in thermoelectric performance of bulk CrSi 2 dispersed with nanostructured SiGe nanoinclusions. J Alloy Comp 2018;765:412−7.
[57] He R, Kraemer D, Mao J, Zeng L, Jie Q, Lan Y, Li C, Shuai J, Kim HS, Liu Y. Achieving high power factor and output power density in p-type half-Heuslers Nb1-xTixFeSb. Proc Natl Acad Sci Unit States Am 2016;113:13576−81.
[58] Snyder GJ, Ursell TS. Thermoelectric efficiency and compatibility. Phys Rev Lett 2003;91:148301.
[59] Snyder GJ, Caillat T. Using the compatibility factor to design high efficiency segmented thermoelectric generators. In: MRS Online Proceedings Library Archive; 2003. p. 793.

Mr. Nagendra Singh Chauhan is a CSIR-Senior Research Fellow at CSIR-National Physical Laboratory, New Delhi, India registered for Ph.D at the Academy of Scientific and Innovative Research (AcSIR), India. He received his M.Tech (Material Science & Technology) degree from Maulana Azad National Institute of Technology, India and his B.E (Mechanical) degree from Savitribai Phule Pune University, India. His current research interests focuses on advanced energy materials and devices for power generation.

Dr. Bathula Sivaiah is a Ph.D (Applied Physics) from Delhi Technological University, India and is currently working as Senior Scientist at CSIR-National Physical Laboratory, India. He received his M.Tech (Materials and Metallurgical Engineering) from Indian Institute of Technology (IIT), Kanpur, and B.Tech (Materials and Metallurgical Engineering) from National Institute of Technology (NIT), Warangal. He is also a Faculty at the Academy of Scientific and Innovative Research (AcSIR), India. He has published more than 50 research papers in scientific journals and presented his research work in more than 10 national and international conferences.

Mr. Avinash Vishwakarma is a Junior Research Fellow at CSIR-National Physical Laboratory, New Delhi, India registered for Ph.D at the Academy of Scientific and Innovative Research (AcSIR), India. He received his Master and Bachelor degree in Science from Banaras Hindu University, India. His current research interest focuses on half-Heusler thermoelectric materials.

Ms. Ruchi Bhardwaj is a Junior Research Fellow at CSIR-National Physical Laboratory, New Delhi, India registered for Ph.D at the Academy of Scientific and Innovative Research (AcSIR), India. She received her M.Sc. degree in Physics from Chaudhary Charan Singh University, Campus, Meerut in 2014. Her current area of research is on thermoelectric materials and has published several research papers in prestigious journals.

Mr. Kishor Kumar Johari is a CSIR-Junior Research Fellow at CSIR-National Physical Laboratory, New Delhi, India registered for Ph.D at the Academy of Scientific and Innovative Research (AcSIR), India. He received his Master and Bachelor degree in Science from M.J.P. Rohilkhand University, Bareilly India. His current research interest lies is in understanding the thermoelectric behaviour of half-Heusler based alloys.

Please cite this article as: Chauhan NS et al., Enhanced thermoelectric performance in p-type ZrCoSb based half-Heusler alloys employing nanostructuring and compositional modulation, Journal of Materiomics, https://doi.org/10.1016/j.jmat.2018.11.003

Dr. Bhasker Gahtori received his Ph.D. degree from Jamia Millia Islamia University, New Delhi in 2010 and is presently working as Scientist in Materials Physics and Engineering Division at CSIR-National Physical Laboratory, India. His current research is focused on Thermoelectric and Magnetic materials. He has published more than 30 research papers in scientific journals and presented his research work in more than 10 national and international conferences.

Prof. Ajay Dhar is an Associate Director (Student Affairs) at Academy of Scientific and Innovative Research (AcSIR), India. He holds Masters Degrees in Science and Philosophy and a doctorate from University of Delhi, India. He was a Chief Scientist & Head (Advance Material & Devices Division) at the CSIR-National Physical Laboratory, New Delhi, India. Dr. Dhar was earlier a post-doctoral fellow and later a visiting faculty at Queen's University, Canada. His current research interests among other include the development of cost-effective and non-toxic materials for efficient thermoelectric devices and rare-earth free permanent magnets.

Please cite this article as: Chauhan NS et al., Enhanced thermoelectric performance in p-type ZrCoSb based half-Heusler alloys employing nanostructuring and compositional modulation, Journal of Materiomics, https://doi.org/10.1016/j.jmat.2018.11.003

Intelligent model for solar energy forecasting and its implementation for solar photovoltaic applications

Gulnar Perveen, M. Rizwan, and Nidhi Goel

Citation: Journal of Renewable and Sustainable Energy **10**, 063702 (2018); doi: 10.1063/1.5027824
View online: https://doi.org/10.1063/1.5027824
View Table of Contents: http://aip.scitation.org/toc/rse/10/6
Published by the American Institute of Physics

Intelligent model for solar energy forecasting and its implementation for solar photovoltaic applications

Gulnar Perveen,[1,a)] M. Rizwan,[2,b)] and Nidhi Goel[3,c)]
[1]*Department of Electronics and Communication Engineering, Delhi Technological University, Delhi 110042, India*
[2]*Department of Electrical Engineering, Delhi Technological University, Delhi 110042, India*
[3]*Department of Electronics and Communication Engineering, IGDTUW, Delhi 110006, India*

(Received 6 March 2018; accepted 12 October 2018; published online 13 November 2018)

As the demand for renewable energy is surging day-by-day, the solar energy data are important for applications in the field of solar photovoltaic (PV) systems. However, there exists a challenge in the collection of data owing to expensive instruments and a limited number of meteorological stations. In addition, the output of the system is largely affected due to variation in sky-conditions; therefore, an intelligent model based on sky-conditions is essential for estimating global solar energy so as to meet the energy requirements. In this work, the sky-based model employing fuzzy logic modelling has been developed and presented to forecast global solar energy using the dew-point as the meteorological parameter along with other known available parameters, namely, sunshine duration, wind speed, ambient temperature, and relative humidity for different sky-conditions, namely, clear sky (type-a), hazy sky (type-b), partially foggy/cloudy sky (type-c), and fully foggy/cloudy sky (type-d) respectively. Simulations have been performed for five meteorological stations across India that represents distinct climate zones such as composite, warm and humid, hot and dry, cold and cloudy, and moderate climate zone respectively, and the performance of the proposed model has been evaluated by using statistical indicators. The applicability of the proposed sky-based model employing fuzzy logic modelling can further be exploited for solar PV systems. The model is implemented in 210 W PV modules in forecasting the power output of solar photovoltaic systems in different sky-conditions. The obtained results reveal that the systems employing fuzzy logic modelling can be implemented for a wide range of applications and provide benefits. Furthermore, to check for accuracy of the proposed model, a comparative analysis has been carried out with the Angstrom model using statistical indicators. The value of the results, however, shows the supremacy of the proposed fuzzy logic prediction model. *Published by AIP Publishing*. https://doi.org/10.1063/1.5027824

NOMENCLATURE

a,b	coefficients [Eq. (A5)] (dimensionless)
e_i	i_{th} estimated data (dimensionless)
G_{sc}	solar constant (W/m^2)
G_T	solar irradiance at standard test condition (STC) (W/m^2)
H_g	global solar radiation (MJ/m^2)
H_o	extraterrestrial solar radiation on horizontal surface (MJ/m^2)
I_s	short circuit current of photovoltaic module at STC (A)

[a)]Email: gulegulnar@gmail.com.
[b)]Author to whom correspondence should be addressed: rizwan@dce.ac.in, Tel.: +91 9891558821
[c)]nnidhi.iitr@gmail.com

L	measured data
L_{max}	highest value of relevant set of data
L_{min}	lowest value of relevant set of data
L_s	normalized/scaled data
m_i	i_{th} measured data (dimensionless)
MPE	mean percentage error (%)
N_{PVP}	photovoltaic arrays in parallel (number)
N_{PVS}	photovoltaic arrays in series (number)
N_{OCT}	temperature of solar panel (^oC)
P_{max}	maximum power of photovoltaic module at maximum power point (MPP) (W)
P_{PV}	output of photovoltaic array in power at MPP (W)
$P_{PV,STC}$	the rated power output of photovoltaic single array at MPP (W)
RMSE	root mean square error (dimensionless)
S	measured sunshine duration (hours)
S_o	maximum possible sunshine duration (hours)
T_{amb}	ambient temperature (°C)
T_d	desired temperature (°C)
T_j	temperature of solar panel (°C)
V_{oc}	open circuit voltage of photovoltaic module at STC (V)
x	number of observed data (dimensionless)
X_{max}	maximum limit of normalized range
X_{min}	minimum limit of normalized range

Greek Symbols

Φ	latitude of the site (^{o})
ω_s	mean sunrise hour angle (^{o})
n_{day}	number of days of the year starting from 1st January (dimensionless)
η_o	optical efficiency (%)
δ	solar declination angle (^{o})
γ	temperature parameter at MPP

I. INTRODUCTION

Due to the growing population of the world, there is a surge in the demand for energy—specifically electricity. The production of electricity contributes the largest share in the emission of greenhouse gases that emanate from the burning of fossil fuel. So, a need has arisen for the clean form of energy, i.e., renewable energy that can contribute to the demand for energy worldwide. Major sources of renewable energy include wind, solar, biomass, and hydro, among which solar energy is the easily foreseeable and predictable form of renewable energy with no greenhouse gas emissions during its generation and its natural flow is also intense as compared to global solar energy use.

In recent times, India has emerged as one of the leading destinations for solar energy based research and applications due to the formation of ISA (International Solar Alliance) in 2016, which is headquartered at NISE (National Institute of Solar Energy). India has influenced many investors from developed countries to excel in the area of solar energy generation. More than 121 countries have joined ISA to exploit the potential of solar energy, thereby reducing the dependence on fossil fuels.

Solar energy is an important parameter for solar photovoltaic applications but the measurement devices of such parameters are not easily available at many of the meteorological centres due to limited spatial coverage and the high cost of the instruments. Therefore, it is viable to forecast global solar energy for such locations where measurements have not been done using meteorological parameters.

Many grid-connected solar power plants have been built using photovoltaics.[1] However, due to the variation in sky conditions, the output of the system is nondeterministic and stochastic. Therefore, an accurate estimation of global solar energy is required for different sky conditions as the accuracy of the system output is greatly affected by the external environmental factors like clouds, dust, moisture, and temperature differences in the atmosphere.

Many previous research studies have focused on providing a forecasting tool in order to predict the photovoltaic power output with good accuracy.[2–5] Most of them were based on autoregressive,[6] autoregressive moving average,[7] and Markov chain.[8] However, such nondeterministic models are inaccurate and found with errors as they are based on the probability estimation. In fact, predicting global solar energy by such models is not easy as it is dependent on mathematical functions. So, to overcome such a drawback, intelligent techniques[9] have been employed for modelling and estimating the solar energy.[10]

Several previous papers have dealt with intelligent modelling techniques, i.e., fuzzy logic based model applied to meteorology. Most of them deal with meteorological predictions like the circulation pattern by fuzzy c-mean,[11] and fuzzy classification of clouds.[12] The concept of fuzzy set theory has been introduced by Zadeh for forecasting solar energy from one of the commonly used parameters like the sunshine duration.[13] Various models have been proposed based on fuzzy modelling of solar irradiance.[14,15] In the past, models have been proposed using the cloudiness index and air temperature data for estimating global solar energy.[16] Fuzzy logic modelling has been proposed for predicting solar energy by using meteorological parameters for clear sky conditions.[17] Most of the previous research studies are based on clear or sunny sky conditions; however, very few literature studies are there that discussed sky-based model like hazy sky, foggy sky, and cloudy sky conditions for predicting global solar energy by employing fuzzy logic modelling.

The objective of the present work is to (i) establish the sky-based model by employing intelligent modelling to estimate global solar energy for each day of the month, defined as clear/sunny sky (type-a), hazy sky (type-b), partially foggy/cloudy sky (type-c), and fully foggy/cloudy sky (type-d) conditions, respectively, using the dew-point as one of the meteorological parameters along with other known available parameters, namely, the sunshine duration, relative humidity, wind speed, and ambient temperature, (ii) carry out simulation for five meteorological stations across India that represents distinct climate zones such as composite, warm and humid, hot and dry, cold and cloudy, and moderate climate zone, respectively, (iii) the performance of the developed sky-based model has been derived by carrying out the comparative analysis of measured data with the estimated data using statistical error tests, (iv) the results obtained by employing the fuzzy logic technique have been further implemented in 210 W HIT (Heterojunction with intrinsic thin layer) PV modules for predicting system power output at maximum power point (MPP) tracking, and (v) further, comparison has been drawn with empirical regression models using statistical indicators to check for accuracy and supremacy of the developed model.

This work is arranged as follows. The methodology where the collection of meteorological data and its normalization is carried out along with mentioning the sky conditions is presented in Sec. II. Section III presents the fuzzy logic modelling for estimating global solar energy. Section IV carries out its implementation for the solar photovoltaic application. Section V is developed to statistical evaluations. Section VI presents results and discussions. Section VII discusses the comparison of the fuzzy logic based model with the Angstrom model. Section VIII brings the conclusion which is followed by Appendix and references.

II. METHODOLOGY

A. Meteorological data

In this work, the recorded hourly data averaged month-wise from the year 2006 to 2016 have been considered which is obtained from IMD (Indian Meteorological Department), NISE (National Institute of Solar Energy), and in collaboration with NIWE (National Institute of Wind Energy).[18,19] The measured data at the meteorological sites include parameters such as

the dew-point,, sunshine duration, global solar radiation, wind speed, ambient temperature, and relative humidity respectively.

The measured data have been obtained for 24 h of duration as per IST (Indian Standard Time). The parameter such as sunshine hours is measured by means of the Campbell-Stokes sunshine recorder and the measurement is done during the availability of sunshine from dawn to dusk as per LAT (Local Apparent Time). Ambient temperature is recorded by using a bimetallic thermograph, and a hygrometer is used to measure the relative humidity and dew point. An electrical anemograph is commonly used to measure wind speed whereas a pyranometer is used to measure global solar energy.

India possesses variation in climates, ranging from hot zones to cold zones with locations of high altitude. The main determining parameters for classifying the climate zones such as relative humidity, ambient temperature, and wind speed are those that most affect the heat exchange between the human body and the surroundings. The two other parameters like solar radiation and dew-point are those that influence the building design.

The criteria for allocating the location to these climate zones depend on weather conditions which prevail for more than 6 months. Based on this condition, Bansal and Minke in 1988 presented the climate zone by evaluating the average of the mean monthly climate data from the 233 different meteorological stations and made it possible to partition/divide the country into five distinct climatic zones as shown in Table I.[20]

B. Normalization

Normalization of the input parameters, namely, sunshine hours, ambient temperature, relative humidity, and wind speed, has been done so to avoid convergence issues and defined in the range of 0.1–0.9 expressed by Eq. (1). The normalization of these parameters has been obtained for five meteorological stations across India and is shown in Tables II–VI

$$\mathrm{Ls} = \left(\left(\left(\frac{\mathrm{X_{max}} - \mathrm{X_{min})}}{(\mathrm{L_{max}} - \mathrm{L_{min})} \right) * (\mathrm{L} - \mathrm{L_{min}}) \right) + \mathrm{X_{min}} \right), \tag{1}$$

where L is the measured data, L_s is the scaled data, L_{max} is the highest value of the relevant set of data, L_{min} is the lowest value of the relevant set of data, X_{max} is the maximum limit of the normalized range, and X_{min} is the minimum limit of the normalized range.

C. Classification of sky conditions

In this work, the sky-based models can be classified as follows:[21]

1. Sunny/clear sky (type-a)

If the duration of the sunshine hour is equivalent to or greater than 9 hour, and the diffuse component of solar energy is equivalent to or lower than 25% of global solar energy.

TABLE I. Climatic zone.

Climate zone	Latitude (°N)	Longitude (°E)	Meteorological station	Ambient temperature (°C)	Relative humidity (%)	No. of clear days
Composite	28.61	77.2	New Delhi, Delhi	This condition prevails when 6 months or more does not occur within any of the below mentioned category.		
Warm and humid	13.08	80.27	Chennai, Tamil Nadu	>30	>55	<20
Hot and dry	26.28	73.02	Jodhpur, Rajasthan	>30	<55	>20
Cold and cloudy	25.56	91.88	Shillong, Meghalaya	<25	>55	<20
Moderate	18.52	73.85	Pune, Maharashtra	25–30	<75	<20

TABLE II. Meteorological data and their normalization for the composite climate zone (Delhi).

	Global solar radiation (MJ/m^2)		Sunshine hours (h)		Ambient temperature (°C)		Relative humidity (%)		Wind speed (m/s)		Dew-point (°C)	
Month	Measured	Normalized	Measured	Normalized	Measured	Normalized	Measured	Normalized	Measured	Normalized	Measured	Normalized
Jan	15.41	0.34	7.85	0.66	16.06	0.45	63.99	0.46	3.20	0.31	7.58	0.52
Feb	30.21	0.61	7.94	0.59	21.55	0.67	59.94	0.45	3.83	0.42	9.07	0.38
Mar	37.41	0.48	7.34	0.71	26.79	0.44	41.00	0.50	3.98	0.36	11.48	0.69
Apr	40.81	0.67	9.22	0.72	34.21	0.55	21.08	0.51	4.19	0.47	10.84	0.40
May	36.32	0.59	8.85	0.64	35.08	0.59	34.66	0.43	4.28	0.41	15.30	0.60
Jun	32.24	0.63	7.60	0.58	34.92	0.48	47.96	0.55	4.11	0.43	21.93	0.55
Jul	24.58	0.53	4.74	0.38	30.32	0.51	78.49	0.53	2.99	0.50	25.92	0.62
Aug	29.00	0.55	5.93	0.52	29.80	0.53	81.26	0.43	3.55	0.50	26.09	0.57
Sep	34.36	0.66	6.68	0.55	31.24	0.63	61.93	0.32	3.08	0.39	22.77	0.41
Oct	31.28	0.65	9.33	0.71	29.87	0.55	43.95	0.34	3.16	0.44	15.41	0.39
Nov	25.44	0.60	7.20	0.55	24.26	0.71	40.82	0.26	2.93	0.40	8.88	0.37
Dec	23.11	0.72	5.81	0.60	19.21	0.59	61.10	0.42	2.78	0.38	10.09	0.41

TABLE III. Meteorological data and their normalization for the warm and humid climate zone (Chennai, Tamil Nadu).

	Global solar radiation (MJ/m^2)		Sunshine hours (h)		Ambient temperature (°C)		Relative humidity (%)		Wind speed (m/s)		Dew-Point (°C)	
Month	Measured	Normalized	Measured	Normalized	Measured	Normalized	Measured	Normalized	Measured	Normalized	Measured	Normalized
Jan	36.72	0.63	8.94	0.70	27.60	0.65	66.31	0.46	4.43	0.42	16.66	0.66
Feb	42.05	0.54	9.74	0.77	28.80	0.54	68.18	0.57	4.58	0.49	21.80	0.72
Mar	42.90	0.79	9.05	0.66	29.66	0.72	68.90	0.48	5.55	0.47	23.52	0.62
Apr	45.11	0.42	9.37	0.61	31.21	0.73	70.92	0.55	7.45	0.48	25.55	0.68
May	38.89	0.70	8.83	0.63	32.21	0.69	58.13	0.57	6.15	0.57	20.61	0.70
Jun	31.35	0.54	7.61	0.64	31.50	0.61	50.16	0.54	5.21	0.43	15.38	0.51
Jul	34.56	0.56	6.77	0.55	31.15	0.51	64.27	0.55	5.40	0.43	22.66	0.72
Aug	33.74	0.63	5.24	0.53	31.50	0.59	61.22	0.45	5.33	0.57	16.88	0.64
Sep	32.47	0.59	6.16	0.58	30.53	0.61	68.07	0.44	4.59	0.54	21.68	0.71
Oct	35.38	0.66	6.94	0.60	30.61	0.67	61.85	0.41	4.15	0.46	18.11	0.62
Nov	34.61	0.62	6.78	0.61	28.21	0.73	67.61	0.50	4.94	0.45	17.32	0.65
Dec	29.99	0.68	7.30	0.62	26.88	0.72	74.83	0.50	5.68	0.21	17.88	0.65

TABLE IV. Meteorological data and their normalization for the hot and dry climate zone (Jodhpur, Rajasthan).

Month	Global solar radiation (MJ/m^2)		Sunshine hours (h)		Ambient temperature (°C)		Relative humidity (%)		Wind speed (m/s)		Dew-Point (°C)	
	Measured	Normalized	Measured	Normalized	Measured	Normalized	Measured	Normalized	Measured	Normalized	Measured	Normalized
Jan	29.40	0.71	9.23	0.68	21.87	0.54	52.68	0.40	2.96	0.41	11.11	0.52
Feb	25.88	0.58	9.71	0.69	23.29	0.40	43.37	0.32	3.67	0.41	10.49	0.27
Mar	41.57	0.66	9.12	0.65	29.30	0.56	43.78	0.42	3.81	0.46	14.23	0.51
Apr	45.53	0.66	9.87	0.11	33.30	0.39	39.97	0.46	4.51	0.42	10.27	0.46
May	44.67	0.66	11.21	0.72	36.17	0.45	54.05	0.45	6.64	0.45	21.58	0.66
Jun	42.40	0.63	8.94	0.68	35.37	0.42	66.53	0.55	6.94	0.40	28.83	0.55
Jul	34.38	0.55	8.04	0.64	31.72	0.65	51.79	0.51	5.32	0.56	22.05	0.56
Aug	29.27	0.59	8.10	0.68	29.12	0.57	38.74	0.41	4.35	0.47	16.69	0.54
Sep	43.06	0.64	9.73	0.67	31.15	0.43	74.12	0.66	4.63	0.50	24.03	0.65
Oct	38.69	0.73	9.79	0.79	30.19	0.57	61.76	0.48	3.46	0.44	21.28	0.59
Nov	34.81	0.59	9.32	0.77	26.31	0.51	33.59	0.32	2.61	0.40	2.73	0.37
Dec	33.15	0.54	8.50	0.35	23.84	0.60	36.78	0.43	2.84	0.41	7.27	0.52

TABLE V. Meteorological data and their normalization for the cold and cloudy climate zone (Shillong, Meghalaya).

	Global solar radiation (MJ/m^2)		Sunshine hours (h)		Ambient temperature (^oC)		Relative humidity (%)		Wind speed (m/s)		Dew-Point (^oC)	
Month	Measured	Normalized	Measured	Normalized	Measured	Normalized	Measured	Normalized	Measured	Normalized	Measured	Normalized
Jan	25.67	0.66	7.46	0.63	18.84	0.59	60.40	0.42	2.78	0.52	10.36	0.67
Feb	31.89	0.66	6.49	0.57	22.13	0.47	54.03	0.50	3.23	0.39	12.16	0.42
Mar	34.11	0.64	7.22	0.63	25.34	0.50	50.56	0.40	3.69	0.52	13.69	0.51
Apr	32.93	0.60	3.79	0.32	25.77	0.50	66.78	0.51	4.09	0.36	18.79	0.51
May	33.66	0.52	4.84	0.48	27.20	0.54	74.97	0.55	4.35	0.36	22.31	0.53
Jun	31.45	0.66	4.18	0.49	28.14	0.72	79.62	0.29	6.21	0.53	24.26	0.61
Jul	14.12	0.5	3.25	0.4	27.19	0.4	82.34	0.6	3.19	0.3	23.84	0.7
Aug	22.09	0.56	2.50	0.44	27.04	0.57	84.82	0.52	3.98	0.45	24.30	0.61
Sep	19.58	0.53	3.29	0.39	27.15	0.43	82.38	0.52	2.72	0.38	23.80	0.65
Oct	22.37	0.46	5.87	0.56	26.31	0.45	71.68	0.50	2.01	0.34	20.75	0.54
Nov	19.46	0.47	7.06	0.63	23.76	0.43	63.47	0.51	1.78	0.27	16.35	0.50
Dec	20.43	0.56	7.60	0.63	21.35	0.50	61.23	0.56	2.56	0.45	17.25	0.52

TABLE VI. Meteorological data and their normalization for the moderate climate zone (Pune, Maharashtra).

	Global solar radiation (MJ/m^2)		Sunshine hours (h)		Ambient temperature (°C)		Relative humidity (%)		Wind speed (m/s)		Dew-point (°C)	
Month	Measured	Normalized	Measured	Normalized	Measured	Normalized	Measured	Normalized	Measured	Normalized	Measured	Normalized
Jan	21.43	0.45	9.50	0.53	22.91	0.56	43.38	0.38	2.42	0.33	9.01	0.39
Feb	19.44	0.61	10.21	0.73	27.01	0.56	40.73	0.49	2.83	0.45	11.50	0.49
Mar	27.62	0.46	9.90	0.69	29.08	0.49	38.98	0.52	2.98	0.43	13.77	0.48
Apr	25.99	0.62	9.97	0.65	30.73	0.51	39.98	0.41	3.14	0.40	16.28	0.46
May	22.09	0.59	10.83	0.72	30.47	0.50	48.62	0.60	4.32	0.50	18.94	0.55
Jun	18.69	0.54	5.07	0.50	26.74	0.52	68.87	0.56	4.25	0.47	20.56	0.55
Jul	16.30	0.51	4.27	0.28	24.56	0.45	80.48	0.53	4.17	0.39	20.93	0.40
Aug	17.32	0.58	4.00	0.44	24.70	0.54	77.79	0.46	4.77	0.43	20.55	0.59
Sep	17.25	0.46	5.57	0.53	25.01	0.41	73.36	0.54	3.79	0.42	19.76	0.50
Oct	10.90	0.47	7.67	0.59	24.63	0.61	65.41	0.46	2.25	0.36	18.09	0.51
Nov	13.81	0.44	8.46	0.61	21.82	0.46	53.75	0.62	2.14	0.47	11.45	0.30
Dec	25.56	0.48	8.74	0.70	24.59	0.62	43.51	0.51	2.70	0.31	10.85	0.40

2. Hazy sky (type-b)

If the duration of the sunshine hour is between 7 and 9 hours, and the diffuse component of solar energy is lower than 50% or greater than 25% of global solar energy.

3. Partially foggy/cloudy sky (type-c)

If the duration of the sunshine hour is between 5 and 7 hour, and the diffuse component of solar energy is lower than 75% or greater than 50% of global solar energy.

4. Fully foggy/cloudy sky (type-d)

If the duration of the sunshine hour is lower than 5 hour, and the diffuse component of solar energy is greater than 75% of global solar energy.

III. FUZZY LOGIC MODELLING FOR SOLAR ENERGY FORECASTING

The proposed sky-based model by employing fuzzy logic modelling to forecast global solar energy using meteorological parameters is implemented for the distinct climate zone across India as discussed in Table I.

Three variables, namely, low, medium, and high, are defined in the proposed model. The key task is the membership function assignment. Here, five membership functions have been defined using fuzzy terms defined as very low, low-medium/low, medium-high/medium, high/high-high, and very high which lie in the range of 0.1–0.9 and a set of rules are described in the fuzzy inference system for estimating global solar energy for each day of the month. The fuzzy membership function for wind speed and sunshine duration is presented inFigs. 1 and 2, respectively.

The defined fuzzy rules have been implemented using the fuzzy logic toolbox of MATLAB for developing the model to estimate global solar energy as shown in Fig. 3.

IV. IMPLEMENTING FUZZY LOGIC MODELLING FOR SOLAR PHOTOVOLTAIC APPLICATION

Generation of power from photovoltaic systems depends on sky-conditions,, solar irradiance, cell temperature, and the topographical position. In this work, the HIT (Heterojunction with intrinsic thin layer) photovoltaic module of 210 W power output is chosen and operated at maximum power point tracking. Since the generation of PV power is greatly influenced by solar irradiance and temperature, so only these parameters are used in this paper. The data which include solar irradiance, cell temperature, and photovoltaic power output is obtained and arranged within 1 h. The data are collected on the daily basis as the availability of solar irradiance during the summer

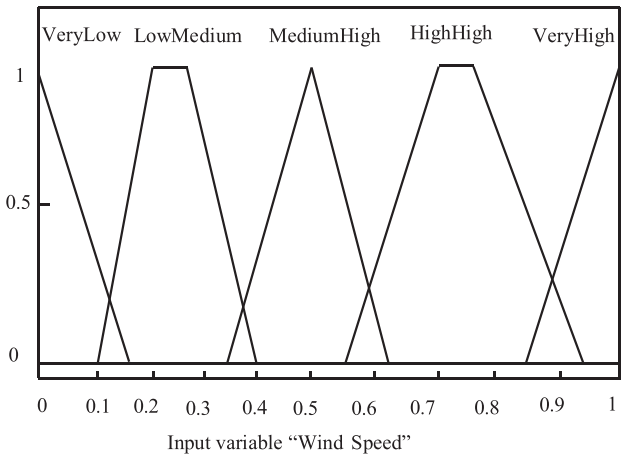

FIG. 1. Graphical representation of fuzzy logic membership functions for wind speed.

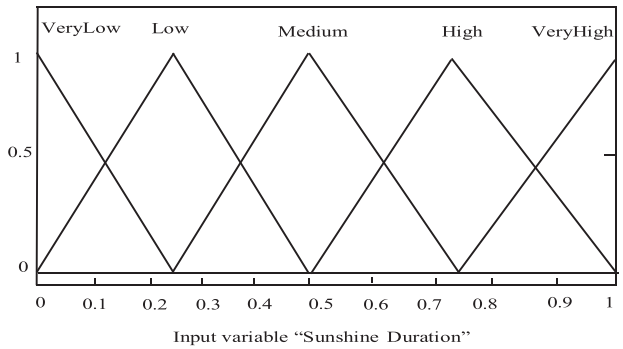

FIG. 2. Graphical representation of fuzzy logic membership functions for the sunshine duration.

season is from morning 6:00 A.M. till evening 18:00 P.M. In the winter season, the variation is from morning 8:00 A.M. till evening 17:00 P.M.

Fuzzy logic modelling has been employed for the prediction of the power output from the solar PV system. The fuzzy system takes solar irradiance, temperature, and weather descriptions as the input follow the process of Fuzzification and rule evaluation, and finally produces output power for forecasting.

Specification details of 210 W HIT photovoltaic modules are as follows:

The efficiency of the module: 16.7%
The efficiency of cell: 18.9%
Short circuit current: 5.57 A
Open circuit voltage: 50.9 V
Ambient operating temperature: −4 °F to 115 °F
N_{OCT} (Normal operating cell temperature): 114.8 °F

Based on the standard test conditions (STC) and influence by input parameters such as solar irradiance and cell temperature, the generation from the photovoltaic system can be defined as follows:[22]

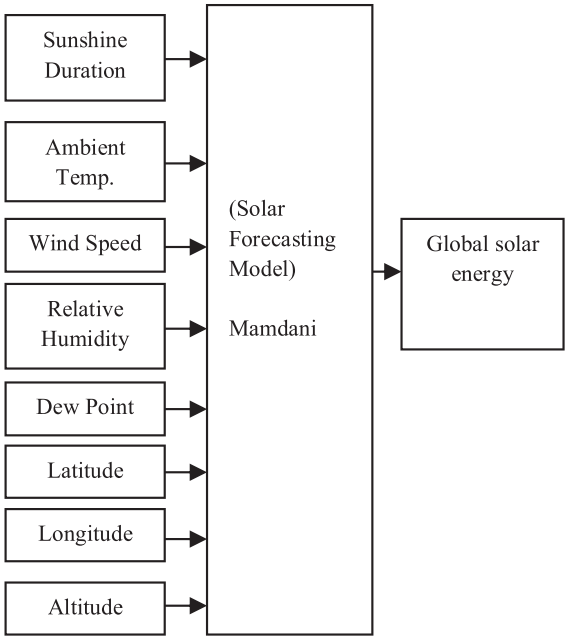

FIG. 3. Model-based on fuzzy logic technique for estimating global solar energy.

$$\mathrm{P_{PV}} = \left[P_{PV,STC}\,\mathrm{X}\,\frac{G_T}{1000}X\,[1-\gamma\,\mathrm{X}\,(T_j-25)]\right]\mathrm{X}\,N_{PVs}\,\mathrm{X}\,N_{PVp}\,, \tag{2}$$

and

$$T_j = T_{amb} + \frac{G_T}{800}\,X\,(N_{OCT}-20), \tag{3}$$

where $\mathrm{P_{PV,STC}}$ is the rated power output of the photovoltaic system of the single array at the MPP, $\mathrm{P_{PV}}$ is the power output of the photovoltaic array at the MPP, $\mathrm{G_T}$ is the solar irradiance in $\mathrm{W/m^2}$ at the STC, $\mathrm{N_{PVS}}$ is the photovoltaic arrays in series in number, γ is a temperature parameter at the MPP, $\mathrm{N_{PVP}}$ is the photovoltaic arrays in parallel in number, $\mathrm{T_{amb}}$ is the ambient temperature in °C, $\mathrm{T_j}$ is the temperature of the solar panel in °C, and $\mathrm{N_{OCT}}$ is a constant.

The average power output of the solar photovoltaic system can be predicted by employing the fuzzy logic technique and is presented in Fig. 4.

V. STATISTICAL EVALUATION

For evaluation of the models, statistical error tests have been carried out, namely, mean percentage error and mean bias error for result comparison.

Mean Percentage Error (MPE) is described as the variation of the forecasted data with the measured data, and the relationship is given by

$$\mathrm{MPE} = \frac{1}{x}\sum\nolimits_{i=1}^{x}\left(\frac{e_i-m_i}{m_i}\right), \tag{4}$$

where x is the number of observed data, and m_i and e_i are the i_{th} measured and estimated data, respectively.

Mean Bias Error (MBE) is expressed by the following equation:

$$\mathrm{MBE} = \frac{1}{x}\sum_{i=1}^{x}(e_i-m_i), \tag{5}$$

where x is the number of observed data, and m_i and e_i are the i_{th} measured and estimated data, respectively. On comparing the measured and the estimated values, the long-term performance can be obtained for correlations, and its ideal value is "zero."

VI. RESULTS AND DISCUSSION

The sky-based model employing fuzzy logic modelling has been developed and presented for predicting global solar energy using meteorological parameters such as the dew-point besides using other commonly known parameters like the sunshine duration, ambient temperature, wind speed, and relative humidity for the distinct climate zone across India. The results obtained using intelligent modelling are then compared with the measured data for five meteorological stations across India that represents the distinct climate zone, namely, composite climate, hot and dry, warm and humid, cold and cloudy, and moderate climate zone, respectively. The performance of the proposed model is then evaluated based on statistical indicators and is presented in Table VII.

Based on the results obtained in Table VII, the following can be briefly summarized:

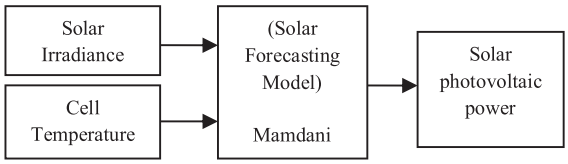

FIG. 4. Model based on fuzzy logic technique for estimating the photovoltaic system power output.

TABLE VII. Estimated global solar energy by employing fuzzy logic modelling for different sky-conditions along with statistical error for the distinct climate zone across India.

Climate zone	Sky conditions	H_g (MJ/m^2)		Sunshine hours (h)	MPE (%)	MBE (%)
		Measured	Fuzzy			
New Delhi (Composite)	Clear/sunny sky (type-a)	29.96	30.20	9.30	1.94	0.24
	Hazy sky (type-b)	29.71	29.76	8.09	0.22	0.05
	Partially foggy/cloudy sky (type-c)	23.93	23.88	6.30	1.96	−0.05
	Fully foggy/cloudy sky (type-d)	23.13	22.54	0.30	−2.56	−0.59
Chennai (Warm and humid)	Clear/sunny sky (type-a)	38.60	36.80	10.28	−4.32	−1.80
	Hazy sky (type-b)	32.98	36.49	8.58	6.82	0.07
	Partially foggy/cloudy sky (type-c)	37.93	37.50	6.61	−0.80	−0.43
	Fully foggy/cloudy sky (type-d)	34.79	35.73	2.26	5.79	0.94
Jodhpur (Hot and dry)	Clear/sunny sky (type-a)	38.63	37.81	12.36	−1.23	−0.82
	Hazy sky (type-b)	36.93	36.35	8.67	1.39	−0.57
	Partially foggy/cloudy sky (type-c)	35.35	31.72	6.63	−7.90	−3.63
	Fully foggy/cloudy sky (type-d)	36.56	38.58	2.84	4.39	2.02
Shillong (Cold and cloudy)	Clear/sunny sky (type-a)	31.30	30.12	9.546	−2.74	−1.18
	Hazy sky (type-b)	24.48	25.45	7.256	5.77	0.97
	Partially foggy/cloudy sky (type-c)	26.25	26.25	4.443	9.05	−0.002
	Fully foggy/cloudy sky (type-d)	32.68	32.41	1.200	0.36	−0.30
Pune (Moderate)	Clear/sunny sky (type-a)	20.25	20.61	10.12	4.75	0.28
	Hazy sky (type-b)	19.70	19.68	8.46	0.89	0.26
	Partially foggy/cloudy sky (type-c)	18.89	18.94	6.08	1.78	0.04
	Fully foggy/cloudy sky (type-d)	16.42	16.01	2.85	−0.89	−0.41

A. Clear/sunny sky (type-a) condition

It is observed that by employing fuzzy logic modelling for estimating global solar energy, the minimum value of mean percentage error for this model is 1.23% which is obtained for the Jodhpur station representing hot and dry climate zones as shown by the computed data presented in Table VII.

This is due to the fact that the climatic condition of Jodhpur is hot and dry as the variation in relative humidity is from 33% to 74% as shown in measured data presented in Table IV, which is generally low, because of low water surface bodies and vegetation.

The sky is generally clear, with high solar irradiance during daytime as the surrounding atmosphere got heated up quite fast. In addition to this, the average hours of the bright sunshine throughout the year is 12.36 h, which is much higher as compared to other meteorological stations as shown by the computed data presented in Table VII. During the night as well, the sky is generally clear; therefore, the heat absorbed by the surface during the daytime got dissipated to the upper atmospheric layer quickly. Hence, during the night the ambient temperature is low which makes it much cooler than during the daytime. Jodhpur is also well-known as the 'Sun City' for clear and sunny weather which prevails throughout the year.

B. Hazy sky (type-b) condition

It is observed from Table VII that the minimum value of mean percentage error by employing fuzzy logic modelling for this model is 0.22% which is obtained for the Delhi composite climate zone.

The reason behind is the presence of high humidity which shows the variation from 35% to 61% during dry periods and 64% to 81% during wet periods as shown in measured data presented in Table II. In addition, the intensity of solar radiation is quite high during summer and

low during monsoon as the average of the bright sunshine hours computed throughout the year is 8.09 h, as shown by computed data presented in Table VII, which is comparatively less as compared to that in the hot and dry climate zone. The sky is generally dull and overcast during monsoon and hazy during summer.

C. Partially foggy/cloudy sky (type-c) condition

It can be seen in Table VII that the minimum average forecasting precision by employing fuzzy logic modelling for this model is 0.80% in mean percentage error for the Chennai station, which represents the warm and humid climate zone.

This is due to the fact that the diffuse radiation component of solar energy is comparatively higher because of cloud cover as the average bright sunshine is 6.61 h only. The reason might be the presence of clouds because of which the heat dissipation from the surface of the earth to the sky during night time is minimal. Hence, the sky is partially cloudy as ambient temperature varies from 30 to 35 °C at daytime and 25 to 30 °C at night time during summer which is quite low. During winter, the variation in maximum ambient temperature is from 25 to 30 °C during the day and 20 to 25 °C during the night. A typical feature of this zone is the relative humidity varying from 58% to 74% throughout the year, which is generally high, as shown by measured data presented in Table III.

D. Fully foggy/cloudy sky (type-d) condition

It is observed that the minimum value of mean percentage error employing fuzzy logic modelling for this model is 0.36% for the Shillong station, which represents the cold and cloudy climate zone as shown by computed data presented in Table VII.

The reason behind is that the intensity of solar insolation is quite low during winter because of the presence of the diffuse component of solar energy which makes winters extremely cold. The summers are comparatively quite pleasant as the variation in maximum air temperature lies between 25 and 30 °C during daytime and 17–27 °C during the night, whereas the winters are comparatively chilly. In addition, the relative humidity shows variation from 50% to 85% which is generally high, as shown by measured data presented in Table V. Sky is generally overcast and cloudy throughout the year except during short summer as the daily average hours of the bright sunshine is 1.20 h only as shown by the measured data presented in Table VII.

In addition, the graphical representation showing the comparison of measured data with the estimated data has been presented in Figs. 5–9 for different sky-conditions for five meteorological stations across India, respectively.

As shown in Figs. 5–9, the predicted data obtained by employing fuzzy logic modelling for different sky-conditions are almost the same as the measured data and the model performance is observed to be satisfactory.

The sunny/clear sky (type-a) model performs best for the Jodhpur station which represents the hot and dry climate zone, as the predicted data exactly match the measured data as shown in Fig. 7(a).

The hazy sky (type-b) model shows the best results for the New Delhi station which represents composite climate zone, as the predicted data exactly match the measured data as shown in Fig. 5(b).

Similarly, the partially foggy/cloudy sky (type-c) model is best for the Chennai station which represents the warm and humid climate zone, as the predicted data exactly match the measured data as shown in Fig. 6(c).

Also, the fully foggy/cloudy sky (type-d) model is best for the Shillong station which represents the cold and cloudy climate zone, as the predicted data exactly match the measured data as shown in Fig. 7(d).

The obtained results are further simulated for solar photovoltaic applications. In this section, the solar radiation data collected from IMD and NISE are used to assess the proposed fuzzy logic model. In the present work, the HIT (Heterojunction with intrinsic thin layer) PV module of 210 W is selected and operated at maximum power point tracking. The data in the input layer comprise cell temperature, solar irradiance, and sky information obtained from NISE and the output layer is the power. The forecasted solar photovoltaic system power output

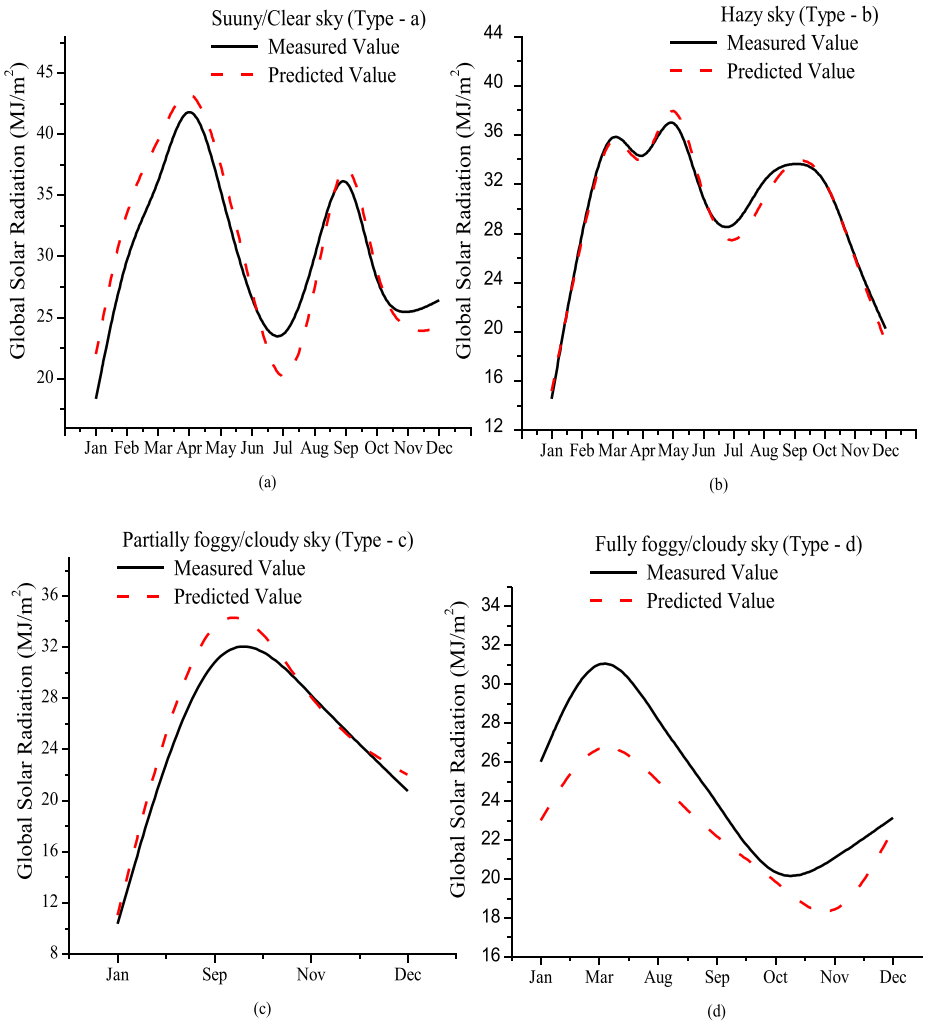

FIG. 5. Comparison of measured data with the forecasted data of global solar energy for composite climate (Delhi).

employing the fuzzy logic technique obtained month-wise for year 2012 for a given solar irradiance level and cell temperature is presented in Table VIII for the Delhi composite climate zone.

Table VIII shows that the mean percentage error (MPE) of the solar photovoltaic system power output averaged month-wise is 0.0581% by employing fuzzy logic modelling, which is within the permissible error limit.

Furthermore, the different sky-conditions affect different forecast behaviour of solar radiation. Pure sunny, hazy, partially foggy/cloudy, and fully foggy/cloudy models are considered and performance has been evaluated based on statistical indicators and results are presented in Table IX. Normally, the day considered here is the combination of different periods of hazy, sunny, partially foggy/cloudy, and fully foggy/cloudy sky-conditions considered during daytime.

In one sunny/clear day, the variation between the measured and the forecasted data using the proposed fuzzy logic methodology is shown in Fig. 11(a). The time considered is from morning 7:00 A.M. till evening 18:00 P.M. As compared to the factor of temperature, here the factor of time plays a major role that mostly affects the solar radiation. The average of mean percentage error calculated between the measured and the forecasted data is observed to be 0.0741% for the sunny-sky model as presented in Table IX.

In one hazy day, the variation between the measured and the forecasted data using the proposed fuzzy logic methodology is shown in Fig. 11(b). The time considered is from morning

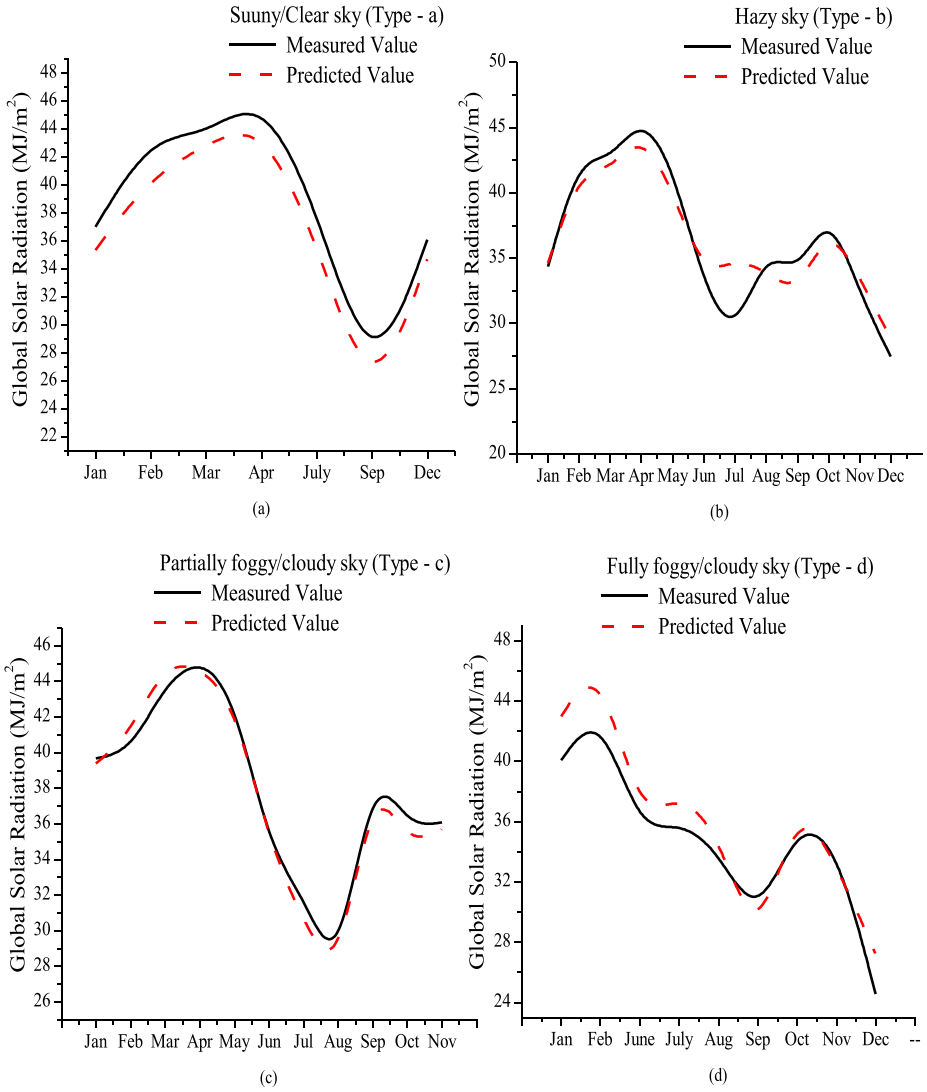

FIG. 6. Comparison of measured data with the forecasted data of global solar energy for warm and humid climate (Chennai, Tamil Nadu).

10:00 A.M. till evening 16:00 P.M. In a hazy-sky day, the sun rays will get obstructed and the factor of temperature affects the solar irradiance most as compared to the time factor, which is not the same as in the case of sunny day. The maximum value of solar irradiance is 519.54 W/m^2 and the averaged of mean percentage error between the measured and the forecasted data is 0.0031% for the hazy-sky model as presented in Table IX.

In one partially foggy/cloudy day, the variation between the measured and the forecasted data using the proposed fuzzy logic methodology is shown in Fig. 11(c). The time considered is from morning 8:00 A.M. till evening 19:00 P.M. The sunshine is partially absorbed by the photovoltaic and partially by the cloud. Here, the solar radiation has a close relationship with both the temperature factor and the time factor. The average of mean percentage error between the measured and the forecasted data for this studied partially foggy/cloudy sky model is 0.0072% as presented in Table IX.

In one fully foggy/cloudy day, the variation between the measured and forecasted data using the proposed fuzzy logic methodology is shown in Fig. 11(d). The time considered is

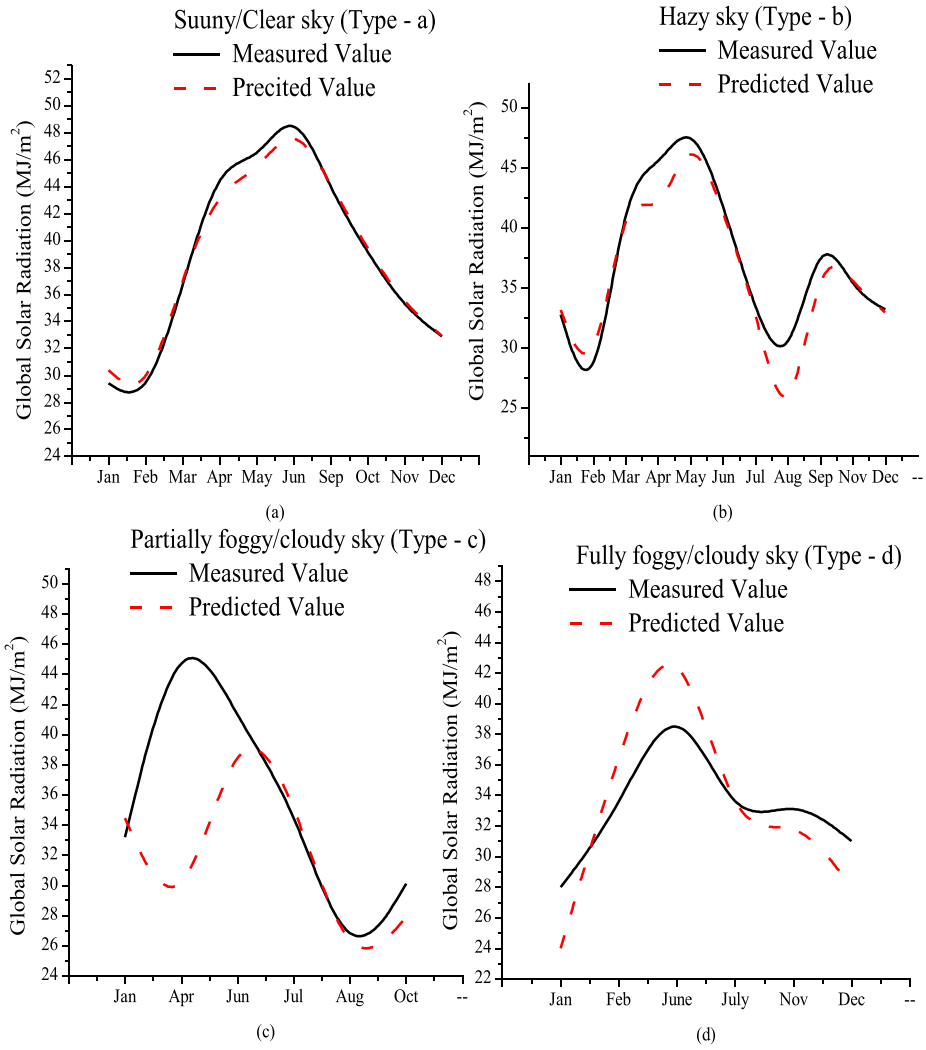

FIG. 7. Comparison of measured data with the forecasted data of global solar energy for hot and dry climate (Jodhpur, Rajasthan).

from morning 9:00 A.M. to evening 15:00 P.M. The maximum value of solar irradiance is 164.25 W/m^2. In this, the sun rays will get fully blocked by the presence of cloud and both the factor of time and temperature will affect the solar radiation. The average of mean percentage error between the measured and forecasted data for this fully foggy/cloudy sky model is 0.0077% as presented in Table IX.

From Table IX, it is observed that out of the four models, especially the sunny-sky and hazy-sky model perform well in forecasting of power of a solar photovoltaic system in the Delhi composite climate zone. In addition, the industrial requirements have been satisfied as the short term photovoltaic power forecasting MPE is not greater than 20%. However, for each of the sky-models, the mean percentage error fluctuates, as presented in Fig. 10.

The variation in mean percentage error for different sky-conditions between the measured and predicted data during day time is shown in Fig. 10. The variations in the error is highest for the sunny/clear sky model in comparison to other sky-conditions, the reason behind is that the average value of solar insolation is relatively large as compared to other sky conditions.

For the Delhi composite climate zone, the hazy-sky model gives the best results with a mean percentage error of 0.0031%, followed by the sunny-sky model, partially foggy/cloudy

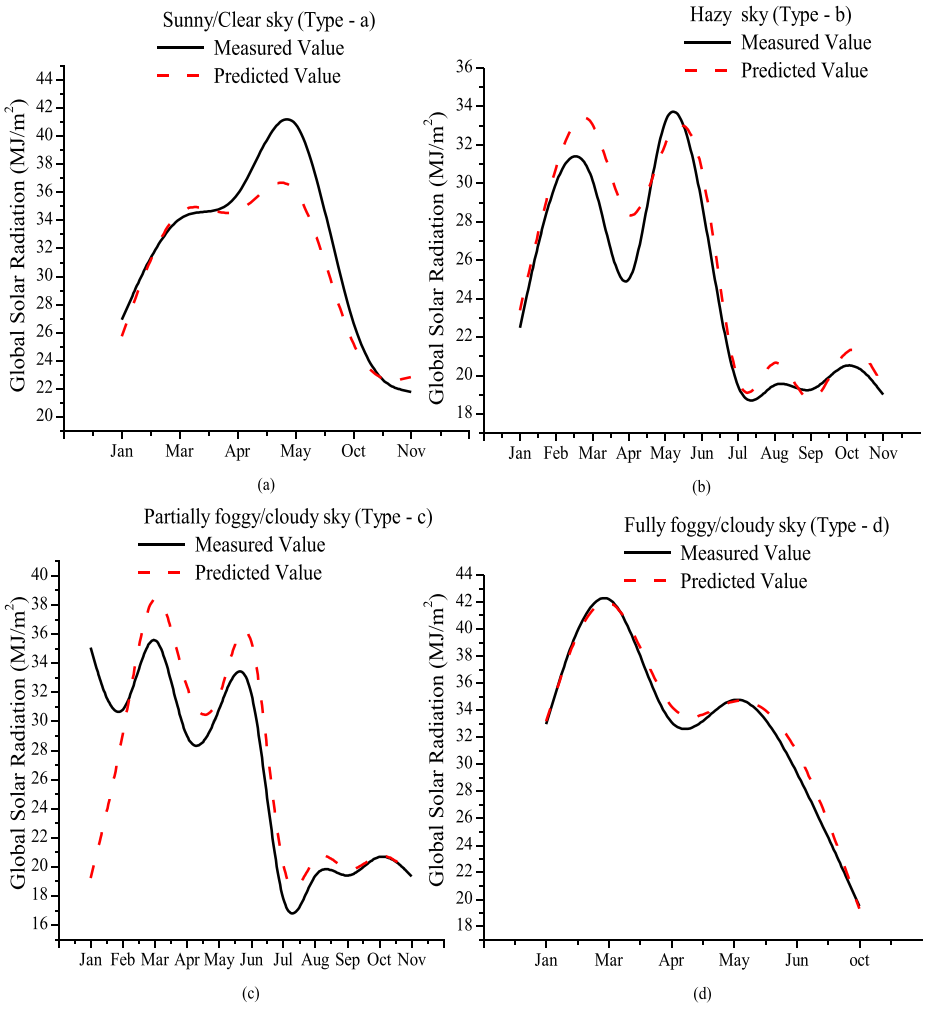

FIG. 8. Comparison of measured data with the forecasted data of global solar energy for cold and cloudy climate (Shillong, Meghalaya).

sky model, and fully foggy/cloudy sky model with a mean percentage error of 0.0741%, 0.0072%, and 0.0077%, respectively, as shown in Table IX. After the study, the average value of forecasting errors of the proposed model is 0.0027% in mean percentage error for the sample photovoltaic installation. The following graph further demonstrates the variation in the measured and the forecasted data for different sky-conditions as shown in Fig. 11.

From Fig. 11, it is learnt that the hazy-sky model (Type-b) shown in Fig. 11(b) outperforms other models as the measured data exactly match the estimated data for the Delhi composite climate zone.

However, for Figs. 11(c) and 11(d), there are significant differences between the measured and the estimated data in partially foggy/cloudy and fully foggy/cloudy models. In the present case, the solar photovoltaic system is installed at NISE, Delhi, where the sunny and hazy day is present during most of the year.

VII. COMPARISON OF THE FUZZY LOGIC BASED MODEL WITH EMPIRICAL REGRESSION MODELS

Empirical models have been developed using the above-mentioned meteorological parameters through linear regression analysis for widely changing climatic conditions across India and are reported in Appendix. The performance of models has been measured using mean

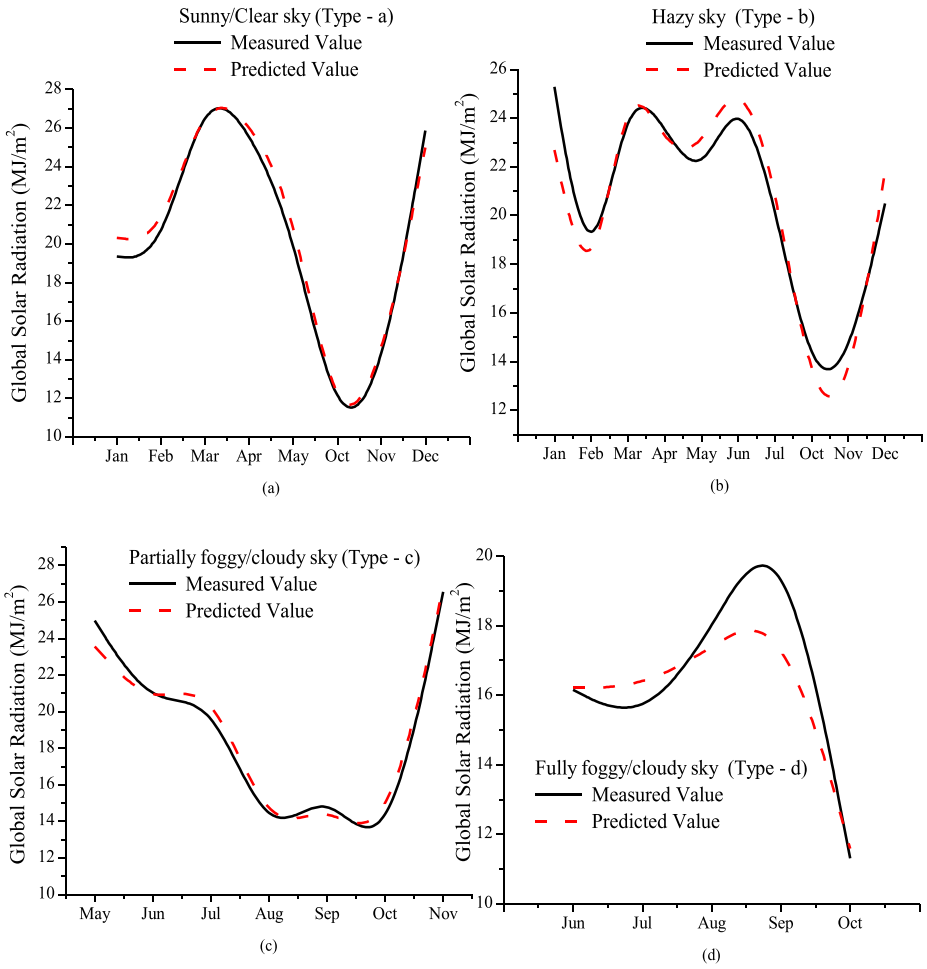

FIG. 9. Comparative analysis of measured and predicted data of global solar energy for moderate climate (Pune, Maharashtra).

TABLE VIII. Forecasted power of the solar photovoltaic system employing 210 W HIT (Heterojunction with an intrinsic thin layer) PV modules averaged month-wise in the Delhi composite climate zone.

Month	Solar irradiance (W/m^2)	V_{oc} (V)	I_{sc} (A)	Cell temperature (°C)	Power (W)		MPE (%)
					Measured	Forecasted	
Jan	361.15	81.47	0.42	28.14	20.80	19.79	−0.0064
Feb	461.52	82.03	0.61	35.69	30.15	30.02	0.0060
Mar	548.24	83.64	0.62	40.12	31.56	31.25	0.0100
April	575.12	79.62	0.60	42.53	30.23	32.56	0.1500
May	559.67	77.35	0.59	46.22	31.05	35.19	0.1938
June	537.17	76.92	0.55	45.24	26.20	26.00	0.0166
July	537.81	76.66	0.05	48.28	24.45	25.72	0.0023
Aug	428.80	76.90	0.47	53.27	22.33	22.59	0.0308
Sep	437.51	77.78	0.50	51.62	23.80	23.99	0.0378
Oct	466.57	78.74	0.63	53.21	29.92	29.40	−0.0090
Nov	369.82	78.48	0.44	45.08	20.85	20.65	−0.0173
Dec	370.84	80.66	0.47	43.36	25.53	32.57	0.2827
Avg.	471.18	79.19	0.50	44.40	26.41	27.48	0.0581

TABLE IX. Forecasted power of a solar photovoltaic system using 210 W HIT PV modules for different sky-conditions in the Delhi composite climate zone.

Sky-conditions	Time (h)	Cell temperature (°C)	Solar irradiance (W/m^2)	Power (W)		MPE (%)
				Measured	Forecasted	
Sunny/clear sky (type-a)	7:00	34.11	140.93	7.00	7.03	0.0036
	8:00	40.55	273.76	15.00	15.00	−0.0002
	9:00	48.14	486.12	30.33	30.34	0.1749
	10:00	52.23	625.25	41.67	41.66	0.1210
	11:00	57.79	783.13	54.17	54.18	0.1271
	12:00	62.86	875.34	60.50	60.50	0.0702
	13:00	64.69	888.95	61.17	61.18	−0.0060
	14:00	63.91	744.96	42.00	42.00	−0.3153
	15:00	61.55	726.73	46.33	46.33	0.3563
	16:00	58.04	549.15	31.50	31.51	−0.3178
	17:00	52.72	361.60	19.33	19.33	−0.4892
	18:00	48.83	204.59	9.80	9.80	−0.6141
	Avg.	53.79	555.04	34.90	34.90	−0.0741
Hazy sky (type-b)	10:00	40.83	123.10	7.00	7.12	0.0218
	11:00	44.49	146.12	9.67	9.70	0.0040
	12:00	43.56	307.56	24.17	24.20	0.0031
	13:00	52.55	519.54	45.50	45.46	−0.0008
	14:00	42.40	467.65	37.33	37.40	0.0018
	15:00	49.36	313.06	21.50	21.50	0.0003
	16:00	41.05	185.35	10.20	10.09	−0.0082
	Avg.	44.89	294.62	22.20	22.21	0.0031
Partially foggy/cloudy sky (type-c)	8:00	45.79	134.08	10.25	10.26	0.0024
	9:00	47.49	179.69	13.00	12.99	−0.0021
	10:00	52.07	355.98	30.33	30.14	−0.0063
	11:00	55.57	463.45	40.17	40.78	0.0130
	12:00	58.38	547.32	44.67	44.39	−0.0117
	13:00	59.96	519.74	33.00	31.40	−0.0372
	14:00	55.52	492.69	41.00	40.93	−0.0001
	15:00	61.30	647.10	52.00	51.69	−0.0105
	16:00	59.64	562.02	34.67	35.16	0.0094
	17:00	50.88	299.99	18.17	18.22	0.0049
	18:00	50.73	235.30	12.83	12.65	−0.0158
	19:00	47.99	156.43	6.50	7.23	0.1405
	Avg.	53.78	382.82	28.05	27.99	0.0072
Fully foggy/cloudy sky (type-d)	9:00	19.08	170.77	10.67	10.75	0.0120
	10:00	19.02	74.87	10.67	10.62	−0.0030
	11:00	23.29	96.49	9.00	8.72	−0.0042
	12:00	18.50	41.20	8.00	8.10	0.0105
	13:00	18.57	140.77	10.33	10.46	0.0500
	14:00	18.59	87.31	11.17	11.14	0.0067
	15:00	17.86	164.25	11.00	10.83	−0.0183
	Avg.	19.27	110.81	10.12	10.09	0.0077

percentage error. The developed model based on the fuzzy logic technique is then compared with the empirical models and the obtained results are shown in Table X.

Table X shows that the fuzzy logic based model has less value of mean percentage error for all meteorological stations. So, the comparison result shows that the model developed by

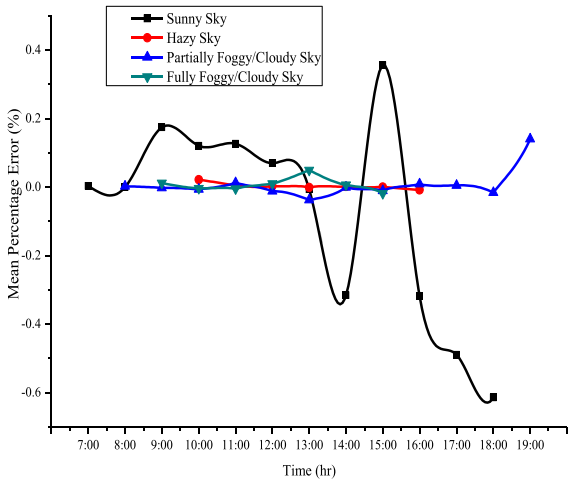

FIG. 10. Mean percentage error of four forecasting sky-based models.

implementing fuzzy logic modelling provides the best result which is accurate and convenient as compared to empirical regression models.

VIII. CONCLUSIONS

In the present work, sky-based models have been developed and presented using fuzzy logic modelling for estimating global solar energy for five meteorological stations across India that represents the distinct climate zone. The meteorological parameters such as the dew-point are considered besides using other known available parameters, namely, the sunshine duration, relative humidity, ambient temperature, and wind speed for different climatic zones. Since there is always ambiguity in climatic conditions, it is difficult to predict the solar energy accurately by using mathematical equations and regression techniques at particular location for different

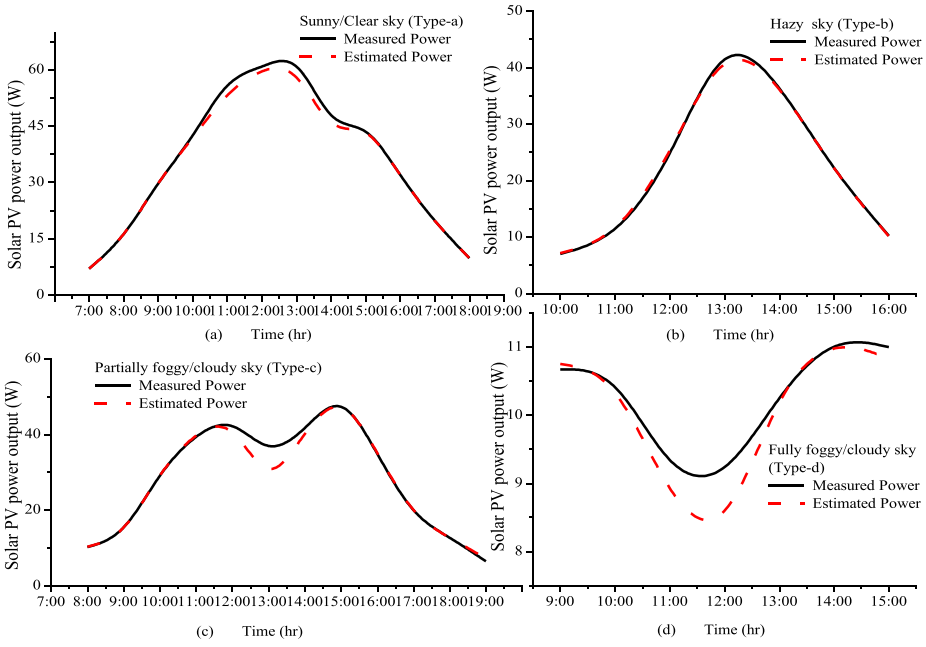

FIG. 11. Graphical representation of the estimated power of a 210 W solar photovoltaic system for different sky-conditions for the composite climate of India (Delhi).

TABLE X. Comparison of the proposed fuzzy logic based model with the Angstrom model.

Station	Measured H_g (MJ/m^2)	Fuzzy		Angstrom	
		H_g (MJ/m^2)	MPE	H_g (MJ/m^2)	MPE
New Delhi (Composite)	18.27	18.28	0.41	18.29	0.70
Chennai (Warm and humid)	19.53	19.51	0.37	19.59	2.25
Jodhpur (Hot and dry)	20.41	20.44	0.02	20.27	0.41
Shillong (Cold and cloudy)	16.45	16.49	0.68	16.88	1.94
Pune (Moderate)	19.36	19.33	0.06	19.86	2.40

sky-conditions. However, such problems may be overcome by employing fuzzy logic modelling for sky-based models using meteorological parameters for different climatic zones across India. Two criteria, namely, mean percentage error and mean bias error, are used to verify the forecasting errors of the proposed modelling approach. Numerical results revealed that the proposed fuzzy logic modelling approach achieves better accuracy and is convenient than the traditional regression methods.

Fuzzy logic modelling has been implemented for solar PV applications as well and a sky-based model employing fuzzy logic modelling has been presented for 1 h ahead power output forecasting of solar photovoltaic systems based upon the principle of fuzzy logic modelling and the characteristics of weather/sky classification. The results obtained through correlation analysis show that the forecasting error of the proposed model is 0.0027% (MPE) for the sample photovoltaic installation. The fuzzy logic approach favours results for the application of the sky-based model in forecasting of photovoltaic power of solar PV systems.

The proposed sky-based model employing fuzzy logic modelling may be further implemented for solar thermal applications that would be helpful for estimating the output of the solar thermal system.

APPENDIX: BRIEF DESCRIPTION OF CONVENTIONAL METHOD

A number of methods have been reported using empirical relationships to estimate global solar radiation, and daily total extraterrestrial radiation H_o is often included in the relationships. H_o was calculated using standard geometric procedures.[23,24] To calculate H_o and S_o at different locations, a program in MATLAB been developed.

The daily extra-terrestrial radiation H_o has been worked out by using the following relation:

$$H_O = \frac{24\times 3600}{\pi} G_{SC}\left(1 + 0.033\cos\frac{360 n_{day}}{365}\right)\times\left(\cos\Phi\cos\delta\sin\omega_s\frac{\pi\omega_s}{180}\sin\Phi\sin\delta\right), \quad \text{(A1)}$$

$$\boldsymbol{\delta} = 23.45\,\sin\left[\frac{360}{365}(n_{day}+284)\right], \quad \text{(A2)}$$

$$\omega_s = \cos^{-1}(-\tan\Phi\tan\delta). \quad \text{(A3)}$$

The value of S_o can be computed from Cooper's formula

$$S_o = \frac{2}{15}\cos^{-1}(-\tan\Phi\tan\delta), \quad \text{(A4)}$$

where G_{sc} is the solar constant, assumed equal to 1367 W/m^2, Φ is the latitude of the site, δ is the solar declination angle, ω_s is the mean sunrise hour angle, and n_{day} is the number of days of the

year starting from January onwards. First of January, n_{day} is equal to 1 and for 31st of December it is 365. S is the monthly mean of the daily hours of bright sunshine; and S_o is the maximum daily hours of sunshine or day length.

1. Angstrom-type model

The first theoretical model for predicting global solar energy based on the duration of sunshine hours has been proposed by Angstrom in 1924.[25] The original form of the Angstrom-Prescott model is

$$H_g/H_o = a + b * (S/S_o), \tag{A5}$$

where a and b are the regression coefficients calculated for each month. In this paper, the above model in its original formulation is used, where regression analysis has been carried out with input parameters, namely, sunshine duration per hour (S/S_o), ambient temperature, dew-point, wind speed, and relative humidity, while the output parameter is the clearness index (H_g/H_o). The estimated global solar energy is obtained by multiplying the estimated clearness index by H_o where H_g is the global solar radiation and H_o is the extra-terrestrial radiation on a horizontal surface.

[1]J. Albrecht, "The future role of photovoltaics: A learning curve versus portfolio perspective," Energy Policy **35**(4), 2296–2304 (2007).
[2]L. L. Kazmerski, "Solar photovoltaics R&D at the tipping point: A 2005 technology overview," J. Electron Spectrosc. Relat. Phenom. **150**, 105–135 (2006).
[3]L. Ran and L. Guang-min, "Photovoltaic power generation output forecasting based on support vector machine regression technique," Electric Power **41**, 74–78 (2008).
[4]J. Shi, W. J. Lee, Y. Liu, Y. Yang, and P. Wang, "Forecasting power output of photovoltaic systems based on weather classification and support vector machines," IEEE Trans. Ind. Appl. **48**(3), 1064–1069 (2012).
[5]H. Yang, C. Huang, Y. Huang, and Y. Pai, "A Weather-based hybrid method for 1-day ahead hourly forecasting of PV power output," IEEE Trans. Sustainable Energy **5**(3), 917–926 (2014).
[6]R. Aguiar and M. Collares-Pereira, "TAG: A time-dependent, autoregressive, Gaussian model for generating synthetic hourly radiation," Sol. Energy **49**(3), 167–174 (1992).
[7]L. L. Mora-Lopez and M. Sidrach-de-Cardona, "Multiplicative ARMA models to generate hourly series of global irradiation," Sol. Energy **63**(5), 283–291 (1998).
[8]A. Maafi and A. Adane, "A two-state Markovian model of global irradiation suitable for photovoltaic conversion," Sol. Wind Technol. **6**(3), 247–252 (1989).
[9]R. Iqdour and A. Zeroual, "Prediction of daily global solar radiation using fuzzy system," Int. J. Sustainable Energy **26**(1), 19–29 (2007).
[10]N. K. Gautam and N. D. Kaushika, "A model for the estimation of global solar radiation using fuzzy random variables," J. Appl. Meteorol. **41**, 1267–1276 (2002).
[11]A. Bardossy, L. Duckstein, and I. Bogardi, "Fuzzy rule-based classification of atmospheric circulation patterns," Int. J. Climatol. **15**(10), 1087–1097 (1995).
[12]B. A. Baum, V. Tovinkere, J. Titlow, and R. M. Welch, "Automated cloud classification of global AVHRR data using a fuzzy logic approach," J. Appl. Meteorol. **36**, 1519–1540 (1997).
[13]Z. Sen, "Fuzzy algorithm for estimation of solar irradiation from sunshine duration," Sol. Energy **63**(1), 39–49 (1998).
[14]V. Gomez and A. Casanovas, "Fuzzy logic and meteorological variables: A case study of solar irradiance," Fuzzy Sets Syst. **126**(1), 121–128 (2002).
[15]V. Gomez and A. Casanovas, "Fuzzy modelling of solar irradiance on inclined surfaces," Sol. Energy **75**, 307–315 (2003).
[16]E. Tulcan-Paulescu and M. Paulescu, "Fuzzy modelling of solar irradiation using air temperature data," Theor. Appl. Climatol. **91**(1–4), 181–192 (2008).
[17]M. Rizwan, M. Jamil, S. Kirmani, and D. P. Kothari, "Fuzzy logic based modelling and estimation of global solar radiation using meteorological parameters," Energy **70**, 685–691 (2014).
[18]P. T. Ajit, *Solar Radiant Energy Over India* (Ministry of New and Renewable Energy and India Meteorological Department, 2009).
[19]See www.niwe.res.in for "Database".
[20]N. K. Bansal and G. Minke, *Climatic Zones and Rural Housing in India* (KernforschungsanlageJülich GmbH, Zentralbibliothek, Jülich, 1988).
[21]A. Chel and G. N. Tiwari, "A case study of a typical 2.32 kW_p stand-alone photovoltaic (SAPV) in composite climate of New Delhi (India)," Appl. Energy **88**, 1415–1426 (2011).
[22]Y. Riffonneau, S. Bacha, F. Barruel, and S. Ploix, "Optimal power flow management for grid connected PV systems with batteries," IEEE Trans. Sustainable Energy **2**(3), 309–320 (2011).
[23]J. A. Duffie and W. A. Beckman, *Solar Engineering of Thermal Processes, 4th edition* (Wiley, New York, April 2013). ISBN: 978-0-470-87366-3.
[24]J. W. Spencer, "Fourier series representation of the position of the Sun," Search **2**, 162–172 (1971).
[25]A. Angstrom, "Solar and terrestrial radiation," Q. J. R. Meteorol. Soc. **50**, 121–125 (1924).

Macro-mechanical Analysis on the Variation of Fibre Orientation in a Composite UAV Landing Gear

IOP Conf. Series: Materials Science and Engineering **422** (2018) 012005 doi:10.1088/1757-899X/422/1/012005

Macro-mechanical Analysis on the Variation of Fibre Orientation in a Composite UAV Landing Gear

Harsh Raj Chauhan[1,a] , Vikas Rastogi[1,b] , Atul Kumar Agarwal[1,c]

[1]Mechanical Engineering, Delhi Technological University, Delhi, India

Email: [a]harshchauhan1995@gmail.com,[b]rastogivikas@gmail.com, [c]atulkumaragarwal@gmail.com

Abstract: Composite materials are increasingly being relied upon for their light weight and high strength to weight ratios and form the backbone of the aerospace industry, which follows a Systems Engineering approach. This paper is an attempt to manifest such an approach at a relatively smaller scale for a composite UAV landing gear. The landing gear acts as a support structure for the fuselage during take-offs and landings and hence needs to be carefully designed, analyzed and manufactured. The strength and weight of a landing gear has to be optimized so as to adhere to the overall aerodynamics and structural integrity of the aerial system. This study is initiated with the design concept of the landing gear and the state of load being acted upon followed by appropriate composite material selection. An approximate number of layers are decided for the composite vacuum layup of the landing gear through iterative experimentation. The fibre orientation of the composite layers is instrumental in gauging the macro-mechanical performance of the composite, thus being the focal point of this study. To execute this, the extensional, coupling and bending stiffness matrices are computed in a mathematical model in MATLAB for different fibre orientations in response to the elastic constants of the fibre and matrix. The global and local strains and curvatures are calculated for a load case and the final combination is down-selected. Corresponding to the down-selected combination, the landing gear is finally fabricated, using Vacuum bag moulding.

Nomenclature:

E1	*=Longitudinal Young's Modulus*
E2	*=Transverse Young's Modulus*
v12	*=Major Poisson's Ratio*
v21	*=Minor Poisson's Ratio*
G12	*=In-plane shear modulus*
[A]	*= Extensional Stiffness Matrix*
[B]	*= Coupling Stiffness Matrix*
[D]	*= Bending Stiffness Matrix*
Nx, Ny	*= Normal force per unit length*
Nxy	*= Shear force per unit length*
Mx, My	*= Bending moments per unit length*
Mxy	*= Twisting moments per unit length*
[Q]	*= Reduced stiffness matrix*
$\overline{[Q]}$	*=Transformed reduced stiffness matrix*
e_x, e_y, e_{xy}	*= Mid-plane strains*

Kx, Ky, Kxy = Mid-plane curvatures
[T] =Transformation matrix
[R] = Reuter matrix
(1,2) = Local axes denomination
(x,y) = Global axes denomination

1. Introduction

Systems Engineering, which supplements the design and development of unmanned aerial vehicles follow an inter-disciplinary approach to tackle complex systems such as this one. The landing gear of an unmanned aerial vehicle (UAV) functions as a shock absorber for the fuselage of the UAV, shielding the payload. The dynamic loads acting on the UAV due to sudden gusts and abrupt maneuvers are fully absorbed by the landing gear. It therefore demands a meticulous structural design of the landing gear of the UAV. With the advent of hybrid materials like composites and smart materials, it calls for careful selection of materials and their macro-mechanical analyses of resulting inner fiber and matrix to reach a design with a high technology readiness level.

2. Statement of Objectives

The design objectives for the composite landing gear are bifurcated into high-level and low-level objectives based on their functionality and dependence. The list of objectives in Table 1 presents the objectives kept in mind while approaching the design problem.

Table 1. Statement of objectives for the design of a composite landing gear

S.no	Parameter/Objective	Value/Range
1	Weight	5-7% of UAV weight
2	Static Load on the landing gear	85-90 N
3	Dynamic Load on the landing gear	150-170 N
4	Factor of safety	1.5
5	Strength/Weight %	130-180
6	Material characteristics	CF fabric/Epoxy matrix
7	Technology Readiness Level	5-7

3. Engineering Design

The landing gear is designed to tested for the static load of 85 N and an assumed dynamic load of 150N [1], it may take during the flight along with suitable safety factor, and several materials are qualitatively judged on a number of parameters. Carbon-fibre is finally selected among a list of other metals and composites. Different grades of carbon fibres are tested ranging from 200-400 gsm through a mathematical model and 400 gsm is finally selected.

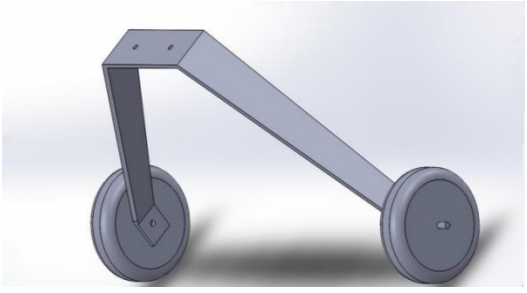

Figure 1. CAD model of the landing gear

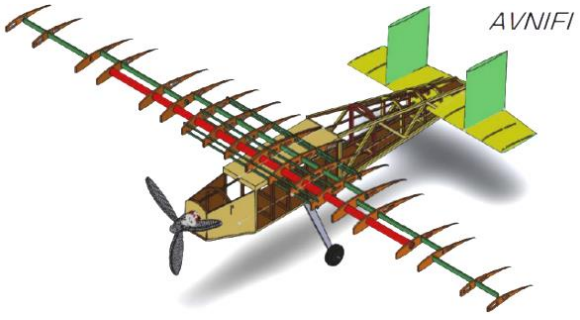

Figure 2. Raw 3D CAD of the UAV

4. Macro-mechanical Analysis

The macro-mechanical analysis of a composite lamina is based on the consideration that the lamina is homogeneous and the average properties of the individual layers are calculated [2]. The stiffness matrices are calculated based on the engineering constants of uni-directional lamina (both fiber and matrix) using a mathematical model.

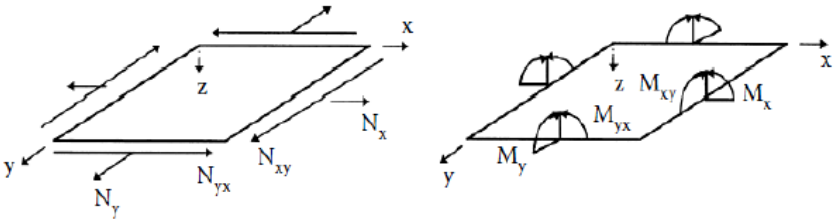

Figure 3. Forces & moments acting on a composite laminate [2]

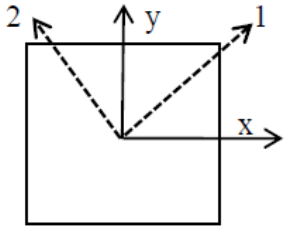

Figure 4. Local & Global axes representation of a lamina [3]

4.1. Mathematical Model.

The mathematical model takes as input, the elastic moduli of the fiber and the matrix of the composite, as specified in [4] to advance to the combined elastic moduli, *E1*, *E2*, *v12* and *G12* to finally calculate the reduced stiffness matrix *[Q]* for each ply of the composite using the following governing equations. (Refer Eq.1 to Eq.4)

$$Q11 = E1 / (1 - \nu12 * \nu21) \quad (1)$$
$$Q12 = E2 * \nu12 / (1 - \nu12 * \nu21) \quad (2)$$
$$Q22 = E2 / (1 - \nu12 * \nu21) \quad (3)$$
$$Q66 = G12 \quad (4)$$

The lamina in consideration is taken as purely orthotropic [5], so the other stiffness coefficients result in value of 0. Based on the reduced stiffness coefficients and restricting the number of plies, the fiber orientation of each ply is arbitrarily taken, considering the ease of fabrication. The number of plies are kept constant at 4, due to restricted weight constraint and the number of test cases are increased to 6 with the following layup.

Layup-1	*Layup-2*	*Layup-3*	*Layup-4*	*Layup-5*
0	0	0	0	0
90	90	45	45	-45
0	90	0	45	45
90	0	45	0	0

Figure 5. Layups with 4 plies each, with their fibre orientations

Each of the layups are separately taken and the transformed reduced stiffness matrix *[Q]* are calculated for each ply. Several assumptions were made in the process, for uniformity in the mathematical model and ease of fabrication.

Assumption 1 : The thickness of the plies were estimated, assuming uniform thickness of matrix(epoxy) and the fibre.

Assumption 2 : The mid-plane of the layup was assumed as origin for calculation of the coordinates of each ply.

Using the stiffness coefficients $[Q_{ij}]$ and the location of each ply, the extensional *[A]* , coupling *[B]* and bending *[D]* stiffness matrices are calculated [1], (Refer Eq.5 to Eq.7)

$A_{ij} = \Sigma[\overline{Q_{ij}}]_k * (h_k - h_{k-1})$ where *i=1,2,6 ; j=1,2,6 ; h_k= coordinate of kth ply* (5)

$B_{ij} = \Sigma[\overline{Q_{ij}}]_k * (h_k^2 - h_{k-1}^2)$ (6)

$D_{ij} = \Sigma[\overline{Q_{ij}}]_k * (h_k^3 - h_{k-1}^3)$ (7)

Corresponding to the obtained matrices *[A]*, *[B]* and *[D]*, the required forces and moments are applied to the final configuration of the layup and the mid-plane strains and curvatures are found by solving 6 simultaneous equations.(Refer to Eq.8)

$$\begin{bmatrix} Nx \\ Ny \\ Nxy \\ Mx \\ My \\ Mxy \end{bmatrix} = \begin{bmatrix} A_{11} & A_{12} & A_{16} & B_{11} & B_{12} & B_{16} \\ A_{12} & A_{22} & A_{26} & B_{12} & B_{22} & B_{26} \\ A_{16} & A_{26} & A_{66} & B_{16} & B_{26} & B_{66} \\ B_{11} & B_{12} & B_{16} & D_{11} & D_{12} & D_{16} \\ B_{12} & B_{22} & B_{26} & D_{12} & D_{22} & D_{26} \\ B_{16} & B_{26} & B_{66} & D_{16} & D_{26} & D_{66} \end{bmatrix} \begin{bmatrix} e\,x \\ e\,y \\ e\,xy \\ Kx \\ Ky \\ Kxy \end{bmatrix} \quad (8)$$

The local and global strains are also evaluated using the transformation operator $[R][T][R]^{-1}$. Finally, 6 variables are calculated through the mathematical model, 3 each for midplane strains and mid-plane curvatures.

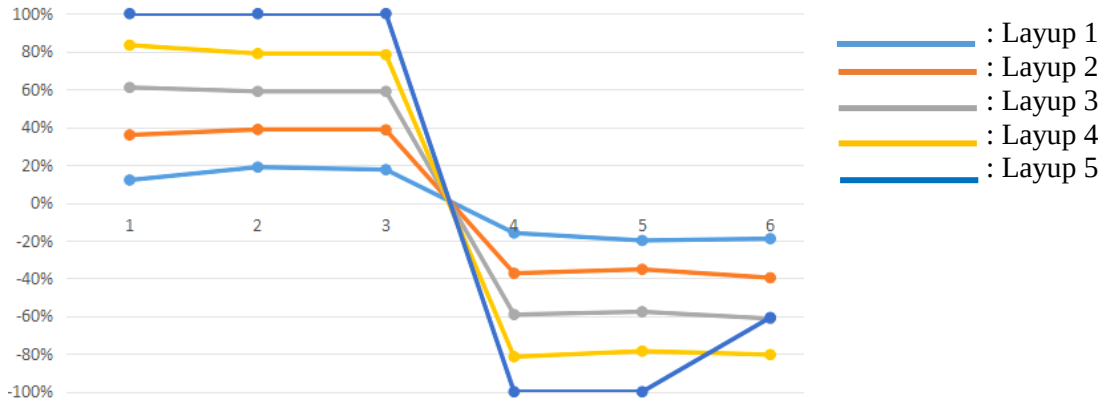

Figure 6. Percentage variation of the values of 6 variables for 5 layups in the mathematical model

4.2. Finite Element Method.

To analyze the accuracy of the results obtained from the mathematical model, a finite element simulation is performed for the composite landing gear with identical material properties and configurations. The finite element method simulation is performed on ABAQUS CAE, in which appropriate material properties of cross-weaved Carbon fibre of 400 gsm is stored, followed by layer selection, input of fibre orientation data and finally load application [6].

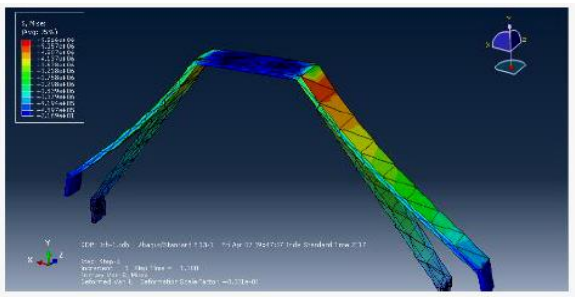

Figure 7. Strain energy contours on landing gear

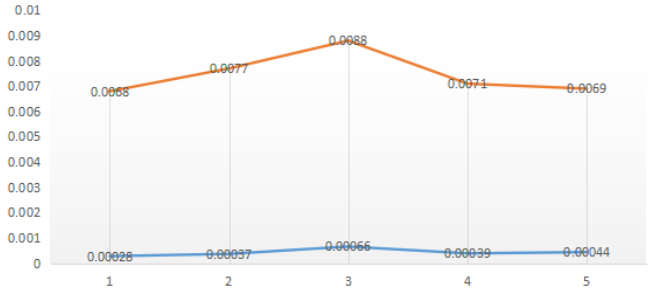

Figure 8. Variations in strains & curvature (FEM)

The results obtained from the finite element model are found to be in close proximity of the results obtained from the mathematical model.

5. Results

The results tabulated below are obtained through the mathematical model developed in MATLAB which represents the mid-plane strains and mid-plane curvatures for each of the 5 composite layups. Layup 1 [0/90/0/90] was found to be the optimal orientation of the fibres in the composite.

Table 2. Mid-plane strains and curvatures for the 5 layups through the mathematical model

Layup	e_x	e_y	e_{xy}	Kx [m]	Ky [m]	Kxy [m]
1	0.000112	0.000188	0.000295	-0.003096	-0.006721	-0.00715
2	0.000223	0.000199	0.000355	-0.004112	-0.005133	-0.00777
3	0.000235	0.000201	0.000344	-0.004215	-0.007541	-0.00812
4	0.000209	0.0002	0.000327	-0.004311	-0.007001	-0.00716
5	0.000156	0.000211	0.000367	-0.003577	-0.00723	0.00738

The results obtained by performing the finite element simulation on the composite landing gear to calculate the mechanical variables are shown in Table 3.

Table 3. Mechanical variables from the finite element simulation

Layup	Max principal stress [Mpa]	Max Strain Energy [J]	Max Equivalent strain	Mean curvature [m]
1	85.7	8.22e9	0.00028	0.0068
2	89.5	8.81e9	0.00067	0.0087
3	80.7	8.34e9	0.00034	0.0077
4	91.7	8.93e9	0.00073	0.0091
5	89.7	8.82e9	0.0070	0.0088

The absolute mean errors obtained for the values of mid-plane strains and curvatures from the 2 methods in Layup 1-5 are approximately 5%, 9%, 7.5%, 12% and 11% respectively.

6. Fabrication

The laminates are fabricated using Vacuum Bagging technique [7] in which the composite material layers are stacked on top of each other using the matrix (Epoxy with a 1:10 ratio of resin and hardener) and then vacuum is created using a sealed plastic bag connected to a vacuum pump. The temperature during the process needs to be increased to accelerate the curing time of the whole layup. This technique is dependent on season temperature, wherein the curing time varies by a large margin in summers compared to winters [7].

Figure 9. Composite layup using carbon fibre

Figure 10. Sealed vacuum layup

The laminates fabricated are then used for physical testing through a 3 point flexural test, before fabricating the actual model. The landing gear, initially designed and followed for a static load of 85N and a dynamic load of 150N behaved structurally well beyond the specified limits, giving a margin of safety of 1.7.

7. Conclusion

The conducted research presents an outline for the engineering analysis of composites in a UAV landing gear. The results of the formulated mathematical model are in close agreement with the Finite Element simulation performed on ABAQUS CAE for 5 different composite layups considered for the landing gear. Fabrication of the small scale laminates for 5 layups followed by a 3 point flexural test validates the design of the composite landing gear. Vacuum Bagging technique has been utilized in the fabrication process of the laminates as well as the actual model. Finally, for a UAV weight of 7.7 kilograms, the landing gear was fabricated with a total weight of 400 grams and reaching a strength/weight percentage of 160%. The technical readiness level of the developed system is observed to be 5.

References

[1] Sadraey M., *Aircraft Design: A Systems Engineering Approach, 2012, Wiley Publications*
[2] Autar K. Kaw: *Mechanics of composite materials, 2nd Edition,*2006 by Taylor & Francis Group, LLC
[3] https://www.asminternational.org/documents/10192/1849770/05287G_Sample_Chapter.pdf
[4] https://snebulos.mit.edu/projects/reference/MIL-STD/MIL-HDBK-17-2F.pdf
[5] Chen, C.H. and Cheng, S. (1967). *Mechanical Properties of Fibre Reinforced Composites,* Journal of Composite Material, 1(1): 30–40.
[6] Klaus Jurgen Bathe: *Finite Element Procedures, 1996 by Prentice Hall, Inc.*
[7]https://www.amtcomposites.co.za/sites/default/files/media/howto/Intro%20to%20Vacuum%20Bagging.pdf

This article has been accepted for publication in a future issue of this journal, but has not been fully edited. Content may change prior to final publication. Citation information: DOI 10.1109/TCC.2018.2878023, IEEE Transactions on Cloud Computing

Maximizing Cloud Revenue using Dynamic Pricing of Multiple Class Virtual Machines

Fadi Alzhouri, *Member, IEEE,* Anjali Agarwal, *Senior Member, IEEE,* and Yan Liu, *Senior Member, IEEE*

Abstract—The Infrastructure as a Service (IaaS) cloud industry that relies on leasing virtual machines (VMs) has significant portion of business values of finding the dynamic equilibrium between two conflicting phenomena: underutilization and surging congestion. Spot instance has been proposed as an elegant solution to overcome these challenges, with the ultimate goal to achieve greater profits. However, previous studies on recent spot pricing schemes reveal artificial pricing policies that do not comply with the dynamic nature of these phenomena. Motivated by these facts, this paper investigates dynamic pricing of stagnant resources in order to maximize cloud revenue. Specifically, our proposed approach manages multiple classes of virtual machines in order to achieve the maximum expected revenue within a finite discrete time horizon. For this sake, the proposed approach leverages the Markov decision processes with a number of properties under optimum controlling conditions that characterize a model's behaviour. Further, this approach applies approximate stochastic dynamic programming using linear programming to create a practical model. Experimental results confirm that this approach of dynamic pricing can scale up or down the price efficiently and effectively, according to the stagnant resources and the load thresholds. These results provide significant insights to maximizing the IaaS cloud revenue.

Index Terms—Cloud computing, Dynamic price, Maximizing revenue, Spot instances, Markov processes, Virtual machines, Multiple classes.

1 Introduction

Cloud computing is one of the most promising breakthrough technologies that promotes the universal use of information and computing resources. Indeed, computing abilities and IT services are marketed as delivery models in terms of the cloud. Infrastructure as a Service (IaaS) cloud service model has many substantial advantages for cloud providers and users alike. Users rent or buy as they use provisioned virtual machines (VMs) instead of physical machines (PMs). On the other hand, the providers lease a variety of shared hardware, software, and IT services in the data center in the form of virtual entities to serve many users simultaneously. Primarily, IaaS providers present cloud computing as a cost-saving and agility technology that has a crucial role not only in the users demand and budget but also in the revenue of the vendors.

Apart from the numerous advantages in this area, price is considered as a crucial issue for all parties. In this respect, many cloud computing enterprises, such as Amazon Elastic Compute Cloud (EC2) [1] and Microsoft Azure [2], adopt various pricing tiers that could be generally categorized into three types: reserved, on-demand, and spot. Reserved pricing type implies long term contract (years) with fixed price but with high service level agreement (SLA). On-demand pricing type allows to pay-as-you-go based on pre-defined time intervals and price with no long term commitment but without interruption. Spot pricing type is like on-demand except that the service could be interrupted [3]. These three tiers belong to two main pricing schemes: static and dynamic. The former is the dominant scheme in cloud computing, and it involves the provider charging the customer a fixed price per virtual machine per unit of time for long-term usage [1], [4], [5], [6]. The latter is the promising scheme, in which the provider charges the customer as long as the customer's bid equals or exceeds the instant price per time. The essence of providing a variety of pricing schemes originates from fundamental economic concepts, which often converge with engineering perspectives.

According to Gartner [7], a well-known research and advisory information technology company, the cloud market profit are expected to grow by 18 percent in 2017. The highest contribution to these profits will come from IaaS. On the other hand, many news about data centers utilization reveal that it is under 20% apart workload peaks as stated in [8], [9], [10], and [11]. According to data in 2015, Amazon states that the average utilization levels were often under 20% [12]. Further, National Resources Defense Council (NRDC) declares that the average server utilization remained low in the annual paper in 2014 [13]. Despite efforts to increase cloud utilization and encourage customers to adopt a particular cloud service, previous reports have indicated that many servers, which are considered as perishable devices from a business perspective, spend the majority of their existence waiting for a request without any revenue. Within this general framework, low utilization poses a barrier to this booming market. Moreover, many research addresses cost saving or static pricing to maximize cloud revenue [14], [15], [16], and the overwhelming majority of cloud firms primarily adopted static pricing scheme [17]. Tackling this

- *F. Alzhouri, A. Agarwal, Y. Liu are with the Department of Electrical and Computer Engineering, Concordia University, Montreal, QC, Canada. E-mail: f_alzh@encs.concordia.ca, aagarwal@ece.concordia.ca, yan.liu@concordia.ca*

Manuscript received July 11, 2017

This article has been accepted for publication in a future issue of this journal, but has not been fully edited. Content may change prior to final publication. Citation information: DOI 10.1109/TCC.2018.2878023, IEEE Transactions on Cloud Computing

challenge encourages cloud providers such as Amazon to adopt Spot Instance or Pay-As-You-Go as a solution. Many others may attempt to follow their lead. Indeed, spot price scheme has a significant role in improving utilization rates and hence maximizing cloud revenue. Nevertheless, the uncertainty of arrival and departure demands and the high state complexity pose a significant challenge to realizing maximum revenue streams in real time.

Stimulated by the above, likewise none of cloud providers reveal many details about spot pricing strategy from technical and economical perspectives. This paper attempts to leverage a thorough analysis of the problem and explores requirements and insights that could be used to address the problem. This synthesis results in the following contributions:

- Exploring the effects of both spot price and available capacity for sale on demand. This contribution will be made through devising a pricing formula derived from economic domains that reflects the inverse proportionality between the price and the available capacity, or the remaining unutilized virtual machines. Obviously, the state of the system fluctuates between an abundance and a paucity of VMs, where the former necessitates a lower price and the latter stimulates a higher price.
- Formulating the maximum expected total revenue. The formulation considers discrete-time stochastic Markov decision processes over a finite horizon. To solve such an optimization problem we employ probabilistic dynamic programming while considering the uncertainty of the arrival and departure rates, respecting multiple classes and fare types unlike [17], and underpinning our formulation using optimum boundary conditions.
- Seeking to make the proposed approach practical, we approximate our stochastic dynamic programming approach using linear programming and develop an optimal pricing strategy algorithm based on linear programming relaxation in order to find the best decision policy in real-time, attempting to reach near-optimal expected revenue.

We validate the proposed approach by comparing its results with the other dynamic pricing methods, namely, [17]. The evaluation results promote interesting performance and theoretical analysis insights.

The rest of the paper is organized in six sections: We introduce our model, formulate and analyze the maximum expected profit under discrete finite horizon Markovian decision in Section 2. Section 3 approximates dynamic programming by linear programming and presents our optimal pricing policy algorithm. Evaluation results are shown in Section 4. In Section 5 we raise debate about one of the real and recent spot pricing schemes, EC2 Spot Instances. Section 6 reviews the related literature work. In Section 7 we summarize and conclude this paper.

2 System Model

2.1 Modeling Assumptions

The model represents infrastructure as a service (IaaS) cloud computing in which the provider rents physical machines

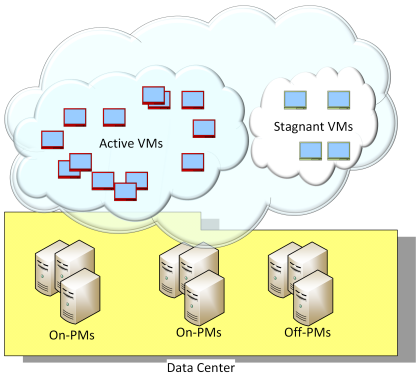

Fig. 1: A system model.

(PMs) of a data center in terms of virtual machines (VMs). Cloud providers do not provide much information regarding the size of their data centers, but according to [18], the estimated size is more than 10,000 servers. We believe the best revenue management is achieved by mutual cooperation between the static and dynamic schemes. On-demand and reserved pricing schemes provide solid and stable revenue, while spot pricing strives to increase the expected profit. As shown in Fig. 1, the state of the system can be described, at any time, as a set of active VMs, or rented, which rely on a set of on-PMs in addition to a set of off-PMs. These active VMs consume considerable capacity of "on" physical machines, but there is still a notable amount that can be considered as stagnant VMs. In this perspective, we use the term "stagnant VMs" to refer to those unrented VMs that still consume operational costs. It is worth noting that when there are high arrival demands, an instance price is very high, and no extra VMs in the stagnant pool in the previous horizon, the system can turn on new PMs in the next horizon if they are available. On the contrary, by applying the [19], [20], and [21] approach in our model, dynamic pricing can be used as a key controlling tool to attenuate cloud congestion. In such a case, increasing the instance price simultaneously increases the departure rate to reduce the load in the system. In particular, the objective of this paper is to determine the best utilization of these stagnant VMs to maximize the revenue of the cloud within a given horizon, sales period. For the sake of clarity, before delving into our approach details, we will use Table 1 notations over the course of the paper. Let a cloud provider have $|N|$ class of VMs where the available classes in the data center is $n \in N = \{1, 2, ..., |N|\}$. The state space C is a set that represents the number of instances of VMs, where $c_j(t) = k$ represents k instance of class $j \in \{1, 2, ..., n\}$ at time t, $c_j(t) \in K \triangleq \{0, 1, ..., k\}$. Based on these notations, the state of the system, the pool of stagnant VMs resources of all classes which are available for sale, at any given interval t is denoted as $C(t) = \{c_1(t), c_2(t), ..., c_n(t)\}$. Assume T is the length of horizon H, then H can be calculated as

$$H \triangleq \sum_{s=1}^{T} \triangle t_s. \quad (1)$$

$\triangle t$ is the shortest time interval that allows only for one request to occur. For simplicity, $\triangle t$ is denoted by t through-

This article has been accepted for publication in a future issue of this journal, but has not been fully edited. Content may change prior to final publication. Citation information: DOI 10.1109/TCC.2018.2878023, IEEE Transactions on Cloud Computing

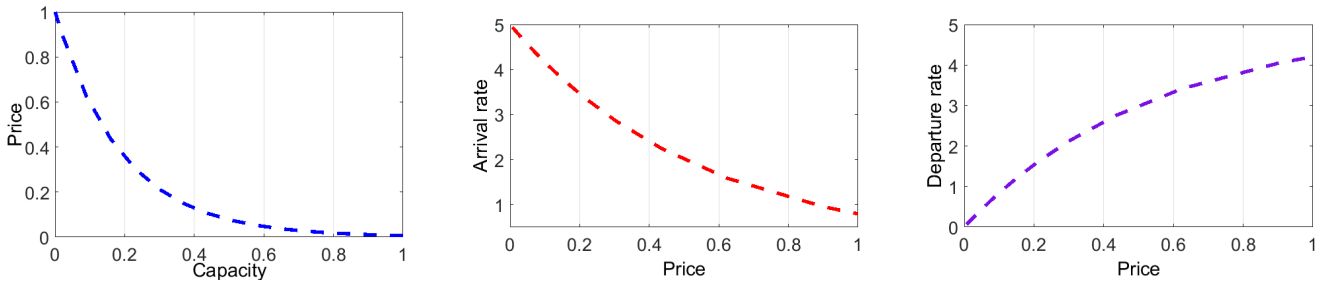

(a) Price versus capacity (b) Arrival rate versus price (c) Departure rate versus price

Fig. 2: Price versus capacity, arrival rate and departure rate

TABLE 1: Key Notations

Notation	Description
$\|N\|$	number of VMs classes.
j *and* l	class indices.
T	time length of sale horizon H.
$\triangle t$	shortest time interval in which only one incident occur.
$c_j(t)$	number of instances of class j available at time t.
$C(t)$	set of all VMs of all classes available for sale at time t. $C(t) = \{c_1(t), c_2(t), \ldots, c_n(t)\}$ in case of n class, otherwise $C(t) = \{c\}$.
a_j	number of demanded VMs of class j.
$R_j(t)$	reward induced from selling one unit of class j at time t.
$\mathbf{R}$	total reward at the end of horizon.
$\rho_j(t)$	price for one unit of class j at time t.
ρ_{max}	maximum price assigned for VM
$\lambda_j(\rho, t)$	arrival rate for class j of price ρ at time t.
$\mu_j(\rho, t)$	departure rate for class j of price ρ at time t.
γ	mean arrival rate in the horizon.
β	mean departure rate in the horizon.
$\mathbf{A}$	request of n class set of VMs.
A^j	request for lease or release amount of class j VMs.
$p_j(t)$	probability of request to hold VM of class j at time t.
$q_j(t)$	probability of releasing VM of class j at time t.
$f(C, t)$	total expected revenue of available resources C at time t.
$\bar{f}(C, t)$	approximate maximum revenue of resources C at time t.
u_j	decision to accept or reject a request for class j.
U	the set of decisions.
π^*	optimal n-vector policy.
P_u	3-dimensional one-step probability transition matrix.
V^*	the optimal expected revenue using linear programming.

out the paper. Practically, the demand includes not merely one class of VMs but perhaps a variety of classes. Each class j of virtual machines directly contributes a reward of $a_j R_j(t)$ to the cloud revenue, where a_j is the quantity of VMs demanded of class j. Then the total reward

$$\mathbf{R} = \sum_{t=1}^{T} \sum_{j=1}^{n} a_j R_j(t),$$

and without a loss of generality let order classes rewards $R_1(t) \leq R_2(t) \leq ... \leq R_n(t)$.

Let $\rho_j(t) \in [0, \rho_{max}]$ denote the price of class j at time t, where $\rho_{max} \leq 1$. We define price as an exponent function of capacity and time as stated in microeconomics literature [17], [22]. For example, $\rho_j(t) = e^{-c_j(t)\epsilon}$, where ϵ is a calibration parameter related to time, and such a definition seems convenient in our case. The empty set of class j, $c_j(t) = 0$, allows the price to grow up to the maximum value as an implicit condition that imposes the cloud to price at $\rho_j(t) = \rho_{max} = 1$ when stock is zero. By contrast, the cloud forces the price to be zero, $\rho_j(t) = 0$, in case of an abundance of capacity $c_j(t) = 1$. Fig. 2a shows the impact of capacity over the course of pricing operation that varies within the interval [0,1].

We can assume, without loss of generality, that demand is a function of arrival or departure rates and time and the demand process is a Poisson process. In addition, we can assume that the accepting and rejecting processes do not affect these rates. The arrival rate related to class j of price ρ at time t is

$$\lambda_j(\rho, t) = \gamma e^{-\alpha \rho_j(t)}, \tag{2}$$

and the departure rate is

$$\mu_j(\rho, t) = \beta(1 - e^{-\alpha \rho_j(t)}), \tag{3}$$

where the mean arrival rate and the mean departure rate in the current horizon respectively $\gamma, \beta \geq 0$ and scaling parameter $\alpha \geq 1$. Note that with $\rho_j(t) = 0$, the lowest price, then $\lambda_j(0, t) = \gamma$ and $\mu_j(0, t) = 0$, and theoretically there is no incentive to leave the system. But when $\rho_j(t) = 1$, the maximum price, then $\lambda_j(1, t) \simeq 0$, indicting that there is no motivation to utilize any VM, and $\mu_j(1, t) \simeq \beta$ forcing customers to leave cloud services. An example of such functions are shown in Figs. 2b and 2c, depicting the harmony with the law of demand curve defined in microeconomics principles [23], [24].

This article has been accepted for publication in a future issue of this journal, but has not been fully edited. Content may change prior to final publication. Citation information: DOI 10.1109/TCC.2018.2878023, IEEE Transactions on Cloud Computing

2.2 Model Formulation

The problem of dynamic pricing strategy can be formulated as a finite horizon Markov decision process under uncertainty. We consider a discrete time horizon in which at any given interval and any possible state of the Markov chain, the system chooses the optimal decision to sell or to wait. To do so, it traverse all stochastic possibilities of subsequent rewards up to the end of horizon, with a view toward gaining the maximum expected revenues.

At any given interval $\triangle t$, for clarity denoted as t, non-investing capacities of resources, represent a finite space C of cardinality $|C| = n$ supplied by cloud for sale, is represented as (C, t) and an n-class request $\mathbf{A} = \{a_1, a_2, \ldots, a_n\}$, demanded by the customer. If the system accepts the request of class j, i.e., $A^j = \{0, \ldots, a_j, \ldots, 0\}$, it moves to the state $(C - A^j, t + 1)$ in the next epoch. In case the system rejects the request, the state becomes $(C, t+1)$. On the other hand, the system moves to the state $(C + A^j, t + 1)$ as a result of releasing class j VM from the customer. At each time interval, Poisson incurs only one request of arrival or departure, if any, with that being a request to hold a class j, which arrives in time t with probability $p_j(t)$, or to release it with probability $q_j(t)$. Instantly, a binary decision u_j, to sell or to wait, must be taken according to the current state. In case of a sale, class j customer offers reward of $a_j R_j(t)$. It is worth noting that in reality two or more requests can happen at a time. This case could be circumvented by considering one request and postponing the rest to the subsequent time intervals. Especially since the time interval is very small.

The chain of decisions from the beginning of horizon $t = 1$ to the end of horizon $t = T$ aims to maximize the total expected revenue $f(C, t)$ derived from Hamilton-Jacobi-Bellman's equations as follows:

$$\begin{aligned} f(C,t) = \max_{\vec{u} \in U} \{ & \sum_{j=1}^{n} p_j(t)(a_j R_j u_j + f(C - A^j, t+1)) \\ & + \sum_{j=1}^{n} q_j(t) f(C + A^j, t+1) \\ & + (1 - (\sum_{j=1}^{n} p_j(t) + \sum_{j=1}^{n} q_j(t))) f(C, t+1) \}, \end{aligned} \tag{4}$$

$\forall t, \ \forall C,$

subject to the terminal conditions:

$$\begin{aligned} & f(C, 0) \triangleq 0, \\ & f(C, T+1) \triangleq 0, \ and \\ & f(0, t) \triangleq 0, \qquad \forall t, \ \forall C. \end{aligned}$$

Before the beginning of horizon, $t = 0$, and after the end of it, $t = T+1$, the revenue must be updated to zero, as well in the situation when all resources are exhausted, $C = 0$, at any time.

Clearly, the maximization process implies a decision to satisfy

$$u_j = \begin{cases} 1 & if \ a_j R_j(t) + f(C - A^j, t+1) \geq f(C, t+1) \\ 0 & otherwise, \end{cases} \tag{5}$$

to judge the more promising action, either to sell, incrementing the reward by $a_j R_j$, or to wait. The value of the objective function (4) from a given state can be briefly formulated to

$$\begin{aligned} f(C,t) = f(C,t+1) + \sum_{j=1}^{n} q_j(t) \triangle f(C + A^j, t+1) \\ + \max_{\vec{u} \in U} \{ \sum_{j=1}^{n} p_j(t)(a_j R_j u_j - \triangle f(C, t+1)), 0 \}, \end{aligned} \tag{6}$$

$\forall t, \ \forall C,$

whereas

$$\triangle f(C, t+1) = f(C, t+1) - f(C - A^j, t+1) \tag{7}$$

is the opportunity cost of available capacity C incurred by incident decision (5). It is noteworthy that the optimal policy is to sell whenever a bid $a_j R_j(t)$ surpasses its associated opportunity cost (7). The implicit effect of releasing resources on the grasped revenue is marked by

$$\triangle f(C + A^j, t+1) = f(C + A^j, t+1) - f(C, t+1). \tag{8}$$

To achieve the cloud's objective (6), namely to maximize the total expected rewards, the system finds

$$u_j^* \in \operatorname*{argmax}_{\vec{u} \in U} \{ \sum_{j=1}^{n} p_j(t)(a_j R_j(t) u_j - \triangle f(C, t+1)) \} \tag{9}$$

every interval t resulting in an optimal n-stage control policy $\pi^* = \{u_1^*, u_2^*, ..., u_n^*\}$ that yields the maximum expected revenue

$$f^*(C, t) \triangleq \sup_{\pi \in \Pi} f(C, t). \tag{10}$$

It should be apparent that the purpose of cloud computing is to find $f^*(C, 1)$ iteratively at the beginning of each horizon and recursively from the end of it. Nevertheless, while Bellman's equation is impractical computationally according to [25] and [26], it identifies the structural properties of the optimal solution.

2.3 Model Properties

From a practical point of view, such large space probabilistic dynamic models can be mathematically analyzed with the goal to match particular properties that characterize the optimal solution, describe how argument changes affect the result, and exhibit effective insights into the approximation of the objective solution. In fact, these properties differ depending on homogeneous or heterogeneous VMs involved in the process, namely one class of VMs or multiple classes.

2.3.1 One Class

To cope the complexity, we will assume that all cloud resources are represented by one class of VMs. In other words, the cloud leases only one class of VMs, which implies the following:

Proposition 1 (Principle of optimality): In-depth analysis of these revenue management problems in the literature shows that the optimal policy exists if $\triangle f(C, t+1)$ is

This article has been accepted for publication in a future issue of this journal, but has not been fully edited. Content may change prior to final publication. Citation information: DOI 10.1109/TCC.2018.2878023, IEEE Transactions on Cloud Computing

monotone[1] in both capacity and time [17], [29].
Theorem 1 (Monotone property): $\triangle f(C,t)$ is monotone in both capacity C and time t.

Proof. To confirm that $\triangle f(C,t)$ is decreasing in C, we have to employ some definitions [30].
Definition 1: $c_i^+ \succeq c_i^-$ for $\forall c_i^+, c_i^- \in C_i$ whereas $\succeq$ is a partial ordering relation on the $|N|$ dimensional set C.
The intent is to show the relation and order between the elements of the targeted space that is implied by the following definition.
Definition 2: $F(\cdot)$ a real-valued function defined on $|N|$ dimensional set C is partially non-decreasing, supermodular, if $F(c^+) \geq F(c^-)$ and it is partially non-increasing, submodular, if $F(c^-) \geq F(c^+)\ \forall c^+, c^- \in C$.

For $t = 0$, $\triangle f(C,0) = 0$, the base case holds corresponding to definitions 1 and 2. Suppose the statement is true for $\triangle f(C,t+1)$. Then, we have

$$\begin{aligned}&\triangle f(c^+,t) - \triangle f(c^-,t)\\ &\quad = f(c^+,t) - f(c^+ - A^j,t) - f(c^-,t)\\ &\qquad + f(c^- - A^j,t). \end{aligned} \tag{11}$$

Assuming the upper condition of the heaviside function (5) is satisfied whenever $j \geq i$, the right-hand side of (6) is maximized. The significance of that is the accepting of any request that offers reward greater than or equal to $a_j R_j$. For the sake of clarity, we refer to those VMs have been released using index l instead of index j. Consequently, the following substitutions are derived from (6):

$$\begin{aligned}&f(c^+,t)\\ &\quad = f(c^+,t+1) + \sum_{l=1}^{n} q_l(t) \triangle f(c^+ + A^l, t+1)\\ &\quad + \max_{\vec{u}\in U}\{\sum_{j=1}^{n} p_j(t)(a_j R_j u_j - \triangle f(c^+,t+1)),0\}, \end{aligned} \tag{12}$$

$$\begin{aligned}&f(c^+ - A^j,t)\\ &\quad = f(c^+ - A^j,t+1) + \sum_{l=1}^{n} q_l(t) \triangle f(c^+ - A^j + A^l, t+1)\\ &\quad + \max_{\vec{u}\in U}\{\sum_{j=1}^{n} p_j(t)(a_j R_j u_j - \triangle f(c^+ - A^j,t+1)),0\}. \end{aligned} \tag{13}$$

Similarly,

$$\begin{aligned}&f(c^-,t)\\ &\quad = f(c^-,t+1) + \sum_{l=1}^{n} q_l(t) \triangle f(c^- + A^l, t+1)\\ &\quad + \max_{\vec{u}\in U}\{\sum_{j=1}^{n} p_j(t)(a_j R_j u_j - \triangle f(c^-,t+1)),0\}, \end{aligned} \tag{14}$$

and

$$\begin{aligned}&f(c^- - A^j,t)\\ &\quad = f(c^- - A^j,t+1) + \sum_{l=1}^{n} q_l(t) \triangle f(c^- - A^j + A^l, t+1)\\ &\quad + \max_{\vec{u}\in U}\{\sum_{j=1}^{n} p_j(t)(a_j R_j u_j - \triangle f(c^- - A^j,t+1)),0\}. \end{aligned} \tag{15}$$

Likewise, substituting the value of each value function (12), (13), (14), and (15) on the right hand side of (11) produces the following:

$$\begin{aligned}&\triangle f(c^+,t) - \triangle f(c^-,t)\\ &= \triangle f(c^+,t+1) - \triangle f(c^-,t+1)\\ &\quad + \sum_{l=1}^{n} q_l(t)(\triangle f(c^+ + A^l,t+1) - \triangle f(c^+ + \triangle A,t+1))\\ &\quad - \sum_{l=1}^{n} q_l(t)(\triangle f(c^- + A^l,t+1) - \triangle f(c^- + \triangle A,t+1))\\ &\quad + \sum_{j=i}^{n} p_j(t)(a_j R_j - \triangle f(c^+,t+1))\\ &\quad - \sum_{j=i}^{n} p_j(t)(a_j R_j - \triangle f(c^+ - A^j,t+1))\\ &\quad - \sum_{j=i}^{n} p_j(t)(a_j R_j - \triangle f(c^-,t+1))\\ &\quad + \sum_{j=i}^{n} p_j(t)(a_j R_j - \triangle f(c^- - A^j,t+1)), \end{aligned} \tag{16}$$

where $\triangle A = A^l - A^j$. □

Obviously, the right-hand side of (16) is nonpositive; since, $\triangle f(c^+,t+1) - \triangle f(c^-,t+1) \leq 0$ and $\triangle f(c^+,t) - \triangle f(c^-,t) \leq 0$ is followed by induction. On one hand, this property reflects the economic intention to decrease the price when the supplied quantity of VMs to the spot market is high and vice versa. On the other hand, it shows the fact that the cloud provider desires to maximize its expected revenue through increasing quantity supplied in case of abundance of stagnant VMs. The rational behined this is increaing the system utilization through price discrimination. As well, $\triangle f(C,t)$ is decreasing in time.

Proof. For the sake of clarity let assume that the request is limited to merely one VM. From (7), we have

$$\triangle f(c,t) = f(c,t) - f(c-1,t) \tag{17}$$

then the following substitutions are derived from (6)

$$\begin{aligned}f(c,t) &= f(c,t+1) + q(t) \triangle f(c + A, t+1)\\ &\quad + \max_{\vec{u}\in U}\{p(t)(aRu - \triangle f(c,t+1)),0\}, \end{aligned} \tag{18}$$

and

$$\begin{aligned}f(c-1,t) &= f(c-1,t+1)\\ &\quad + q(t) \triangle f(c-1+A, t+1)\\ &\quad + \max_{\vec{u}\in U}\{p(t)(aRu - \triangle f(c-1,t+1)),0\}. \end{aligned} \tag{19}$$

1. The function that preserves the order according to its variables is called monotone function. Particularly, this property denotes to non-decreasing function and concave in the above context [27], [28].

This article has been accepted for publication in a future issue of this journal, but has not been fully edited. Content may change prior to final publication. Citation information: DOI 10.1109/TCC.2018.2878023, IEEE Transactions on Cloud Computing

From previous proof, we have

$$\triangle f(c,t+1) - \triangle f(c-1,t+1) \leq 0, \quad (20)$$
$$\triangle f(c+A,t+1) - \triangle f(c-1+A,t+1) \leq 0, \quad (21)$$

and therefore

$$p(t)(aRu - \triangle f(c,t+1)) \leq p(t)(aRu - \triangle f(c-1,t+1)).$$

Hence,

$$\max_{\vec{u}\in U}\{p(t)(aRu - \triangle f(c,t+1)),0\} \leq \max_{\vec{u}\in U}\{p(t)(aRu - \triangle f(c-1,t+1)),0\}. \quad (22)$$

Substituting the value of (18), (19), (20), (21), and (22) on the right hand side of (17) results the following:

$$\triangle f(c,t) \geq \triangle f(c,t+1) \quad \square$$

This is sensible because the chance of rejecting a request is higher at the beginning of a horizon than it is at the end of the horizon. For more information about the non-decreasing and non-increasing properties of a value function, including its representations in this area, we refer the reader to [30], [31] and [32].

Theorem 2 (Concavity property): $f(C,t)$ is concave in C, $C = \{c\}$.

Proof: For this purpose, the same approach of [17] can be adopted.

The property in Theorem 1 shows that the total expected revenue increases as the capacity offered to the spot market increases. The property of Theorem 2 shows that the percentage of this increase decreases as the capacity increases. Indeed, these properties have significant importance not merely because they reveal an economic nature, but also have a crucial role in search space reduction for optimization purposes. Especially, when considering the feasible solution of linear programming to solve such a problem as is clear in Section 3.

2.3.2 Multiple Classes

So far both the above theorems are true under a strict condition. All cloud resources are represented only by one class of VMs, which is admittedly a large assumption that requires further investigation. Consequently, we have to propose properties of multiple class model. In other words, the customer is able to request a variety of VMs simultaneously (i.e. one VM of the first class, zero VM of the second class, three VMs of the third class, and so on). Each VM class has a particular price as in Fig. 3. The prices vary depending on the available capacity at a certain time, as we previously mentioned. Notably, incorporating the operational costs for each VM class is beyond the scope of this paper. Theorem 3 (Non-Monotone property): $\triangle f(C,t)$ is not necessarily monotone in the available capacity C.

Proof. Let $\triangle f(C,t)$ be supermodular in C, which represents the remaining capacity of all classes. For simplicity, assume that $C = \{c_1, c_2\}$ is limited to two classes of VMs, (c_1, c_2) and (c_1', c_2') are two states in the cloud, where $c_1 \succeq c_1'$ and $c_2' \succeq c_2$. Since $\triangle f(C,t)$ is supermodular, we can write the following inequality [33].

$$\triangle f((c_1,c_2)) + \triangle f((c_1',c_2')) \leq \triangle f((c_1,c_2)\vee(c_1',c_2')) + \triangle f((c_1,c_2)\wedge(c_1',c_2')), \quad (23)$$

which yields

$$\triangle f((c_1,c_2)) + \triangle f((c_1',c_2')) \leq \triangle f((c_1,c_2')) + \triangle f((c_1',c_2)). \quad (24)$$

Rearranging (24) as follows

$$\triangle f((c_1,c_2)) - \triangle f((c_1',c_2)) \leq \triangle f((c_1,c_2')) - \triangle f((c_1',c_2')) \quad (25)$$

which represents the sufficient condition, increasing differences, for supermodularity. Therefore, $\triangle f(C,t)$ is still monotone similar to its status in one class model. However, suppose $c_1 = c_1'+1$, $c_2' = c_2+1$ and suppose reward of class 1 and 2 are R_1 and R_2 respectively where $R_1 < R_2$ and the probability of selling one VM of class 1 is higher than it is for class 2. Substituting in (25)

$$\triangle f((c_1'+1,c_2+1)) < \triangle f((c_1',c_2+1)) \quad (26)$$

and

$$\triangle f((c_1',c_2)) < \triangle f((c_1'+1,c_2)). \quad (27)$$

Adding (26) and (27) and rearranging gives

$$\triangle f((c_1'+1,c_2)) - \triangle f((c_1',c_2)) \geq \triangle f((c_1'+1,c_2')) - \triangle f((c_1',c_2')). \quad (28)$$

$\square$

This shows decreasing differences, which is a contradiction for supermodularity.

The non-monotonicity property demonstrates the economic phenomenon of rejecting the request when the customer's bid is worthy for a class of VMs and not worthy for another class simultaneously, namely in a single request. The underlying rationale is in the multiple classes system where the request is either entirely accepted or rejected. This behaviour of the total expected revenue implies extra complexity to the problem because the optimal solution may be local not global.

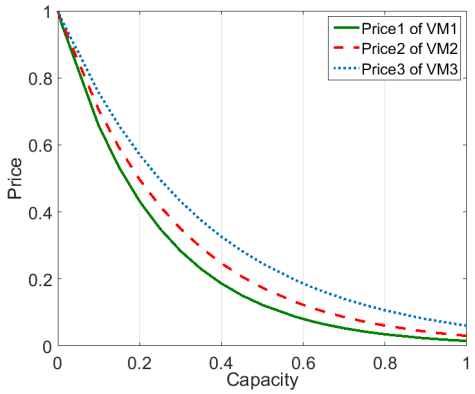

Fig. 3: Prices for multiple classes

This article has been accepted for publication in a future issue of this journal, but has not been fully edited. Content may change prior to final publication. Citation information: DOI 10.1109/TCC.2018.2878023, IEEE Transactions on Cloud Computing

3 Dynamic Programming Approximation

Approximate dynamic programming is one of the most well known approaches used to steer clear of dimensionality. The seminal effort on this context is also credited to Bellman [34]. The linear program of such a problem can be written as:

$$\begin{aligned} V = \max_{X} & \sum_{j} R_j X_j \\ \text{s.t.} \quad & X_j \leqslant C_j \quad \forall j \\ & X_j \leqslant \sum_{t} p_j(t) \quad \forall j \\ & \sum_{t} q_j(t) \leqslant X_j \quad \forall j \\ & X_j \geqslant 0 \quad \forall j \end{aligned} \tag{29}$$

Obviously, to obtain the maximum expected value V of selling X_j expected units of class j, we have to solve (29) frequently over the horizon. Approximate dynamic programming using linear programming is broadly studied in this area. While [35] proves linear programming provides lower bound of objective values for cost-to-go dynamic formulation, [36] captured upper bound of optimal values. From this preservative, once the linear formulation is used to capture an optimal solution of (29), the corresponding approximate optimal solution of (4) can be obtained by accepting any request that holds the following inequality:

$$a_j R_j + \bar{f}(C - A^j, t+1) \geq \bar{f}(C, t+1),$$

where $\bar{f} = V^*$. The outline of the proposed cloud revenue maximization using the approximate dynamic programming algorithm is given in Algorithm 1. We refer to this algorithm as Cloud Revenue Maximization-Dynamic Pricing (CRM-DP). CRM-DP relies on values of linear approximation of the original dynamic programming values. Note that lines 2 to 4 initialize the maximum number of VMs for each class available for sale, and lines 5 to 7 assign the reward for each class of VM before the announcement of sale. In particular, this reward is evaluated in terms of ρ at the end of horizon, namely the end of sale period $t = T$. Hence the system calculates the expected revenue for each state as stated in line 8. Lines 9 to 13 can be updated every time epoch to satisfy the heterogeneous nature of demands. The one-step probability matrix P_u, also known as the stochastic matrix, represents the probability transitions from any state to others for each decision u. More specifically, it is constructed depending on the expected demand, and the probability to request VM and probability to release it. This can be expressed as a transition from one state to another considering the decision to accept ($u = 1$) and to reject ($u = 0$) the request. Using this general framework, the probability transition matrix in case of accept the request, P_1, can be represented as

$$P_1 = \begin{bmatrix} p_{11} & p_{12} & \cdots & p_{1k} \\ \vdots & \vdots & \ddots & \\ p_{k1} & p_{k2} & \cdots & p_{kk} \end{bmatrix},$$

where p_{nm} is the probability to transfer from state n to state m in case of accepting the request. It is worth mentioning that

$$\sum_{m=1}^{k} p_{nm} = 1$$

and $p_{nm} \geq 0$.

On the other hand, the probability transition matrix in case of reject the request, P_0, can be represented as an identity matrix $P_0 = \boldsymbol{I}_{kk}$. Line 14 adjusts t to be the period immediately before the end of horizon T. Thereafter lines 16-25 iterate backward to the beginning of horizon $t = 0$. In each iteration, the system computes both the approximated maximum revenue of the current state of cloud resources $\bar{f}(C, t+1)$ and of the next state $\bar{f}(C - A^j, t+1)$ that results from excluding requested VMs from the current state. Line 19 evaluates the worth action, either to sell or to wait for a more promising request in the future. It is worth noting that the arrival of request A^j initiates the system to start the iteration in order to reveal the correct action.

Algorithm 1 CRM-DP

```
1: Initialization :
2: for each class j, j = {1, ..., n} do
3:    c_j(0) = max. number of VMs available for sale
4: end for
5: for each class j, j = {1, ..., n} do
6:    R_j(T) = initial value
7: end for
8: Set f(C, T) for all states
9: for all u ∈ U do
10:   for all c_j ∈ C do
11:      Set one-step probability transition matrix P_u
12:   end for
13: end for
14: t = T − 1
15: Compute:
16: while t ≥ 0 do
17:      f̄(C, t + 1)
18:      f̄(C − A^j, t + 1)
19:   if (a_j R_j + f̄(C − A^j, t + 1) ≥ f̄(C, t + 1)) then
20:      u = 1    "Accept"
21:   else
22:      u = 0    "Reject"
23:   end if
24:   t = t − 1
25: end while
```

Before delving into analyzing the complexity details of CRM-DP algorithm, we focus first on the big picture from an optimization viewpoint. Stochastic dynamic programming problems are generally intractable. However, [37] states that some sort of such problems under restrictive assumptions are NP-hard. Consequently, linear programming approximation has been used to move the problem to a tractable domain. In terms of work done for solving linear programming problems, researchers propose many approaches that provide algorithms of P class [38] and [39]. In this context, the complexity of solving (29) is $O(k)$. Based on the above, it is easy to deduce CRM-DP's complexity. Initializing number of VMs available for sale for n class requires $O(n)$ time. Similarly, assigning reward for each class requires $O(n)$. Setting

This article has been accepted for publication in a future issue of this journal, but has not been fully edited. Content may change prior to final publication. Citation information: DOI 10.1109/TCC.2018.2878023, IEEE Transactions on Cloud Computing

the expected revenue for each state in line 8 requires $O(k^n)$ time. Then to setup P_u the system consumes $O(k^{2n})$ time. To judge which decision is more worthy, accept or reject, the system derives approximate maximum expected revenue for both states C and $C - A^j$ using linear programming approximation. As this process iterates T epochs, it takes $O(Tk)$ of time. Consequently, the complexity of CRM-DP algorithm is $O(max(k^{2n}, Tk))$. It is worth noting that the total number of classes n is relatively small in real-world problems and likewise the number of time intervals T.

4 Performance Evaluation

In this section, we present detailed numerical results of optimal revenue to validate the optimal policy and value function properties. Our discussion addresses two main scenarios, the first restricts cloud's VMs to one class, which is a coarse scenario, whereas the second considers a cloud of multiple classes of VMs. We provide the expected optimal revenue comparisons through soft and robust demand rates. We also discuss the mutual effect of demand rate on optimal revenue. For both soft and robust rates, we study the dynamics of price over the horizon. Then, we present the running time of our formulation after approximation (CRM-DP) compared with Hong's approach [17].

4.1 One Class Scenario

In this scenario, we assume that the cloud has merely one class of VMs and the maximum capacity of VMs allowed for the dynamic pricing scheme, namely spot market, C is set to 100 VMs. The length of the horizon and the price are normalized to $[0, 1]$, where the one hour decision horizon length is divided into 60×60 intervals; each decision interval t is 2.7×10^{-4} seconds. We argue that this time interval satisfies Poisson distribution condition, one event at a time.

4.1.1 Impact of Demand Rate

Figs. 4a and 4b present the expected optimal revenue within the last 10 slots of variant capacities. We observe that the optimal revenue converges with the value at the beginning of the horizon and monotonically decreases close to the closing time, which satisfies model properties in Section 2.3.1. In case of soft arrival demands $(\gamma = 10)$, the optimal revenue rapidly decreases in time, particularly at extreme capacity $(C = 100)$, as shown in Fig. 4a. Moreover, Fig. 4b reveals that a very high demand has a minor effect on short remaining time $(f^*_{\gamma=10}(100, 0.9975) = 8.96$ versus $f^*_{\gamma=60}(100, 0.9975) = 11.13)$. Fig. 4c demonstrates how the time has a weak influence on the revenue in soft arrival rate $(\gamma = 5)$, apart from closing time, as compared with a strong effect. In the case of robust arrival rate $(\gamma = 40)$ over the entire horizon, this is reasonable because it reflects the natural phenomenon of more time, more gain. Thus, the results of Fig. 4 correlate with the monotone property of the value function in Section 2.3.1.

4.1.2 Optimal Price

Fig. 5 depicts the results for two different cases. When $\gamma = 5$ (low arrival rate), the optimal price decreases with a slight consumption of capacity, indicating the attraction of more customers, as shown in Fig. 5a at the beginning of horizon until the time 0.027 where the price decreases from $\$0.030$ to $\$0.029$ since there are no bids. Further, a considerable decrease in capacity leads to a rapid increase in price, indicating attempts to increase the expected revenue. This is clearly shown within the interval $[0.027, 0.055]$, between the two vertical dotted lines. Furthermore, when $\gamma = 60$ as shown in Fig. 5b, it is easy to note that the optimal price and remaining capacity are inversely related. However, the model attempts to limit the rise in price at the fourth quarter of the time horizon. Thus, Fig. 5b implies that a high demand rate and capacity consumption increases the optimal price, especially at open time.

4.1.3 Optimal Policy

Recalling from Section 2.2, with a view to achieving maximum expected revenue over the horizon, we must select the optimal decision u^* (9) that leads to the optimal policy π^*. The corresponding numerical results are presented in Fig. 6. Here, we assume that the total capacity is $C = 20$, with two different demand rates. Fig. 6a shows that the optimal policy π^* is $\{0, 1, 1, 1, 1, 1, 1, 1, 1, 1\}$, where the remaining VMs is 9 and the demand rate $(\gamma = 5)$ is low. By contrast, Fig. 6b shows that it is $\{0, 0, 0, 1, 1, 1, 1, 1, 1, 1\}$ when the demand rate $(\gamma = 10)$ is higher. This means that it is better to reject the request when there is enough time to sell, in

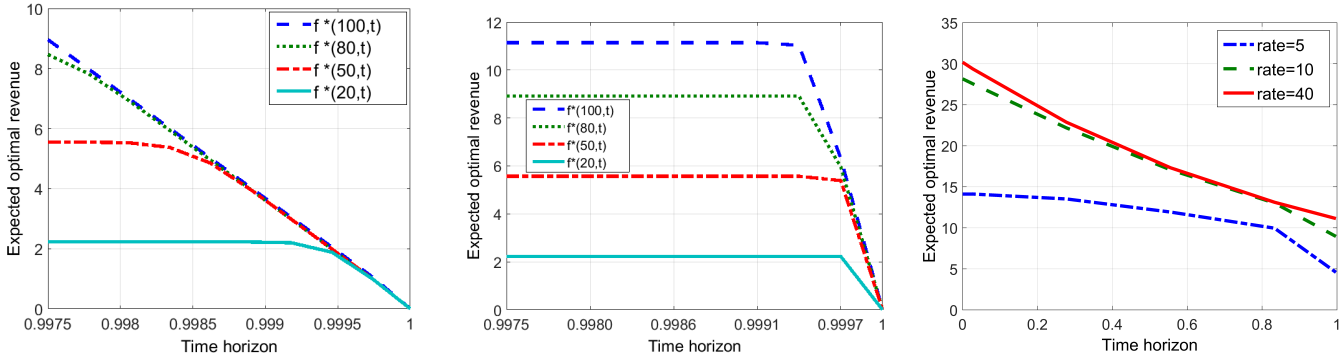

(a) Mean rate $\gamma = 10$ (b) Mean rate $\gamma = 60$ (c) Revenue vs. rates

Fig. 4: Expected optimal revenue (One class scenario)

This article has been accepted for publication in a future issue of this journal, but has not been fully edited. Content may change prior to final publication. Citation information: DOI 10.1109/TCC.2018.2878023, IEEE Transactions on Cloud Computing

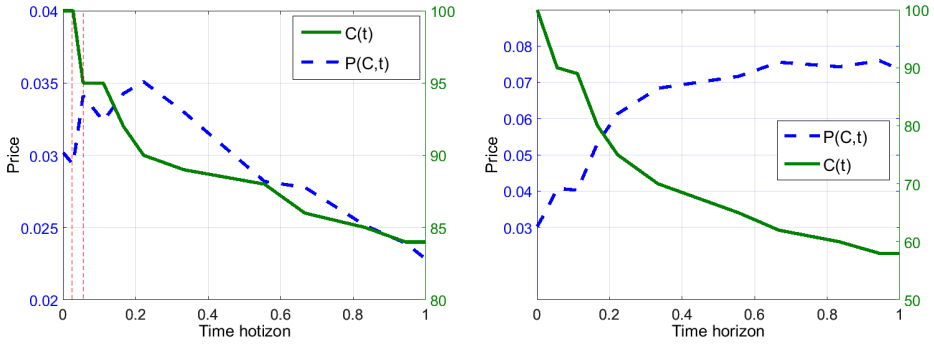

(a) Low mean rate $\gamma = 5$ (b) High mean rate $\gamma = 60$

Fig. 5: Optimal price (One class scenario)

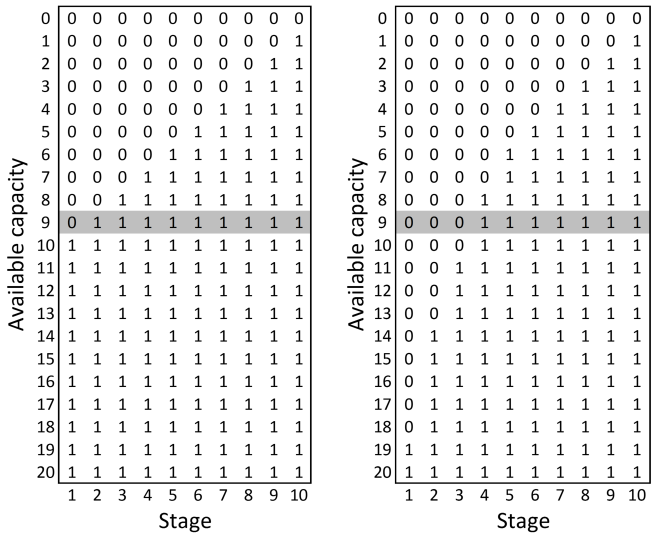

(a) Optimal Policy with $\gamma = 5$ (b) Optimal policy with $\gamma = 10$

Fig. 6: Optimal policy with entire capacity $C = 20$ and variant rates (One class scenario)

case of robust demand, to aim at higher profit in the future. Surprisingly, the result points out to accept all subsequent identical requests that offer rewards exceeded or equal to the first accepted reward until the end of horizon in case of homogeneous demand, namely stable arrival and departure rates.

4.1.4 *Sample Path Revenue*

This section proceeds by attempting to answer the question about the values of expected optimal revenue and price in a practical cloud environment. In this regard, we simulate a system of 100 VMs available for spot market with starting normalized prices \$ 0.0277 and \$ 0.030, for low and high rates respectively. They are remarkably low and are nearly equivalent to some classes of Amazon's Spot Instances [3]. The simulation execution, fulfilled many times, generates a random sample path revenue and price for both low and high demand rates using Poisson distributions. Fig. 7 demonstrates the application of our model in low demand rate $\gamma = 10$. Fig. 7a shows the expected cumulative revenue within 1 hour horizon in which the customers consume 11 VMs generating the capacity path from 100 to 89 VMs and resulting in \$ 0.261 at the end of horizon. It is clear that the revenue grows as a linear stair-step. Our dynamic pricing scheme records accepted prices as shown in Fig. 7b. The price level generally decreases over the horizon, from \$ 0.0277 to \$ 0.0182 with local increases in some intervals as in $[0.2, 0.3]$ time interval. The price level increase from \$ 0.0261 to \$ 0.0267 aims to increase the revenue in case of market recovery. Indeed, the price has the same characteristics observed in theoretical analysis, Fig. 5a.

On the other side, simulating the model considering very high demand rate $\gamma = 120$ achieves cumulative revenue \$ 24.59 at the end of horizon as shown in Fig. 8a. Further, the revenue seemingly grows exponentially and all stagnant resources, 100 VMs available for spot market, have been utilized before the end of the horizon. Furthermore, the optimal price steadily grows with more differentiation in the second half of the horizon and hence peaks near the end of it as exhibited in Fig. 8b.

4.2 Multiple Classes Scenario

For simplicity, we assume that the system has three classes of VMs $C = \{c_1(t), c_2(t), c_3(t)\}$ with homogeneous demand rates. The maximum quantity allowed to share in spot market is 30, so the cloud could supply up to $C = \{30, 30, 30\}$ for spot market.

4.2.1 *Impact of Demand Rate*

Fig. 9 present the expected optimal revenue within the last 10 slots for three cases of cloud. It should be easy to note that the demand rates, both low and high, have analogous effects on the optimal revenue as in one class scenario. For instance, Fig. 9a shows that the expected optimal revenue peaks with approximately $f^*_{\gamma=2}(10, 10, 10, 0.9975) = 5.89$ at time 0.9975, 10 slots before the end of horizon. Then, it rapidly decreases at the end of horizon in case of low demand rate ($\gamma = 2$). Likewise, the expected optimal revenue amounts to $f^*_{\gamma=30}(10, 10, 10, 0.9975) = 65.96$ at the same time and decreases at the end of horizon in case of high demand rate ($\gamma = 30$), which is illustrated in Fig. 9b.

This article has been accepted for publication in a future issue of this journal, but has not been fully edited. Content may change prior to final publication. Citation information: DOI 10.1109/TCC.2018.2878023, IEEE Transactions on Cloud Computing

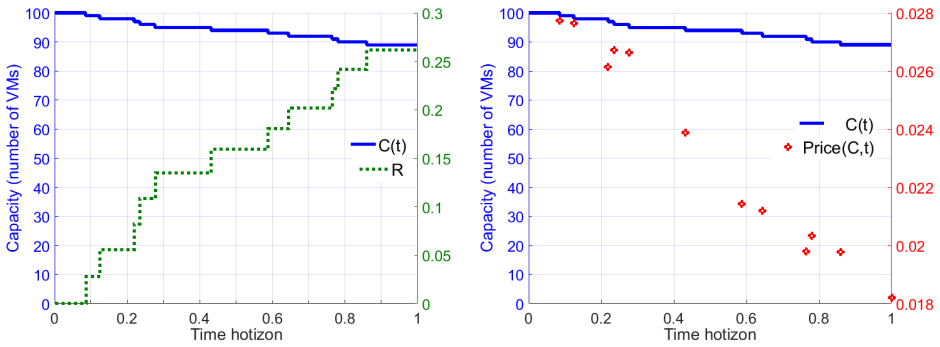

(a) Capacity and reward (b) Capacity and price

Fig. 7: Random walk, low rate $\gamma = 10$

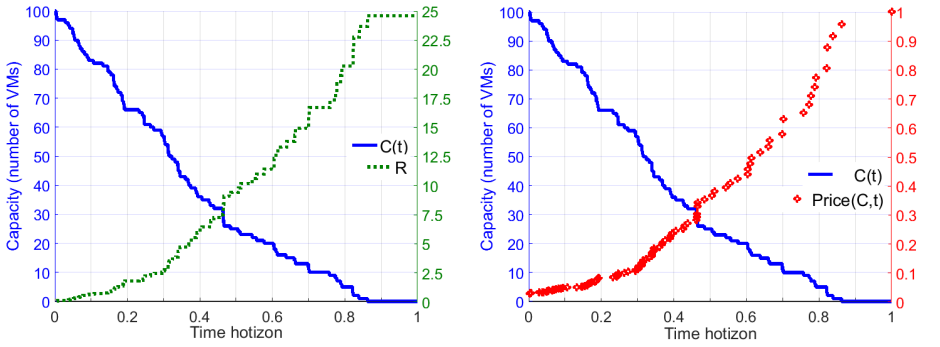

(a) Capacity and reward (b) Capacity and price

Fig. 8: Random walk, high rate $\gamma = 120$

At first glance, the variation between these two scenarios seems somewhat insignificant, but closer auditing reveals that multiple classes scenario tends to reap more revenue even at a lower demand ratio. The expected revenue of the total 30 VMs is $f^*_{\gamma=2}(10, 10, 10, 0.9975) = 5.89$ with demand ratio $\frac{2}{30} = 0.06$ in case of multiple classes versus $f^*_{\gamma=10}(50, 0.9975) = 5.55$ with demand ratio $\frac{10}{50} = 0.2$ in case of one class scenario Fig.4a.

4.2.2 Expected optimal revenue

In this debate, the reader might wonder about the monotonicity of the revenue function. Fig. 10 depicts the result of expected optimal revenue. When the mean arrival rate $\gamma = 2$, the length of horizon is 3600 intervals, and at the beginning of the horizon the state of the cloud is in the range $C \in [\{0, 0, 0\}, \{2, 2, 2\}]$. For the sake of clarity, state 1 represents $C = \{0, 0, 0\}$ and state 26 represents $C = \{2, 2, 2\}$. The interesting point in this figure, is that the optimal revenue increases in general, but absolutely it is not monotone. Indeed, this legalizes our theoretical and mathematical analysis and proof shown in Section 2.3.2. Moreover, these results coincide with the economic rationale: one class of VMs could raise cloud revenue more than others depending on how much the customer is willing to pay for each class of VMs. To compute the optimal revenue of the current available capacity $C = \{2, 2, 2\}$, namely the system is in state 26 and Markov decision process implies traversing 26 states. For instance, assume the current state is $C = \{c_1, c_2, \ldots, c_n\}$, then the system traverses

$$S = (\prod_{j=1}^{n}(c_j + 1)) - 1$$

states. Furthermore, the proposed cloud model has two actions, accept or reject, which implies 2^S possible policies. Finding the best policy among such a massive number of policies is a very significant issue.

4.2.3 Optimal Policy

While managing bids over the course of the horizon, which multiple classes cloud aims to maximize the revenue, it would be too interesting to select the optimal decision u^* (9) that results in the optimal policy π^* as in case of one class scenario. To reveal the optimal policy, we should observe numerical results presented in Fig. 11. The figure records the results, taking into consideration that the current capacity available for spot market is $C = \{2, 2, 2\}$ and the demand rate $\gamma = 2$. Consequently, the figure shows that the optimal policy π^* is $\{0, 0, 1, 1, 1, 1, 1, 1, 1\}$; since, the demand $(\gamma = 2)$ is low and the supply is high relative to the demand. It is worth noting that in our previous experiments to solve one class of VMs, the optimal policy is to accept in all cases after the first acceptance in any stage if the capacity

This article has been accepted for publication in a future issue of this journal, but has not been fully edited. Content may change prior to final publication. Citation information: DOI 10.1109/TCC.2018.2878023, IEEE Transactions on Cloud Computing

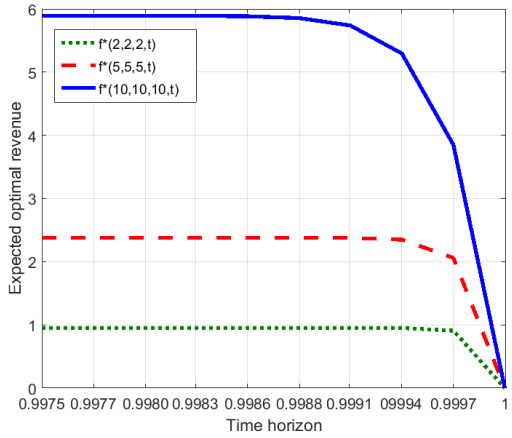

(a) Mean rate $\gamma = 2$

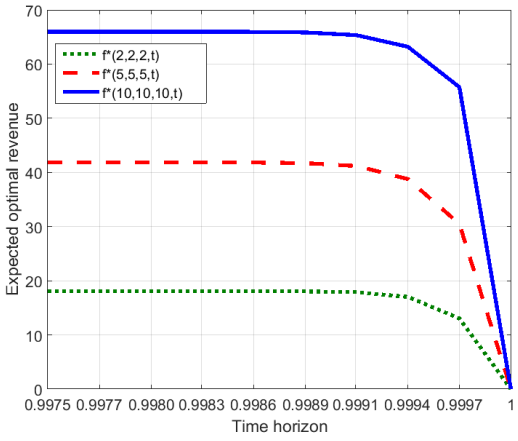

(b) Mean rate $\gamma = 30$

Fig. 9: Expected optimal revenue (Multiple classes scenario)

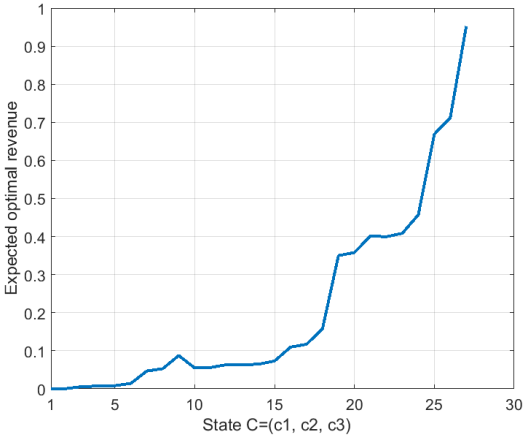

Fig. 10: The optimal revenue with mean arrival rate $(\gamma = 2)$ after $T = 3600$ interval

is above the corresponding first acceptance, Fig. 6, whereas, in multiple classes of VMs, this scenario does not hold in all

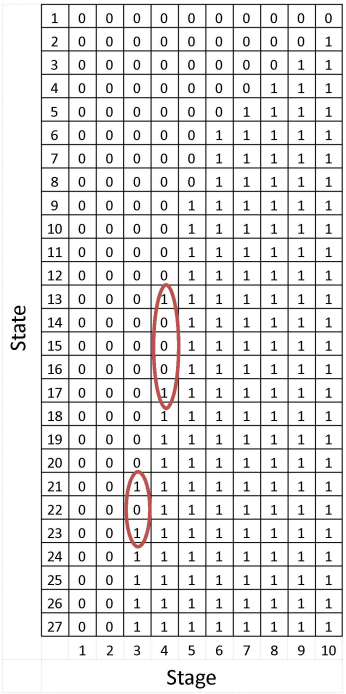

(a) Optimal Policy with $\gamma = 2$

Fig. 11: Optimal policy with entire capacity $C = \{2, 2, 2\}$ and variant rates

cases, such as in stage 3 in Fig. 11, red marker, and so it does in stage 4. This satisfies the model properties in Section 2.3.2, namely the optimal expected revenue is not monotone.

4.3 Comparative Analysis

To expose the extent of the progress have been achieved by our approach (CRM-DP), we study the performance of the most closest approach to ours [17], which we name as Hong. Apart from the multiple classes characteristics, the study includes the evaluation of performance in terms of computing time and price behaviour. For this estimation, we use an Intel Core i7 CPU, 3.6 GHz and 32 GB RAM. First, Fig. 12a indicates the difference in running time between the two methods. Particularly when the number of stages exceeds 500, Hong's growth is linearly proportional to the stages. Unlike CRM-DP, Hong would then be considered to be impractical in this field because the decision should be fulfilled in real time, as is clear in our method. This confirms our approximation in Section 3. Second, in order to evaluate the optimal price behaviour, the experiment assumes that the current pool of stagnant VMs contains 90 VMs out of 100 VMs and the horizon's length is 1 hour like in [17]. To be more credible, the comparison considers merely the behaviour of the optimal price as an evaluating criterion but not the explicit value of the price since the variation in price parameters for each approach. Fig. 12b shows that Hong's approach almost preserves the opening price through the first half of the horizon then gradually increases the price until it peaks at the end of the horizon. On the other hand, CRM-DP's optimal price decreases and increases occasionally according to the supply and demand principle and time

This article has been accepted for publication in a future issue of this journal, but has not been fully edited. Content may change prior to final publication. Citation information: DOI 10.1109/TCC.2018.2878023, IEEE Transactions on Cloud Computing

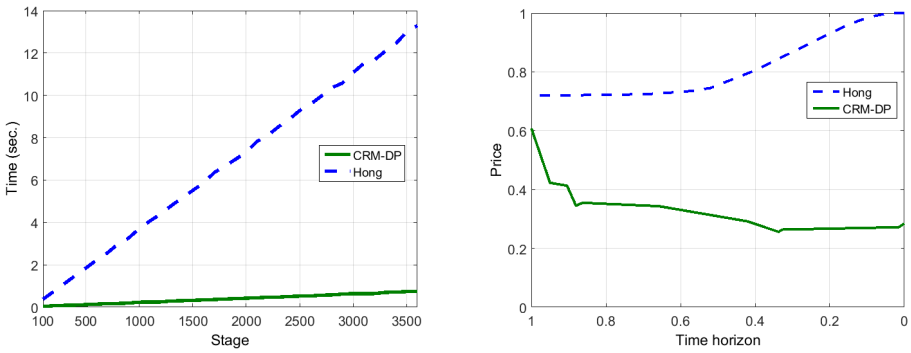

(a) Running time of $f(C = 100)$ (b) CRM-DP price vs Hong price

Fig. 12: CRM-DP vs Hong

as well. At the beginning, the price decreases in order to optimize sales and then the value is adjusted according to observed demands. However, the price generally decreases over the horizon; since, the demand is very low. Hong's price shows a monotonic increase in both low and high demands, as well as low and high capacities. Moreover, [17] claims that the price is independent of the available capacity in case of high capacity and hence, the time is the dominant factor. In fact, this type of dynamic behavior is more suitable for airline seats than cloud because the seating capacity always decreases over the horizon until the departure time, also referred to as, the end of the horizon, and the time is the most crucial factor determining the price. However, in cloud the story is different because the capacity, number of stagnant VMs, decreases or increases alike. Subsequently, CRM-DP shows more dynamic and harmonic behavior with the cloud environment because our approach scale up or down the optimal price according to supply and demand principle. As demonstrated in Figs. 5, 7, and 8, the price increases when the demand rises or when the supply decreases and it decreases when the demand decreases or when the supply increases.

5 Discussion

5.1 Amazon EC2 Spot Instances

Without a doubt, Amazon Web Services (AWS) drastically changes IaaS cloud market through it's Spot Instances. It draws cloud providers and research attention to this type of pricing particularly at the outset; since, the information about the adopted mechanism was scarce. While a large body of studies about Spot Instances have focused on discovering Amazon spot pricing strategy, the studies nearly exclusively analysed over a long time of pricing history (year, month, or a week), e.g. [40] and [41]. The overwhelming majority has concluded that the price adjusted artificially or at least it is bounded within predetermined values [40], [42]. To expand on the findings from the previous research, we study pricing history for Amazon specifically after it reveals slightly about its Spot Instances mechanism. The interesting point that attracts our attention is the prices almost vary based on minutes not months, weeks, or even days. Hence, the prices over one day for c1.meduim VM (Linux/UNIX usage) were monitored through three data centres zones us-west-2a, us-west-2b, and us-west-2c. Fig. 13 shows the prices gathered from 14 Aug 2016 at 19:27:34 to the same time in 15 Aug 2016. It is obvious that,

- The prices are stable for a long time, namely hours, in us-west-2c and us-west-2b, whereas the price varies within minutes in us-west-2a. We deem the demand rates, number of bids, in addition to the capacity of VMs pool, underlie the price changes in a certain time.
- Nevertheless, the price fluctuates between two controlling boundaries.

Further, back to evoke some observations from those whom are interested in this issue [42], [43], unexpected spikes such as the price for m2.2xlarge instances in one zone were found in Sept, 2011. To cope with this debate, Amazon recently discloses some information about its strategy. The customers bid the maximum price they are willing to pay per instance on Amazon's Spot Instances, and the request is accepted if the bid price overrides the presented spot price [44]. Amazon claims that in case all VMs of Spot Instance pool are already utilized, the new customer must bid higher than the current Spot price in order to force the lowest bidder to waive his instance to the new customer. However, from our perspective, this declaration is not convincing. First, according to Amazon's strategy, the customer will bid as close to the current price to save his budget, which contradicts with price spikes; second, it opens the door to manipulations.

6 Related Work

The interesting concept, virtualization, in addition to rapid changes in hardware and software factors raise many significant challenges in cloud computing revenue management problem and vault it to be non-modest optimization problem. The pioneer cloud that takes on dynamic price as a solution for stagnant cloud resources was Amazon. The cloud spot market was launched in 2009 by Amazons Spot Instances [45]. However, its adopted pricing strategy did not become known until the late of 2015. This enticed researchers to analyze its spot pricing mechanism in detail

This article has been accepted for publication in a future issue of this journal, but has not been fully edited. Content may change prior to final publication. Citation information: DOI 10.1109/TCC.2018.2878023, IEEE Transactions on Cloud Computing

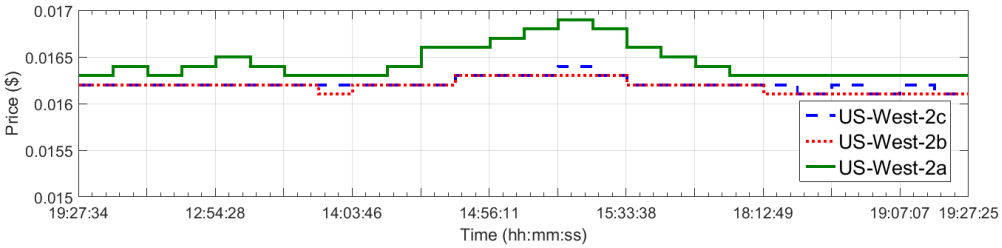

(a) Amazon VM.

Fig. 13: VM class=c1.medium us-west-2a us-west-2b us west-2c have taken 14 Aug 2016 19:27:34 to 15 Aug 2016 19:27:34

and to broadly evaluate static and dynamic pricing schemes in cloud computing businesses aimed at maximizing cloud turnover values. While extensive research has examined static pricing schemes to increase profits through reducing the costs, little attention has focused on dynamic pricing schemes. For example, [40] analyzes the spot instances pricing for a year of four data centers of EC2 and statistically modeled spot price dynamics as a mixture of Gaussian distribution hourly and daily, which was a weak match for some instance types. Additionally, the accuracy of the results varies according to the number of components and the study is limited to a maximum of 4 components (VMs). Otherwise, [46] presents a microeconomic approach to meet the equilibrium point that satisfies, first, the consumer's budget and performance, and second, the vendor's profits. The cloud dynamically adjusts the number of VMs available for each user corresponding to the amount of money paid. However, the model absolutely assumes that cloud's response time and users' willingness to pay are inversely proportional and such a model is profitable when there is sufficient resources to satisfy all requests. By mimicking the natural selection process, [47] shows how the genetic algorithm model in a competitive cloud environment can evolve the price from naive to a convenient value to maximize profits. However, a brokers' platform is required. Likewise, some business mechanisms, such as negotiation, inspire [48] to adopt a PTN-price and time slot negotiations-mechanism. Its time slot utility function captures an agent's different scales of satisfaction for various time slots, using the "burst mode" algorithm. Whereas, auction induces [6] to model a dynamic auction, where customers may arrive to reserve a VM for many intervals, while a price dynamically changes according to proposed capacity allocations. [49] agrees and induces a heuristic approach to reduce the exponential complexity. Furthermore, [50] provides truthful real-time auction mechanism for cloud resource provisioning considering only one class of resources and discriminates three types of customers to ensure the truthfulness. Ultimately, this type of auctions is fruitful from a practical point of view merely when high arrival rates are met. [51] identifies the best hybrid cloud deployment and adopts a dynamic resource allocation model that accepts the request based on the utilization level in clouds. However, the model is restricted to identical physical machines clouds. [52] discusses the effect of remaining unused slots on maximizing the social welfare but not the revenue of cloud providers. In other words, it tries to find the balance between users themselves from one side and between users and providers from another side based on hourly charged slots. Others try to implicate all pricing schemes, reserved, on-demand, and spot, in a single problem [53]. This approach has encountered many obstacles which resulted in rigorous assumptions and a reduction of the granularity. By dividing the capacity by 100, the time slot is one hour, one class of VM, and pseudo optimal algorithm. [54] proposes a dynamic pricing algorithm to maximize profit of cloud that consists of distributed datacenters. The suggested algorithm considers the power consumption in each geographic zone and assigns the price according to many factors, type of job, length of time requested, number of physical servers, number of VMs desired to do the job, and others. In other words, the algorithm schedules and distributes the arrival jobs to reduce the operational costs. Indeed this type of algorithm is more appropriate to on-demand pricing schemes not for spot pricing schemes. Needless to say, exploiting some characteristics of services would relatively increase returns, but the main issue remains the management of abstract VM as a commodity. From this perspective, [17] designs a revenue maximization system based on a continuous-time finite horizon with the stochastic demands of arrival and departure of an IaaS cloud. Then, [41] tackles the same problem as infinite horizon revenue maximization. In [55], we maximize cloud revenue through dynamic discrimination of VMs' prices using discrete finite horizon Markovian decisions and hence, we utilize a column generation approach in order to increase decision-making speed in [56]. This paper is approximately comparable with [17] and related to [55] , except that it addresses multiple classes of VMs, derives some properties for both one class and multiple classes clouds that validate the functionality of our proposed model, and leverages a practical model using linear programming. These differences contribute to a more efficient performance from both the technical and practical perspectives.

7 Conclusion

The use of thoughtful spot price of virtual machines has a significant role in contemporary cloud economy because it not only directly related to their revenue, but it also mitigates cloud congestion. Both the uncertainty of arrival and departure demands and the high state complexity pose a challenge to address revenue maximization in real time. Therefore, this paper proposed CRM-DP, a systematic approach towards the challenging aim of cloud revenue

This article has been accepted for publication in a future issue of this journal, but has not been fully edited. Content may change prior to final publication. Citation information: DOI 10.1109/TCC.2018.2878023, IEEE Transactions on Cloud Computing

maximization, which is specifically tailored towards dynamic price of stagnant VMs of both one class and multiple classes. To inspire, CRM-DP we incurred a formulation of profit maximization, using a discrete finite horizon, characterization of optimal properties and controlling conditions, and an approximation of dynamic processes using linear programming. An interesting point of the results is that the multiple class plan is more profitable than one class. Unlike the previous methods of maximizing cloud profitability that focus on feasibility, our CRM-DP shows practical and new dynamic analysis insight. Additionally, the numerical results capture and define the optimal policy and demonstrate our analysis. This work amounts to a step ahead in IaaS cloud revenue maximization. It also opens the door to many ideas for future work such as creating more efficient dynamic algorithms to involve different classes of VMs.

REFERENCES

[1] *Amazon EC2 Pricing*. Amazon Web Services Inc. Seattle, WA 98108-1226. [Online]. Available: http://aws.amazon.com/ec2/pricing/

[2] *Azure pricing*. Microsoft Azure. Redmond, WA 98052-6399. [Online]. Available: https://azure.microsoft.com/en-us/pricing/details/virtual-machines/

[3] *Amazon EC2 Spot Instances Pricing*. Amazon Web Services Inc. Seattle, WA 98108-1226. [Online]. Available: https://aws.amazon.com/ec2/spot/pricing/

[4] *Pricing*. Google Inc. Mountain View, CA 94043 USA. [Online]. Available: https://cloud.google.com/pricing/

[5] *Virtual Servers*. SoftLayer Technologies. Dallas, Texas. [Online]. Available: http://www.softlayer.com/virtual-servers

[6] W. Wang, B. Liang, and B. Li, "Revenue maximization with dynamic auctions in IaaS cloud markets," in *IEEE/ACM 21st International Symposium on Quality of Service (IWQoS)*, 2013, pp. 1–6.

[7] *Gartner Says Worldwide Public Cloud Services Market to Grow 18 Percent in 2017*. Gartner, Inc. Stamford, CT 06902 USA. [Online]. Available: http://www.gartner.com/newsroom/id/3616417

[8] A. V. Nimkar and S. K. Ghosh, "Towards full network virtualization in horizontal iaas federation: Security issues," *Journal of Cloud Computing: Advances, Systems and Applications*, vol. 2, no. 1, pp. 48:1–48:13, 2013.

[9] C. Reiss, A. Tumanov, G. R. Ganger, R. H. Katz, and M. A. Kozuch, "Towards understanding heterogeneous clouds at scale: Google trace analysis," *Intel Science and Technology Center for Cloud Computing, Technical Report*, 2012. [Online]. Available: http://www.pdl.cmu.edu/PDL-FTP/CloudComputing/ISTC-CC-TR-12-101.pdf

[10] *Infrastructure as a Service (IaaS) market share in first half of 2015, by vendor*. Statista Inc. New York, NY 10004. [Online]. Available: https://www.statista.com/statistics/478143/iaas-vendor-market-share-ranking-worldwide/

[11] C. Delimitrou and C. Kozyrakis, "Quasar: Resource-efficient and qos-aware cluster management," *ACM SIGARCH Computer Architecture News*, vol. 42, no. 1, pp. 127–144, 2014.

[12] *Cloud Computing, Server Utilization, & the Environment*. Amazon Web Services Inc. Seattle, WA 98108-1226. [Online]. Available: https://aws.amazon.com/blogs/aws/cloud-computing-server-utilization-the-environment/

[13] *Data Center Efficiency Assessment*. Natural Resources Defense Council. New York, NY 10011. [Online]. Available: https://www.nrdc.org/sites/default/files/data-center-efficiency-assessment-IP.pdf

[14] S. Yi, D. Kondo, and A. Andrzejak, "Reducing costs of spot instances via checkpointing in the amazon elastic compute cloud," in *IEEE 3rd International Conference on Cloud Computing*, 2010, pp. 236–243.

[15] B. Javadi, R. K. Thulasiramy, and R. Buyya, "Statistical modeling of spot instance prices in public cloud environments," in *Fourth IEEE International Conference on Utility and Cloud Computing*, 2011, pp. 219–228.

[16] J. Cao, K. Hwang, K. Li, and A. Y. Zomaya, "Optimal multiserver configuration for profit maximization in cloud computing," *IEEE Transactions on Parallel and Distributed Systems*, vol. 24, no. 6, pp. 1087–1096, 2013.

[17] H. Xu and B. Li, "Dynamic cloud pricing for revenue maximization," *IEEE Transactions on Cloud Computing*, vol. 1, no. 2, pp. 158–171, 2013.

[18] We power the Microsoft Cloud. Microsoft. One Microsoft Way, Redmond, Washington. [Online]. Available: http://www.microsoft.com/en-us/server-cloud/cloud-os/global-datacenters.aspx

[19] N. Jin, G. Venkitachalam, and S. Jordan, "Dynamic congestion-based pricing of bandwidth and buffer," *IEEE/ACM Transactions on Networking (TON)*, vol. 13, no. 6, pp. 1233–1246, 2005.

[20] I. C. Paschalidis and J. N. Tsitsiklis, "Congestion-dependent pricing of network services," *IEEE/ACM Transactions on Networking*, vol. 8, no. 2, pp. 171–184, 2000.

[21] S. Sen, C. Joe-Wong, S. Ha, and M. Chiang, "Incentivizing time-shifting of data: a survey of time-dependent pricing for internet access," *IEEE Communications Magazine*, vol. 50, no. 11, pp. 91–99, 2012.

[22] P. Cramton, "Review of the reserves and operable capability markets: New englands experience," in *in the First Four Months, White Paper, Market Design Inc*, 1999.

[23] R. G. Lipsey and C. Harbury, *First Principles of Economics*. Oxford University Press, 1992.

[24] N. Mankiw, *Principles of Economics, 2ed Edition*. Harcourt Brace & Company, Orlando, FL, 2001.

[25] E. L. Williamson, "Airline network seat inventory control: Methodologies and revenue impacts," Massachusetts Institute of Technology, Flight Transportation Laboratory, Technical Report, Tech. Rep., 1992. [Online]. Available: http://hdl.handle.net/1721.1/68123

[26] M. Agarwal, V. S. Borkar, and A. Karandikar, "Structural properties of optimal transmission policies over a randomly varying channel," *IEEE Transactions on Automatic Control*, vol. 53, no. 6, pp. 1476–1491, 2008.

[27] G. Gratzer, *Lattice Theory: First Concepts and Distributive Lattices*. Dover Publications, 2009.

[28] G. B. Price, "Definitions and proporties of monotone functions," *Bulletin of the American Mathematical Society*, vol. 46, pp. 77–80, 1940.

[29] J. Keilson and A. Kester, "Monotone matrices and monotone Markov processes," *Stochastic Processes and their Applications*, vol. 5, no. 3, pp. 231–241, 1977.

[30] M. Shaked and J. G. Shanthikumar, *Stochastic orders and their applications*. Boston : Academic Press, 1994.

[31] A. Krokhin and B. Larose, "Maximizing supermodular functions on product lattices, with application to maximum constraint satisfaction," *SIAM Journal on Discrete Mathematics*, vol. 22, no. 1, pp. 312–328, 2008.

[32] A. Krause and D. Golovin, "Submodular function maximization," in *Tractability: Practical Approaches to Hard Problems*, 2014.

[33] D. M. Topkis, *Supermodularity and Complementarity*. Princeton University Press, 1998.

[34] R. Bellman, R. Kalaba, and B. Kotkin, "Polynomial approximation–a new computational technique in dynamic programming: Allocation processes," *Mathematics of Computation*, vol. 17, no. 82, pp. 155–161, 1963.

[35] G. J. Gordon, "Approximate solutions to Markov decision processes," *Carnegie Mellon University, Ph.D. thesis*, 1999.

[36] I. C. Paschalidis and J. N. Tsitsiklis, "Congestion-dependent pricing of network services," *IEEE/ACM Transactions on Networking*, vol. 8, no. 2, pp. 171–184, 2000.

[37] A. Shapiro and A. Nemirovski, *On Complexity of Stochastic Programming Problems*. Springer US, 2005.

[38] N. Karmarkar, "A new polynomial-time algorithm for linear programming," *Combinatorica*, vol. 4, no. 4, pp. 373–395, 1984.

[39] N. Megiddo, *On the complexity of linear programming*. Cambridge University Press, 1987.

[40] B. Javadi, R. K. Thulasiram, and R. Buyya, "Statistical modeling of spot instance prices in public cloud environments," in *Fourth IEEE International Conference on Utility and Cloud Computing (UCC)*, 2011, pp. 219–228.

[41] H. Xu and B. Li, "Maximizing revenue with dynamic cloud pricing: The infinite horizon case," in *IEEE International Conference on Communications (ICC)*, 2012, pp. 2929–2933.

This article has been accepted for publication in a future issue of this journal, but has not been fully edited. Content may change prior to final publication. Citation information: DOI 10.1109/TCC.2018.2878023, IEEE Transactions on Cloud Computing

[42] O. A. Ben-Yehuda, M. Ben-Yehuda, A. Schuster, and D. Tsafrir, "Deconstructing Amazon EC2 spot instance pricing," in *IEEE Third International Conference on Cloud Computing Technology and Science*, 2011, pp. 304–311.
[43] *What to do when Amazons spot prices spike*. Knowingly Inc. Knowingly Corporation 401 Congress Avenue, Suite 1540 Austin, TX 78701-3851. [Online]. Available: https://gigaom.com/2011/12/27/how-to-deal-with-amazons-spot-server-price-spikes/
[44] *Amazon EC2 Spot Instances*. Amazon Web Services Inc. Seattle, WA 98108-1226. [Online]. Available: https://aws.amazon.com/ec2/spot/
[45] *What's New*. Amazon Web ServicesInc. Inc. Seattle, WA 98108-1226. [Online]. Available: http://aws.amazon.com/about-aws/whats-new/2009/
[46] K. Tsakalozos, H. Kllapi, E. Sitaridi, M. Roussopoulos, D. Paparas, and A. Delis, "Flexible use of cloud resources through profit maximization and price discrimination," in *IEEE 27th International Conference on Data Engineering (ICDE)*, 2011, pp. 75–86.
[47] M. Macías and J. Guitart, "A genetic model for pricing in cloud computing markets," in *Proceedings of the ACM Symposium on Applied Computing*, 2011, pp. 113–118.
[48] S. Son and K. M. Sim, "A price- and-time-slot-negotiation mechanism for cloud service reservations," *IEEE Transactions on Systems, Man, and Cybernetics, Part B (Cybernetics)*, vol. 42, no. 3, pp. 713–728, 2012.
[49] U. Lampe, M. Siebenhaar, A. Papageorgiou, D. Schuller, and R. Steinmetz, "Maximizing cloud provider profit from equilibrium price auctions," in *IEEE Fifth International Conference on Cloud Computing*, 2012, pp. 83–90.
[50] H. Zhang, H. Jiang, B. Li, F. Liu, A. V. Vasilakos, and J. Liu, "A framework for truthful online auctions in cloud computing with heterogeneous user demands," *IEEE Transactions on Computers*, vol. 65, no. 3, pp. 805–818, 2016.
[51] L. Du, "Pricing and resource allocation in a cloud computing market," in *Proceedings of the 12th IEEE/ACM International Symposium on Cluster, Cloud and Grid Computing (CCGrid)*, 2012, pp. 817–822.
[52] H. Jin, X. Wang, S. Wu, S. Di, and X. Shi, "Towards optimized fine-grained pricing of IaaS cloud platform," *IEEE Transactions on Cloud Computing*, vol. 3, no. 4, pp. 436–448, 2015.
[53] A. N. Toosi, K. Vanmechelen, K. Ramamohanarao, and R. Buyya, "Revenue maximization with optimal capacity control in infrastructure as a service cloud markets," *IEEE Transactions on Cloud Computing*, vol. 3, no. 3, pp. 261–274, 2015.
[54] J. Zhao, H. Li, C. Wu, Z. Li, Z. Zhang, and F. Lau, "Dynamic pricing and profit maximization for the cloud with geo-distributed data centers," in *IEEE INFOCOM 2014 IEEE Conference on Computer Communications*, 2014, pp. 118–126.
[55] F. Alzhouri and A. Agarwal, "Dynamic pricing scheme: Towards cloud revenue maximization," in *IEEE 7th International Conference on Cloud Computing Technology and Science (CloudCom)*, 2015, pp. 168–173.
[56] F. Alzhouri, A. Agarwal, Y. Liu, and A. S. Bataineh, "Dynamic pricing for maximizing cloud revenue: A column generation approach," in *Proceedings of the 18th ACM International Conference on Distributed Computing and Networking (ICDCN)*, 2017, pp. 22:1–22:9.

PLACE PHOTO HERE

Fadi Alzhouri received the M.Sc. degree in computer engineering from Kuwait University, in 2007. While continuing the M.Sc. degree, he worked on Natural language processing and Artificial intelligence. He is currently pursuing the Ph.D. degree with the Department of Electrical and Computer Engineering, Concordia University, Montreal, Canada. His research interests are in the fields of Cloud Computing, Internet of things, Operations Research, and Optimization.

PLACE PHOTO HERE

Anjali Agarwal (SM03) received her Ph.D. (Electrical Engineering) in 1996 from Concordia University, Montreal, M.Sc. (Electrical Engineering) in 1986 from University of Calgary, Alberta, and B.E. (Electronics and Communication Engineering) in 1983 from Delhi College of Engineering, India. She is currently a Professor in the Department of Electrical and Computer Engineering at Concordia University, Montreal. Prior to joining faculty in Concordia, she has worked as a lecturer in IIT Roorkee, and as a Protocol Design Engineer and a Software Engineer in industry. Her current research interests are in the various aspects of cloud networks, heterogeneous networks, and wireless networks including security and virtualization of cognitive radio networks.

PLACE PHOTO HERE

Yan Liu is an Associate Professor at the Electrical and Computer Engineering Department, Concordia University, Canada. Her research interests are big data stream processing, cloud software architecture, distributed computing, software performance engineering, and adaptive systems. She was a senior scientist at the Pacific Northwest National Laboratory in Washington State where she led R&D projects on data intensive computing for a wide range of domains. She was a senior researcher at National ICT Australia after PhD graduation from The University of Sydney, Australia . She is a member of the IEEE and ACM.

Modelling of structural and material parameters of optical planar waveguide to control birefringence

[1]Yaman Parasher*, [2]Akshay Kaushik, [3]Dr. Gurjit Kaur, [4]Prabhjot Singh
[1]Department of Electronics and Communication Engineering, School of ICT, Gautam Buddha University, Greater Noida, India
[2]Department of Electronics and Communication Engineering, Sanskar College of Engineering and Technology, Ghaziabad, India
[3]Department of Electronics and Communication Engineering, Delhi Technological University, Delhi, India
[4]Salesforce.com EMEA Ltd, San Francisco, CA, USA
parasheryaman19@gmail.com, akshaykaushik002@gmail.com, gurjeet_kaur@rediffmail.com, prabhjot27@gmail.com*

Abstract:

Birefringence is observed when layers in the optical planar waveguide exhibits stresses at elevated temperature. To design birefringence free waveguide structure, we carefully modelled the structural, material parameters with the help of a thermal stress formula.

OCIS codes: (230.0230) Optical Devices; (230.7370) Waveguides

.

1. Introduction

The effect of birefringence has always been a key issue in integrated photonic technologies. It occurs mainly due to the different coefficient of expansions of layers of waveguide and substrate that makes up a complete planar waveguide. In order to deal with this problem, many solutions like the ultraviolet irradiation [1], mid-infrared processing [2], employment of stress-relief grooves [3,4] and addition of Si thin films and doped layers [5-7] on the surface of optical planar waveguide have been used. But due to the complex and time processing process they weren't considered as an ideal option to reduce birefringence in waveguide. Therefore In this summary we have used thin film approximation based thermal stress formula[8] derived for general optical planar waveguide structure to address the composite nature of layers within the waveguide under force equilibrium and strain compatibility conditions. In simple terms the proposed work provide an analytical way to evaluate optimal value of structural, material and temperature parameters needed to achieve a waveguide with reduced birefringence effect before the process of fabrication. Thereby avoiding unnecessary wastage of resources and time.

The summary is arranged as follows. In section 2, we provide an analysis to the derived thermal stress formula that has been employed for the given purpose. In section 3, we provide the results and conclude the work with discussion of the merits of the thermal stress formula along with potential applications.

2. Analysis

The thermal stress formula [8] for the optical planar waveguide is described as

$$\sigma_{waveguide} = E_{core}\,\Delta T\left\{\frac{(\alpha_{substrate}-\alpha_{core})\gamma_c\gamma_t\gamma_l + (\alpha_{substrate}-\alpha_{upperclad})(1+\gamma_l+\gamma_t)}{\gamma_c(1+\gamma_t)(1+\gamma_l)}\right\} \quad (1)$$

Here, E represents elastic modulus, γ is Poisson's ratio, σ is the thermal stress, α is the thermal coefficient of expansion and ΔT presents the differential temperature. Also, γ_c , γ_t , γ_l are the ratios defined as $\gamma_c = E_{core}/E_{upperclad}$, $\gamma_t = t_{core}/t_{cladding}$, $\gamma_l = w_{core}/w_{cladding}$,respectively ; E_{core},$E_{upperclad}$ represents the biaxial stress of the waveguide core and upper cladding layer respectively ; t_{core} , $t_{cladding} = t_{upperclad} + t_{lowerclad}$,w_{core} , $w_{cladding}$ are the thicknesses and widths of core and cladding respectively ; α_{core}, $\alpha_{upperclad}$,$\alpha_{substrate}$ is the thermal coefficient of expansion of the core ,upper cladding and substrate respectively .In Eq. (1) $\sigma_{waveguide}$ presents the thermal induced stress in the planar waveguide structure. Eq. (1) shows that there are three categories in total that affects the thermal stress of the optical planar waveguide. The first category comprises of structural parameters

(γ_t ,γ_l), second consist of material parameters (α_{core} ,$\alpha_{upperclad}$,$\alpha_{substrate}$,γ_c, and E_{core}), while the third one is the temperature parameter ΔT .

The dependence of the thermal stress of the optical planar waveguide structure on the structural parameters has been shown in 6 figures for a general waveguide glass layer where for Fig 1(a) ,following values has been set α_{core} = 1.50 x 10^{-6}/K, $\alpha_{upperclad}$ = 3.40 x 10^{-6}/K ,$\alpha_{substrate}$=3.20 x 10^{-6}/K ,γ_c=1, ΔT=-1000K and E_{core}=4.20 X 10^{11} Pa. While on other hand remaining figures from (b) to (f) alters one value at a time, detail of which has been shown in the caption of the figure.

In the result section an attempt has been made to show the variation of thermal stress within the waveguide structure when parameters among these three categories are varied. This analysis is important as it will enable us to select value of optimal design parameters within these three categories, required to reduce birefringence effect to acceptable levels.

2. Results and Conclusion

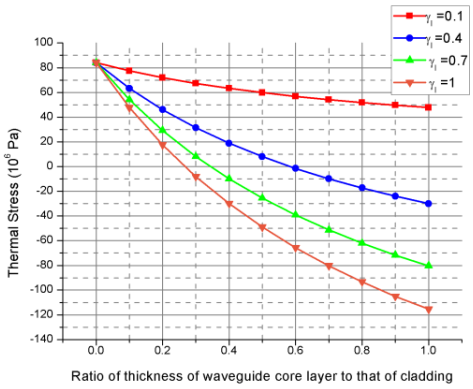

(a)

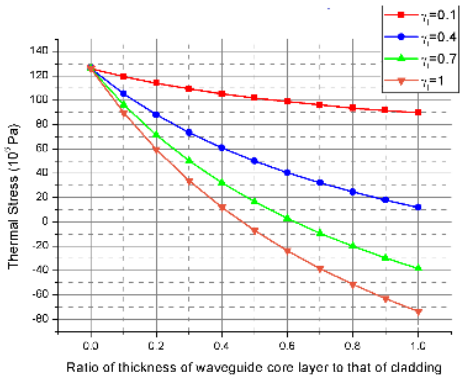

(b)

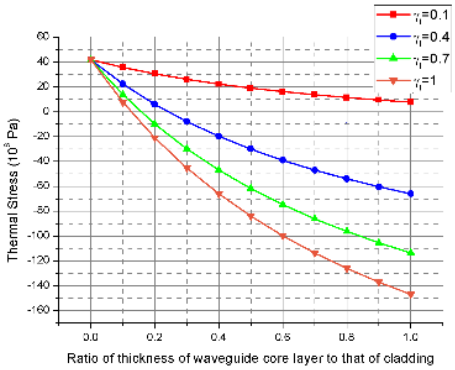

(c)

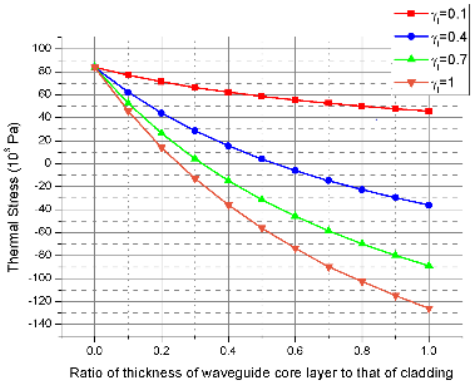

(d)

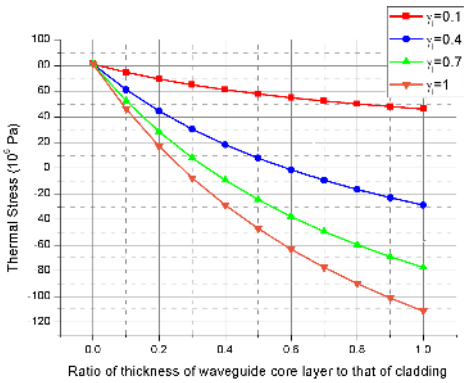

(e)

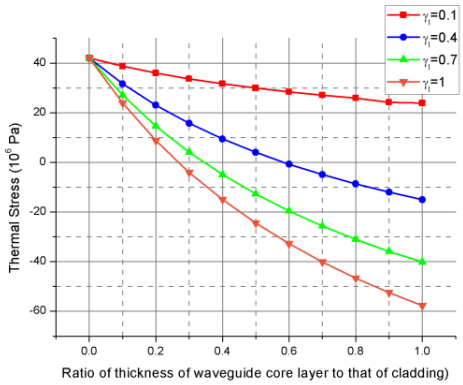

(f)

Fig. 1. (a) Thermal Stress of the waveguide structure as a function of γ_l and γ_t with (b) $\alpha_{substrate}$=3.1 x 10^{-6}/K, (c) $\alpha_{upperclad}$=3.2 x 10^{-6}/K,(d) α_{core}=1.4 x 10^{-6}/K,(e) E_{core}=4.054 x 10^{-11} Pa,(f) ΔT= -500K

Fig 1(a-f) shows a transition from tensile to compressive in the thermal stress of the planar waveguide structure with structural parameters γ_l= 0.4, γ_l= 0.7 and γ_l= 1. From this we learn that, if we model these parameters to set the stress at point zero, birefringence free waveguide structure can be obtained. Fig represents variation in the thermal stress in the planar waveguide structure as a function of structural parameters for different parameters from the values that has been taken for the very first case. Here, we find that there is a transition in the thermal stress from tensile to compressive if model the value of the following parameters α_{core} ,$\alpha_{upperclad}$,$\alpha_{substrate}$,γ_c , however there no such transition was observed when we do bring changes in E_{core} and ΔT. Through all this we find that under certain conditions, there was a transition in the thermal stress of the waveguide structure from tensile to compressive. Thus by carefully modelling the discussed structural and material parameters, one can achieve a birefringence free waveguide structure. This technique could be useful in designing PLC devices with low polarization sensitivities.

5. References

[1] J. Canning, M. Aslund, A. Ankiewiez, M. Dainese, H. Fernando, J.K. Sahu, L. Wosinski, "Birefringence control in plasma enhanced, chemical vapor deposition planar waveguides by ultraviolet irradiation", Appl. Opt. 39 (24), 4296–4299 (2000).

[2] J. Canning, M. Aslund," Birefringence compensation improved fringe contrast and trimming in an integrated asymmetric MachZehnder interferometer using mid-IR laser processing ", Opt. Mater. 14 (2) , 175–183 (2000).

[3] C. Nadler, M. Lanker, E. Wildermuth, W. Hunziker, H. Melchior, "Polarization insensitive wavelength multiplex- ers using stress release grooves", in Proceedings of the ECOC 98, 129–130 (1998).

[4] C.K. Nadler, E.K. Wildermuth, M. Lanker, W. Hunziker, H. Melchior," Polarization insensitive, low loss, low crosstalk wavelength multiplexer modules ", IEEE J. Sel. Top. Quantum Electron. 5, 1407–1412 (1999).

[5] H. Takahashi, Y. Hibina, Y. Ohmmori, M. Kawachi, "Polarization insensitive arrayed waveguide wavelength multiplexer with birefringence compensation film", IEEE Photon. Technol. Lett. 5 ,707–708 (1993).

[6] M. Okuno, A. Sugito, K. Jinguji, M. Kawachi,"Birefrin- gence control of silica waveguides on silicon and its application to a polarization-beam splitter/switch ", J. Lightwave Technol. 12 ,625–633 (1999).

[7] J. canning, "Birefringence control in planar waveguides using doped top layers ", Opt. Commun. 191,225–228 (2001).

[8] Xiuli Zhao,Chunfei Li ,Y.Z. Xu, "Stress-induced birefriengence control in optical planar waveguides",Optics Letter 28 (7),564-566 (2003).

Available online at www.ijapie.org

INTERNATIONAL JOURNAL OF ADVANCED PRODUCTION AND INDUSTRIAL ENGINEERING

IJAPIE-2018-10-422, Vol 3 (4), 11-14

IJAPIE
Connecting Science & Technology with Management.
A Journal for all Products & Processes.

Overview of Welding Using Microwave Radiation

Uma Gautam, Vipin*
(Department of Mechanical Engineering, Delhi Technological University, New Delhi, India)
Email: vipin@dce.ac.in

Abstract : *The application of the microwaves is increasing rapidly in material processing due to its unique characteristics of volumetric and rapid heating. Volumetric heating means that materials can absorb microwave energy directly and internally and convert it to heat. Its characteristic leads to controlled, selective, uniform and rapid heating. Microwave energy can be used for the processing of a wide variety of materials, where heat is generated from within the material instead of via radiation heat transfer from external heating elements. This paper introduces microwave heating, its characteristics and effect of process parameter on welding. In this review paper, the work carried out by the researches in the field of microwave joining of similar and dissimilar materials in the past decade by various researchers.*

Keywords: *Hybrid Heating, Process Parameter, Welding Time, Refractory Brick.*

1. INTRODUCTION

1.1. Brief History and Applications of Microwave Heating

Microwaves are part of the electromagnetic spectrum with frequencies ranging from 300 MHz to 300 GHz and corresponding wavelengths between 1 m and 1 nm respectively, Amit et al [2013]. There was need of Microwave technology during Second World War due to the demand for better radar technology for detection of enemy aircraft and submarines, Wong and Gupta [2015]. In 1945, Dr. Percy Spencer from Raytheon filed a patent for using microwaves to process food leading to the introduction of commercial microwave ovens in 1947 but due to its large size and high cost, found limited usage in industries, Gupta and Jain [2015]. Originally, microwaves were used for communication. In 1950, microwave energy was used to heat materials. After that, microwave heating had been successfully used in the following fields: tempering meat, precooking bacon, preheating rubber slugs, vulcanizing rubber, drying pasta, drying crushed oranges, etc., Wong and Gupta [2015]. In 1960s, a smaller and cheaper domestic microwave oven was introduced and the sale of microwave ovens grew rapidly in 1970s and has since become a common kitchen appliance in many households, Karanbir et al [2015]. Microwave heating is used most commonly for the heating of food due to the good microwave susceptibility of water molecules in the food and has been increasingly applied for processing of polymers, ceramics, metals, minerals, chemicals, composites and biological subjects, Srinath et al [2011]. In the late 1980s, there was growing interest in high temperature microwave processing of materials, with some successful applications at laboratory scale, for example, sintering of ceramics, microwaves are justified as a potential heating mechanism to replace some conventional heating methods, Srinath et al [2015].

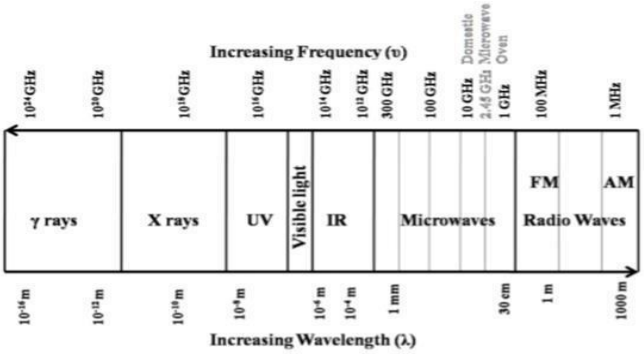

Fig 1 classification of electromagnetic waves

1.2 Fundamentals of Microwave Heating

One of the descriptions of the characteristics of microwave heating was in a Scientific American article in 1943 where it was mentioned that heat was generated from within the object and involves no transfer of heat to it. This is fundamentally different from conventional heating where heat is usually transferred to an object via conduction, convection or radiation. In conventional heating using an oven or furnace, the heating source first, has to heat up the entire volume of air and walls of the container before thermal energy is transferred from the surface of the object to the interior through conduction. But in microwave heating, due to the penetrative nature of microwaves, the object directly

absorb the microwave energy and heat is generated from within the object and do not require substantial heating of the environment.

1.3 Introduction to microwave materials processing

Microwave heating is a process which uses electromagnetic energy in the frequency range of 300 MHz to 300 GHz. In microwave heating the material is subjected to an electromagnetic wave that oscillates the molecules of material, there by generating heat. Microwaves are directly absorbed by the material thus causes volumetric heating. This volumetric heating is only obtained by microwave processing and it reduces time, energy as well as it is eco-friendly.

1.4 Characteristics of Microwave heating process

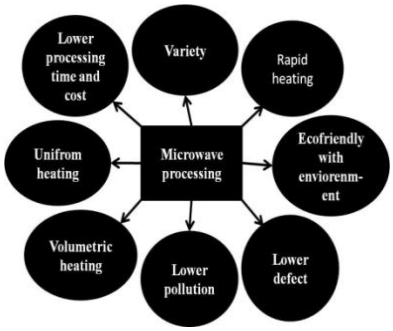

Fig 2 characteristics of Microwave Heating

a) **Clean energy:** It does not require medium, it propagates by only changing the electric field and magnetic field. It can propagate even in vacuum. It reaches the object and penetrates without heating air.

b) **Internal heating:** Microwave will reach the object to be heated at same speed of light, then it enters into the object as a wave and by getting absorbed, the object generates heat therefore microwave heating is internal heating.

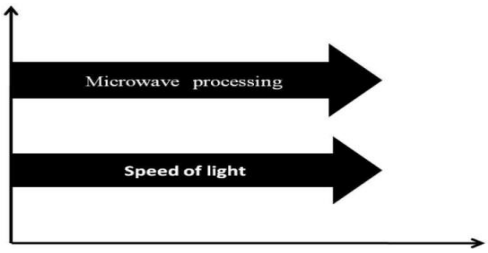

Fig 3 Comparison of transmission speed of microwave same as light

In microwave heating, the heat will be generated in the object by absorption of microwaves which has inverse heating profile. It heats the object internally and heat flows from inward direction to outward direction which reduces heat loss and rapid heating is achieved.

c) **Rapid heating:** It generates heat on their own by penetration of microwaves, not necessary to consider about heat conduction that is why rapid heat is possible by microwaves.

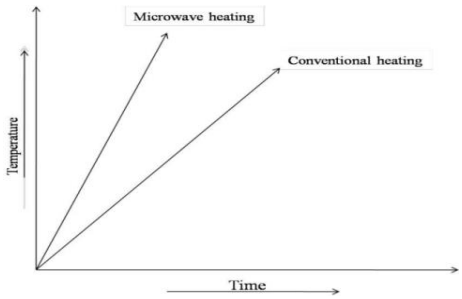

Fig 4 Microwave heating vs. conventional heating

d) **Heating uniformity:** It heat uniformly i.e. it gives volumetric heating effect can. Each part of heated object generate heat, so even for those object with complicated shape, it can be heated relatively uniform.

e) **Lower power consumption:** The microwave heating of material involves direct absorption of radiations by material, it provides higher rate of heat transfer in comparison of conventional methods and attains higher temperature in shorter time, this reduce overall consumption of power.

2. METHODOLOGY

1. Selection of specimen which is to be joined (Both the specimen can be similar or dissimilar)
2. A cavity is made on the refractory brick of the size of the specimen. Then specimen is cleaned with emery paper and acetone.
3. The joint is applied with the slurry (mixture of epoxy and nickel powder).
4. The specimen is placed in the cavity.
5. Graphite sheet is placed on the specimen.
6. Charcoal power is poured above the graphite sheet.
7. The whole refractory brick is placed in the microwave oven.
8. The microwave oven is set to 900W.
9. The time is calculated using stopwatch to determine the time required for the formation of joint between the two specimens.

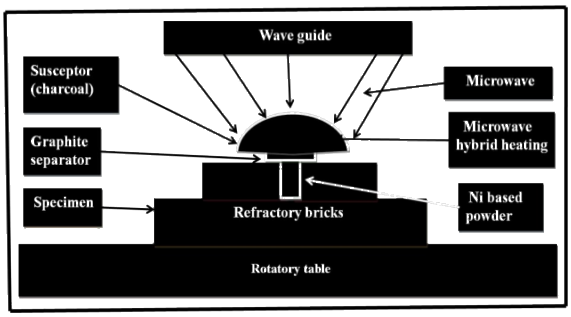

Fig 5 Schematic microwave hybrid heating processing

3. EFFECT OF PROCESS PARAMETERS

3.1 Effect of time

- It is important parameter to consider time for which specimen is kept in the in microwave. It was observed that:
- For stone charcoal melting point was not reached after 12-15 minutes and even red hot condition was not observed.
- For wooden charcoal melting point was observed after 10-12 minutes.
- For graphite powder red hot condition was observed after 2-3 minutes and melting point was observed around 6 minutes.

3.2 Positioning of Work Piece

Intensity of microwaves varies from point to point inside the microwave oven. So it is necessary to position the work-pieces at a point where maximum amount of microwaves reach to the work-pieces to achieve the proper melting in least time. After number of experiments it was observed that 16 mm height at the center of base plate was appropriate for the maximum intensity of microwave energy.

3.3 Length of Specimen

Length is also one of the major parameter which was observed during experimentation. No melting was observed in all the experiments conducted on specimen having more than 10 mm length. So it was tried to keep the specimen length as short as possible and the average length of each specimen was 8mm.

3.4 Thickness of Slurry

Very fine thickness is required for good quality joint. If the thickness applied is more than the appropriate value (0.2-0.3mm approx.) then there will be gap at the joint and the possibility of mismatching occurs because slurry burns within 10 to 15 sec.

3.5 Susceptor Material

The basic purpose of susceptor material is to prevent the direct exposure of material in microwaves. When it comes in contact with the microwaves, it absorbs the microwave energy, burns and raises the temperature of work-pieces up to its melting point.

4. CONCLUSION

In the present paper, it was concluded that, microwave processing is emerging as a innovative technology with many advantages over conventional processing. There is, therefore, increasing industrial application of microwave energy for heating, drying, curing and sintering of materials. Until 2000, microwave processing of materials mostly was confined to ceramics, semimetals, inorganic and polymeric. The most recent significant development in the microwave processing has been the sintering, brazing, joining and melting of metals also.

REFERENCES

[1] Amit Bansal, Apurbba Kumar Sharma, and Shantanu Das, “Metallurgical and mechanical characterization of mild steel-mild steel joint formed by microwave hybrid heating process” Indian Academy of Sciences, vol. 38, part 4, pp. 679–686, 2013

[2] Prateek Gupta and Sudhir Kumar, “ Investigation of Stainless Steel Joint Fabricated Through Microwave Energy” Materials and Manufacturing Processes, vol 29, issue 8, pp.1–6, 2014

[3] Dheeraj Gupta, Satnam Singh, Vivek Jain, and Rohit Kumar, “Joining of Bulk Cast Iron Through Microwave Energy”, International Journal for Technological Research in Engineering, vol 2, issue 7, issn no. 2347-4718, pp.1079-1084, 2015

[4] Lucky Bagha, Shankar Shegal and Amit Thakur, “ Comparative Analysis of Microwave based Joining/Welding of SS304- SS304 using Different Interfacing Materials” MATEC Web of Conferences 57, 03001, *ICAET - 2016*

[5] Thomas Dutta, Shrey Sanwaria., S. Vanesh, Sri Dhinakaran., “Analysis of Microwave Welding of Stainless Steel” vol 5 issue 4, issn no. (Online): 2347-3878, pp. 92-95, 2017

[6] Satnam Singh, Dheeraj Gupta and Vivek Jain, “Recent applications of microwaves in materials joining and surface coatings” Journal of Engineering Manufacture, pp. 1-15, 2015

[7] S.Singh, D. Gupta, V. Jain, and A. Sharma, “Microwave Processing of Materials and Applications in Manufacturing Industries: A Review,” Mater. Manuf. Process., pp. 37–41, 2014.

[8] Balmukund Dhakar, Satyajit Chatterjee and Kazi Sabiruddin, “Influence of process parameters on the formation of phases and mechanical properties of plasma sprayed Al2O3–Cr2O3 coatings” Materials Research Innovations, pp.1-10, 2016

[9] Lucky Bagha, Shankar Sehgal, Amit Thakur and Harmesh Kumar, “Effects of powder size of interface material on selective hybrid carbon microwave joining of SS304–SS304” Journal of

Manufacturing Processes, issn no.1526-6125, pp. 290-295, 2017

[10] Kanwarjeet Singh and Satpal Sharma, "Development and Characterizations of Co-based Microwave Clad" ELK Asia Pacific Journals, 978-93-85537-06-6, 2017

[11] Srinath M. S, A. K Sharma and Pradeep Kumar, "Microwave Processing of Metallic Joints and their Characterisation" i-manager's Journal on Mechanical Engineering, vol. 1, issue no. 1, 2011

[12] M.S. Srinath, Apurbba Kumar Sharma and Pradeep Kumar, "Investigation on microstructural and mechanical properties of microwave processed dissimilar joints", Journal of Manufacturing Processes, pp.141–146, 2011

[13] Dheeraj Gupta, Prabhakar M. Bhovi, Apurbba Kumar Sharma and Sushanta Dutta, "Development and characterization of microwave composite cladding", Journal of Manufacturing Processes, pp.243–249, 2012

[14] Wai Leong, Eugene Wong and Manoj Gupta, "Using Microwave Energy to Synthesize Light Weight/Energy Saving Magnesium Based Materials: A Review", Journal of *technologies*, ISSN 2227-7080,2015.

Available online at www.ijapie.org

INTERNATIONAL JOURNAL OF ADVANCED PRODUCTION AND INDUSTRIAL ENGINEERING

IJAPIE-2018-10-425, Vol 3 (4), 24-26

IJAPIE
Connecting
Science & Technology
with Management.

A Journal for all
Products & Processes.

Possessions Vehicle Pursuer and Burglary Recognition Scheme by Way of Fervor Fighting Sytem by Means of IOT

[1]Rani Medhashree[*], [2]Manjula B[*], [3]Devendra Kumar S M
([1,]Department of Electronics and Communications, Delhi Technological University, Delhi, India,*
[2]ECE. EIT, Ummathur Chamarajanagara, Karnataka - India
[3]Govenrment Engineering College, Bangalore, India)
Email: manjulabiligiri24@gmail.com

Abstract : *Vehicle following frameworks were first executed for the delivery business since individuals needed to know where every vehicle was at some random time. Nowadays, be that as it may, with innovation developing at a quick pace, robotized vehicle following framework is being utilized in an assortment of approaches to track and show vehicle areas continuously. This paper proposes a vehicle following framework utilizing GPS/GSM/GPRS innovation and a Smartphone application to give better administration and savvy answer for clients to track vehicle and products.*

Keywords: *Global Positioning System, Android, Vehicle Thefy, Tracking.*

1. INTRODUCTION

The merchandise burglary can be recognized and a programmed water sprinkling framework is turned ON at whatever point there is fire recognition in the vehicle and for each occasion the message is sent the proprietor. The primary main impetus for this quickened development in Cell phone use is the accessibility of a substantial assortment of utilizations to address the issues of an extensive variety of clients. In our undertaking we built up a Cell phone application alongside the in-vehicle GPS beacon. This GPS framework intended for clients in arrive development and transport business, gives constant data, for example, area, speed and expected landing time of the client is moving vehicles in a brief and simple to-peruse organize The applications incorporate checking driving execution of a parent with a teenager driver. Vehicle following frameworks acknowledged in buyer vehicles as a robbery anticipation and recovery gadget. In the event that the burglary distinguished, the framework sends the SMS to the vehicle proprietor. After that vehicle proprietor sends the SMS to the controller, issue the vital signs to stop the engine. The vehicle following and burglary discovery.

In light of perceptions of the operational issues experienced in vehicle following, the creators attempted a writing audit concerning following frameworks for systems. Subsequently, a hole in the assemblage of information was identified, and the accompanying exploration issue was figured: "How to develop following frameworks material to here and now multi-organization systems?". Presently we are confronting issues like products of vehicles being burglary by the driver of the vehicles, bursting of into flames while the vehicles in development, and liquor utilization by driver which may prompts incidental issues and gas spillages in vehicles. We have proposed a novel technique for vehicle following and robbery identification used to track the burglary vehicle by utilizing GPS and GSM innovation. This framework puts into the dozing mode vehicle dealt with by the proprietor or approved people; generally, goes to dynamic mode. The method of tasks changed by people or remotely. At the point when the burglary recognized, the capable individuals send SMS to the miniaturized scale controller, at that point issue the control signs to stop the motor engine. After that every one of the entryways bolted. To open the entryways or to restart the motor approved individual needs to enter the passwords. In this technique, effectively track the vehicle place and entryways bolted.

2. METHODOLOGY

Sensors are the key part for the improvement of remote sensor arrange. When all is said in done, the model takes a shot at sensors, ADC converter, microcontroller, UART convention, GSM module. With current sensor innovation, these fundamental highlights can be caught and translated.

A. BASIC APPROACH

At the point when products burglary the sensors in a module detects the progressions happened and after that naturally the module itself sends data about the condition to the concerned individual which for this situation is the proprietor of the vehicle. Currently GPS vehicle following guarantees their wellbeing as voyaging. This vehicle following framework found in customers vehicles as a robbery avoidance and

protect gadget. Vehicle proprietor or Police take after the flag discharged by the following framework to find a victimized vehicle in parallel the stolen vehicle motor speed going to diminished and pushed to off. After switch of the motor, engine can't restart without authorization of secret phrase.[1] This framework introduced for the four wheelers, Vehicle following normally utilized in naval force administrators for naval force administration capacities,
directing, send off, on board data and security. The applications incorporate observing driving execution of a parent with a teenager driver. Vehicle following frameworks acknowledged in buyer vehicles as a robbery anticipation and recovery gadget. On the off chance that the robbery recognized, the framework sends the SMS to the vehicle proprietor.[2] After that vehicle proprietor sends the SMS to the controller, issue the fundamental signs to stop the engine. [3] In this task, the investigated related innovation in the vehicle following framework.

B. ARCHITECTURE

The remote sensor system will comprise of a microcontroller, different sorts of sensors, for example, confront location, gas spillage sensor, liquor sensor, robbery identifier and fire identification sensor.[10] If there should arise an occurrence of crisis the microcontroller will transmit the required data by a message to the base station unit utilizing the GSM module.

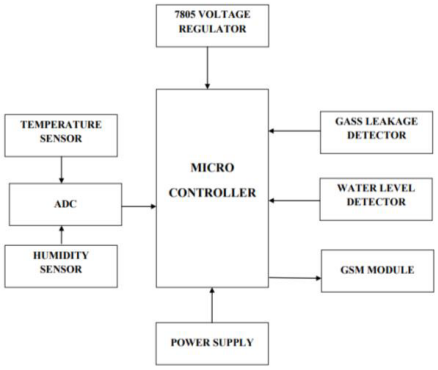

Fig 1 System Architecture

Amid crisis conditions on the off chance that one sensor distinguishes the progressions it sends an information to the microcontroller which breaks down this and pass a message to the proprietor, in any crisis conditions proprietor can get the area or photograph to the mail ID gave to it utilizing web just by squeezing a specific catch.

3. IMPLEMENTATION AND RESULTS

A vehicle following framework is an electronic gadget, introduced in a vehicle to empower the proprietor or an outsider to track the vehicle's place. This paper proposed to plan a vehicle following framework that works utilizing GPS and GSM innovation. This framework constructed in view of implanted framework, utilized for following and situating of any vehicle by utilizing Worldwide Situating Framework (GPS) and Worldwide framework for portable correspondence (GSM). This outline will constantly watch a moving Vehicle and report the status of the Vehicle on request.

A. EMBEDDED C

Embedded C is a programming dialect for microcontrollers that are utilized particularly for the installed frameworks. This implanted C writing computer programs was gotten tied up with the photo to address the normal issues[14]. Inserted C nearly utilizes every one of the kinds of punctuation and semantics that are same as in work arranged C programming dialect, for instance it can the main( ) work or any factor definitions or any control explanations, clusters, structures.

B. ANDROID SDK

- Software Development Kit includes a comprehensive set of development tools. [14]
- Android applications are bundled in apk arrange and put away under/information/application organizer on the Android Operating Systems. Android applications are bundled in apk arrange and put away under/information/application organizer on the Android OS.[15]

C. ECLIPSE

Eclipse is a coordinated improvement condition (IDE) utilized in PC programming, and is the most generally utilized Java IDE. [6].
The underlying codebase started from IBM Visual Age.[8] The Shroud programming advancement pack (SDK), which incorporates the Java improvement instruments, is intended for Java designers. Clients can expand its capacities by introducing modules composed for the Shroud Stage, for example, improvement toolboxes for other programming dialects, and can compose and contribute their own module modules. Since the presentation of the OSG execution (Equinox) in adaptation 3 of Shroud, modules can be stopped halted progressively and are named (OSGI) bundles[9]

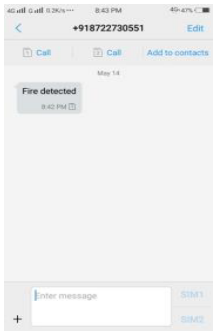

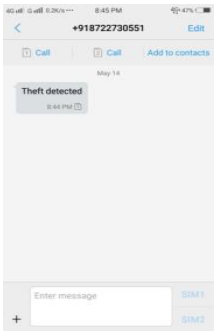

4. CONCLUSION

This task offers a savvy plan of following and checking the vehicles which causes the organizations to give high caliber of administration. This plan can give the area of the vehicles and merchandise of the administration with a mistake under 10m on account of moderate speed and clear condition and the framework give the precise landing vehicle and give the area of the vehicle and products in Google outline both client and chairman. This framework diminishes the disarray for holding up to the vehicle of remote clients for getting

merchandise on time with appropriate security if any fire smother framework is included and gives vehicle and products following at any area, administration and fire checking is finished.

A. Future Enhancements

This task is finished when you watch, yet we need to execute more things.

1) Online Chat ·
2) Overseas Service
3) Pickup Request On chat
4) Expanded geographical research

REFERENCES

[1] Ala-Risku, T., Ka ¨rkka ¨inen, M. and Holmstro ¨m, J. (2003), "Evaluating the applicability of merge-in-transit: a step-by-step process for supply chain managers", International Journal of Logistics Management (forthcoming

[2] Chiang, Y. Chang, F., H. Wang, H. (2010). Toward Real-Time Precise Point Positioning: Differential GPS Based on IGS Ultra Rapid Product,SICE Annual Conference, The Grand Hotel, Taipei, Taiwan August 18-21.

[3] Asaad M. J. Al-Hindawi, IbraheemTalib, "Experimentally Evaluation of GPS/GSM Based System Design", Journal of Electronic Systems Volume 2 Number 2 June2012

[4] KunalMaurya ,Mandeep Singh, Neelu Jain, "Real Time Vehicle Tracking System using GSM and GPS Technology- An Anti-theft Tracking System," International Journal of Electronics and Computer Science Engineering. ISSN 2277-1956/V1N3-1103-110

[5] VikramKulkarni&ViswaprakashBabu,"embedded smart car security system on facedetection',specialissueofIJCCT,ISSN(Online):2 231-0371, ISSN(Print):0975-7449,volume-3, issue-1

[6] V.Ramya, B. Palaniappan, K. Karthick,"Embedded Controller for Vehicle In-Front Obstacle Detection and Cabin Safety AlertSystem", International Journal of Computer Science & Information Technology (IJCSIT) Vol 4, No 2, April 2012.

[7] Kai-Tai Song, Chih-Chieh Yang, of NationalChiao Tung University, Taiwan, "Front Vehicle Tracking Using Scene Analysis", Proceedings of the IEEE International Conference on Mechatronics & Automation 2005.

[8] Chen Peijiang, Jiang Xuehua, "Design andImplementation of Remote monitoring system based on GSM," vol.42, pp.167-175. 2008.

[9] Albert Alexe, R.Ezhilarasie, "Cloud ComputingBased Vehicle Tracking Information Systems", ISSN: 2229 - 4333 (Print) | ISSN: 0976 - 8491 (Online) IJCST Vol. 2, Issue 1, March 2011

[10] R.Ramani, S.Selvaraju, S.Valarmathy, R.ThangamB.Rajasekaran, "water-level monitor for bore well and water tank based on GSM", International Journal of engineering science and technology (IJEST), ISSN: 0975-5462, volume4-N0:10, october2012.

[11] Garstone, S. (1995), "Electronic data interchange (EDI) in port operations", Logistics Information Management, Vol. 8 No. 2, pp. 30-3. Giannopoulos, G.A. (2003),

[12] "The application of information and communication technologies in transport", European Journal of Operational Research, Vol. 152 No. 2, pp. 302-20. Halmepuro, J. and Nyste ´n, C. (2003),

[13] Interview with Department Manager JormaHalmepuro and Expediter ChristerNyste ´n from Jaakko Po ¨yryOy, 23 January. Harris, E. (1999), "Project risk assessment: a European field study", British Accounting Review, Vol. 31, pp. 347-71. Huvio, E., Gro ¨nvall, J. and Fra ¨mling, K. (2002),

[14] "Tracking and tracing parcels using a distributed computing approach", NOFOMA'2002 Conference, Trondheim, 13-14 June. ISI Industry Software (2003), press release 10 February, available at: www.isiindustrysoftware.com/ news/kvaerner.html (accessed 20 February). Janah, M. and Wilder, C. (1997),

[15] "FedEx special delivery", Information Week, No. 654, 27 October, pp. 42-60. Jansen, M.H. (1998), "The environment as a resource; developing environmental information systems based on enterprise resource-planning software", PhD thesis, Eindhoven University of Technology, Eindhoven. Kaplan, R.S. (1998),

[16] "Innovation action research: creating new management theory and practice", Journal of Management Accounting Research, Vol. 10, pp. 89-118. Ka ¨rkka ¨inen, M., Ala-Risku, T. and Fra ¨mling, K. (2003a), "The product centric approach – a solution to supply network information management problems?", Computers in Industry, Vol. 52 No. 2, pp. 147-59.

[17] "Intelligent products: a step towards a more effective project delivery chain", Computers in Industry, Vol. 50 No. 2, pp. 141-51. Kasanen, E., Lukka, K. and Siitonen, A. (1993)

[18] "The constructive approach in management accounting", Journal of Management Accounting Research, Vol. 5, Fall, pp. 243-64. King, J. (1999),

[19] "Shipping firms exploit IT to deliver e-commerce goods", Computerworld, Vol. 33 No. 31, p. 24. Kullstro ¨m, T. (2003), interview with Tom Kullstro ¨m,

Journal of Applied Polymer Science

Rheokinetic studies and compressive response of high performance polybenzoxazine syntactic foams

A. V. Ullas,[1,2] Pratibha Sharma,[1,2] Devendra Kumar,[1] Prasun Kumar Roy[2]
[1]Department of Applied Chemistry and Polymer Technology, Delhi Technological University, Delhi 110042, India
[2]Centre for Fire, Explosive and Environment Safety, DRDO, Timarpur, Delhi 110054, India
Correspondence to: P. K. Roy (E-mail: pk_roy2000@yahoo.com)

ABSTRACT: Polybenzoxazines are finding increasing usage in demanding applications where high temperature stability is required, especially in the field of aerospace. In this work, thermally stable bisphenol F-based polybenzoxazine [poly(BF-a)] syntactic foams containing varying volume fractions (30–60%) of hollow glass microballoons (HGMs) were prepared and their mechanical response in the quasi-static regime was established. The effect of introducing glass microballoons on the curing profile of benzoxazine resin was studied using both nonisothermal differential scanning calorimetry and rheometry. Temperature-sweep experiments were performed to arrive at the optimal processing window of the benzoxazine-glass microballoons formulations, particularly in terms of viscosity, gelation temperature, and time. Thermally accelerated ring-opening polymerization of the benzoxazine resin led to complete curing of the syntactic foam formulations, as assessed by calorimetric studies. The thermal degradation behavior of the poly(BF-a)/HGM was studied using thermogravimetric analysis. As expected, the density of the syntactic foam specimens decreased with increasing microballoon content. Maximal increase in the specific compressive properties of the poly(BF-a)/HGM samples was observed in formulations containing 40% volume fraction of glass microballoons. © 2018 Wiley Periodicals, Inc. J. Appl. Polym. Sci. **2018**, *135*, 47234.

KEYWORDS: benzoxazine; bisphenol F; compression; density; microballoons

Received 27 June 2018; accepted 18 September 2018
DOI: 10.1002/app.47234

INTRODUCTION

The high-tech aerospace industry is in a continual search of materials with high thermal stability, robust mechanical response, and most importantly low density, which directly translates to benefits in the form of low fuel consumption.[1] In this context, syntactic foams offer their excellent candidature and are hence trending as light-weight construction materials with high specific structural properties, especially as "core component" in sandwich structures.[2,3] In general, polymeric syntactic foams are prepared by dispersing hollow fillers in a suitable polymeric resin. What is interesting in the context of syntactic foam is that it is possible to obtain a wide range of mechanical properties by judicious choosing the constituents, that is, the polymeric resin, filler type, and its volume fraction.[4–6]

Among all hollow fillers, glass microballoons (HGMs) are most extensively used, in view of their economic viability, low coefficient of thermal expansion, and chemical inertness.[7] Polymeric resins such as epoxies,[8–11] polyurethanes,[12] silicones,[13] and phenolic resins[14] have been used in the past as matrix material for syntactic foams. Surprisingly, the potential of benzoxazines for this purpose has not yet been duly explored.[15,16] Polybenzoxazines are well-known for their excellent thermal stability, and are particularly suitable for preparation of highly filled composites in view of their low melt viscosity and excellent wettability.[17–19] In addition, polybenzoxazines exhibit interesting properties such as negligible curing shrinkage,[20] low water absorption,[21] high glass-transition temperature,[22] and high char yield.[23,24] Benzoxazines polymerize via thermally accelerated ring-opening reaction and generate no volatile by product, a major processing benefit for the production of void free composites.[21] In the last few years, polybenzoxazines are emerging as strong contenders, even for engineering polymers like imides and epoxies.[25,26] Attempts toward preparation of benzoxazine-based cellular foams are rather scarce,[15,16] and mostly deal with conventional bisphenol A-based polybenzoxazines [poly(BF-a)]. One of the most interesting features associated with benzoxazines is the possibility of molecular designing flexibility,[27–29] which greatly increase the scope of these materials.[30,31] A wide range of mechanical properties can be obtained by varying the reactants used for preparation

Additional Supporting Information may be found in the online version of this article.

of benzoxazine, that is, amine and phenol.[32,33] We believe that the properties of benzoxazine-based syntactic foams can be significantly improved by changing the type of resin. Bisphenol F-based benzoxazines exhibit substantially better properties than bisphenol A-based resin in terms of flame retardance, dimensional and chemical resistance, mechanical response, economic considerations, and environmental concerns.[34,35] Therefore, we considered it of interest to prepare syntactic foams based on bisphenol F.

Conventional processing techniques for syntactic foams include casting, extrusion and rotational molding, or buoyancy methods, where the procedure adopted is dependent upon the microballoon loading and the type of polymeric material.[7,36,37] In most cases, the viscosity of the resin–filler formulation increases tremendously with increasing microballoon loading. High microballoon content presents difficulty during stir casting of the formulation. Therefore, systematic understanding of the flow behavior of resin-microballoon formulation becomes an essential aspect for smooth processing of specimens. Literature reports the use of diluents for improving the flow behavior, to ease the processability issues associated with highly filled formulations.[38] Unfortunately, the subsequent removal of the diluent results in void formation, which adversely affects the mechanical performance and higher production costs. It is therefore essential to establish the processing window of the formulations to ascertain optimal conditions required for processing of syntactic foams. In this context, rheological studies can generate invaluable data. Unfortunately, systematic rheological studies on syntactic foam formulations are rather scarce, with most of the studies dealing with thermoplastic-HGM formulations.[39–41]

Here, in this work, we attempt the preparation of bisphenol F benzoxazine-based syntactic foam containing increasing loadings of HGMs. In the present study, the rheological behavior of benzoxazine-HGM formulations has been systematically studied to gain an insight into the optimal conditions required for processing of these syntactic foams. The compressive properties of bisphenol F-based benzoxazine syntactic foams have been compared with the existing literature. An appreciable enhancement in the compressive performance of the foams advocates a strong need to develop polybenzoxazines syntactic foams.

EXPERIMENTAL

Materials

Bisphenol F-aniline (BF-a)-based benzoxazine resin with a density of 1.24 g cm^{-3} was obtained from Anabond (Chennai, India). The nuclear magnetic resonance (^{1}H-NMR) spectrum of BF-a resin is presented in Figure S1, Supporting Information. HGMs (HGM K46, 3M) were used as hollow fillers for the preparation of syntactic foams. The HGMs exhibited a density of 460 kg m^{-3} with isotactic crush strength 6000 psi (41 MPa). The wall thickness, radius ratio mean diameter, and thermal conductivity of the selected HGM are ~1.29 μm, 0.9, 40 μm, and 0.153 Wm^{-1} K^{-1} at 21 °C, respectively.

Rheological Studies

Anton Paar Rheometer MCR-102 was used to study the rheological behavior of the polybenzoxazine (PBz)/HGM formulations using parallel plate geometry (diameter 25 mm and gap thickness was maintained at 1 mm) and is equipped with 200 mNm torque transducer. A constant strain of 0.5% and an angular frequency of 10 rad s^{-1} were maintained throughout the rheological experiments. Temperature-sweep experiments were performed over a range of temperature in three intervals: 30–150 °C at 5 °C/min, 150–280 °C at 3 °C/min, and finally at 280 °C for 1 h. Subsequently, isothermal experiments were performed in oscillatory mode at 200 °C. The viscoelasticity of the formulations in terms of complex viscosity (η*), shear storage modulus (G'), and shear loss modulus (G'') with respect to temperature were monitored.

Processing of Polybenzoxazine Syntactic Foams

Finely powdered bisphenol F benzoxazine resin was mixed with HGMs at different volume fractions (30–60% v/v). The procedure adopted for the processing syntactic foams involved introduction of pre-calculated amounts of finely powdered BF-a resin and microballoons in a Teflon mold. The contents were subjected to a compressive force of ~10 MPa and the formed pellet was subjected to a controlled curing program (150 °C for 15 min, 180 °C for 15 min, and 200 °C for 60 min). The details of the specimens prepared along with their sample designations have been mentioned in Table S1, Supporting Information. Neat polybenzoxazine specimens have been referred to as poly(BF-a) and the compositions containing glass microballoons have been referred to as poly(BF-a)/MB (X) where X indicates the volume fraction of HGM present in the specimen. For example, poly(BF-a) containing 40% v/v of glass microballoons has been designated as poly(BF-a)/MB (40).

Density of Syntactic Foams

The amount of HGM and benzoxazines microspheres was calculated as per eq. (1).

$$\frac{\text{Mass}_{\text{HGM}}}{\text{Mass}_{\text{composite}}} = \frac{\rho_{\text{HGM}} \times \phi_{\text{HGM}}}{\rho_{\text{HGM}} \times \phi_{\text{HGM}} + \rho_{\text{matrix}} \times \phi_{\text{matrix}}} \quad (1)$$

where ρ_{HGM} and ρ_{matrix} refer to the density of HGM (460 kg m^{-3}) and benzoxazine resin (1200 kg m^{-3}), respectively, and ϕ_{HGM} and ϕ_{matrix} refer to the desired volume fractions of HGM and resin. Theoretical density of syntactic foam (ρ_{th}) was calculated according to the standard rule of mixtures [eq. (2)].

$$\rho_{\text{th}} = \rho_{\text{HGM}} \times \phi_{\text{HGM}} + \rho_{\text{matrix}} \times \phi_{\text{matrix}} \quad (2)$$

The density of the foam was experimentally determined by averaging the mass: volume ratio of five specimens as per ASTM D1622–98. The ratio of theoretical and experimental densities was used to quantify the air void porosity trapped in the matrix during fabrication according to eq. (3),

$$\text{Void volume}\% = \frac{\rho_{\text{th}} - \rho_{\text{ex}}}{\rho_{\text{th}}} \times 100 \quad (3)$$

Quasi-Static Testing

Mechanical testing under compression mode was carried out using universal testing machine (International Equipments, Mumbai, India). Standard specimens (12 mm diameter, 6 mm thick) were compressed at a rate of 1.3 mm min^{-1}. Five

specimens of each configuration were tested and the load–displacement data obtained from the tests was used to obtain stress–strain curves for the calculation of compressive strength. The area under the stress–strain curve till plateau region was quantified to determine the amount of energy absorbed by the foams [eq. (4)].[42]

$$E_a = \frac{1}{2}(\rho_c \times \varepsilon_{crush}) + (\rho_c \times \varepsilon_{crush}) \quad (4)$$

where E_a, ρ_c, and ε_{crush} refer to the energy absorbed, compressive yield strength, and crushing strain of the foam, respectively.

Differential scanning calorimetry (DSC, TA instruments Q 20, NewCastle, DELAWARE, USA) was used for studying the thermal behavior of the samples. For dynamic DSC scans, the sample (5 ± 1 mg) was sealed in aluminum pans, and heated from 30 to 350 °C at 10 °C min^{-1}. N_2 was purged at rate of 50 mL min^{-1} to minimize oxidation of the sample during the curing process. Prior to the experiments, the instrument was calibrated for temperature and enthalpy using standard indium and zinc. Thermal equilibrium was regained within 1 min of sample insertion, and the exothermic reaction was considered to be complete when the recorder signal leveled off to the baseline. Fourier transform infrared (FTIR) spectra of specimens were recorded in the wavelength range 4000–600 cm^{-1} using a Thermo scientific FTIR (Nicolet 8700) analyzer with an attenuated total reflectance crystal accessory. Thermal degradation behavior was investigated using PerkinElmer Diamond simultaneous thermogravimetry (STG)–differential thermal analysis under nitrogen atmosphere (flow rate = 50 mL/min) over the temperature range 50–700 °C. A heating rate of 10 °C min^{-1} and sample mass of 5.0 ± 0.5 mg was used for each experiment.

RESULTS AND DISCUSSION

Rheokinetic studies were performed to arrive at the optimal conditions for processing of the poly(BF-a)/HGM syntactic foams. The mechanical response of cured syntactic foams was evaluated under quasi-static regime.

Curing of Benzoxazine Resin

Benzoxazine monomers (Bz) reportedly undergo polymerization reaction via thermally accelerated cationic ring opening which results in the formation of a stable crosslinked polybenzoxazine network.[43] Among many factors, ring strain associated with the heterocyclic oxazine ring and the stability of the iminium ion drives the polymerization reaction forward.[28] The reaction has been reported to be autocatalytic in nature in view of catalytic activity of the reactive species generated *in situ*.[44,45] Several mechanisms have been reported for the ring-opening polymerization of the 1,3-benzoxazine monomer.[46–50] At elevated temperatures, the oxonium cation undergoes ring opening to form a reactive iminium species, which further undergo monomer insertion steps. The repetitive addition of monomer leads to the formation of crosslinked polybenzoxazine system as presented in Figure 1.

Nonisothermal DSC traces (Figure 2) reveal that ring-opening polymerization in BF-a initiates at 216 °C and reaches its peak at 231 °C. The curing profile remains practically unaffected by the addition of HGMs into the resin, even at higher loading. The onset and peak temperature associated with the curing of all the formulations are presented in Table S2, Supporting Information. The enthalpy associated with the polymerization reaction was also found to decrease with increasing concentration of HGMs, attributable to the reduced amount of monomer in the formulation.

Rheokinetics of BF-a/HGM Formulations

The processing conditions employed for the preparation of syntactic foam define the end properties of the material. In this context, the most crucial parameter is the viscosity of the formulation, which builds up continuously during the curing reaction. The dependence of the complex viscosity on temperature is presented in Figure 3. The BF-a resin exhibits a melting at ~65 °C, and the viscosity of the resin remains sufficiently low till 200 °C, to permit solventless processing of the formulations. Further increase in temperature resulted in ring opening of the oxazine moieties, thereby forming Mannich bases. Subsequently, a gel-type structure is formed, following which an exponential rise in viscosity is observed, due to crosslinking within the linear chains. The rheological behavior of the BF-a/HGM formulations is also included in Figure 3. In line with previous studies,[33,51] introduction of HGMs results in an increase in the viscosity of the resin with the extent of increase being proportional to the amount of HGM loading. The "gel" point at which the free flow of the medium is restricted due to increased entanglement between the growing polymeric chains,[52] was evidenced at ~205 °C for BF-a and remained unaffected due to introduction of the glass balloons.

Rheological studies on benzoxazine/HGM formulations were performed under isothermal conditions also (T = 200 °C), and the results are presented in Figure 4. A slight increase in the gel time (crossover point of storage and loss modulus)[53–55] was evidenced, especially in formulations containing higher loadings of the microballoons, which can be attributed to the hydrogen bonding interactions between the phenolic groups of formed oligomers with that of the surface silanol groups of the glass microballoons. This interaction limits the catalytic activity of the oligomer, suppressing the autocatalytic effect. Alternative explanation for the same could be the lowered concentration of BF-a due to high loading of HGMs and thus availability to react with another monomer is affected. The BF-a resin was observed to undergo gelation at ~3690 s (Figure S2, Supporting Information), which increase to ~3800 s upon addition of HGMs (60% v/v).

Mechanical Properties of Syntactic Foams

Syntactic foams were fabricated as per the processing conditions reported in the experimental section. The pellets formed post compression were subjected to a controlled curing program (150 °C for 15 min, 180 °C for 15 min and 200 °C for 60 min). The polymerization of BF-a/HGM specimen can be followed by FTIR studies (Figure 5).[56] The characteristic absorptions of BF-a benzoxazine monomer observed at 1230 and 1030 cm^{-1} are attributable to the asymmetric and symmetric stretching of C–O–C group, respectively. In addition, the absorption at 1321 cm^{-1} is attributable to -CH_2- wagging and the peaks at 929 and 1498 cm^{-1} are associated with the trisubstituted benzene ring, which diminishes on polymerization. The benzoxazine monomer

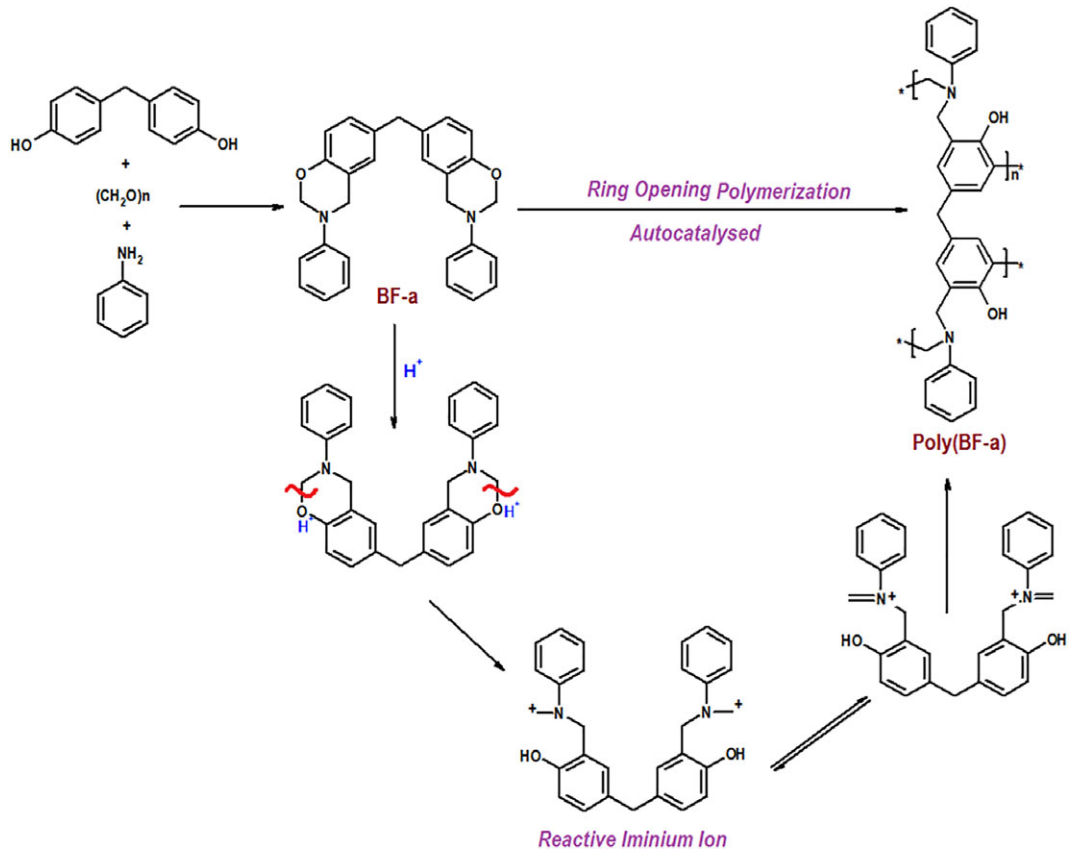

Figure 1. Scheme showing the synthesis and ring opening polymerization of BF-a. [Color figure can be viewed at wileyonlinelibrary.com]

undergoes polymerization and generates hydroxyl groups, which participate in intramolecular six-membered hydrogen bonding[28,57] (Figure S3, Supporting Information), which was evidenced by the appearance of peak at 3433 cm^{-1}. The presence of these hydroxyl groups is expected to result in enhanced interaction with surface of the glass microballoons. In addition to this, a new peak (1479 cm^{-1}) was observed which was assigned to the tetrasubstituted benzene rings occurring in the polybenzoxazine.

Syntactic foams primarily comprise of three distinct phases, that is, matrix, microballoons, and voids.[58] Porosity in matrix is indicative of the amount of air which tends to get entrapped within the matrix during the processing stages. Also, the possibility of microballoon rupture cannot be ruled out completely. The processing of syntactic foams should be performed such that damage of the microballoons is minimized, as their rupture will lead to an increase the density of the specimen. The designation of the

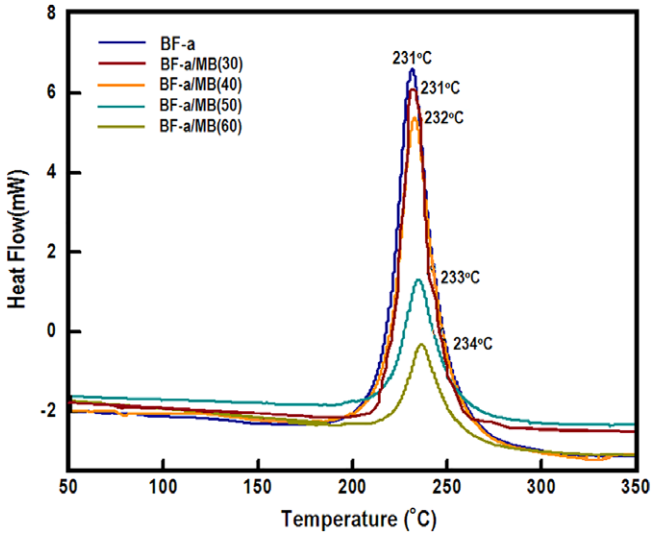

Figure 2. Curing profile of BF-a/glass microballoons formulation. [Color figure can be viewed at wileyonlinelibrary.com]

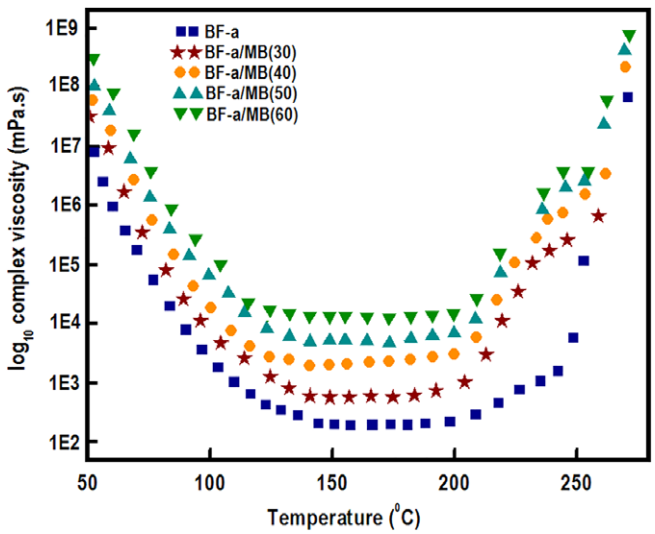

Figure 3. Viscosity–temperature curve of BF-a/HGM formulations. [Color figure can be viewed at wileyonlinelibrary.com]

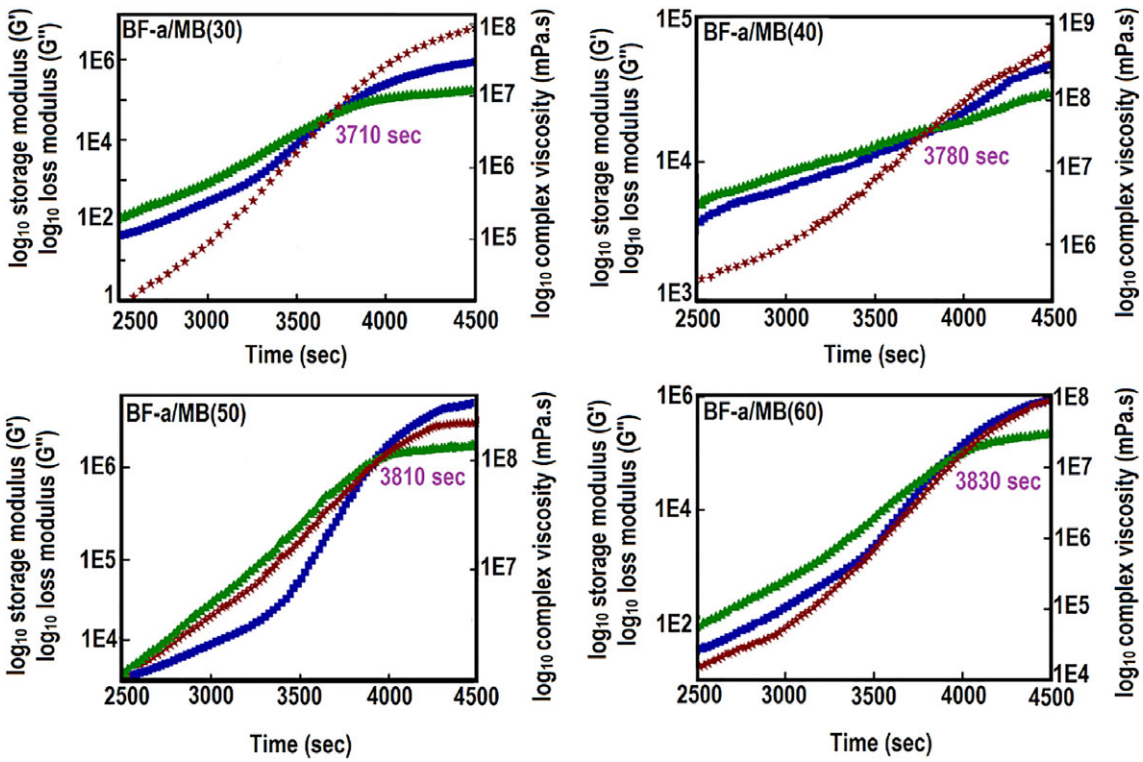

Figure 4. Increase in complex viscosity, storage, and loss modulus due to curing of the BF-a/HGM formulations under isothermal conditions (T = 200 °C). [Color figure can be viewed at wileyonlinelibrary.com]

specimens, with their respective theoretical as well as experimental densities and void content are presented in Table I.

As expected, cellular samples containing glass microballoons exhibit relatively lower densities than neat poly(BF-a) specimens. However, the experimental density of poly(BF-a)/HGM specimens was much lower than the theoretically predicted values. The difference in the densities was used to estimate the void percentage, which is included in Table I. It is particularly interesting to notice the large voidage in specimens containing high microballoon loading which indicates that the resin is unable to penetrate into the interstitial positions available within the microballoons.

It is appropriate to compare the mechanical performance of cellular structures in terms of specific mechanical properties, where the density of the material is kept in consideration. The quasi-static properties of the syntactic foams under compressive loading containing varying loading of microballoons (30–60% v/v) are presented in Figure 6 and Table S3, Supporting Information. Compressive strength of the specimens was found to decrease with increasing microballoon loading. Microballoon crushing is the primary mechanism responsible for the energy absorption of the foams in compressive mode,[59] which is usually quantified in terms of the area under the stress–strain curve till the end of plateau region. It is clear that the specific properties reach maxima at 40% glass microballoon loading. However, it is to be noted that the observed mechanical properties of polybenzoxazine-HGM foams are significantly higher than those reported for epoxy-HGM composites. For a representative bisphenol A-based epoxy resin, the compressive strength has been reported to be ~105 MPa,[60] which decreases to ~25 MPa at 60% loading of hollow microballoon (K15, density = 0.15 g cc^{-1}).[60] Cured cycloaliphatic epoxies exhibit relatively higher compressive strength ~140 MPa, which decreases to 60 MPa, as the glass microballoon loading increased to 60% v/v.[6] The compressive strength of vinyl ester–HGM (S22) (30–60% v/v) syntactic foams lies in between ~56 and24 MPa.[61]

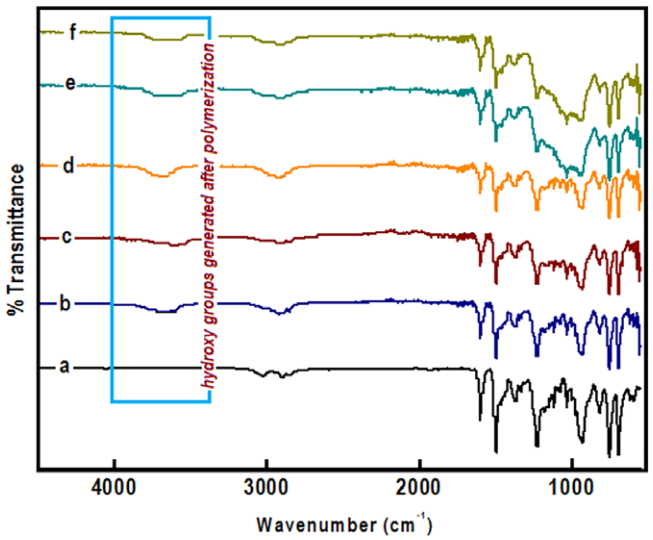

Figure 5. FTIR spectra of cured benzoxazine-HGM foams (a) BF-a, (b) poly(BF-a), (c) poly(BF-a)/MB (30), (d) poly(BF-a)/MB (40), (e) poly (BF-a)/MB (50), and (f) poly(BF-a)/MB (60). [Color figure can be viewed at wileyonlinelibrary.com]

Table I. Sample Designations, Densities, and Void Content of the PBz/HGM Syntactic Foams

Specimen designation	Theoretical density (g cm^{-3})	Experimental density (g m^{-3})	Void content (% v/v)
Poly(BF-a)	1.24	1.19 ± 0.01	4.0 ± 0.3
Poly(BF-a)/MB (30)	1.00	0.97 ± 0.08	3.0 ± 0.2
Poly(BF-a)/MB (40)	0.93	0.88 ± 0.06	5.3 ± 0.4
Poly(BF-a)/MB (50)	0.85	0.80 ± 0.05	5.8 ± 0.3
Poly(BF-a)/MB (60)	0.77	0.72 ± 0.06	6.0 ± 0.4

Representative compressive stress–strain curves of poly(BF-a)/HGM syntactic foams at different microballoon volume fractions are presented in Figure 7. The stress–strain curves reveal an initial linear elastic (Hookean) region, followed by an energy absorbing plateau region. The peak stress value is the compressive strength of the sample and the plateau region is visualized by an increase in strain without an appreciable increase in stress. In this plateau region, the microballoons are subjected to extensive compressive loads, which result in their crushing. Beyond this, there is an exponential increase in stress without any appreciable increase in strain: a region signaling the onset of densification.[58]

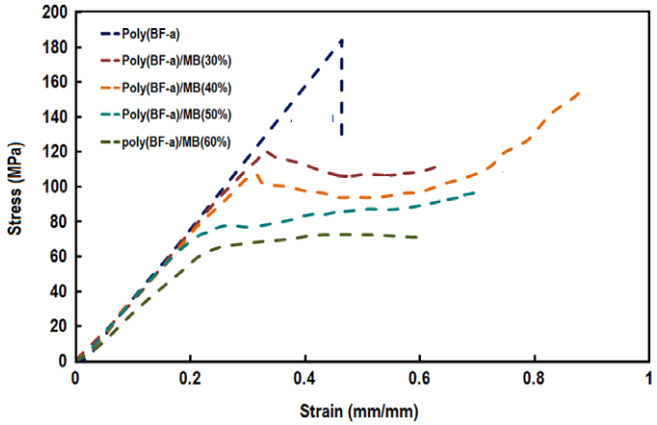

Figure 7. Stress–strain curves of poly(BF-a)/HGM specimens with different microballoon loadings (0–60%). [Color figure can be viewed at wileyonlinelibrary.com]

Thermal Property

Thermogravimetry (TG)-differential thermogravimetry (DTG) traces of poly(BF-a)/HGM syntactic foams containing HGMs in nitrogen atmosphere are presented in Figure 8. PBF-a began to lose weight at 280 °C and shows three-stage degradation centered approximately at 310, 430, and 520 °C, with the middle peak exhibiting the maximum rate of weight loss. Hemvichian and Ishida have performed a detailed analysis on the thermal decomposition of aromatic amine-based polybenzoxazines.[62] The degradation mechanism involves cleavage of C–C, C–O, and C–N bonds or chain scissions in the polybenzoxazine network which generated benzene derivatives, amines, phenolic compounds, and Mannich base compounds as primary decomposition products. Primary decomposition products further recombine or undergoes degradation to generate the secondary decomposition products such as 2,3-benzofuran derivatives, isoquinoline derivatives, biphenyl compounds, and phenanthridine and are crucial for char formation. These products after successive dehydrogenation, crosslinking, and aromatization finally leads to the formation of highly crosslinked molecules, that is, char.[62] The profile associated with the thermal degradation of poly(BF-a) was found to remain unaltered, except for the substantial increase in the char content, from 48 to 83% (at 600 °C) as the microballoon loading increased to 60%. van Krevelen's equation[51,63] was used to estimate the LOI (limiting oxygen index) values of the syntactic foam formulations, which indicates the minimum amount of oxygen (%) sufficient maintain combustion of the material. The same was calculated to be 36 for poly(BF-a) and increase substantially to 50 for poly(BF-a)/MB (60). The increased char yield is indicative of the improved fire retardance of the composites.

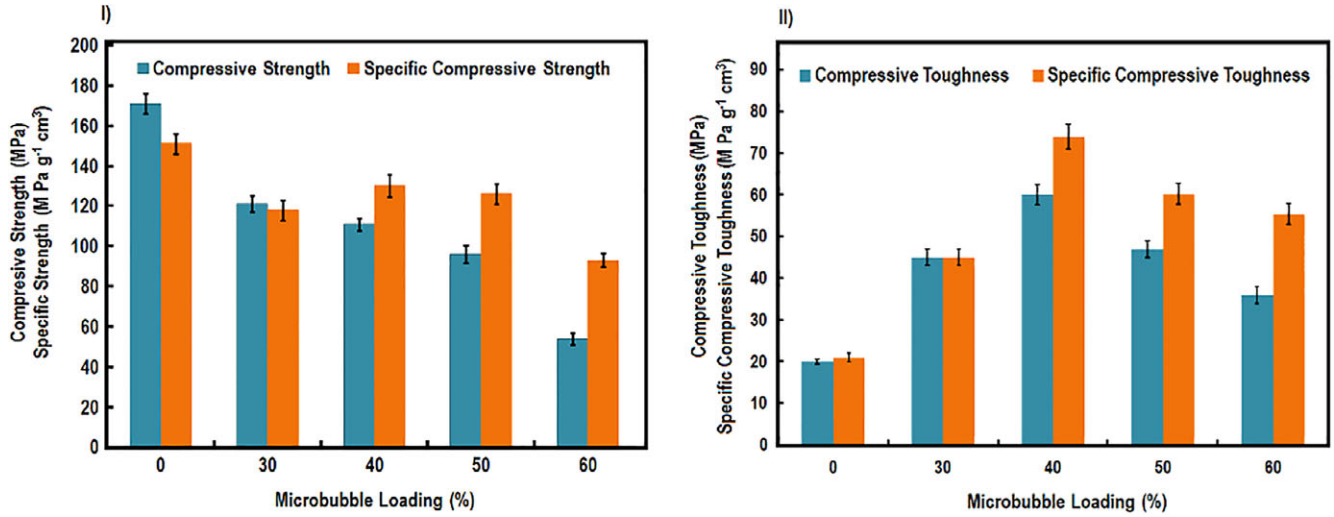

Figure 6. (I) Compression and specific compressive strength and (II) toughness and specific toughness of poly(BF-a)/HGM specimens at different microballoon loadings (0–60%). [Color figure can be viewed at wileyonlinelibrary.com]

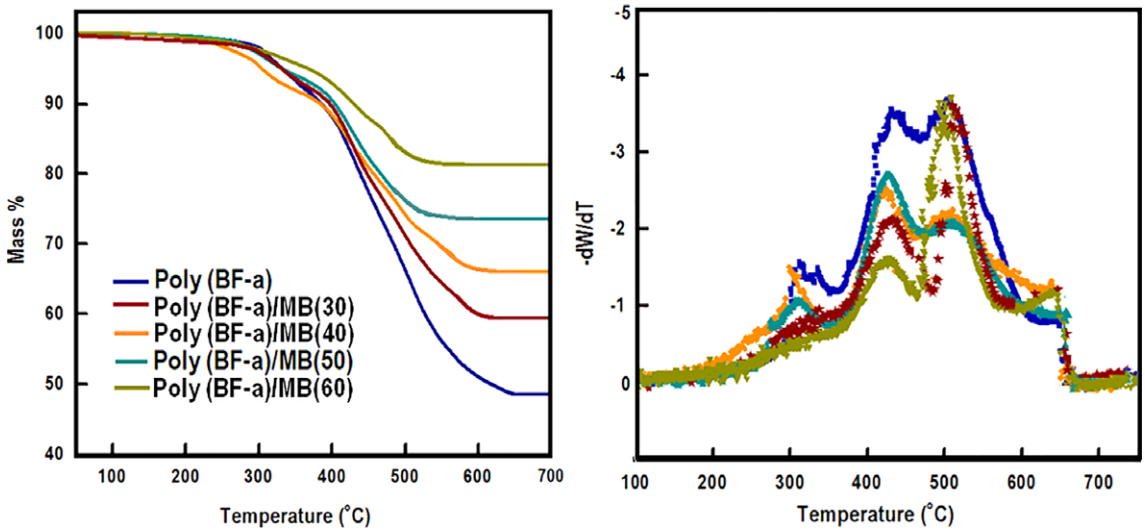

Figure 8. TG-DTG traces of poly(BF-a) and poly(BF-a)/HGM syntactic foams. [Color figure can be viewed at wileyonlinelibrary.com]

CONCLUSIONS

Poly(BF-a)/HGM syntactic foams were prepared for high performance applications. Effect of incorporation of HGMs on the curing parameters of BF-a was investigated using nonisothermal DSC. The processing window of the poly(BF-a)/HGM formulations was obtained through detailed rheological investigations. Temperature-sweep experiments reveal that the gelation point (crossover point of loss and storage modulus) for all the formulations remains unaffected on increasing the volume fraction of HGMs. However, gel time obtained from isothermal rheological experiments increases with increasing volume fraction of HGMs. Complete curing of the specimens under the optimized conditions was confirmed through FTIR. Associated with a diminution in specific gravity, the void percentage of syntactic foam increased with an increase in microballoon content. Poly(BF-a) syntactic foams under compressive loading shows excellent performance, which can be credited to the high compressive response of the glass balloons as well as the polymer matrix. Syntactic foams with HGM volume fraction 40%, was optimized with highest energy absorption under compressive loading. TG traces ensures high thermal stability of the prepared foams with T5% > 300 °C and char yield above 50%, thereby promoting their use in demanding applications.

ACKNOWLEDGMENTS

The authors gratefully acknowledge Director, CFEES for providing logistic support to perform this work.

REFERENCES

1. Gupta, N.; Zeltmann, S. E.; Shunmugasamy, V. C.; Pinisetty, D. *JOM*. **2014**, *66*, 245.
2. John, M.; Li, G. *Smart Mater. Struct.* **2010**, *19*, 075013.
3. Hiel, C.; Dittman, D.; Ishai, O. *Composites*. **1993**, *24*, 447.
4. Bardella, L.; Genna, F. *Int. J. Solids Struct.* **2001**, *38*, 7235.
5. Gupta, N.; Woldesenbet, E.; Mensah, P. *Compos. Part A: Appl. Sci. Manuf.* **2004**, *35*, 103.
6. Ullas, A. V.; Kumar, D.; Roy, P. K. *J. Appl. Polym. Sci.* **2018**, *135*, 45882.
7. Shutov, F. A. Chromatography/Foams/Copolymers; Springer Berlin Heidelberg: Heidelberg, Germany, **1986**. p. 63.
8. Gupta, N.; Nagorny, R. *J. Appl. Polym. Sci.* **2006**, *102*, 1254.
9. Ullas, A. V.; Qayyum, B.; Kumar, D.; Roy, P. K. *Polym. Plast. Technol. Eng.* **2016**, *55*, 1797.
10. Ullas, A. V.; Rahamattulah; Kumar, D.; Roy, P. K. *Polym. Plast. Technol. Eng.* **2016**, *55*, 937.
11. Ullas, A. V.; Sharma, P.; Chandel, P.; Sharma, P.; Kumar, D.; Roy, P. K. *Def. Sci. J.* **2018**, *68*, 210.
12. Shah, D. U.; Vollrath, F.; Porter, D. *Polym. J.* **2015**, *56*, 93.
13. Kenig, S.; Raiter, I.; Narkis, M. *J. Cell. Plast.* **1984**, *20*, 423.
14. McIlroy, H.. Bendix Corp., Kansas City, MO: **1980**.
15. Santhosh Kumar, K.; Reghunadhan Nair, C.; Ninan, K. *J. Appl. Polym. Sci.* **2008**, *108*, 1021.
16. Santhosh Kumar, K.; Reghunadhan Nair, C.; Ninan, K. *J. Appl. Polym. Sci.* **2008**, *107*, 1091.
17. Ishida, H.; Rimdusit, S. *Thermochim. Acta*. **1998**, *320*, 177.
18. Rimdusit, S.; Tanthapanichakoon, W.; Jubsilp, C. *J. Appl. Polym. Sci.* **2006**, *99*, 1240.
19. Sharma, P.; Kumar, D.; Roy, P. K. *ChemistrySelect*. **2016**, *1*, 6941.
20. Ishida, H.; Low, H. Y. *Macromolecules*. **1997**, *30*, 1099.
21. Ishida, H.; Allen, D. J. *J. Polym. Sci. Part B: Polym. Phys.* **1996**, *34*, 1019.
22. Lin, C. H.; Chang, S. L.; Shen, T. Y.; Shih, Y. S.; Lin, H. T.; Wang, C. F. *Polym. Chem.* **2012**, *3*, 935.
23. Kim, H.; Brunovska, Z.; Ishida, H. *Polym. J.* **1999**, *40*, 6565.
24. Ghosh, N.; Kiskan, B.; Yagci, Y. *Prog. Polym. Sci.* **2007**, *32*, 1344.
25. Yagci, Y.; Kiskan, B.; Ghosh, N. N. *J. Polym. Sci. Part A: Polym. Chem.* **2009**, *47*, 5565.
26. Shen, S. B.; Ishida, H. *Polym. Compos.* **1996**, *17*, 710.

27. Chernykh, A.; Agag, T.; Ishida, H. *Polym. J.* **2009**, *50*, 382.
28. Ishida, H. Handbook of Benzoxazine Resins; Elsevier: Cleveland, Ohio, **2011**. p. 3.
29. Sharma, P.; Lochab, B.; Kumar, D.; Roy, P. K. *ACS Sustain. Chem. Eng.* **2015**, *4*, 1085.
30. Sharma, P.; Shukla, S.; Lochab, B.; Kumar, D.; Roy, P. K. *Mater. Lett.* **2014**, *133*, 266.
31. Sharma, P.; Lochab, B.; Kumar, D.; Roy, P. K. *J. Appl. Polym. Sci.* **2015**, *132*, 42832.
32. Allen, D. J.; Ishida, H. *J. Appl. Polym. Sci.* **2006**, *101*, 2798.
33. Shukla, S.; Mahata, A.; Pathak, B.; Lochab, B. *RSC Adv.* **2015**, *5*, 78071.
34. Liu, J.; Ishida, H. *Macromolecules*. **2014**, *47*, 5682.
35. Liu, J.; Agag, T.; Ishida, H. *Polym. J.* **2010**, *51*, 5688.
36. Bunn, P.; Mottram, J. T. *Composites*. **1993**, *24*, 565.
37. Islam, M. M.; Kim, H. S. *Mater. Manuf. Process.* **2007**, *22*, 28.
38. Ambika Devi, K.; John, B.; Reghunadhan Nair, C.; Ninan, K. *J. Appl. Polym. Sci.* **2007**, *105*, 3715.
39. Pötschke, P.; Fornes, T. D.; Paul, D. R. *Polym. J.* **2002**, *43*, 3247.
40. Xiao, H.-W.; Huang, S.-Q.; Jiang, T. *J. Appl. Polym. Sci.* **2004**, *92*, 357.
41. Jain, A. K.; Gupta, N. K.; Nagpal, A. K. *J. Appl. Polym. Sci.* **2000**, *77*, 1488.
42. Raghu, P., Kunigal, S. and Larry, R. 48th AIAA/ASME/ASCE/AHS/ASC Structures, Structural Dynamics, and Materials Conference, Honululu Hawaii, 26 April 2007.
43. Wang, Y.-X.; Ishida, H. *Polym. J.* **1999**, *40*, 4563.
44. Shi, Z.; Yu, D. S.; Wang, Y.; Xu, R. *Eur. Polym. J.* **2002**, *38*, 727.
45. Jang, J.; Shin, S. *Polym. J.* **1995**, *27*, 601.
46. Burke, W. J. *J. Am. Chem. Soc.* **1949**, *71*, 609.
47. Burke, W. J.; Stephens, C. W. *J. Am. Chem. Soc.* **1952**, *74*, 1518.
48. Riess, G.; Schwob, J. M.; Guth, G.; Roche, M.; Laude, B. In Advances in Polymer Synthesis; Culbertson, B. M.; McGrath, J. E., Eds., Springer: Boston, MA, **1985**. p. 27.
49. McDonagh, A. F.; Smith, H. E. *J. Org. Chem.* **1968**, *33*, 8.
50. Chutayothin, P.; Ishida, H. *Macromolecules*. **2010**, *43*, 4562.
51. Sharma, P.; Kumar, D.; Roy, P. K. *Polym. J.* **2018**, *138*, 343.
52. Pratibha, S.; Devendra, K.; Roy, P. K. *ChemistrySelect*. **2017**, *2*, 5372.
53. Li, C.; Han, Q.; Guan, Y.; Zhang, Y. *Soft Matter*. **2014**, *10*, 8245.
54. Tung, C.-Y. M.; Dynes, P. J. *J. Appl. Polym. Sci.* **1982**, *27*, 569.
55. Rimdusit, S.; Ishida, H. *Rheol. Acta*. **2002**, *41*, 1.
56. Gârea, S.-A.; Iovu, H.; Nicolescu, A.; Deleanu, C. *Polym. Test.* **2007**, *26*, 162.
57. Ishida, H.; Lee, Y. H. *J. Polym. Sci. Part B: Polym. Phys.* **2001**, *39*, 736.
58. Gupta, N.; Kishore; Woldesenbet, E.; Sankaran, S. *J. Mater. Sci.* **2001**, *36*, 4485.
59. Dimchev, M.; Caeti, R.; Gupta, N. *Mater. Des.* **2010**, *31*, 1332.
60. Swetha, C.; Kumar, R. *Mater. Des.* **2011**, *32*, 4152.
61. Gupta, N.; Shunmugasamy, V. C. *Mater. Sci. Eng. A*. **2011**, *528*, 7596.
62. Hemvichian, K.; Ishida, H. *Polym. J.* **2002**, *43*, 4391.
63. van Krevelen, D. W. *Polym. J.* **1975**, *16*, 615.

International Journal of Research in Engineering and Innovation (IJREI)
journal home page: http://www.ijrei.com
ISSN (Online): 2456-6934

Thermodynamic analysis of vapour compression refrigeration systems using multiple evaporators at different temperatures with compound compression, individual and compound expansion valves with flash intercoolers

R.S. Mishra

Department of Mechanical & Production Engineering, Delhi Technological University Delhi, India

Abstract

In this investigation comparison and impact of environmental friendly refrigerants (R1234yf, , R1234ze, R227ea, R134a, R236fa, R245fa and R-32) on multiple evaporators at different temperature with compound compression and flash intercooler with individual and multiple throttle valves was carried out on the basis of energetic -exergetic approach. The Numerical computation was done for both systems and Comparison was done in terms of coefficient of performance, rational efficiency and total system defect. It was observed that for all considered refrigerants second law & first law efficiency of system-1 is higher (approximately 6.29% to 7.2%) than system-2 conversely system defect of system-2 is higher than system-1.In terms of energetic efficiency, rational efficiency and system defect for both systems, R32 shows minimum performance and performances of R123, R245fa and R236fa better with comparison of other selected refrigerants for system-1 and system-2. The performance of HFC-134a and HFO refrigerants were compared and it was observed that the performance of HFC134a and HFO-1234ze are similar with the 1% performance differences while HFO-1234yf has slightly less around 2 to 3% lower than HFC-134a which can replace HFC-134a in near future.

Keywords: Thermodynamic performances, Energy-Exergy Method, Irreversibility Analysis, Vapour Compression Refrigeration System

1. Introduction

Nowadays most of the energy utilize in cooling and air conditioning in industrial as well as for domestic applications. In addition with energy consumption, using of refrigerants in cooling and air conditioning having high GWP and ODP are responsible for global warming and ozone depletion. The primary requirements of ideal refrigerants is having good physical and chemical properties, due to good physical and chemical properties such as non-corrosiveness, non-toxicity, non- flammability, low boiling point, Chlorofluorocarbons (CFCs) have been used over the last many decades. But hydrochlorofluorocarbons (HCFCs) and Chlorofluorocarbons (CFCs) having large amount of chlorine content as well as high GWP and ODP, so after 90s refrigerants under these categories are almost prohibited [1].Most of the study has been carried out for the performance evaluation of vapour compression refrigeration system using energetic analysis. But with the help of first law analysis irreversibility destruction or losses in components of system unable to determined [2], so exergetic or second law analysis is the advanced approach for thermodynamic analysis which give an additional practical view of the processes [3,4,5]. In addition to this second law analysis also provides new thought for development in the existing system [6].In this paper great emphasis put on saving of energy and using of ecofriendly refrigerants due to increase of energy crises, global warming and depletion of ozone layer. In this investigation the work input required running the vapour compression refrigeration system reduced by using compound compression and work input further decrease by flash intercooling between two compressors using of ecofriendly refrigerants.

Corresponding author: R. S. Mishra
Email Address: hod.mechanical.rsm@dtu.ac.in

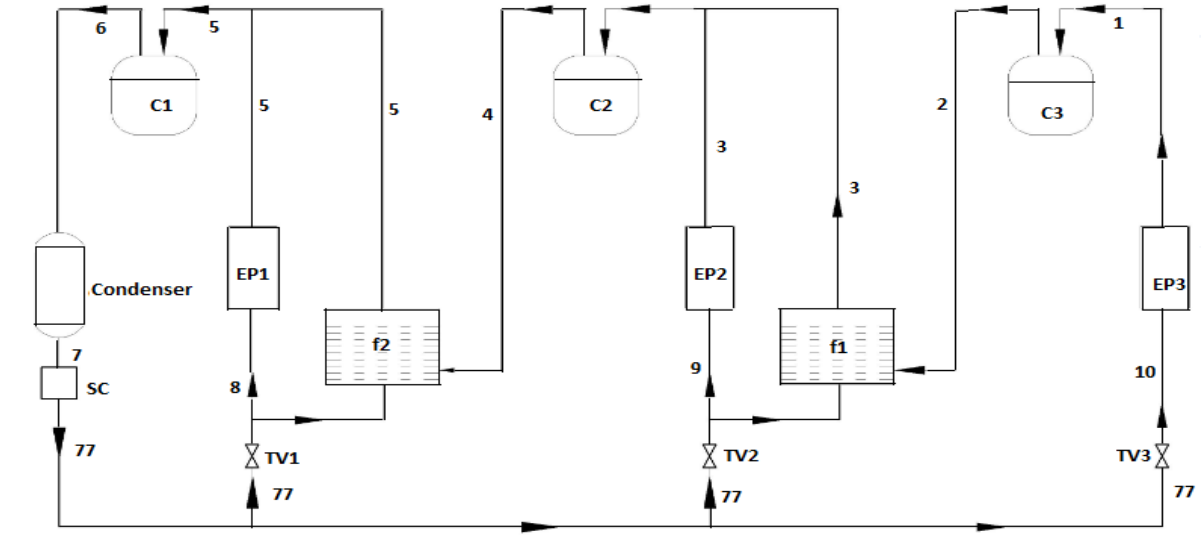

Figure 1: Multiple evaporators with compound compression and flash intercooler with individual throttle valves

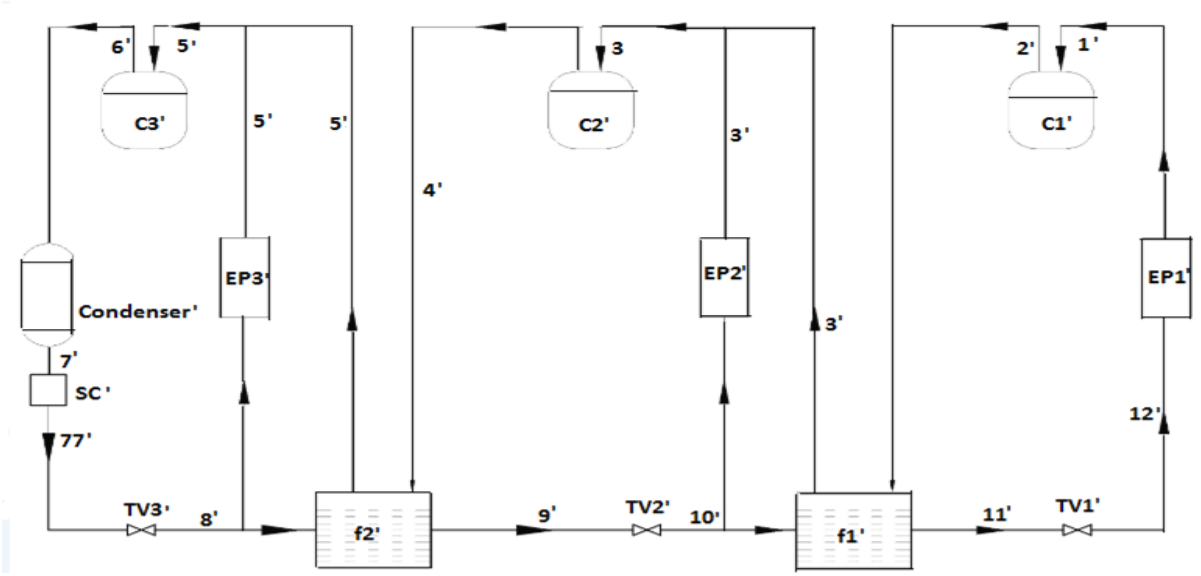

Figure 2: Multiple evaporators with compound compression and flash intercooler with multiple throttle valves

2. Thermodynamic modelling Energy –Exergy analysis of Vapour compression refrigeration systems using multiple evaporators at different temperatures with compound compression, flash intercooler and individual throttle valves (system-1)

Multiple evaporators at different temperatures with compound compression, flash intercooler and individual throttle valves (system-1) consists of compressors (C1, C2, C3) throttle valves (TV1, TV2, TV3), condenser and evaporators(EP1, EP2, EP3) as shown in Fig.1.

Exergy at any state is given as

$$X = (\Phi - \Phi_0) - T_0(s - s_0) \quad (2.1)$$

2.1 Energetic analysis

2.1.1 Mass flow analysis

$$\dot{m}_{c1} = \dot{m}_{e1} = \frac{\dot{Q}_{e1}}{(\Phi_1 - \Phi_{10})} \quad (2.2)$$

$$\dot{m}_{e2} = \frac{\dot{Q}_{e2}}{(\Phi_3 - \Phi_9)} \quad (2.3)$$

$$\dot{m}_{f1} = \frac{\dot{m}_{c1}(\Phi_2 - \Phi_3)}{(\Phi_3 - \Phi_9)} \quad (2.4)$$
$$\dot{m}_{c2} = \dot{m}_{c1} + \dot{m}_{e2} + \dot{m}_{f1} \quad (2.5)$$
$$\dot{m}_{e3} = \frac{\dot{Q}_{e3}}{(\Phi_5 - \Phi_8)} \quad (2.6)$$
$$\dot{m}_{f2} = \frac{\dot{m}_{c2}(\Phi_4 - \Phi_5)}{(\Phi_5 - \Phi_8)} \quad (2.7)$$
$$\dot{m}_{c3} = \dot{m}_{c2} + \dot{m}_{e3} + \dot{m}_{f2} \quad (2.8)$$

2.1.2 Power required running the compressors

$$P_{c1} = \frac{\dot{m}_{c1}(\Phi_2 - \Phi_1)}{60} \quad (2.9)$$
$$P_{c2} = \frac{\dot{m}_{c2}(\Phi_4 - \Phi_3)}{60} \quad (2.10)$$
$$P_{c3} = \frac{\dot{m}_{c3}(\Phi_6 - \Phi_5)}{60} \quad (2.11)$$

2.1.3 Energetic performance

$$\text{Energetic performance} = \frac{\dot{Q}_e}{P_c * 60} \quad (2.12)$$

2.2 Rate of exergy loss due to irreversibilties ($T_o\dot{S}_{gen}$) in various components of system-1

Compressors

$$(\mathrm{T_o\dot{S}_{gen}})_{c1} = \dot{W}_{c1} + \dot{m}_{c1}(X_2 - X_1) \quad (2.13)$$
$$(\mathrm{T_o\dot{S}_{gen}})_{c2} = \dot{W}_{c2} + \dot{m}_{c2}(X_4 - X_3) \quad (2.14)$$
$$(\mathrm{T_o\dot{S}_{gen}})_{c3} = \dot{W}_{c3} + \dot{m}_{c3}(X_6 - X_5) \quad (2.15)$$

Total irreversibility due to compressors

$$\Psi_c = (\mathrm{T_o\dot{S}_{gen}})_{c1} + (\mathrm{T_o\dot{S}_{gen}})_{c2} + (\mathrm{T_o\dot{S}_{gen}})_{c3} \quad (2.16)$$

Evaporators

$$(\mathrm{T_o\dot{S}_{gen}})_{e1} = \dot{m}_{e1}(X_1 - X_{10}) - \dot{Q}_{e1}\left(1 - \frac{T_0}{T_{r1}}\right) \quad (2.17)$$
$$(\mathrm{T_o\dot{S}_{gen}})_{e2} = \dot{m}_{e2}(X_3 - X_9) - \dot{Q}_{e2}\left(1 - \frac{T_0}{T_{r2}}\right) \quad (2.18)$$
$$(\mathrm{T_o\dot{S}_{gen}})_{e3} = \dot{m}_{e3}(X_5 - X_8) - \dot{Q}_{e3}\left(1 - \frac{T_0}{T_{r3}}\right) \quad (2.19)$$

Total irreversibility due to evaporators

$$\Psi_e = (\mathrm{T_o\dot{S}_{gen}})_{e1} + (\mathrm{T_o\dot{S}_{gen}})_{e2} + (\mathrm{T_o\dot{S}_{gen}})_{e3} \quad (2.20)$$

Condenser

$$\Psi_{cond} = (\mathrm{T_o\dot{S}_{gen}})_{cond} = \dot{m}_{c3}(X_6 - X_7) - \dot{Q}_e\left(1 - \frac{T_0}{T_r}\right) \quad (2.21)$$

Throttle Valves

$$(\mathrm{T_o\dot{S}_{gen}})_{tv1} = \dot{m}_{e1}(X_{77} - X_{10}) \quad (2.22)$$
$$\left(\mathrm{T_o\dot{S}_{gen}}\right)_{tv2} = (\dot{m}_{e2} + \dot{m}_{f1})(X_{77} - X_9) \quad (2.23)$$
$$(\mathrm{T_o\dot{S}_{gen}})_{tv3} = (\dot{m}_{e3} + \dot{m}_{f2})(X_{77} - X_8) \quad (2.24)$$

Total irreversibility due to throttle valves

$$\dot{\Psi}_{tv} = (\mathrm{T_o\dot{S}_{gen}})_{tv1} + (\mathrm{T_o\dot{S}_{gen}})_{tv2} + (\mathrm{T_o\dot{S}_{gen}})_{tv3} \quad (2.25)$$

Subcooler

$$\dot{\Psi}_{sc} = (\mathrm{T_o\dot{S}_{gen}})_{sc} = \dot{m}_{c3}(X_7 - X_{77}) \quad (2.26)$$

Flash intercoolers

$$(\mathrm{T_o\dot{S}_{gen}})_{f1} = \dot{m}_{f1}(X_9 - X_3 + \dot{m}_{c1}(X_2 - X_3) \quad (2.27)$$
$$(\mathrm{T_o\dot{S}_{gen}})_{f2} = \dot{m}_{f2}(X_8 - X_5) + \dot{m}_{c1}(X_4 - X_5) \quad (2.28)$$

Total irreversibility due to flash intercoolers

$$\dot{\Psi}_f = (\mathrm{T_o\dot{S}_{gen}})_{f1} + (\mathrm{T_o\dot{S}_{gen}})_{f2} \quad (2.29)$$

Total irreversibility destruction in system-1

$$\sum \Psi_k = \Psi_e + \Psi_c + \Psi_{cond} + \Psi_{tv} + \Psi_{sc} + \Psi_f \quad (2.30)$$

3. Energy–Exergy analysis of Vapour compression refrigeration systems using multiple evaporators at different temperatures with compound compression, flash intercooler and multiple throttle valves (system-2)

The main components of Multiple evaporators at different temperatures with compound compression, flash intercooler and multiple throttle valves (system-2) are compressors ($C1', C2', C3'$) throttle valves ($TV1', TV2', TV3'$), condenser ($cond'$) and evaporators ($EP1', EP2', EP3'$) as shown in Fig. 2. Exergy at any state is given as

$$X = (\Phi - \Phi_0) - T_0(s - s_0) \quad (3.1)$$

3.1 Energetic analysis

3.1.1 Mass flow analysis

$$\dot{m}_{c1'} = \dot{m}_{e1'} = \frac{\dot{Q}_{e1'}}{(\Phi_{1'} - \Phi_{12'})} \quad (3.2)$$
$$\dot{m}_{e2'} = \frac{\dot{Q}_{e2'}}{(\Phi_{3'} - \Phi_{10'})} + \dot{m}_{c1'}\left(\frac{x_{10'}}{1 - x_{10'}}\right) \quad (3.3)$$
$$\dot{m}_{f1'} = \frac{\dot{m}_{c1'}(\Phi_{2'} - \Phi_{3'})}{(\Phi_{3'} - \Phi_{10'})} \quad (3.4)$$
$$\dot{m}_{c2'} = \dot{m}_{c1'} + \dot{m}_{e2'} + \dot{m}_{f1'} \quad (3.5)$$
$$\dot{m}_{e3'} = \frac{\dot{Q}_{e3'}}{(\Phi_{5'} - \Phi_{8'})} + \dot{m}_{c2'}\left(\frac{x_{8'}}{1 - x_{8'}}\right) \quad (3.6)$$
$$\dot{m}_{f2'} = \frac{\dot{m}_{c2'}(\Phi_{4'} - \Phi_{5'})}{(\Phi_{5'} - \Phi_{8'})} \quad (3.7)$$

3.1.2 Power required for running the compressors

$$P_{c1'} = \frac{\dot{m}_{c1'}(\Phi_{2'}-\Phi_{1'})}{60} \quad (3.8)$$

$$P_{c2'} = \frac{\dot{m}_{c2'}(\Phi_{4'}-\Phi_{3'})}{60} \quad (3.9)$$

$$P_{c3'} = \frac{\dot{m}_{c3'}(\Phi_{6'}-\Phi_{5'})}{60} \quad (3.10)$$

3.1.3 Energetic performance

$$\text{Energetic performance} = \frac{\dot{Q}_{e'}}{P_{c'}*60} \quad (3.11)$$

3.2 Rate of exergy loss due to irreversibilities ($T_o\dot{S}_{gen}$) in various components of system-2

Compressor

$$(T_o\dot{S}_{gen})_{c1'} = \dot{W}_{c1'} + \dot{m}_{c1'}(X_{2'} - X_{1'}) \quad (3.12)$$

$$(T_o\dot{S}_{gen})_{c2'} = \dot{W}_{c2'} + \dot{m}_{c2'}(X_{4'} - X_{3'}) \quad (3.13)$$

$$(T_o\dot{S}_{gen})_{c3'} = \dot{W}_{c3'} + \dot{m}_{c3'}(X_{6'} - X_{5'}) \quad (3.14)$$

Total irreversibility due to compressors

$$\dot{\Psi}_{c'} = (T_o\dot{S}_{gen})_{c1'} + (T_o\dot{S}_{gen})_{c2'} + (T_o\dot{S}_{gen})_{c3'} \quad (3.15)$$

Evaporators

$$(T_o\dot{S}_{gen})_{e1'} = \dot{m}_{e1'}(X_{1'} - X_{12'}) - \dot{Q}_{e1'}\left(1 - \frac{T_0}{T_{r1'}}\right) \quad (3.16)$$

$$(T_o\dot{S}_{gen})_{e2'} = \dot{m}_{e2'}(X_{3'} - X_{10'}) - \dot{Q}_{e2'}\left(1 - \frac{T_0}{T_{r2'}}\right) \quad (3.17)$$

$$(T_o\dot{S}_{gen})_{e3'} = \dot{m}_{e3'}(X_{5'} - X_{8'}) - \dot{Q}_{e3'}\left(1 - \frac{T_0}{T_{r3'}}\right) \quad (3.18)$$

Total irreversibility due to evaporators

$$\dot{\Psi}_{c'} = (T_o\dot{S}_{gen})_{c1'} + (T_o\dot{S}_{gen})_{c2'} + (T_o\dot{S}_{gen})_{c3'} \quad (3.19)$$

$$\dot{\Psi}_{cond'} = (T_o\dot{S}_{gen})_{cond'} = \dot{m}_{c3'}(X_{6'} - X_{7'}) - \dot{Q}_{e'}\left(1 - \frac{T_0}{T_{r'}}\right) \quad (3.20)$$

Throttle Valves

$$(T_o\dot{S}_{gen})_{tv1'} = \dot{m}_{e1'}(X_{11'} - X_{12'}) \quad (3.21)$$

$$(T_o\dot{S}_{gen})_{tv2'} = \dot{m}_{c2'}(X_{9'} - X_{10'}) \quad (3.22)$$

$$(T_o\dot{S}_{gen})_{tv3'} = \dot{m}_{c3'}(X_{77'} - X_{8'}) \quad (3.23)$$

Total irreversibility due to throttle valves

$$\dot{\Psi}_{tv'} = (T_o\dot{S}_{gen})_{tv1'} + (T_o\dot{S}_{gen})_{tv2'} + (T_o\dot{S}_{gen})_{tv3'} \quad (3.24)$$

$$\dot{\Psi}_{sc'} = (T_o\dot{S}_{gen})_{sc'} = \dot{m}_{c3'}(X_{7'} - X_{77'}) \quad (3.25)$$

Flash intercoolers

$$(T_o\dot{S}_{gen})_{f1'} = \dot{m}_{f1'}(X_{10'} - X_{3'}) + \dot{m}_{c1'}(X_{2'} - X_{3'}) \quad (3.26)$$

$$(T_o\dot{S}_{gen})_{f2'} = \dot{m}_{f2'}(X_{8'} - X_{5'}) + \dot{m}_{c2'}(X_{4'} - X_{5'}) \quad (3.27)$$

Total irreversibility due to flash intercoolers

$$\dot{\Psi}_{f'} = (T_o\dot{S}_{gen})_{f1'} + (T_o\dot{S}_{gen})_{f2'} \quad (3.28)$$

Total irreversibility destruction in system-1

$$\sum \dot{\Psi}_{k'} = \dot{\Psi}_{e'} + \dot{\Psi}_{c'} + \dot{\Psi}_{cond'} + \dot{\Psi}_{tv'} + \dot{\Psi}_{sc'} + \dot{\Psi}_{f'} \quad (3.29)$$

3.3 Computation of Rational Efficiency

$$\text{Rational efficiency} = \frac{\text{Exergy of cooling load of evaporators}}{\text{Compressors work}} = \frac{\dot{EP}}{\dot{W}} \quad (3.30)$$

For System-1, the rational efficiency or exergetic efficiency can be expressed as

$$\text{Rational efficiency} = \frac{(\dot{Q}_{e1}+\dot{Q}_{e2}+\dot{Q}_{e3}) - T_o\left(\frac{\dot{Q}_{e1}}{T_{r1}}+\frac{\dot{Q}_{e2}}{T_{r2}}+\frac{\dot{Q}_{e3}}{T_{r3}}\right)}{P_{c'}*60} \quad (3.31)$$

For System-2, the rational efficiency or exergetic efficiency can be expressed as

$$\text{Rational efficiency} = \frac{\left(\dot{Q}_{e1'}+\dot{Q}_{e2'}+\dot{Q}_{e3'}\right) - T_o\left(\frac{\dot{Q}_{e1}}{T_{r1'}}+\frac{\dot{Q}_{e2}}{T_{r2'}}+\frac{\dot{Q}_{e3}}{T_{r3'}}\right)}{P_{c'}*60} \quad (3.32)$$

4. Result and Discussion

For carrying out the energetic and exergetic analysis a numerical model has been developed. Comparison of multiple evaporators at different temperatures with compound compression and flash intercooler with individual and multiple throttle valves and impact of chosen refrigerants on these systems was made using Engineering Equation Solver software [7].In this investigation following assumptions were made

1. Loads ($\dot{Q}_{e1}$, $\dot{Q}_{e2}$ and $\dot{Q}_{e3}$) on the evaporators EP_1, EP_2 and EP_3 are 35KW, 70KW and 105KW respectively.
2. Dead state temperature (T_0): 298K
3. Difference between evaporator and space temperature (T_r-T_e):5K.
4. Adiabatic efficiency of compressor (η_c):76%.
5. Dead state enthalpy (Φ_0) and entropy (s_0) of the refrigerants have been calculated corresponding to the dead state temperature (T_0) of 298K.
6. Temperature of evaporators EP_1, EP2 and EP3 are 263K, 273K and 283K respectively.
7. Condenser Temperature (T_c): 313 K
8. Degree of sub cooling (ΔT_{sc}): 10K.

Analysis of multi-stage vapour compression refrigerator and flash intercooler with individual or multiple throttle valves has been done in terms of COP, second law efficiency and irreversibility destruction. Energetic and exergetic performance of system-1 is higher than system-2 for selected temperature range of condenser and evaporators with chosen ecofriendly refrigerants. For both systems M 32 shows minimum thermal performance in terms of COP, second law efficiency and irreversibility. The validation of results for system-1 is given Table-1(a) respectively.

4.1 For System-1: Vapour compression refrigeration systems using multiple evaporators at different temperatures with compound compression, flash intercooler and individual throttle valves

Table-1(a): Validation of Results of VCRS for 100% compressor efficiency:Q_EVA_1=35"kW" Q_EVA_2=70"kW" Q_EVA_3=105 "kW"

Parameter	Program	Ref [12]
COP	6.44	6.50
Total Work (KW)	32.61	32.77

The performance of actual systems were carried out and shown in Table-1(b) & table-1(c) respectively. It was observed that system-2 gives less thermodynamic performance than system-1 for all refrigerants.

Table-1(b) Thermal Performances (First law efficiency and Second law efficiency, etc.) of vapour compression refrigeration system using alternative refrigerants (for Compressor efficiency_1= Compressor efficiency_2= Compressor efficiency_3=0.80) $T_{_EVA}$_1=263"K", $T_{_EVA}$_2=278"K", $T_{_EVA}$_3=283"K", T_R_1=268"K", T_R _2=283"K", T_R_3=288"K",

Refrigerants	COP	EDR	% ETA_II	Exergy_Fuel (KW)	Exergy_ Product (KW)	Rational efficiency	Second Law efficiency
R12	5.134	1.963	0.3375	40.9	13.81	0.3375	0.5747
R134a	5.091	1.988	0.3347	41.25	13.81	0.3347	0.5699
R1234yf	5.0	2.042	0.3287	42.0	13.81	0.3287	0.5597
R1234ze	5.112	1.975	0.3361	41.08	13.81	0.3361	0.5722
R-32	4.89	2.111	0.3215	42.95	13.81	0.3215	0.5473
R227ea	4.902	2.103	0.3223	42.84	13.81	0.3223	0.5488
R236fa	5.093	1.986	0.3346	41.23	13.81	0.3348	0.5701
R245fa	5.26	1.892	0.3458	39.93	13.81	0.3458	0.5888
R123	5.299	1.87	0.3484	39.63	13.81	0.3484	0.5932

Table-1.(c) Exergy Destruction of various components based on exergy of fuel of vapour compression refrigeration system using alternative refrigerants (for Compressor efficiency_1= Compressor efficiency_2= Compressor efficiency_3=0.80) $T_{_EVA}$_1=263"K", $T_{_EVA}$_2=278"K", $T_{_EVA}$_3=283"K", T_R_1=268"K", T_R _2=283"K", T_R_3=288"K",

Refrigerants	% loss Eva	% loss valve	% loss Condenser	% loss comp	% Loss_ Subcooler	% Loss_ (F1+F2)	% Loss_ Total
R12	10.34	7.058	27.91	18.87	2.039	0.02573	66.25
R134a	10.26	7.744	27.35	18.94	2.208	0.0240	66.53
R1234yf	8.505	8.545	28.21	19.23	2.632	0.00107	67.13
R1234ze	9.905	8.066	26.91	19.27	2.231	0.00393	66.39
R-32	9.892	7.104	30.63	17.76	2.366	0.1042	67.85
R227ea	9.733	10.28	25.67	19.29	2.806	0.0059	67.77
R236fa	10.30	8.199	26.62	19.30	2.095	0.000753	66.52
R245fa	10.51	6.29	27.8	19.25	1.553	0.009836	65.42
R123	10.38	5.634	28.63	19.06	1.429	0.02436	65.16

4.2 System-2 :Vapour compressor refrigeration system with Multiple evaporators at different temperatures with compound compression, multiple expansion valves and flash intercoolers

Table-2(a): Validation of Results of VCRS for 100% compressor efficiency using following loads Q_EVA_1=105"kW" Q_EVA_2=70"kW" Q_EVA_3=35"kW"

Parameter	Program	Ref [13]
COP	6.193	5.56
Total Work (KW)	33.91	38.4

The performance of actual systems were carried out and shown in Table-2(b) & table-2(c) respectively. It was observed that system-2 gives less thermodynamic performance than system-1 for all refrigerants. Although eco-friendly alternative nine refrigerants can replace R12 for domestic application because R12 has high GWP and ODP. It was observed that R123 gives better thermodynamic performances and also R245fa give similar (slightly less) performance than R123 refrigerant.

Table-2(b) Thermal Performances (First law efficiency and Second law efficiency, etc.) of vapour compression refrigeration system using alternative refrigerants (for Compressor efficiency_1= Compressor efficiency_2= Compressor efficiency_3=0.80) T_EVA_1=263"K", T_EVA_2=278"K", T_EVA_3=283"K", T_R_1=268"K", T_R_2=283"K", T_R_3=288"K", T_sub Cooler=303 "K" T_Cond=313"K"

Refrigerants	COP	EDR	ETA_II	Exergy_Fuel (KW)	Exergy_Product (KW)	Rational efficiency	II Law efficiency
R12	4.913	1.925	0.3419	42.75	14.62	0.3419	0.6538
R134a	4.864	1.954	0.3315	43.18	14.62	0.3315	0.6473
R1234yf	4.763	2.074	0.3395	44.09	14.62	0.3395	0.6338
R123456	4.877	1.946	0.3395	43.06	14.62	0.3395	0.6491
R-32	4.718	2.045	0.3284	44.51	14.62	0.3284	0.6279
R227ea	4.654	2.087	0.324	45.12	14.62	0.324	0.6194
R236fa	4.852	1.961	0.3377	43.28	14.62	0.3377	0.6457
R245fa	5.028	1.857	0.350	41.77	14.62	0.350	0.6691
R123	5.073	1.832	0.3531	41.39	14.62	0.3531	0.6752
R507a	4.541	2.164	0.3161	46.24	14.62	0.3161	0.6044

Table-2.(c) Exergy Destruction of various components based on exergy of fuel of vapour compression refrigeration system using alternative refrigerants (for Compressor efficiency_1= Compressor efficiency_2= Compressor efficiency_3=0.80) T_EVA_1=263"K", T_EVA_2=278"K", T_EVA_3=283"K", T_R_1= 268 "K", T_R_2=283"K", T_R_3=288"K",

Refrigerants	% loss Eva	% loss valve	% loss Condenser	% loss comp	% Loss_ Sub-cooler	% Loss_ (F1+F2)	% Loss_ Total	Rational efficiency
R12	8.514	9.223	26.74	19.29	1.984	0.06303	65.81	0.3419
R134a	8.261	10.15	26.19	19.35	2.144	0.0472	66.15	0.3315
R1234yf	6.386	11.27	27.09	19.59	2.534	0.0001	66.85	0.3395
R1234ze	7.822	10.6	25.86	19.62	2.152	0.0001	66.05	0.3395
R-32	8.194	9.226	28.58	18.84	2.355	0.4131	68.39	0.3284
R227ea	7.195	13.47	24.61	19.65	2.673	0.0001	67.6	0.324
R236fa	8.143	10.85	25.57	19.74	2.01	0.001834	66.23	0.3377
R245fa	8.748	8.398	26.75	19.70	1.501	0.03014	65.0	0.350
R123	8.792	7.499	27.53	19.55	1.385	0.07858	64.69	0.3531
R507a	7.275	9.226	23.89	19.42	3.517	0.0122	68.39	0.3161

The thermodynamic analysis developed in section 2 have been modified for finding the performances of systems-3.

4.3 System-3 : Vapour compressor refrigeration system with Multiple evaporators at different temperatures with compound compression, multiple expansion valves and flash intercoolers

Table-3(a) :Validation of Results of VCRS for 100% compressor efficiency using following loads Q_EVA_1=105"kW" Q_EVA_2=70"kW" Q_EVA_3=35"kW"

Parameter	Program	Ref [13]
COP	5.7940	4.90
Total Work (KW)	36.25	42.64

Table-3(b) Thermal Performances (First law efficiency and Second law efficiency, etc.) ofvapour compression refrigeration system using alternative refrigerants (for Compressor efficiency_1= Compressor efficiency_2= Compressor efficiency_3=0.80) T_EVA_1=263"K", T_EVA_2=278"K", T_EVA_3=283"K", T_R_1=268"K", T_R_2=283"K", T_R_3=288"K",

Refrigerants	COP	EDR	ETA_II	Exergy_Fuel (KW)	Exergy_Product (KW)	Rational efficiency	Second Law efficiency
R12	4.332	1.296	0.4588	48.48	22.24	0.4445	0.5765
R134a	4.28	1.336	0.4532	49.07	22.24	0.4382	0.5696
R1234yf	4.177	1.405	0.4423	50.23	22.24	0.4293	0.5559
R-32	4.151	1.383	0.4395	50.6	22.24	0.4289	0.5524
R227ea	4.08	1.849	0.4321	51.47	22.24	0.4145	0.543
R236fa	4.272	1.357	0.4524	49.15	22.24	0.4347	0.5686
R245fa	4.44	1.244	0.4702	47.3	22.24	0.4544	0.5908
R123	4.485	1.207	0.475	46.2	22.24	0.4608	0.5969

Table-3.(c) Exergy Destruction of various components based on exergy of fuel of vapour compression refrigeration system using alternative refrigerants (for Compressor efficiency_1= Compressor efficiency_2= Compressor efficiency_3=0.80) $T_{\_EVA}\_1=263$"K", $T_{\_EVA}\_2=278$"K", $T_{\_EVA}\_3=283$"K", T_R_1= 268 "K", T_R_2=283"K", T_R_3=288"K",

Refrigerants	% loss Eva	% loss valve	% loss Condenser	% loss comp	% Loss_ Subcooler	% Loss_ (F1+F2)	% Loss_ Total
R12	5.297	8.778	25,89	19.37	1.876	0.08344	57.54
R134a	5.843	9.616	25.61	19.41	2.039	0.06972	56.17
R1234yf	5.076	10.54	26.92	19.62	2.438	0.00255	57.03
R-32	4.741	9.463	27.61	18.84	2.223	0.4131	57.01
R227ea	7.302	12.52	24.85	19.65	2.596	0.0001	58.55
R236fa	6.626	9.795	25.27	19.69	1.926	0.001834	56.53
R245fa	5.455	7.434	25.91	19.61	1.419	0.03014	54.56
R123	4.65	6.687	26.42	19.51	1.302	0.07858	53.91

The thermodynamic analysis developed in section 3 have been modified for finding the performances of systems-4.

4.4 System-4 : Vapour compressor refrigeration system with Multiple evaporators at different temperatures with compound compression, multiple expansion valves and flash intercoolers

Table-4(a) :Validation of Results of VCRS for 100% compressor efficiency using following loads Q_EVA_1=105"kW" Q_EVA_2=70"kW" Q_EVA_3=35"kW"

Parameter	Program	Ref [13]
COP	5.797	5.56
Total Work (KW)	36.25	38.4

Table-4(b) Thermal Performances (First law efficiency and Second law efficiency, etc.) of vapour compression refrigeration system using alternative refrigerants (for Compressor efficiency_1= Compressor efficiency_2= Compressor efficiency_3=0.80) $T_{\_EVA}\_1=263$"K", $T_{\_EVA}\_2=278$"K", $T_{\_EVA}\_3=283$"K", T_R_1=268"K", T_R_2=283"K", T_R_3=288"K",

Refrigerants	COP	EDR	% ETA_II	Exergy_Fuel (KW)	Exergy_Product (KW)	Rational efficiency	Second Law efficiency
R12	4.589	1.143	0.4860	45.76	22.24	0.4445	0.6107
R134a	4.576	1.159	0.4846	45.89	22.24	0.4382	0.6089
R1234yf	4.537	1.188	0.4805	46.29	22.24	0.4293	0.6038
R-32	4.396	1.227	0.4656	47.77	22.24	0.4289	0.5851
R227ea	4.492	1.231	0.4757	46.75	22.24	0.4145	0.5978
R236fa	4.616	1.159	0.4877	45.60	22.24	0.4347	0.6129
R245fa	4.70	1.096	0.4977	44.68	22.24	0.4544	0.6255
R123	4.709	1.081	0.4986	44.6	22.24	0.4608	0.6266

Table-4.(c) Exergy Destruction of various components based on exergy of fuel of vapour compression refrigeration system using alternative refrigerants (for Compressor efficiency_1= Compressor efficiency_2= Compressor efficiency_3=0.80) $T_{\_EVA}\_1=263$"K", $T_{\_EVA}\_2=278$"K", $T_{\_EVA}\_3=283$"K", T_R_1= 268 "K", T_R_2=283"K", T_R_3=288"K",

Refrigerants	% loss Eva	% loss valve	% loss Condenser	% loss comp	% Loss_ Subcooler	% Loss_ (F1+F2)	% Loss_ Total
R12	4.146	4.748	25,27	19.41	1.876	0.08344	55.55
R134a	4.599	5.092	24.91	19.46	2.039	0.06972	56.19
R1234yf	3.686	5.247	26.03	19.68	2.438	0.00255	57.07
R-32	3.66	5.193	26.97	18.84	2.223	0.4131	57.11
R227ea	5.872	6.463	23.90	19.72	2.596	0.0001	58.55
R236fa	5.294	3.837	24.5	19.74	1.926	0.001834	56.53
R245fa	4.272	5.066	25.3	19.70	1.419	0.03014	54.56
R123	3.574	3.535	25.87	19.55	1.302	0.07858	53.92

5. Conclusion

Analysis multiple evaporators at different temperature with compound compression and flash intercooler with individual throttle valves and multiple evaporators at different temperature with compound compression and flash intercooler with multiple throttle valves have been made in terms of energetic efficiency, exergetic efficiency and irreversibility destruction and from the current study following conclusions were made:

(i) Energetic and exergetic performance of system-1 is higher than system-2 for selected temperature range of condenser and evaporators for chosen ecofriendly refrigerants.

(ii) System defect in sytem-1is less as compare with system-2, therefore system-1 is better system than system-2 for

selected ecofriendly refrigerants.

(iii) R32 shows minimum performance in terms of first law efficiency, second law efficiency and system defect for both systems.

(iv) Performances of R245fa are slightly lower than R123 however it's higher than R236fa and R134a better with comparison of other selected refrigerants for system-1 and system-2. But R123 containing chrine content although has lower GWP and R227ef, R236fa and R245fa are high GWP than R134aand limited to industrial application, therefore R1234yf is recommended for both systems for replacing HFC-134a refrigerant in near future.

References

[1] D. Mohanti and P.Hasan, "Analysis of mechanical properties of aluminium alloy, International journal of research in engineering and innovation, vol. 2 issue 4 Dec. 2001, pp. 2127-2130

[2] Camelia Stanciu,Adina Gheorghian,Dorin Stanciu, Alexandru Dobrovicescu(2011)-Exergy analysis and refrigerant effect on the operation and performance limits of a one stage vapour compression refrigeration system,Termotehnia, 36-42

[3] V. Siva Reddy,N. L. Panwar ,S. C. Kaushik(2011)-Exergetic analysis of a vapour compression refrigeration system with R134a, R143a, R152a, R404A, R407C, R410A, R502 and R507A,Clean Techn Environ Policy,14:47–53

[4] J.U. Ahamed, R. Saidur, H.H. Masjuki(2011)-A review on exergy analysis of vapor compression refrigeration system, Renewable and Sustainable Energy Reviews,15: 1593–1600

[5] Szargut D, Petela R, Egzergia(1965),WNT

[6] Szargut J, Morris D, Steward F(1998)-Exergy analysis of thermal, chemical and metallurgical processes.,New York: Hemisphere Publishing Corporation

[7] Saidur R, Masjuki HH, Jamaluddin MY(2007)-An application of energy and exergyanalysis in residential sector in Malaysia. Energy Policy, 35:1050–63.

[8] Klein, S.A., Alvarado, F., 2005. Engineering Equation Solver, Version 7.441. F Chart Software, Middleton, WI.

[9] Arora & Domkundwar (2009), Refrigeration and air conditioning, Dhanpat Rai & Sons, New Delhi.

Nomenclature

COP	coefficient of performance (non-dimensional)
VCR	vapour compression refrigeration
CFC	chlorofluorocarbon
HCFC	hydrochlorofluorocarbon
$\dot{Q}$	rate of heat transfer (kW)
$\dot{W}$	work rate (kW)
T	temperature (K)
ΔT_{sc}	degree of subcooling
$\dot{E}P$	exergy rate of product (kW)
TV	throttle valve
φ	dryness fraction(non-dimensional)
EP	evaporator
Ψ	specific enthalpy (kJ/kg)
$\dot{E}D$	rate of exergy destruction (kW)
E_x	exergy rate of fluid (kW)
$\dot{m}$	mass flow rate (kg/s)
s	specific entropy (kJ/kgK)
$\dot{E}F$	exergy rate of fuel (kW)
η	efficiency (non-dimensional)
c	compressor
sc	sub-cooler
ODP	ozone depletion potential
GWP	global warming potential

Subscript

e	evaporator
comp	compressor
o	dead state
r	refrigerant, space to be cooled
TV	throttle valve
sc	subcooler
k	kth component
cond	condenser
ev	expansion valve
ex	exergetic

Cite this article as: R.S. Mishra, Thermodynamic analysis of vapour compression refrigeration systems using multiple evaporators at different temperatures with compound compression, individual and compound expansion valves with flash intercoolers, *International journal of research in engineering and innovation (IJREI)*, vol 2, issue 6 (2018), 581-588.